CHIRAL IRIDIUM(III) AND RUTHENIUM(II) COMPLEXES AS PHOSPHORESCENT SCAFFOLDS FOR HETEROMETALLIC SUPRAMOLECULAR SELF-ASSEMBLY

Diego Rota Martir

A Thesis Submitted for the Degree of PhD
at the
University of St Andrews

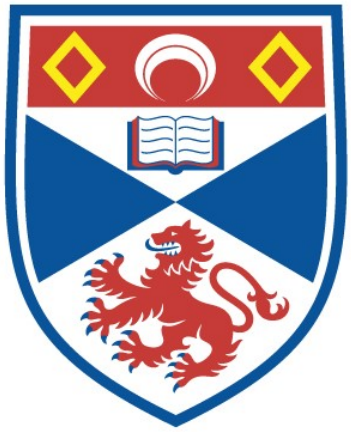

2018

Chiral Iridium(III) and Ruthenium(II) Complexes as Phosphorescent Scaffolds for Heterometallic Supramolecular Self-Assembly

Diego Rota Martir

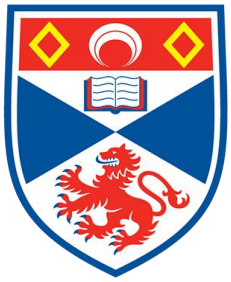

University of
St Andrews

This thesis is submitted in partial fulfilment for the degree of

Doctor of Philosophy (PhD)

at the University of St Andrews

March 2018

Candidate's declaration

I, Diego Rota Martir, do hereby certify that this thesis, submitted for the degree of PhD, which is approximately 70,000 words in length, has been written by me, and that it is the record of work carried out by me, or principally by myself in collaboration with others as acknowledged, and that it has not been submitted in any previous application for any degree.

I was admitted as a research student at the University of St Andrews in September 2014.

I confirm that no funding was received for this work.

Date Signature of candidate

Supervisor's declaration

I hereby certify that the candidate has fulfilled the conditions of the Resolution and Regulations appropriate for the degree of PhD in the University of St Andrews and that the candidate is qualified to submit this thesis in application for that degree.

Date Signature of supervisor

Permission for publication

In submitting this thesis to the University of St Andrews we understand that we are giving permission for it to be made available for use in accordance with the regulations of the University Library for the time being in force, subject to any copyright vested in the work not being affected thereby. We also understand, unless exempt by an award of an embargo as requested below, that the title and the abstract will be published, and that a copy of the work may be made and supplied to any bona fide library or research worker, that this thesis will be electronically accessible for personal or research use and that the library has the right to migrate this thesis into new electronic forms as required to ensure continued access to the thesis.

I, Diego Rota Martir, have obtained, or am in the process of obtaining, third-party copyright permissions that are required or have requested the appropriate embargo below.

The following is an agreed request by candidate and supervisor regarding the publication of this thesis:

Printed copy

Embargo on all of print copy for a period of 1 year on the following ground(s):

- Publication would preclude future publication

Supporting statement for printed embargo request

Not all the material in this thesis has been published at the current stage.

Electronic copy

Embargo on all of electronic copy for a period of 1 year on the following ground(s):

- Publication would preclude future publication

Supporting statement for electronic embargo request

Not all the material in this thesis has been published at the current stage.

Title and Abstract

- I agree to the title and abstract being published.

Date Signature of candidate

Date Signature of supervisor

Underpinning Research Data or Digital Outputs

Candidate's declaration

I, Diego Rota Martir, understand that by declaring that I have original research data or digital outputs, I should make every effort in meeting the University's and research funders' requirements on the deposit and sharing of research data or research digital outputs.

Date Signature of candidate

Permission for publication of underpinning research data or digital outputs

We understand that for any original research data or digital outputs which are deposited, we are giving permission for them to be made available for use in accordance with the requirements of the University and research funders, for the time being in force.

We also understand that the title and the description will be published, and that the underpinning research data or digital outputs will be electronically accessible for use in accordance with the license specified at the point of deposit, unless exempt by award of an embargo as requested below.

The following is an agreed request by candidate and supervisor regarding the publication of underpinning research data or digital outputs:

Embargo on all of electronic files for a period of 1 year on the following ground(s):

- Publication would preclude future publication

Supporting statement for embargo request

Not all the material in this thesis has been published at the current stage.

Date Signature of candidate

Date Signature of supervisor

"This is why alchemy exists," the boy said. So that everyone will search for his treasure, find it, and then want to be better than he was in his former life. Lead will play its role until the world has no further need for lead; and then lead will have to turn itself into gold. That's what alchemists do. They show that, when we strive to become better than we are, everything around us becomes better, too.

Paulo Coelho, The Alchemist

Abstract

This thesis explores the design, synthesis and optoelectronic properties of supramolecular photoactive materials based on chiral iridium(III) and ruthenium(II) metalloligands. Our design strategies aim to create a high concentration of chromophoric units that, when self-assembled in well-defined geometrical arrangements, exhibit emergent photophysical properties.

The first chapter provides an overview of the fundamental photophysical properties of transition metal complexes and a brief introduction to bimolecular energy and electron transfer processes. Special attention will then be devoted to describing the photophysical properties and applications of supramolecular photoactive materials based on iridium(III) luminophores. We begin by describing iridium-based soft materials such as ion-paired iridium complexes commonly known as soft-salts, liquid crystals, supramolecular gels, colloidal structures and assemblies developed through H-bonding and π-π-stacking interactions. Next, we describe luminescent iridium-based coordination polymers, metal-organic frameworks (MOFs) and discrete structures, followed by an overview of luminescent Ir-based macrocycles, capsules and cages. Guest Ir(III) complexes encapsulated within the cavities of cage-type structures are also presented. Finally, the last part of the first chapter provides a summary on the development of phosphorescent cages based on ruthenium(II) complexes, describing their photophysical properties and applications.

Chapter 2 describes the synthesis, characterisation and optoelectronic properties of two families of iridium(III) complexes of the form of $[Ir(C\hat{}N)_2(dtBubpy)]PF_6$ (where C^N is ppy = 2-phenylpyridinato, mesppy = 2-phenyl-4-mesytilpyridinato and dtBubpy is 4,4′-di*tert*-butyl-2,2′-bipyridine) in both their Λ- and Δ-enantiopure and racemic configurations. Light-Emitting Electrochemical Cells (LEECs) using Λ and Δ enantiomers as well as the racemic mixture of both families have been prepared and the device performances were tested. Importantly, different solid-state photophysical properties exist between enantiopure and racemic emitters, which are also reflected in the device performances.

Chapter 3 discusses the self-assembly of racemic and enantiopure iridium or ruthenium metalloligands of the form of $[M(L\hat{}X)_2(qpy)]^{n+}$ (M is either Ir with L^X: mesppy and dFmesppy or Ru with L^X: dtBubpy) with Pd^{2+} ions, to form chiral iridium(III) and

ruthenium(II) supramolecular cages of the general composition of $[Pd_4M_8]^{n+}$. Both families of cages are phosphorescent. The iridium cages provides a suitably sized cavity to host large guest molecules. Encapsulation and energy transfer have been observed between the green/blue-emitting complexes $[Ir(C\hat{}N)_2(CN)_2]^-$ (C^N is either ppy or dFppy: 4,6-difluorophenylpyridinato) and the red-emitting cage $[Pd_4Ir_8]^{16+}$. The ruthenium cage, on the other hand, exhibits a near infra-red emission with a photoluminescence quantum yield of 6.9%, which is remarkably high considering the emission maximum of 710 nm.

In chapter 4 we report dynamic supramolecular diads and triads composed of the iridium or ruthenium metalloligands $[M(L\hat{}X)_2(qpy)]^{n+}$ and zinc tetraphenylporphyrin (ZnTPP) assembled through non-covalent interactions between the distal pyridine moieties of the qpy ligand and the zinc of ZnTPP. The assemblies have been comprehensively characterised in solution by NMR spectroscopies and the crystal structures of the Ir-ZnTPP assemblies have been elucidated by X-ray diffraction. The optoelectronic properties of the assemblies and the electronic interaction between the iridium or ruthenium and porphyrin chromophoric units have been explored with detailed photophysical measurements, supported by time-dependent density functional theory (TD-DFT) calculations. Radiative energy transfer is observed between the Ir donor and the ZnTPP acceptor, while photoinduced electron transfer is promoted from ZnTPP to the Ru complex.

Chapter 5 discusses a phosphorescent coordination polymer formed through the self-assembly between the iridium complex $[Ir(mesppy)_2(qpy)]PF_6$ with $AgPF_6$ through $N_{qpy}\cdots Ag\cdots N_{qpy}$ linear coordination. The structure of the coordination polymer has been characterised by x-ray crystallography and its emission properties investigated in $MeNO_2$ by steady-state and time-resolved emission spectroscopy. Interestingly, the silver metal ions promoted a red-shift in the emission of the coordination polymer in $MeNO_2$ but did not adversely influence the photoluminescence quantum yield and emission lifetime of the polymer, which remained almost unchanged compared to the Ir metalloligand.

Declaration

I fully acknowledge that the work presented in this thesis is my own. However, the nature of the research undertaken during my PhD is highly interdisciplinary, and thus contributions from collaborators and co-authors are listed below.

Chapter 1: I am the primary author of the text. Major aspects of this text were published as a review article.

Diego Rota Martir, Eli Zysman-Colman, Supramolecular Iridium(III) Assemblies, *Coord. Chem. Rev.* **2018**, 364, 86-117

Chapter 2: Synthesis, characterisation and the spectroscopy described in this chapter was carried out by me. Single crystals were grown by me while crystals data collection and structure solving was performed by Dr. David B. Cordes at the University of St Andrews. Light-Emitting electrochemical cells (LEECs) were fabricated by Dr. Antonio Pertegàs and Dr. Cristina Momblona in the group of Dr. Henk Bolink at the University of Valencia. The spectroscopic data analysis was carried out by me, x-ray structure analysis was done Dr. David B. Cordes and Prof. Alexandra M. Z. Slawin, while the LEECs data analysis was carried out by Dr. Antonio Pertegàs, Dr. Cristina Momblona and Dr. Henk Bolink. I am the primary author the text. The work described in this chapter was published:

Diego Rota Martir, Cristina Momblona, Antonio Pertegàs, David B. Cordes, Alexandra M. Z. Slawin, Henk J. Bolink, and Eli Zysman-Colman, *ACS Appl. Mater. Interfaces*, **2016**, 8, 33907-33915

Chapter 3: Synthesis, characterisation and spectroscopy of the complexes was carried out by me. The self-assembly, the spectroscopy of the supramolecular cages was carried out by me. Single crystals were grown by me while crystals data collection and structure solving of all the iridium complexes are supramolecular cages was performed by Dr. David B. Cordes. Prof. Alexandra M. Z. Slawin carried out the crystals data collection and structure solving of the ruthenium complex $[Ru(dtBubpy)_3(qpy)](PF_6)_2$. The preliminary simulation of the structures of the iridium cages was carried out by me with the help of Dr. Herbert A. Fruchtl (University of St Andrews), while the DFT structures optimisation were carried out by Dr. Daniel Escudero and Prof. Denis Jacquemin (University of Nantes). The preliminary simulation of the ruthenium cage was carried out by me while its DFT

structure optimisation and TD-DFT calculations were carried out by Dr. Daniel Escudero and Prof. Denis Jacquemin. HR-ESI-MS spectra of supramolecular cages were collected by Stuart L. Warriner and me at the University of Leeds. Transmission Electron Microscopy measurements of Ru cages were carried out by Ross Blackley (University of St Andrews). I am the primary author the text. Part of the work describing the supramolecular iridium and ruthenium cages was published:

Diego Rota Martir, Daniel Escudero, Denis Jacquemin, David B. Cordes, Alexandra M. Z. Slawin, Herbert A. Fruchtl, Stuart L. Warriner, and Eli Zysman-Colman, *Chem. Eur. J.* **2017**, 23, 14358-14366

Diego Rota Martir, David B. Cordes, Alexandra M. Z. Slawin, Daniel Escudero, Denis Jacquemin, Stuart L. Warriner and Eli Zysman-Colman, *Chem. Commun.* **2018**, accepted manuscript

Chapter 4: Synthesis, characterisation, spectroscopy and electrochemistry of the iridium complexes and Ir-ZnTPP assemblies was carried out by me. The ^{1}H NMR titration experiments of the Ir-ZnTPP assemblies were carried out by me with the help of Dr. Tamara Kosikova and Prof. Douglas Philp (University of St Andrews). The fitting of the data to obtain the association constants was done by Prof. Douglas Philp and me. Low temperature NMR experiments were carried out by Melanja Smith (University of St Andrews). Synthesis, characterisation, spectroscopy and electrochemistry of the ruthenium complexes was carried out by Mattia Averardi (visiting student at the University of St Andrews). The preparation and spectroscopic investigation of the Ru-ZnTPP assemblies was done by Mattia Averardi under my supervision. The ^{1}H NMR titration experiments of the Ru-ZnTPP assemblies were carried out by Mattia Averardi under my supervision, while the fitting of the data to obtain the association constants was done by me. TD-DFT calculations were carried out by Dr. Daniel Escudero and Prof. Denis Jacquemin (University of Nantes). Streak camera investigation was carried out by Dr. Gordon J. Hedley in the group of Prof. Ifor D. W. Samuel (University of St Andrews). I am the primary author of the text. The work in this chapter has been published:

Diego Rota Martir, Gordon J. Hedley, David B. Cordes, Alexandra M.Z. Slawin, Daniel Escudero, Denis Jacquemin, Tamara Kosikova, Douglas Philp, Daniel M. Dowson, Sharon E. Ashbrook, Ifor D. W. Samuel, and Eli Zysman-Colman, *Dalton Trans.* **2016**, 45, 17195-17205

Diego Rota Martir, Mattia Averardi, Daniel Escudero, Denis Jacquemin, and Eli Zysman-Colman, *Dalton Trans.* **2017**, 46, 2255-2262

Chapter 5: Synthesis, characterisation and spectroscopy of the iridium-silver polymer was carried out by me. Single crystals were grown by me while crystals data collection and structure solving was performed by Dr. David B. Cordes. I am the primary author the text.

The complete list of publications arising from work in this Ph.D. (including those that do not form the body of this thesis) is reported in the appendix.

Research Data access statement

Research data underpinning this thesis are available at [DOI]:
http://dx.doi.org/10.17630/b2ccc0c6-5a00-420e-92d4-d4d64173d259

Acknowledgements

I have to thank many people inside and outside St Andrews for taking part of my Ph.D. journey.

Firstly and foremost I would like to thank Dr. Eli Zysman-Colman for the constant support, guidance and help provided me throughout my time in St Andrews and abroad.

I would like to thank all of the St Andrews chemistry staff, in the stores and in the services: a special gratitude goes to Dr. David B. Cordes and Alexandra M. Z. Slawin for the x-ray crystallography and to Dr. Tomas Lebl for helping with NMR techniques. Thank you also to the many collaborators I had the pleasure to work with for various projects; Prof. Ifor Samuel, Dr. Ashu Bensal, Dr. Gordon J. Hedley for the work carried out on OLED devices and streak camera experiments; Dr. Henk J. Bolink, Dr. Cristina Momblona and Dr. Antonio Pertegàs for the LEEC devices; Dr. Daniel Escudero and Prof. Denis Jacquemin for computations; Dr. Stuart L. Warriner for the ESI-MS experiments; Prof. Michaele J. Hardie, Dr. Victoria E. Pritchard and Samuel Oldknow for the interesting work carried out on supramolecular cages; Prof. Douglas Philp and Tamara Kosikova for helping with NMR experiments and data fitting; Dr. Herbert A. Fruchtl for the help with the molecular simulation; Dr. Daniel M. Dawson and Prof. Sharon E. Ashbrook for solid-state NMR experiments.

Thank you to Dr. Nitin T. Patil and all the group members at NCL Pune, and to Prof. Makoto Fujita, Dr. Hiroki Takezawa and all the group members at The University of Tokyo for hosting me in their institutions and supporting me during the collaborative projects.

Thank you to all the great colleagues I had the pleasure to work with during my time spent in St Andrews, Pune and Tokyo. A special thank you to the guys I began this PhD with: Dr. Nail Shavaleev, Dr. Adam Henwood, Mark Huyton, Claus Hierlinger, Mattia Averardi, Ben Armitage, Laura Abad Galan and Dr. Michael Yin Wong. Thank you to the great people who joined the group at later stages: Dr. Amlan Pal, Dave Hall, Nidhi Sharma, Mattia Fontani, Antonella Pizzolante, Lucie Delforce, Boyi Song, Chenfei Li, Dr. Rajamalli Pachai Gounder, Dongyang Chen, Jiyu Tian, Hannah Bosch, Ana Neferu, Bryony Hockin, Dr. Graeme Copley. Thank you also to the rest of the EZC group, the countless colleagues and friends for our great time together.

I want to thank my family in Bergamo. Thank you to my lovely mom Mariangela, dad Francesco and brother Daniele. There are too many things I have to thank you for. I only

say - You are the stepping stones of my achievements and the best examples I could have ever had. I would like to extend my warmest gratitude to all my relatives (Rota Martir, Rota, Pagani, Agostinelli), to Angelo, Caterina and Eugenio and to all of my friends from Italy and from all over the world for being part of my journey and supporting me during these years.

Last but not least I would like to thank Giusy, my adventure companion. Thank you!

Contents

Abbreviations, Acronyms and Terminology

Acronym	**Expansion**
(N)IR	(Near) Infrared
(P)eT	(Photoinduced) electron Transfer
(P)ET	(Photoinduced) Energy Transfer
1-,2-,3-D	One-, Two-, Three-Dimensional
2DQ	1,1′-ethylene-2,2′-bipyridilynium
A	Acceptor
A*	Excited state Acceptor
acac	Acetylacetonate
ACN	Acetonitrile
AFM	Atomic Force Microscopy
BMIM-PF_6	1-butyl-3-methylimidazolium hexafluorophosphate
BODIPY	Borondipirromethane
bpdc	Para-biphenyldicarboxylate
bpy	2,2′-bipyridine
btl	1,1′-dibenzyl-4,4′-bis-1H-1,2,3-triazolyl
CAN	Cerium Ammonium Nitrate
CD	Circular Dichroism
CIE	Commission Internationale de l'*É*clairage
CNdt	2-methyl-N-methylydynepropan-2-aminium
COD	1,5-cyclooctadiene
COSY	Correlated spectroscopy
CP	Coordination Polymer
Cp*	Pentamethylcyclopentadienyl
CT	Charge Transfer
CTAB	Cetyltrimethyl Ammonium Bromide
CV	Cyclic Voltammetry
cyclam	1,4,8,11-tetraazacyclotetradecane
D	Donor
D*	Excited state Donor

Acronym	**Expansion**
D-A	Donor-Acceptor
dap	1,12-diazaperylene
dc-bpyH	2,2′-bipyridine-5,5′-dicarboxylic acid
DCM	Dichloromethane
dc-ppy	2-phenylpyridine-5,4′-dicarboxylic acid
DEF	Diethylformamide
detrz	3,5-diethyl-1H-1,2,4-triazolate
dFmesppy	2-(2,4-difluorophenyl)-4-(2,4,6-trimethylphenyl)pyridinato
dFphtl	1-benzyl-4-(2,4-difluorophenylato)-1H-1,2,3-triazole
dFppy	4,6-difluorophenylpyridinato
dFptrBz	1-benzyl-4-(2,4-difluorophenyl)-1H-1,2,3-triazole
ΔG_{CS}	Free energy change
DLS	Dynamic Light Scattering
DMAP	4-dimethylaminopyridine
DMF	Dimethylformamide
DMPA	2,2-dimethoxy-2-phenylacetophenone
DMSO	dimethylsulfoxide
dmtrz	3,5-dimethyl-1H-1,2,4-triazolate
DOSY	Diffusion ordered spectroscopy
dppH	2-pyridyl phosphonic acid
dppp	1,3-diphenylphosphinopropane
dptrz	3,5-dipropyl-1H-1,2,4-triazolate
DPV	Differential Pulse Voltammetry
dtBubpy	4,4′-di-*tert*-butyl-2,2′-bipyridine
E	Potential
$E_{0,0}$	Zero-zero energy
$E_{1/2}{}^*$	Excited state redox potential
ECL	Electrochemiluminescence
ECS	Radical ion pair state energy
EDTA	Ethylendiaminetetraacetic acid
ee	Enantiomeric excess
EL	Electroluminescence
$E^{ox}_{1/2}$	Half-wave oxidation potential
E^{pa}	Anodic oxidation potential
E^{pc}	Cathodic oxidation potential
EQE	External Quantum Efficiency
$E^{red}_{1/2}$	Half-wave reduction potential
ESI-MS	Electronspray ionisation Mass Spectrometry
Fc	Ferrocene
GS	Ground State
G_S	Ion-pair stabilization energy
HCPK	1-hydroxycyclohexyl phenyl ketone
hd-bpy	4,4′-diheptadecyl-2,2′-bipyridine
HETCOR	Heteronuclear Correlation

Acronym	**Expansion**
HMBC	Heteonuclear Multiple Bond Correlation
HMPP	2-hydroxy-2-methylpropiophenone
HMQC	Heteonuclear Multiple Quantum Correlation
HOMO	Highest Occupied Molecular Orbital
hqx	2,3-diphenylquinoxaline
HR-MS	High-Resolution Mass Spectrometry
IC	Internal Conversion
IL	Ionic Liquid
ILCT	IntraLigand Charge Transfer
IQE	Internal Quantum Efficiency
ISC	Intersystem Crossing
iTMC	Ionic Transition Metal Complex
ITO	Indium Tin Oxide
k_{nr}	Non-radiative decay rate constant
k_q	Bimolecular quenching rate constant
k_r	Radiative decay rate constant
K_{SV}	Stern-Volmer Constant
LC	Liquid Crystal
LED	Light-Emitting Diodes
LEEC	Light-Emitting Electrochemical Cell
LLCT	Ligand-to-Ligand Charge Transfer
LMCT	Ligand-to-Metal Charge Transfer
λ_{PL}	Emission wavelength
lum	Luminance
LUMO	Lowest Unoccupied Molecular Orbital
MC	Metal-Centred
mesppy	2-phenyl-4-mesytilpyridinato
MLCT	Metal-to-Ligand Charge Transfer
MO	Molecular Orbital
MOF	Metal-Organic Framework
mppy	2-(p-tolyl)pyridine
NMR	Nuclear Magnetic Resonance
non-bpy	4,4′-dinonyl-2,2′-bipyridine
OFET	Organic Field Effect Transistor
OLED	Organic Light-Emitting Diodes
OPV	Organic Photovoltaic
OTf	Trifluoromethyl sulfonate
P123	Poly(ethylene glycol)-block-poly(propylene glycol)-block-poly(ethylene glycol)
PEDOT:PSS	Poly(3,4-ethylenedioxythiophene)polystyrene sulfonate
PEG	Polyethylene glycol
Φ_{PL}	Photoluminescence quantum yield
piq	Isophenylisoquinoline
PL	Photoluminescence
PMD	Photochemical Molecular Devices

Acronym	**Expansion**
PMMA	Polymethyl methacrylate
PMO	Periodic Mesoporous Organosilica
PPE	Poly(phenyleneethynylene)
PPN	Bis(triphenylphosphine) iminium cation
ppy	2-phenylpyridinato
ppyPh	2-(3- phenylphenyl)pyridinato
ptz-Me	5-methyl-2-phenyltetrazole
PVS	Propyl Viologen Sulfonate
qpy	4,4′:2′,2″:4″,4‴ -quaterpyridine
R_A	Radius of the Acceptor
R_D	Radius of the Donor
R_{DA}	Donor-to-Acceptor distance
ROMP	Ring-Opening Metathesis Polymerisation
r_s	Hydrodynamic radius
SANS	Small-Angle Neutron Scattering
SAXS	Small-Angle X-ray Scattering
SCE	Saturated Calomel Electrode
SDA	Structure-Directing Agent
SEM	Scanning Electron Microscopy
S_n	n^{th} singlet state
SOC	Spin-Orbit Coupling
SSL	Solid-State Lighting
$t_{1/2}$	Device lifetime
tae	1,1,2,2-tetraacetylethane
TAP	Tetraarylporphyrin
τ_{PL}	Photoluminescence lifetime
TBACN	Tetrabutyl ammonium cyanide
tcb	1,3,5-tricyanobenzene
TD-DFT	Time-Dependent Density Functional Theory
TEA	Triethylamine
TEM	Transmission Electron Microscopy
TEOS	Tetraethyl orthosilicate
T_n	n^{th} triplet state
TNT	Trinitrotoluene
TOF	Turnover frequency
TOF-MS	Time-of-Flight Mass Spectrometry
t_{on}	Device turn-on time
TPP	Tetraphenylporphyrin
tpt	2,4,6-tris(pyridin-4-yl-1,3,5-triazine)
tpy	2,2′,6′,2″-terpyridine
trz	1,2,3-triazolate
UV	Ultraviolet
WAXS	Wide-Angle X-ray Scattering
WOLED	White Organic Light-Emitting Diodes
XRD	X-ray power diffraction

List of Figures, Schemes and Tables

Chapter 1

Introduction

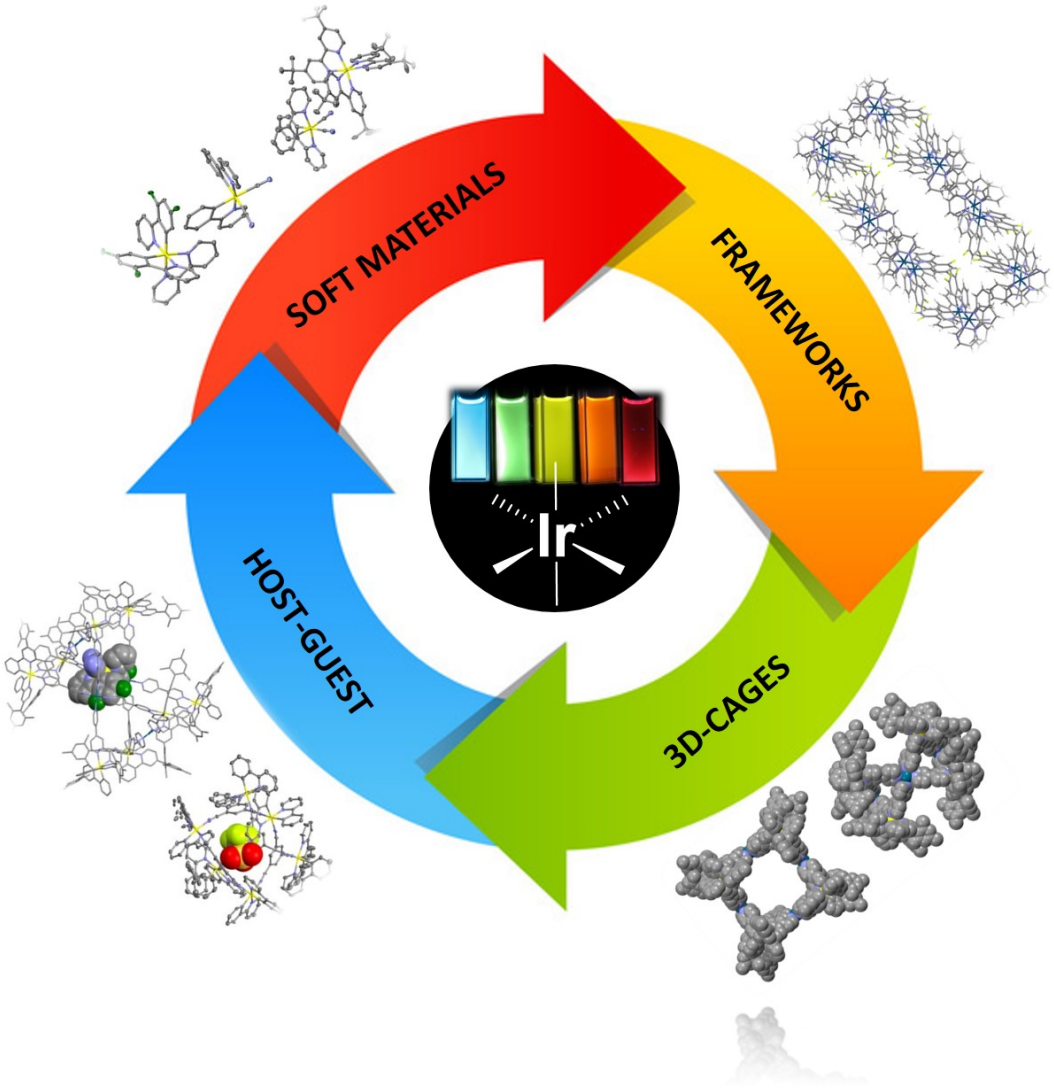

Many iridium(III) and ruthenium(II) complexes are phosphorescent molecules. In these compounds emission of light occurs from the triplet state due to efficient inter-system crossing (ISC) from the singlet manifold to the triplet, mediated by spin-orbit coupling of the heavy metal centre. These complexes are robust with excellent thermal and chemical stability.[1]

Iridium complexes generally exhibit high photoluminescence quantum yields and relatively short excited state lifetimes and, depending on the nature of the ligands, emission can be easily tuned across the visible spectrum. As a result, an increasing interest in these complexes has resulted over the past decade. Indeed, iridium(III) complexes have been used as emitters in solid-state lighting, as photosensitisers in solar cells, for hydrogen evolution and photoredox catalysis with organic substrates as well as luminescent probes in biology and as sensors for environmentally relevant analytes.[2, 3]

Ruthenium complexes, by contrast, are generally poorly emissive, their emission energies fall within a narrow range and thus their use as luminophores is limited. On the other hand, these complexes easily access multiple oxidation states and therefore enjoy a rich history in photocatalysis and as redox active materials.[4] The use of Ru(II) complexes in Dye Sensitised Solar Cells (DSSC), water splitting, biological labelling and as anticancer agents is also prominent.[5, 6]

The vast majority of the reports on Ir(III) and Ru(II) chromophores involve their use as mononuclear complexes. The investigation of these complexes as phosphorescent components of self-assembled systems has however garnered increasing attention in recent years and this first chapter aims to document the advances made in this area. As iridium complexes cover the majority of this thesis, special emphasis will be devoted to describing the photophysical properties and applications of supramolecular photoactive materials based on Ir(III) chromophores. Since the photophysical properties of these supramolecular materials highly depend on the electronic states of mononuclear transition metal complexes, an understanding of how they arise is crucial for providing the basis for exploring them in detail. Therefore, the molecular orbital (MO) theory approach will be initially used to explain the light absorption and light emission properties of these complexes, highlighting the important kinetic considerations that underpin these processes. The investigation of energy and electron transfer processes in supramolecular photoactive materials has been focus of great attention in recent years and thus a brief introduction to these processes will be also given.

1.1 Photophysics of octahedral coordination compounds

1.1.1 MO theory approach

MO theory provides correlations between metal, ligand, and molecular orbitals.[7] Exemplary MO diagrams illustrating the relevant electronic states for octahedral complexes are shown for $[Ir(NH_3)_6]^{3+}$ (**Figure 1a**) and $[Ir(CN)_6]^{3-}$ (**Figure 1b**).[8]

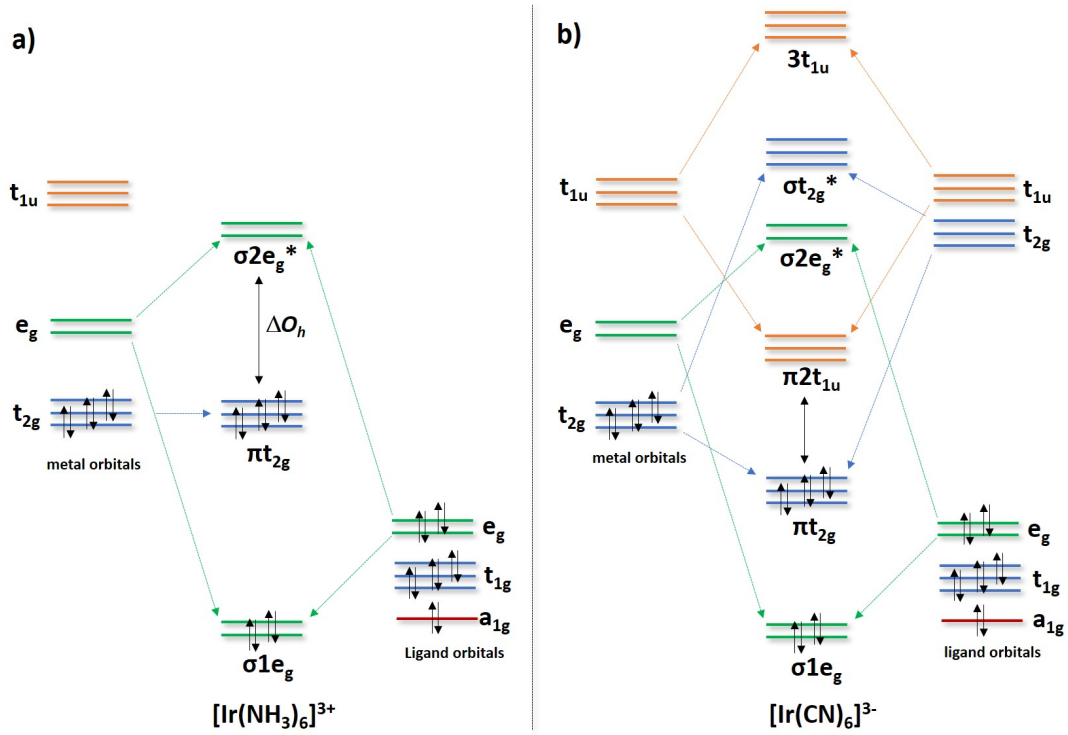

Figure 1. Simplified MO diagrams for **a)** $[Ir(NH_3)_6]^{3+}$ and **b)** $[Ir(CN)_6]^{3-}$

The main difference between the electronic structures of these two complexes resides in the nature of the ligands.[9] In $[Ir(NH_3)_6]^{3+}$, the six coordinating NH_3 ligands are purely σ-donating in nature. Therefore, the two doubly degenerate Ir(III) orbitals of e_g symmetry ($d_{x^2\text{-}y^2}$ and d_{z^2}) are destabilised in energy as a result of antibonding interactions with the σ-orbitals of NH_3, while the three Ir(III) triply degenerate orbitals of t_{2g} symmetry (d_{xy}, d_{xz} and d_{yz}) are unperturbed and thus do not change in energy upon formation of the complex.[8] In this case, the Ir(III) t_{2g} constitutes the Highest Occupied Molecular Orbital (HOMO) while the e_g constitutes the Lowest Unoccupied Molecular Orbital (LUMO). As both the HOMO and LUMO are localised on the Ir(III) metal centre with no contribution from the coordinating ligands, the optical transition that promotes electron transfer from HOMO to LUMO is defined as Metal-Centred (MC) in nature.[9] It is important to mention that MC transitions for centrosymmetric molecules are theoretically forbidden by the

Laporte symmetry selection rule. Therefore, the oscillator strengths (f), which expresses the probability of absorption or emission of electromagnetic radiation between two energy levels, associated with these transitions are generally weak and very often close to zero. As a result, MC transitions are generally characterised by low molar absorptivities, the result of ligand-induced fluxional distorsions, and high non-radiative decays of excited state by vibrations, internal conversions and energy exchange with solvent molecules.[10]

In complex $[Ir(CN)_6]^{3-}$ (**Figure 1b**), the six coordinating CN ligands are σ-donating but have also vacant orbitals of π-symmetry (t_{2g} and t_{1u}) that can interact with the Ir-based t_{2g} and t_{1u} orbitals.[7] This leads to the stabilisation of the metal t_{2g} orbitals, that constitutes the HOMO, and the formation of ligand based t_{1u} orbital which, being lower in energy than the Ir e_g orbital, constitutes the LUMO. As the HOMO is formally localised on the Ir centre and the LUMO resides on the CN ligand, the HOMO-LUMO transition is defined as Metal-to-Ligand Charge Transfer (MLCT) in nature. MLCT transitions involve electron transfer between two states of the same symmetry that are allowed by the Laporte symmetry selection rule and thus generally characterised by relatively high oscillator strength.[10]

Importantly, the metal and ligand orbital interactions and the electronics of the complexes can be often modulated by the nature of the ligand. This is particularly evident for cyclometalated Ir(III) complexes of the type of $[Ir(C\hat{}N)_2(N\hat{}N)]^+$, where C^N is the cyclometalating ligand with 2-phenylpyridinato (ppy) as the most studied archetype, and N^N is the ancillary ligand with 2,2′-bipyridine (bpy) as the most common archetype.[2] Indeed, for these complexes the HOMO is largely localised on the Ir centre and the phenyl rings of the C^N ligands while the LUMO is spatially separated and lie on the N^N ancillary moiety. As a result of the spatial separation between the HOMO and LUMO levels, for this family of complexes it is possible to control the energies of these states by adjusting the energy of the metal and ligand orbitals through substituent functionalisation.[11–13] As an example, the introduction of electron-withdrawing substituents (such as fluorine atoms or CF_3 substituents) on the phenyl component of the C^N ligand can stabilise the HOMO by removing electron density from the Ir centre and aryl ring whereas the introduction of electron-donating group (such as CH_3 or O-CH_3 substituents) on the N^N ancillary ligand can destabilise the LUMO orbital. Thus, following this strategy a larger HOMO-LUMO gap can be achieved, leading to the preparation of green or blue-emitting complexes. On the other hand, the introduction of electron-donating substituents on the C^N ligand and/or electron-withdrawing moieties on the N^N ligand can reduce the HOMO-LUMO gap leading to yellow or even red-emitting complexes.[11]

It is important to mention that in addition to MC and MLCT, there are four other states to be aware of in transition metal complexes: 1) Ligand-to-Metal Charge Transfer (LMCT), which involve transitions from ligand orbitals to metal e_g* orbitals; 2) Ligand Centred (LC) in which the electrons are transferred between π and π* orbitals of one of

the ligand; 3) Intraligand Charge Transfer (ILCT), which involve transitions between two moieties of one of the ligand and 4) Ligand-to-Ligand Charge Transfer (LLCT) in which the electrons are transferred between the cyclometalating ligand and the ancillary N^N chelator. In contrast to symmetry-forbidden MC states, there are no symmetry restrictions on these other states, and thus they are generally characterised by high molar absorptivities.[9, 10, 14]

1.1.2 The Jablonski diagram and light emission

We have discussed how the metal and ligand orbital interactions can modulate the electronics of transition metal complexes and thus the nature of their optical transitions.

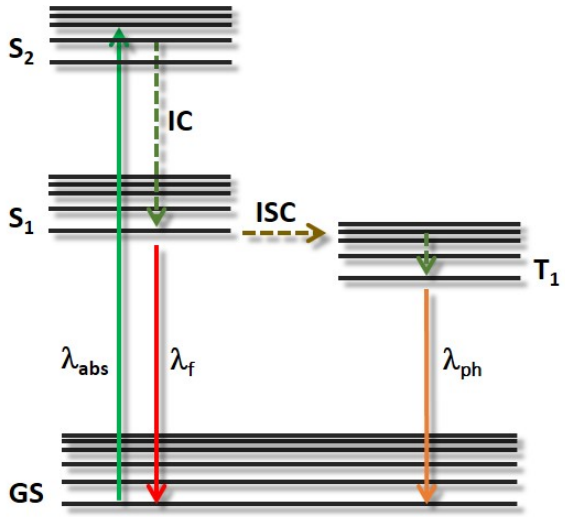

Figure 2. Simplified Jablonski diagram showing the possible excited state kinetic processes. Absorption of light (λ_{abs}, solid green arrow, timescale: 10^{-15} s), vibrational relaxation and internal conversion (IC, dotted green arrow, timescale: 10^{-14} - 10^{-11} s), fluorescence (λ_f, red line, timescale: 10^{-9} - 10^{-7} s), intersystem crossing (ISC, dotted okra line, time scale variable) and phosphorescence (λ_{ph}, solid orange line, timescale: 10^{-3} - 10^{-2} s).

Photochemical processes in a molecule begin with the absorption of light, excitation of electrons to a singlet excited state (S_n) and subsequent relaxation to the lowest vibrational level of the excited state (S_1) through internal conversion and dissipation of energy from the molecule to its surroundings.[10, 14, 15] The electron in S_1 state can either relax back to the ground state (GS) via further dissipation of energy following non-radiative paths such as internal conversion and vibrations or, as illustrated in the Jablonski diagram in **Figure 2**, via emission of photons (radiative decay).[16] When the photon emission is not prohibited by the spin selection rule (from S_1 to GS, $\Delta S = 0$), the process is very fast at

the nanosecond time scale and it is called fluorescence (red arrow in **Figure 2**). Emission of fluorescence is exhibited for example by π-conjugated organic molecules such as pyrene, perylene or anthracene, porphyrins, boron dipyrromethane (BODIPY) compounds and many others.[17]

Transition metal complexes such as iridium, ruthenium and platinum are characterised by a high charge on their nucleus that exert significant force on the orbiting electrons, the orbital motions of which become so fast that allow them to interact with their own spin.[18, 19] Spin-orbit coupling (SOC) is very efficient in these complexes and result in a change of electron spin multiplicity from the first excited singlet state S_1 to the first excited triplet state T_1 at a much faster rate than most other competing processes. Indeed, for iridium, ruthenium and platinum complexes ISC is assumed to be so efficient that there is quantitative conversion all of the generated S_1 states into T_1 states. Radiative relaxation from T_1 to GS, which is called phosphorescence (orange arrow in **Figure 2**), is theoretically spin forbidden ($\Delta S \neq 0$) and can therefore be easily differentiated from fluorescence due to its much longer microsecond timescale.[9, 10]

Considering these processes from a kinetic point of view, the radiative constant (k_r) quantifies the rate of which a molecule in its excited state relaxes to GS by emitting light, while the non-radiative decay constant (k_{nr}) includes the rate constants of all other processes that lead to deactivation of the excited state. The photoluminescence quantum yield, Φ_{PL}, quantifies the ratio of photons emitted by the chromophore to photons absorbed and it is defined with the equation (**1**).[6, 14, 15]

$$\Phi_{PL} = \frac{k_r}{k_r + k_{nr}} \quad (\mathbf{1})$$

In this thesis Φ_{PL} values will be used very often to determine the photoluminescence efficiency of emitting compounds.

1.2 Introduction to energy and electron transfer

As discussed in the previous section, following absorption of light and concomitant population of excited states, a molecule can relax back to the ground state by emitting light (fluorescence or phosphorescence) or by radiationless deactivation such as internal conversion. However, over the past fifty years the dynamic quenching of excited states involving donor-acceptor systems based on combinations of multi-chromophoric arrays has been an area of great interest to photochemists.[20, 21] A bimolecular quenching processes involving a donor chromophore and an acceptor (quencher) molecule is classified into two general pathways: energy transfer and electron transfer.[22, 23]

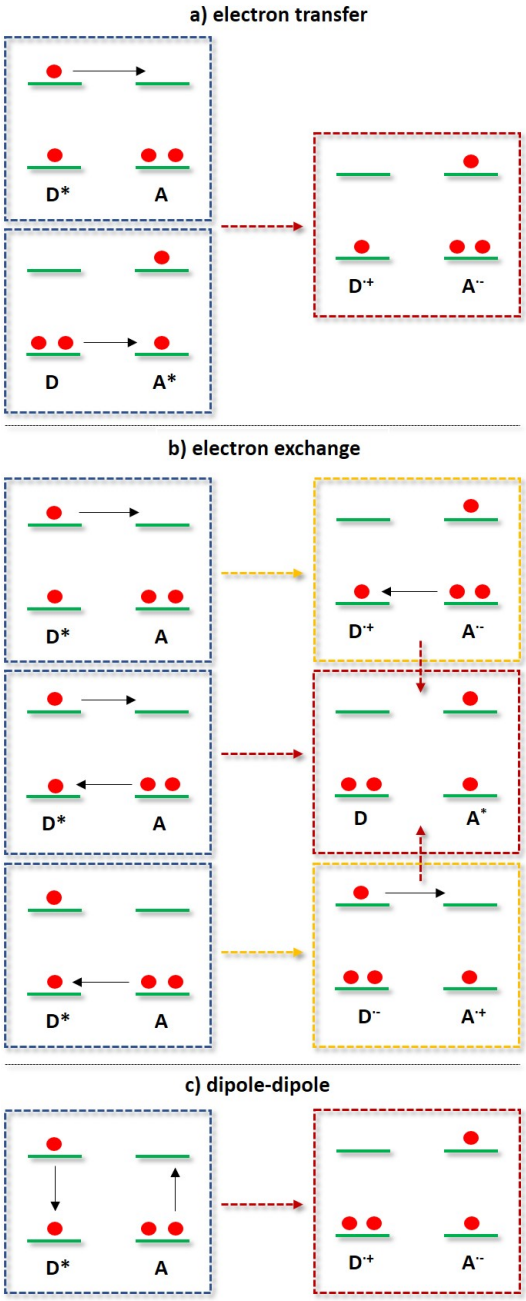

Figure 3. Schematic description of electron motion in electron- and energy-transfer quenching mechanisms (D = donor and A = acceptor). The solid circles represent electrons while green lines represent HOMO and LUMO levels. **a)** electron transfer results in a radical ion pair. Energy transfer proceeds by **b)** an electron-exchange or **c)** dipole-dipole (Coulombic) mechanism. Blue squares indicate initial states following photoexcitation; yellow squares represent intermediate states and red squares represent final states after electron or energy transfer.

According to a simplified molecular orbital picture (**Figure 3**), energy and electron transfer between two chromophoric units can be formally described in term of electronic

motion between occupied and unoccupied molecular orbitals of a donor (D) and an acceptor (A) molecule.

Quenching by electron transfer strictly requires orbital overlap between the donor and the acceptor. It is a one electron process in which the electron jumps from an occupied orbital of one reactant to an unoccupied orbital of the other (**Figure 3a**).[22, 24–26] This process leads to the formation of a radical ion pair or a charge-transfer complex $[D]^{\cdot+}$-$[A]^{\cdot-}$ that is generally non-emissive. The energy of the radical ion pair state (E_{CS}) and free energy change (ΔG_{CS}) associated with the formation of the charge-separated state is generally determined by the Rehm–Weller equation,[27] which takes into account both the spectroscopic excited state energy of the donor ($E_{0,0}$) and the thermodynamics of the overall electrochemical redox characteristics associated with the electron transfer process. Importantly, electron transfer between two chromophores can only take place if the excited state energy of the donor, $E_{0,0}$, is all available as free energy to promote the excited state redox processes. Photoinduced electron transfer is particularly relevant in chapter 4 when discussing the optoelectronic interactions between supramolecular dynamic iridium-porphyrins and ruthenium-porphyrins diads and triads. Therefore, more insights about the nature and understanding of electron transfer processes will be highlighted in chapter 4.

Energy transfer between two chromophoric units can take place through three fundamentally different mechanisms: 1) electron exchange, which is generally known as Dexter energy transfer; 2) dipole-dipole, which is known as Förster resonance energy transfer and 3) radiative mechanism.[28] Similar to electron transfer, the electron exchange mechanism requires orbital overlap between the donor and the acceptor, and involve two single independent electron transfers that result in the formation of the donor's ground state (D) and acceptors' excited state (A*) (red square in **Figure 3b**).[29] This process can be promoted as a single step involving two concomitant electron transfers, or in two steps characterised by an initial one-electron transfer promoting the formation of a radical ion pair (yellow squares in **Figure 3b**) and a subsequent electron transfer to generate the final excited state acceptor, A*, and ground state donor, D.[22]

Energy transfer by the dipole-dipole mechanism (**Figure 3c**), on the other hand, does not require orbital overlap between the donor and the acceptor molecules. Indeed, it operates by Coulombic resonance interactions (the transmitter-antenna mechanism)[30], in which the oscillating electrons of an excited-state donor are coupled with those of the acceptor and are quenched by an induced dipole interaction.[31, 32]

The Stern-Volmer relationship (eq. **2**) is generally used to explore the kinetics of a photophysical intermolecular excited state deactivation process by bimolecular energy transfer via Dexter or Förster mechanisms.[33]

$$\frac{I^0{}_f}{I_f} = 1 + k_q \tau^0 [Q] \quad (\mathbf{2})$$

In eq. **2** $I^0{}_f$ is the emission intensity, or rate of luminescence, of the donor molecule without a quencher, I_f is the emission intensity, or rate of luminescence, of the donor in the presence of the quencher, k_q is the bimolecular quenching rate constant, τ^0 is the lifetime of the emissive excited state of the donor in the absence of the quencher and [Q] is the concentration of the quencher. The product $k_q \cdot \tau^0$ is generally known as the Stern-Volmer Constant, K_{SV}. K_{SV} can be easily determined from the slope of the plot $I^0{}_f / I_f$ - 1, which can be experimentally obtained by spectroscopic analysis, against the quencher concentration [Q]. However, eq. **2** is only valid with the assumption that the quenching process is diffusion-limited and purely collisional quenching takes place.[34]

Electron transfer and energy transfer by electron exchange require a close approach for effective orbital overlap. As a result, these mechanisms can only be promoted in bimolecular systems where the donor-acceptor distance is less than 10 Å.[22, 28] In contrast, Coulombic energy transfer does not involve orbital overlap and can be effective from collision distances of less than 10 Å, and up to separation distances as large as 100 Å.[30, 31, 35, 36] However, spin conservation is normally observed in both electron and energy transfer as the overall spin of the radical ion pair (electron transfer) or the spin of the acceptor's excited state (energy transfer) match the spin of the donor's excited state.

So far we have briefly discussed electron transfer processes and energy transfer mechanisms that operate via electron exchange (Dexter energy transfer) or dipole-dipole interactions (Förster resonance energy transfer). However, energy transfer can also be promoted via a mechanism that does not involve electronic interactions between the donor and the acceptor, which therefore behave as independent species. This mechanism is generally known as radiative energy transfer. Immediately one might ask, if there is no interaction between the donor and the acceptor chromophores, how can energy transfer occur? the answer is simple. Energy transfer can easily occur when the emission of light by the excited donor, D*, is subsequently absorbed by a ground state acceptor.[37] In this mechanism the acceptor does not influence the emission properties of the donor molecule, whose excited state characteristics remain unchanged by the presence of the acceptor. Furthermore, in contrast to the Dexter and Förster mechanisms, in radiative energy transfer the "energy delivery" mechanism does not involve a physical encounter between the chromophoric units. Instead, it only requires that the emission spectrum of the excited donor (D*) partially overlaps with the absorption spectrum of acceptor (A). Examples of this mechanism will be given in chapter 4 when discussing the iridium-porphyrin assemblies.

1.3 Supramolecular iridium(III) assemblies

The term molecular self-assembly applies to pathways that produce a final product directly and spontaneously when the correct components are mixed under appropriate conditions.[38] Self-assembly plays an integral role in the structure and function of biological systems[39, 40] and it is implicated in a variety of functional materials.[41] In Nature self-assembly is generally based on numerous hydrogen bounding, electrostatic, van der Waals, and other weak inter- and intra-molecular interactions working synergistically to assemble, for example, secondary and tertiary structures of proteins, which then provide well-defined local environments to mediate biochemical transformations.[42] Similarly, in natural photosynthesis organisms optimise solar energy conversion through the self-organised assembly of photofunctional chromophores.[43, 44] Over the last two decades, molecular self-assembly has played a key role in the construction of a variety of elegant and intricate synthetic nanostructures, including molecular crystals and liquid crystals,[45] colloids and micelles,[46] gels,[47, 48] polymers[49, 50] and nanoscale structures of high symmetry, such as 3D-frameworks,[51] metal-organic polygons and polyhedra.[52, 53] As the properties of these materials highly depend both on the nature of their components and the interactions between them, the explicit manipulation of the building blocks and the non-covalent forces that hold the constituents together has promoted the evolution of functional properties, which have been exploited in numerous advanced technologies. For example, liquid crystals have found application as anisotropic organic semiconductors in organic field effect transistors (OFETs), Organic Light-Emitting Diodes (OLEDs) and Organic Photovoltaic devices (OPVs).[45, 54] Due to their large surface area and biocompatibility, colloids and micelles are very important for water purification, cleansing action of soap and food formulation.[55, 56] Hydrogels and polymers are key components in materials for medicine, food science and cosmetics.[57–59] Nanostructured materials such as molecular crystals, frameworks or 3D-polyhedral structures exhibit interesting optical, magnetic and catalytic properties, which have been rapidly exploited in diverse applications such as in catalysis, magnetic devices and gas purification.[60–62]

In recent years, there has been an increasing interest in the construction of photoactive supramolecular assemblies through the incorporation of luminescent building blocks.[63–66] This immediately generates possibilities for assembling in very close proximity a high concentration of chromophoric units through non-covalent interactions, thereby achieving photophysical properties that are difficult to obtain in conventional molecular materials. Besides modulating the optoelectronic properties of the emissive compounds as a function of the assembly, their organisation into ordered structures can also radically change the physical properties of the bulk materials.[67] As a result, nanomaterials that exhibit both fascinating physical and photoactive properties have been one of the main areas of interest in supramolecular chemistry in recent years.[63, 68, 69]

Cyclometalated iridium(III) complexes as luminescent components for self-assembly has become increasingly popular in recent years. This part of the introduction provides an exhaustive summary on the development of photoactive self-assembled materials based on iridium(III) complexes, giving special emphasis to their photophysical properties, and highlighting their applications. Depending on the nature of the ligands, iridium(III) complexes can be cationic, neutral and anionic. The vast majority of cationic iridium(III) complexes possess the general motif $[Ir(C\hat{}N)_2(N\hat{}N)]^+$.[11] Homoleptic neutral iridium complexes possess the general formula $[Ir(C\hat{}N)_3]$ and are frequently studied as their facial geometric isomer.[70] Heteroleptic neutral complexes generally possess the structural motif $[Ir(C\hat{}N)_2(X)]$, where X is an anionic bidentate ligand such as acetylacetonates, oxazolines or thiazolines whereas, negatively charged cyclometalated iridium(III) complexes typically possess the composition $[Ir(C\hat{}N)_2(Y)_2]^-$, where Y is typically an anionic monodentate ligand such as CN^-, NCS^- and NCO^-.

We begin by describing iridium-based soft materials such as ion-paired iridium complexes commonly known as soft-salts, liquid crystals, supramolecular gels, colloidal structures and assemblies developed through H-bonding and π-π-stacking interactions. Next, we turn our attention to describing luminescent iridium-based coordination polymers, metal-organic frameworks (MOFs) and discrete structures, followed by an overview of luminescent Ir-based macrocycles, capsules and cages. Guest Ir(III) complexes encapsulated within the cavities of cage-type structures are also presented giving attention in describing the changes of the luminescent properties of the guest iridium complexes due to their physical and optoelectronic interactions with the host materials. Finally, the last part of this chapter provides an exhaustive summary on the development of phosphorescent cages based on ruthenium(II) complexes, describing their photophysical properties and applications.

1.3.1 Soft materials

Molecular aggregation induced by non-covalent interactions between Ir(III) chromophores can have tremendous impact on the properties of materials. Desirable photophysical properties such as emission tuning, enhanced photoluminescence quantum yield, longer excited state lifetimes, and energy and electron transfer processes can be achieved by controlling the aggregation and organisation of Ir(III) emitters in soft materials.

1.3.1.1 Soft salts

The term "soft salt" describes ionic materials that are composed of two or more organometallic components characterised by complementary charges and assembled into complex salts through Coulombic interactions. The majority of the reported soft salts incorporating iridium have consisted of a cationic iridium complex married with an anionic iridium

complex.

The first examples of iridium soft salts were reported in 2010 by Thompson and co-workers[71] (**Figure 4**) and De Cola and co-workers[72] (**Figure 5a**) who assembled via salt metathesis reactions blue- and green-emitting anionic Ir(III) complexes with yellow- and orange-emitting cationic iridium complexes.

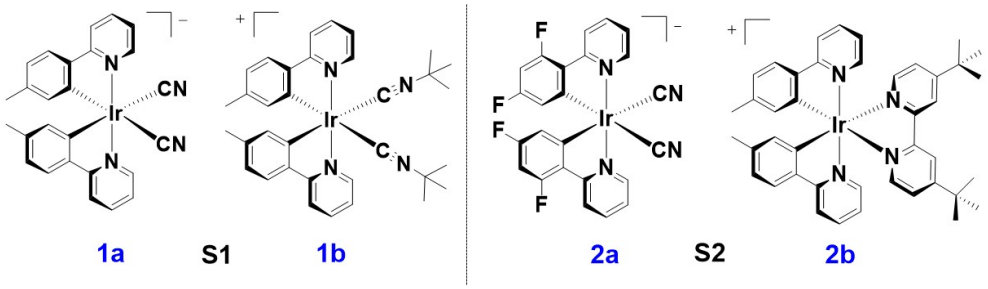

Figure 4. Chemical structure of soft salt **S1** (left) and **S2** (right).

Soft salt **S1** was prepared by assembling the anionic green-emitting Ir(III) complex Na[Ir(mppyH)$_2$(CN)$_2$], Na**1a** with the cationic yellow-emitting Ir(III) complex [Ir(mppyH)$_2$ (CNdt)$_2$]Cl, 1b**Cl** (mppyH is 2-(p-tolyl)pyridine and CNdt is 2-methyl-N-methylydynepropan-2-aminium), while **S2** contains the anionic blue-emitting Ir(III) complex Na[Ir(dFppy)$_2$(CN)$_2$], Na**2a** (dFppyH is 4,6-difluorophenylpyridine) with the cationic orange-emitting Ir(III) complex [Ir(mppyH)$_2$(dtBubpy)]Cl, **2b**Cl (dtBubpy is 4,4′-di-tert-butyl-2,2′-bipyridine) (**Figure 4**). In degassed MeCN the complexes Na**1a** and **1b**Cl exhibited vibronic ligand-centered (^{3}LC) emission profiles, respectively, at λ_{PL} = 472 nm and λ_{PL} = 458 nm with photoluminescence quantum yield of Φ_{PL} = 70% and Φ_{PL} = 38%, and photoluminescence lifetimes of τ_{PL} = 4.0 µs and τ_{PL} = 36.7 µs. Similarly, complex Na**2a** exhibited a vibronic ^{3}LC emission at λ_{PL} = 448 nm with a Φ_{PL} of 70% and a τ_{PL} = 4.1 µs, while complex **2b**Cl showed a broad mixed metal-to-ligand and ligand-to-ligand charge transfer (^{3}MLCT/^{3}LLCT) emission centered at λ_{PL} = 586 nm with a lower Φ_{PL} of 21% and a shorter τ_{PL} of 0.43 µs. The photoluminescence spectra of the soft salts **S1** and **S2** exhibited a concentration dependence, which impacted the degree of emission quenching of the anion by the cation via Dexter energy transfer. Taking **S2** as an example, at a relatively low concentration of 10^{-5} M its luminescence profile was dominated by the emission at λ_{PL} = 448 nm, characteristic of the blue-emitting anion **2a**. This high-energy emission gradually decreased as a function of increasing concentration of **S2** from 10^{-5} M to 10^{-3} M and, at a concentration greater than 10^{-3} M, only the orange emission exhibited by the cation **2b** at λ_{PL} = 586 nm was observed. Based on a bimolecular quenching model, a quenching rate constant k_q of 1.71 x 10^{10} $M^{-1}{\cdot}s^{-1}$, close to the diffusion limit in acetonitrile (2 x 10^{10} $M^{-1}{\cdot}s^{-1}$), was calculated.

Similarly, De Cola and co-workers assembled the green-emitting anionic Ir(III) complex of composition NBu$_4$[Ir(ppy)$_2$(CN)$_2$], NBu$_4$**3a**, with the yellow-emitting cationic Ir(III)

complex [Ir(dFppy)$_2$(bpy)]Cl, **3b**Cl (**S3**, **Figure 5**), and the blue-emitting anionic Ir(III) complex K**2a** with the orange-emitting cationic Ir(III) complex [Ir(ppy)$_2$(bpy)]Cl, **4b**Cl (**S4**, **Figure 5a**).

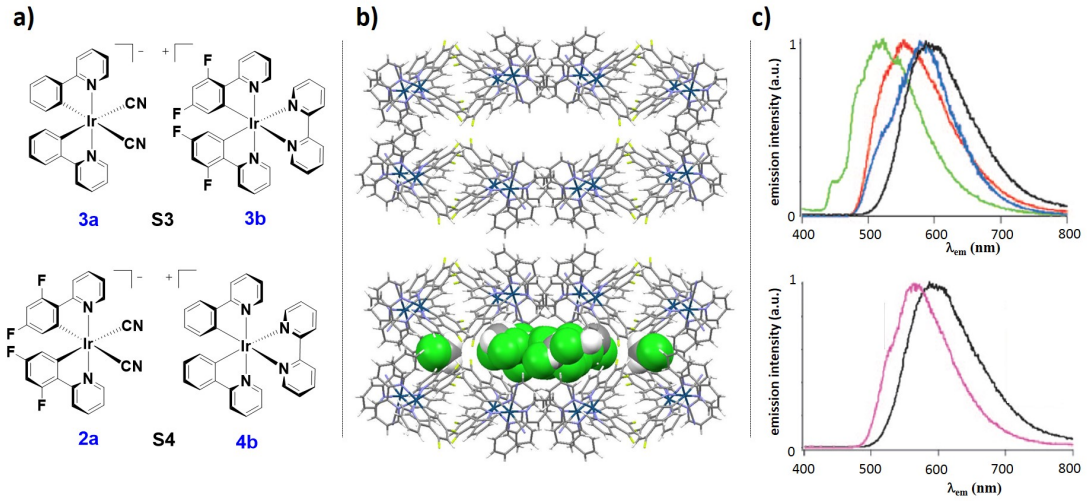

Figure 5. **a)** Chemical structures of complex salts **S3** (top) and **S4** (bottom). **b)** crystal packing of salt **S3** highlighting the channel running along the crystallographic c axis (top) and illustration of the dichloromethane solvent molecules (space-filling representation) inside the channel and pockets of **S3** (bottom). The remaining solvent molecules are omitted for clarity. **c)** top: normalised emission spectra of dried **S4** (black line), **S4** with toluene intercalated (blue line), complexes **2a** (red line) and **4b** (green line); bottom: normalised emission spectra of **S4** (black line) and **S4** intercalating anthraquinone (pink line). Part **c)** is adapted with permission. Copyright 2010, Wiley-VCH.[72]

The X-ray single crystal structure of **S4** showed that this soft salt forms a 3D porous network where small solvent molecules such as dichloromethane, amyl acetate, ethyl acetate, diethyl ether, toluene or anthraquinone could be easily intercalated (**Figure 5b**). The emission properties of the single crystals of the microcrystalline salts **S3** and **S4** were investigated both under vacuum in the absence of guest molecule inclusion and after loading guest molecules into their networks. In degassed CH_2Cl_2, complex NBu_4**3a** emitted yellow light with a λ_{PL} at 564 nm while **3b**Cl emitted in the blue-green with a λ_{PL} at 502 nm. The emission of the crystal of **S3** in its dry form exhibited a red-shifted emission at λ_{PL} = 591 nm. Analogously, the dried crystal of **S4** exhibited a red-shifted emission at λ_{PL} = 596 nm compared to the emission of both K**2a** and **4b**Cl, which exhibited, respectively, λ_{PL} = 554 nm and λ_{PL} = 460 nm. The red-shifted emission of both **S3** and **S4** compared to the corresponding mononuclear complexes were attributed to strong π-π-interactions between the C^N ligands of complementary iridium complexes of opposite charge present in the crystal networks, promoting Dexter energy transfer from the high energy anionic Ir donors **3a** and **2a** to the low energy cationic Ir acceptors **3b** and **4b**,

and additionally promoting exciplex formation and emission from correspondingly lower-energy excited states. Importantly, the emission properties of the crystals **S3** and **S4** could be efficiently modulated by trapping guest molecules within their porous networks. For example, the intercalation of toluene or anthraquinone into **S4** led to blue-shifted emission of the soft-salt, respectively, at λ_{PL} = 590 nm and λ_{PL} = 580 nm, compared to the dried crystal. An enhanced emission was observed when toluene was absorbed into **S4** due to the disruption of the π-π-interactions whereas the emission was quenched when anthraquinone was intercalated within the crystal of **S4** as a function of the photoinduced electron transfer from the **S4** donor to the anthraquinone acceptor (**Figure 5c**).

Sandroni and Zysman-Colman[73] reported the first example of a three component heterometallic ion-pair assembly, **S5** (**Figure 6**) involving two equivalents of complex NBu_4**3a** (**Figure 5a**) associated with the red-emitting $[Ru(dtBubpy)_3]Cl_2$ **5b**Cl_2 (**Figure 6a**). Upon photoexcitation into the ruthenium complex ^{1}MLCT absorption band in MeCN, **5b**Cl_2 exhibited the characteristic broad ^{3}MLCT emission centered at λ_{PL} = 630 nm, which is complementary in color compared to the ^{3}LC emission exhibited by complex NBu_4**3a** (λ_{PL} = 477 nm in degassed MeCN).

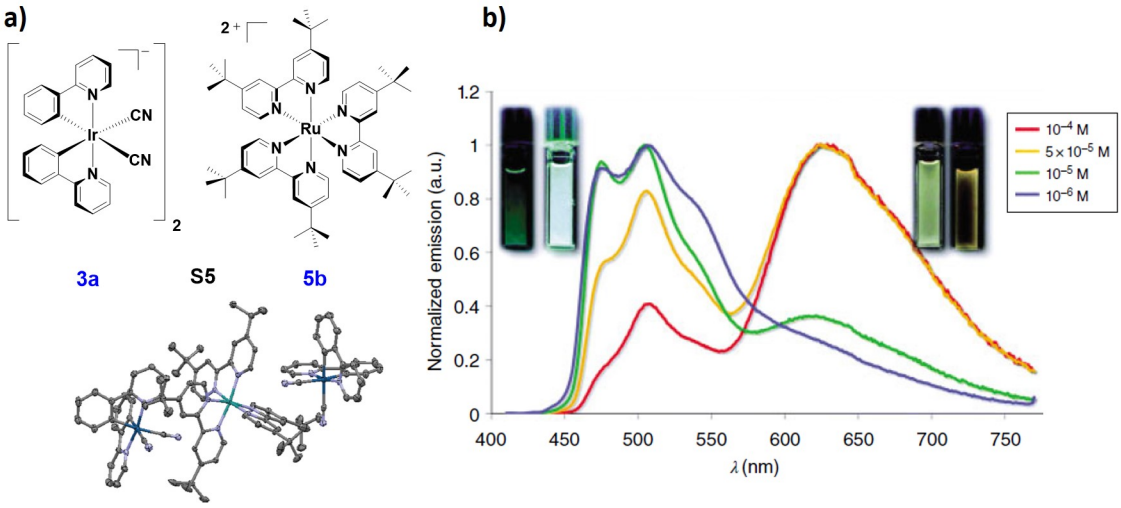

Figure 6. **a)** Chemical structure of the soft salt **S5** with its single crystal x-ray structure; **b)** normalised emission spectra of **S5** recorded in deaerated MeCN at 298 K at different concentrations (λ_{exc} = 390 nm). Insets are images of MeCN solutions of **S5** at different concentrations. Image **b)** is adapted from ref [73] with permission from The Royal Society of Chemistry.

Soft salt **S5** nicely illustrates how the emission properties can be modulated upon changes in concentration and medium. At low concentration, the emission of **S5** is dominated by the structured ^{3}LC emission of **3a**. As the concentration increases, due to increased

efficiency of the Förster energy transfer from the anionic Ir(III) donor to the cationic Ru(II) acceptor, the emission profile of **S5** resembles increasingly that of the lower-energy emission of the Ru(II) complex **5b** (**Figure 6b**). In contrast to the emission behavior observed for **S3** and **S4**, the emission of **S5** did not involve either excimers or exciplexes. Further, as a function of the solvent polarity, the electrostatic interaction of the cation and anion could be modulated and therefore the magnitude of the energy transfer between the two. Solvents of high polarity, such as DMSO, MeOH or EtOH, solvated strongly the ions, leading to their weak association, poor energy transfer and an emission dominated by **3a**. Less polar solvents such as CH_2Cl_2 or MeCN promoted the formation of intimate ion pairs, resulting in shorter distance between the Ir and Ru ions and more efficient energy transfer, and an emission profile that resembles that of **5b**.

Soft salt **S5** exhibited a significantly enhanced ECL (electrochemiluminescence) signal at similar energy to **5b**.[74] This observation is rather unusual considering that for the vast majority of multichromophoric species, the ECL signals could be addressed at different potentials and thus produce multiple emissive readouts.[75–77] The ECL efficiency of **S5** was determined to be 2.51%, which is intermediate between the ECL efficiencies of the ionic components **3a** (2.83%) and **5b** (2.14%). The higher ECL efficiency for **S5** compared to **5b** is due to the $[Ir]^{\cdot-}$-$[Ru]^{\cdot+}$ annihilation process, where $[Ir]^{\cdot-}$ acts as a co-reactant and thus reduces the energy required to emit light from the excited [Ru]*.

Godbert and co-workers[78] synthetised green-emitting anionic Ir complexes bearing an unsual bidentate orotate dianion as the ancillary ligand (NBu_4**4a** and NBu_4**4b** in **Figure 7a**). These complexes exhibited high photoluminescence quantum yields of Φ_{PL} = 69% and Φ_{PL} = 58%, respectively, with emission maxima, respectively, at 530 nm and 536 nm. When NBu_4**4a** and NBu_4**4b** were respectively assembled with the cationic complex $[Ir(ppy)_2(py\text{-}am)]Cl$ (**6b**Cl in **Figure 7a**, py-am is 2-pycolylamine), which itself shows an emission at λ_{PL} = 490 nm with a Φ_{PL} of 52%, highly emissive soft salts, **S6a** and **S6b** (**Figure 7a**) were obtained. **S6a** and **S6b** are unusual examples of soft salts in which the cation (**6b**) is the donor unit, while the anions (**4a** and **4b**) are the acceptors. The emission of **S6a** and **S6b** involved contributions from both ions with λ_{PL}, respectively, at 480, 525 nm and 486, 532 nm and high Φ_{PL} values of 81% and 83%, respectively.

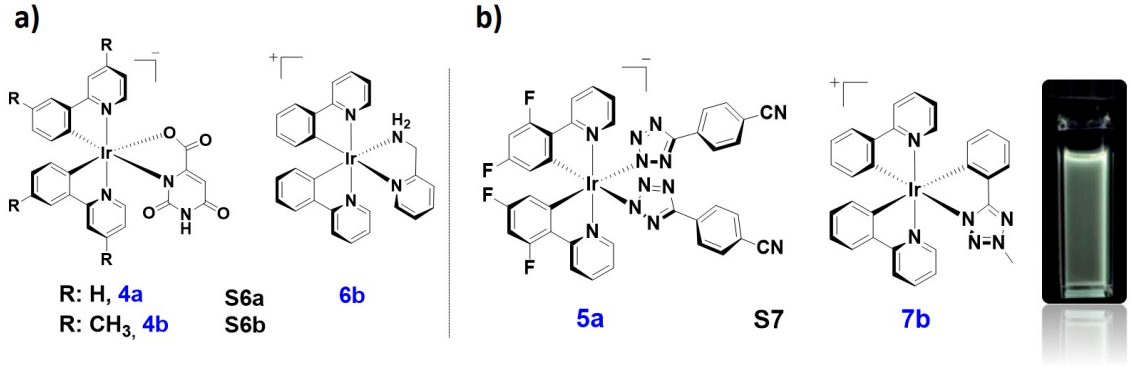

Figure 7. **a)** chemical structure of soft salts **S6a** and **S6b** and **b)** chemical structure of the white-emitting soft salt **S7**. Inset is image of air-equilibrate CH_2Cl_2 solution of **S7**. The inset image is adapted from ref [79] with permission from The Royal Society of Chemistry.

A white-emitting soft salt was obtained by Stagni and co-workers[79] by assembling the blue-emitting anionic Ir(III) complex NBu_4**5a** (**Figure 7b**), bearing dFppy as C^N ligands and 4-benzonitrile tetrazolate as ancillary ligands, with the red-emitting $[Ir(ppy)_2(ptz\text{-}Me)]Cl$ complex (ptz-Me is 5-methyl-2-phenyltetrazole) (**7b**Cl, **Figure 7b**). In aerated CH_2Cl_2, complex NBu_4**5a** exhibited a structured emission profile typical of emission from a ^{3}LC/^{3}MLCT state with λ_{PL} at 462 nm and 492 nm and a Φ_{PL} of 3.3%. Complex **7b**Cl, by contrast, exhibited a broad emission profile with λ_{PL} = 686 nm and a Φ_{PL} of 2.7%. As both the anionic and cationic complexes **5a** and **7b** contributed almost equally to the emission of **S7** in aerated CH_2Cl_2, and energy transfer between the two ions played a minor role, an almost pure white-light (CIE: x = 0.3288, y = 0.3284) with λ_{PL} at 460 nm, 490 nm and 680 nm and a Φ_{PL} of 2.8% was emitted by the assembly. The poor energy transfer in **S7** is probably due to the presence of the bulky 4-benzonitrile tetrazolate in **5a** that restricts its interaction with the cation **7b**.

In the context of electroluminescence devices, neutral Ir complexes have been extensively used in Organic Light-Emitting Diodes (OLEDs),[80–82] whereas cationic Ir(III) complexes have been explored more explicitly as emitters in Light-Emitting Electrochemical Cells (LEECs).[83, 84] OLED and LEEC technologies will be further discussed in Chapter 2. Covalently linked dinuclear iridium complexes have been scarcely investigated as emitters in solid-state lighting, with only one example available for use in LEECs[85] and few for OLEDs.[86–92] However, iridium-based soft salts have demonstrated reasonable performance as emitter materials in OLEDs. The main advantage of using soft salts in lighting devices relies on the capacity to introduce two phosphorescent centers in one complex ion, while controlling the intermolecular separation of the two metal centers through non-covalent interactions. The first examples of iridium soft salts used in OLEDs were reported by Thompson and co-workers.[71] In OLED technologies the two most important parameters to evaluate the device efficiency are the External Quantum Efficiency (EQE), which defines

the ratio of the number of photons emitted from the device to the number of electrons passing through the device, and the luminance, which defines the intensity of light emitted from the OLED per unit area in a given direction. It is worth mentioning that OLED devices fabricated by using the green-emitting *fac*-[Ir(ppy)$_3$] complex exhibited a high EQE of 21.3% and a luminance of over 23000 cd·m^{-2}. The first use of *fac*-[Ir(ppy)$_3$] in OLEDs was reported by Thompson and co-workers in 1999,[93] and since then it is still among the best performing metal complexes used in OLED devices.[2] Notably, OLEDs fabricated by using **S2** (**Figure 4**) as the emitting material exhibited an external efficiency, EQE, of 4.7% and a luminance of over 7428 cd·m^{-2} (λ_{PL} = 586 nm). The good performance of the OLED could be directly linked to the suitable alignment of the HOMO-LUMO levels of the two ionic components of the soft salt. Unfortunately, the relatively low Φ_{PL} of 18% exhibited by **S6** in thin films limited the efficiency of the device. When **S6** was used as the emitter in a single-layer LEEC, the device failed to turn on under voltages ranging from 2.5 V to 7 V, a result of the poor ionic mobility of the ions of **S6**.

Dumur, Mayer and co-workers[94] also explored the use of a soft salt emitter in OLEDs, the composition of which consisted of the anionic NBu$_4$[Ir(dFppy)$_2$(NCS)$_2$], NBu$_4$**6a**, with the cationic complex [Ir(ppy)$_2$(non-bpy)]PF$_6$ **8b**PF$_6$ (**Figure 8a**, non-bpy is 4,4′-dinonyl-2,2′-bipyridine). The nonyl chains were introduced to **8b**PF$_6$ to enhance the solubility of the resultant **S8** in organic solvents and thus improve the thin film morphology in solution-processed devices. Soft salt **S8** exhibited luminescence centered at approximately 550 nm in CH_2Cl_2 solution, thin film and in electroluminescent devices. The OLEDs fabricated with **S8** as the emitting material exhibited a low external quantum efficiency of 0.66% and a luminance of 1114 cd·m^{-2} (λ_{EL} = 553 nm).

Two iridium soft salts based on ion-paired dinuclear cationic, and mononuclear anionic complexes were reported by Mayer and co-workers[95] and investigated as emitting materials in OLEDs (**Figure 8b**). The unit bridging the two iridium centers in the dinuclear cationic complexes consisted either of a carbazole derivative for **9b**PF$_6$ or a phenylene group in the case of **10b**PF$_6$. Both dinuclear complexes **9b**PF$_6$ and **10b**PF$_6$ exhibited low λ_{PL} in degassed CH_2Cl_2 of 9.1% and 15.0%, respectively, attributed to intramolecular quenching between the two iridium luminophores. As the phenylene bridge favored the communication between the two iridium centers, the electroluminescence performance using **S10** was poorer than that using **S9** with respective maximum peak current efficiencies of 0.06 and 0.44 cd·A^{-1} and maximum brightness of 101 and 1022 cd·m^{-2}.

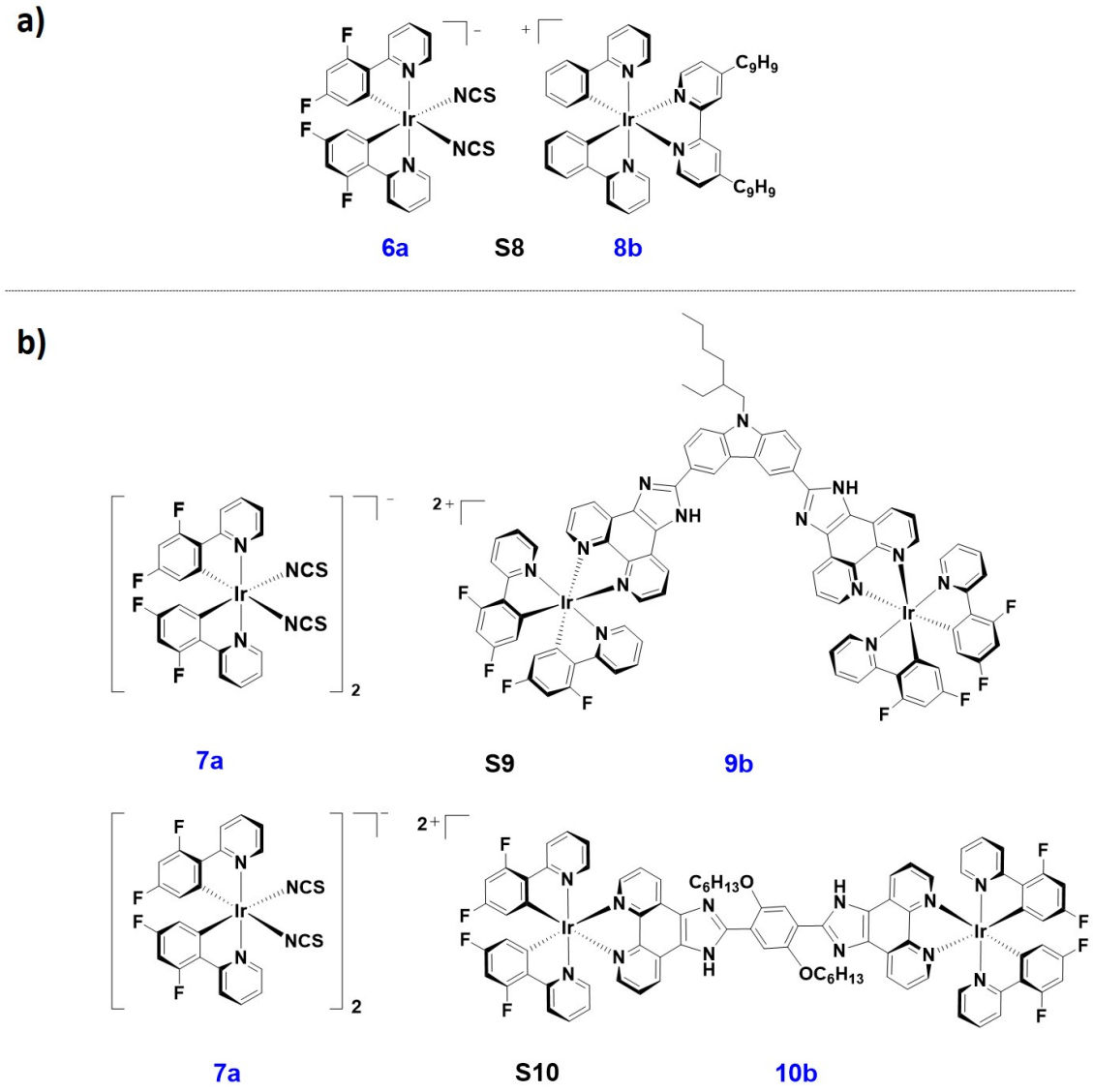

Figure 8. Chemical structures of iridium soft salts used in OLEDs. **a) S8** and **b) S9** (top) and **S10** (bottom).

Intracellular pH is a crucial parameter associated with cellular behavior and pathological conditions such as cell proliferation, apoptosis, drug resistance, enzymatic activity and ion transport.[96] Abnormal cellular pH is an indicator of inappropriate cellular function, which is associated with many diseases such as stroke, cancer, and Alzheimer.[97] It is thus pivotal to monitor pH alteration in biological cells and tissues to understand physiological and pathological processes.[98] In this context, Wong, Zhao and co-workers[99] recently illustrated that soft salts can also be rationally designed to act as efficient probes for lifetime imaging of intracellular pH. Indeed, they designed the soft salt **S11** (**Figure 9a**) formed by the assembly of the cationic complex **11b**Cl, bearing a qpy (qpy = 4,4′:2′,2″:4″,4‴-quaterpyridine) as the ancillary ligand, with the anionic complex NBu_4**2a** (**Figure 4**). Specifically, complex **11b**Cl is pH sensitive as the protonation or deprotonation of its distal

pyridine units gives rise to changes in the emission of **S11**, which can be easily detected by both steady-state and time-resolved luminescence spectroscopy. The cationic complex **11b**Cl showed a broad orange-red emission in deareated MeCN centered at λ_{PL} = 625 nm, which decreased dramatically in intensity with decreasing pH (**Figure 9b**). By contrast, the structured blue-emission exhibited by the anionic counterpart NBu_4**2a** (λ_{PL} = 451, 475 nm) was not affected by changes in pH.

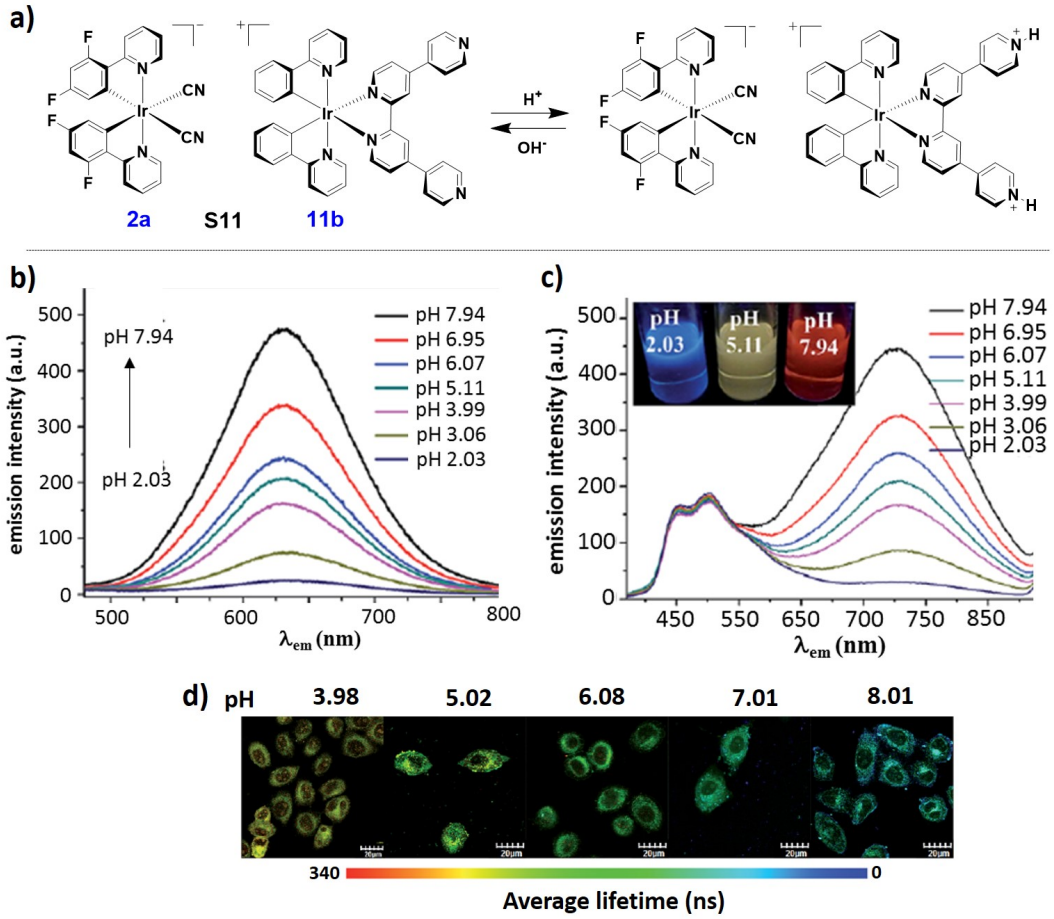

Figure 9. **a)** Design concept of the ratiometric design probe and chemicals structures of **2a**, **11b** and soft salt **S11**. **b)** changes in the phosphorescence emission spectra of **11b** (2.0 x 10^{-5} M) in the pH range of 2.03 – 7.94 in MeCN/buffer (1:9, v/v). **c)** changes in the phosphorescence emission spectra of **S11** (2.0 x 10^{-5} M) in the pH range of 2.03 – 7.94 in MeCN/buffer (1:9, v/v). **d)** phosphorescence lifetime images of **S11** in living Hep-G2 cells (incubated at 37 °C for 1h) at different pH values. Images **b)**, **c)** and **d)** are adapted from ref. [99] with permission from The Royal Society of Chemistry.

The phosphorescence spectral changes of **S11** at different pH values are illustrated in **Figure 9c**. Enhanced phosphorescence at λ_{PL} = 625 nm was observed at basic pH, while at acidic pH the emission of **11b** was quenched due to the protonation of the qpy

ligand. Thus, at basic pH the emission of **S11** was dominated by the orange emission of **11b**, the result of efficient energy transfer from **2a**, while at acidic pH the emission of **S11** was dominated by the structured blue emission of the donor anion. Such a change in phosphorescence from blue to orange with increasing pH values was only observed when **2a** was combined with the cation **11b**, the emission intensity of which is highly pH dependent. The change in photoluminescence from blue to orange with increasing pH was also detected using confocal luminescence microscopy after incubation of **S11** in living HepG-2 cells (**Figure 9d**).

Similarly, Zhao and co-workers[100] used an ion-paired iridium complex (**S12**, **Figure 10a**), composed of a cationic complex functionalised with α,β-unsaturated ketone moieties (**12b**PF_6), and the anionic complex NBu_4**3a** (**Figure 5a**), for ratiometric and time-resolved luminescence sensing and imaging of intracellular biothiols cysteine and homocysteine. These analytes were chosen as they participate in the process of cellular growth in living cells. The sensing capacity of **S12** towards thiol analytes is due to their rapid Michael addition with the α,β-unsaturated ketone moieties of **12b** thereby promoting a strong enhancement of the emission of the cation acceptor at λ_{PL} = 560 nm, while only slightly influencing the photophysics of the donor complex at λ_{PL} = 485, 505 nm (**Figure 10b,c**).

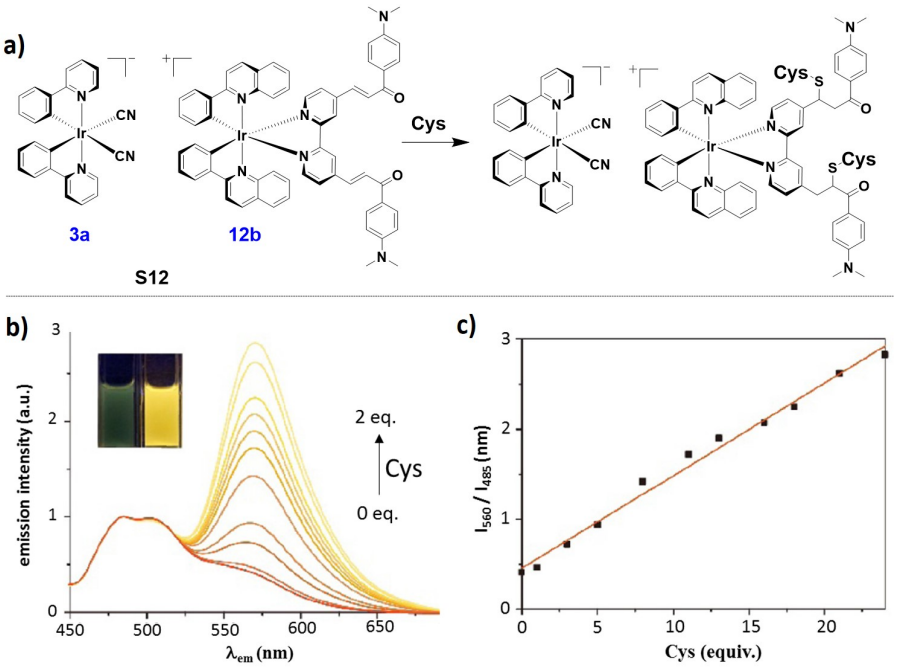

Figure 10. **a)** chemical structures of **3a**, **12b** and soft salt **S12** and sensing mechanism of **S12**. **b)** changes in phosphorescence emission spectra of **S12** in MeCN/H_2O (3:2, v/v) with various amount of cysteine added (from 0 to 2 equivalents). Insets are images of **S12** without cysteine (left) and with two equivalent of cysteine (right). **c)** titration curve plotted with emission intensity at 560 nm over that at 485 nm as a function of cysteine equivalents. Images **b)** and **c)** are adapted from ref. [100] - published by OSA publishing.

Schanze and co-workers[101] reported an ion-paired assembly between the anionic poly(phenyleneethynylene) electrolyte ($PPESO_3^-$) and the cationic Ir(III) complex **4b**Cl (**Figure 5a**). Upon excitation of **4b**-$PPESO_3^-$ in methanol at 355 nm, the emission of $PPESO_3^-$ at λ_{PL} = 450 nm was completely quenched as a result of Dexter energy transfer from $PPESO_3^-$ to **4b** with a calculated quenching constant (k_q) of around 10^5 M^{-1}. A weak phosphorescence from **4b** was observed at λ_{PL} = 610 nm. Subsequent to the Dexter energy transfer, ultra-fast back-transfer from the triplet state of **4b** located at 2.25 eV to the triplet state of $PPESO_3^-$ located between 2.0 – 2.2 eV was detected by transient absorption spectroscopy. By contrast, back-energy transfer was not observed when $PPESO_3^-$ was assembled with the Ir(III) complex of composition $[Ir(hqx)_2(bpy)]Cl$ (hqx is 2,3-diphenylquinoxaline), which possesses a triplet state at 1.96 eV, which is too low in energy to sensitise the formation of the triplet state of $PPESO_3^-$. This study demonstrates that Ir(III) complexes with appropriate triplet energy can serve to sensitise the triplet state in conjugated polymers.

1.3.1.2 Liquid crystals

Liquid crystals (LC) are considered as the "fourth state of matter" as their properties are intermediate between those of crystalline solids and those of liquids. Most liquid crystals are neutral organic compounds.[45] However, ionic liquid crystals can also be formed by incorporating anions and cations into the molecule of the LC.[102] Ionic metallomesogens, for instance, are liquid crystals based on transition metal complexes.[103] The driving force for the formation of metallomesogens are the interactions, generally van der Waals, between the anisotropic molecules promoting high self-organization of the materials into rod-like, disc-like or nematic columnar phases.[45] Early examples of LC iridium complexes took advantage of the square-planar geometry or iridium(I) metal centres. Complex **LC1** (**Figure 11**) is a dinuclear complex bearing a mesomorphic ligand that, due to its elongated shape, displayed a smectic phase at higher temperature (between 142 °C and 169 °C) compared to related mononuclear complexes (between 104 °C and 128 °C) of the composition of $[IrCl(CO)_2L]$, where L are 4-stilbazole or 4-styrylpyridine derivatives bearing long alkoxy chains.[104, 105]

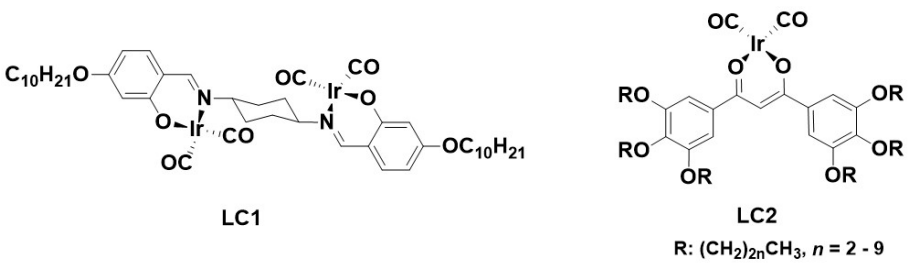

Figure 11. Chemical structure of **LC1** (left) and **LC2** (right).

LC2 (**Figure 11**) is based on an iridium dicarbonyl β-ketonate functionalised with alkoxy chains that crystallised with a strict antiparallel arrangement of the Ir centres to produce one-dimensional chains that displayed disordered columnar hexagonal phases (Col_{hd}).[106, 107] Interestingly, for n = 3, 4, 5, the complexes were liquid crystalline already at 0 °C and remained so up to 130 °C.

The first example of a LC based on a luminescent cyclometalated Ir(III) complex (**LC3**, **Figure 12**) was reported by Ghedini and co-workers.[108] **LC3** is the cationic complex $[Ir(ppy)_2(bpy\text{-}C8)]PF_6$ bearing a bipyridine functionalised at the 4,4′-position with [3,4,5-(trioctyloxy)benzoyloxymethyl] units as the ancillary ligand.

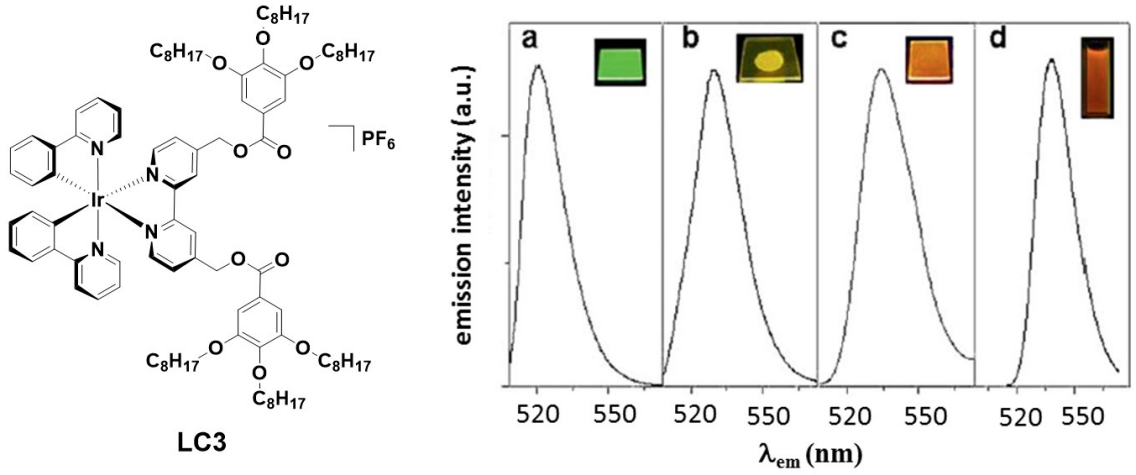

Figure 12. Chemical structure of **LC3** (left) and its emission spectra (right) collected from **a)** crystalline film (green), **b)** mesophase film (yellow), **c)** amorphous film (orange-red) and **d)** CH_2Cl_2 solution. Insets are images of samples under UV illumination. Images **a)**, **b)**, **c)** and **d)** are adapted with permission. Copyright 2010, Wiley-VCH.[108]

This complex exhibited a monotropic columnar hexagonal phase when the sample was cooled rapidly (>10 °C/min), and this mesophase was stable within the temperature range of 120 °C - 20 °C. Upon subsequent heating, crystallisation was observed at 94 °C and isotropisation occurred at 184 °C. When the sample was slowly cooled, only the crystalline phase was observed. Interestingly, the different phases exhibited different emission properties. In deaerated CH_2Cl_2 **LC3** exhibited an orange-red emission at λ_{PL} = 600 nm with a Φ_{PL} of 12% and an emission lifetime, τ_{PL}, of 320 ns, corresponding to a mixed ^{3}LLCT/^{3}MLCT transition (LLCT = ligand-to-ligand charge transfer). Unlike the modest Φ_{PL} of **LC3** in solution, enhanced luminescence was detected in the two condensed phases. The emission of the liquid-crystalline and crystalline phases were both blue-shifted, respectively, at λ_{PL} = 560 nm and 520 nm, with significantly higher Φ_{PL} of 39% and 48%, respectively, compared to those observed in CH_2Cl_2 (**Figure 12**). The blue shifts accompanied by the enhanced

emission intensities exhibited by **LC3** on moving from solution to the liquid-crystalline phase and finally to the crystalline solid are due to the reduced aggregation quenching phenomena and the increasing molecular rigidity present in the condensed phases.

Bruce, Williams and co-workers[109] used cyclometalated Ir(III) complexes bearing anisotropic polycatenar 2,5-diphenylpyridine ligands to prepare the liquid crystalline complexes **LC4**-**LC9** illustrated in **Figure 13**. Complex **LC4** was formed by cleavage of the corresponding μ-dichloro-bridged iridium dimers with dimethyl sulfoxide. Complex **LC4** showed both lamellar and columnar rectangular phases. However, **LC4** exhibited a weak emission at λ_{PL} = 580 nm with a low Φ_{PL} of 0.5% in degassed CH_2Cl_2 and lacked chemical stability. The subsequent reaction of **LC4** with $AgPF_6$ in MeCN yielded **LC5**, which was found to be slightly more emissive and more stable than **LC4**. **LC5** exhibited a columnar mesophase between 145 °C and 163 °C, and emission in degassed CH_2Cl_2 at λ_{PL} of 520 nm, with a Φ_{PL} of 1.3% and a τ_{PL} of 1750 ns. In search as additional luminescent iridium-based LCs, attention then turned to neutral complexes bearing acetylacetonate (acac) as the ancillary ligand.

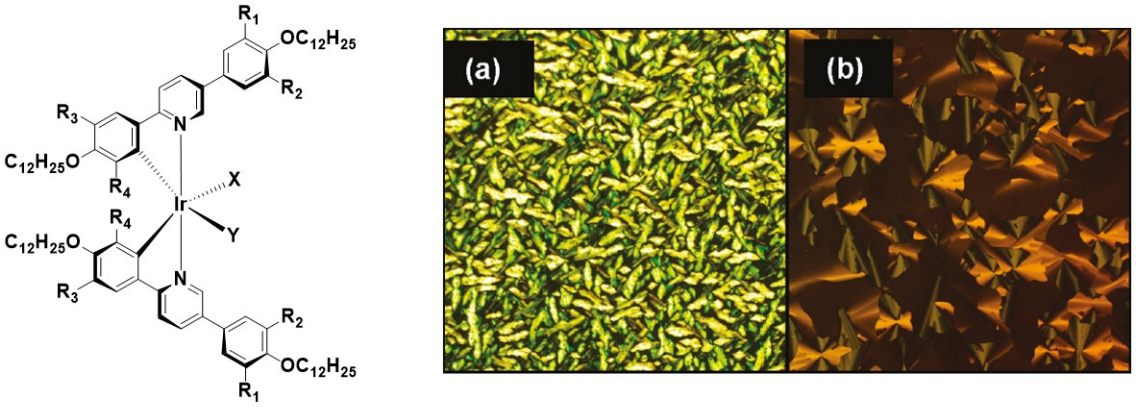

R_1, R_2, R_3, R_4 = H; X = Cl; Y = dmso: **LC4**
R_1, R_2, R_3, R_4 = H; X, Y = MeCN: **LC5**
R_1, R_3 = -$OC_{12}H_{25}$; R_2, R_4 = H; X, Y = acac: **LC6**
R_1, R_2, R_3 = -$OC_{12}H_{25}$; R_4 = H; X, Y = acac: **LC7**
R_1, R_2, R_3, R_4 = -$OC_{12}H_{25}$; X, Y = acac: **LC8**
R_1, R_2, R_3 = -$OC_{12}H_{25}$; R_4 = H; X, Y = Cl-dimer: **LC9**

Figure 13. Chemical structure of the LC molecular complexes and optical texture of complexes **(a) LC5** (155 °C on cooling) and **(b) LC9** (43 °C on cooling). Images **a)** and **b)** are adapted with permission from ref. [109]. Copyright 2011, American Chemical Society.

Complexes **LC6** and **LC7** were not liquid crystalline. It was indeed discovered that three polycatenar chains on each of the C^N ligands were necessary to confer liquid crystallinity upon the complexes. Thus, **LC8** was both LC in nature and emissive, exhibiting a columnar hexagonal phase between 31 °C and 66 °C and emission at λ_{PL} = 582 nm with

a Φ_{PL} of 9.1%; no emission lifetime was reported. The μ-dichloro-bridged iridium dimer **LC9** (**Figure 13**) also exhibited a columnar liquid crystal phase from room temperature to 75 °C. This iridium dimer was, however, weakly emissive at λ_{PL} = 570 nm, exhibiting a low Φ_{PL} of 0.8% accompanied by a relatively long τ_{PL} of 5.1 µs.

In a subsequent work[110] by the same authors, a series of dinuclear Ir(III) complexes were prepared based on ppy derivatives functionalised with four, five and six polycatenar chains as cyclometalating ligands, and 1,1,2,2-tetraacetylethane (tae) acting as both the ancillary and bridging ligand to connect two iridium centers (**Figure 14a**).

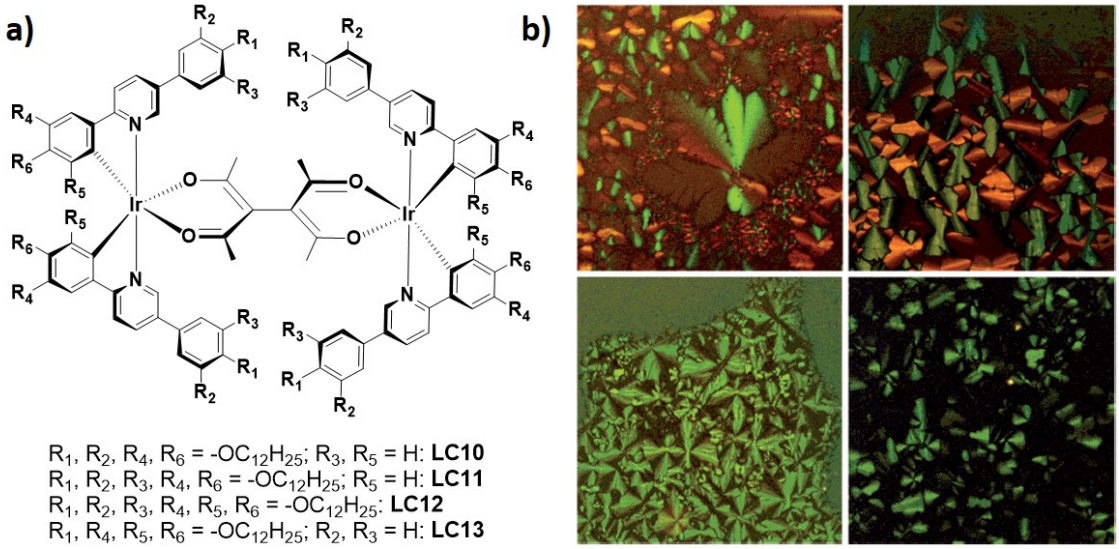

Figure 14. **a)** Chemical structures of **LC10**, **LC11**, **LC12** and **LC13**. **b)** optical micrograph (on cooling) of complexes: **LC11** isomer 1, 100 °C (top-left); **LC11** isomer 2, 60 °C (top-right); **LC10** racemate, 85 °C (bottom-left); **LC13**, 133 °C (bottom-right). Image **b)** is adapted with permission. Copyright 2012, Wiley-VCH.[110]

LC10, **LC11**, **LC12** and **LC13** were all similarly mesomorphic, showing a columnar hexagonal mesophase with a fern-like feature. Considering that the corresponding mononuclear acac complexes **LC6** and **LC7** were not mesomorphic in nature, the bridging tae ligand changes the geometries of the molecules, making them more disc-like and inducing mesomorphism in the same manner as the bridging chlorides did in **LC9**. However, unlike **LC9**, complexes **LC10**, **LC11**, **LC12** and **LC13** were all very emissive in CH_2Cl_2 solution at room temperature, all exhibiting similar orange luminescence between 578 nm and 588 nm with Φ_{PL} of approximately 50% and Φ_{PL} of around 4.0 µs. As the two iridium centers in all of the dinuclear complexes are asymmetric, two diastereomeric forms, i.e. *meso*-form with Λ,Δ-stereochemistry, and racemate-form with Λ,Λ- and Δ,Δ-stereochemistry, can be obtained. For μ-dichloro-bridged iridium dimers only the racemic form is generally obtained because of steric hindrance. However, as the tae bridging ligand keeps the iridium centers

more distant compared to the chloro bridging ligands, the formation of both diastereomers (meso and racemic) was observed for complexes **LC10**, **LC11**, **LC12** and **LC13**. In the case of complex **LC11**, the two racemates were separated by column chromatography into the enantiopure analogs without identifying their respective absolute configuration. Despite both isomers exhibiting identical emission properties (λ_{PL} = 558, 663 nm, Φ_{PL} = 43%) and columnar hexagonal phases (**Figure 14b**), their isomorphic temperature ranges differed from 79 – 126 °C for one isomer to 63 - 95 °C for the other.

Baranoff and co-workers[111] recently reported a modular approach to the design of mesomorphic phosphorescent iridium complexes. In their design, rod-shaped difluorobiphenyl cyclohexyl mesogenic groups were grafted onto the non-chromophoric acac ligand of the core structure [Ir(C^N)$_2$(acac)] in complexes **LC14**, **LC15**, **LC16** and **LC17** (**Figure 15**). The C^N ligands (ppy and dFppy) dictated the photophysical properties of the complexes while the mesogenic units of the functionalised acac ligands controlled the mesomorphic properties of the materials.

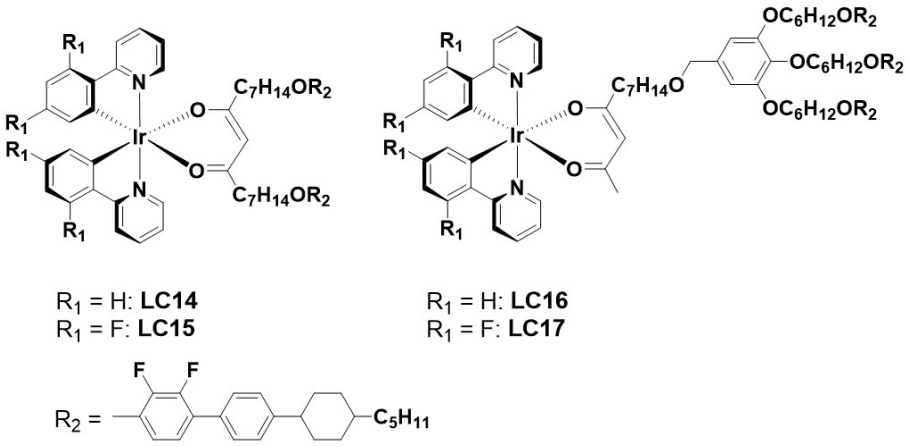

Figure 15. Chemical structures of **LC14**, **LC15**, **LC16** and **LC17**.

In degassed CH_2Cl_2 solution, the complexes **LC14** and **LC16** bearing dFppy C^N ligands exhibited sky-blue emissions centered at λ_{PL} = 482 nm, with Φ_{PL} of 64% and 65% and τ_{PL} = 1.2 µs and 1.0 µs, respectively. **LC15** and **LC17** bearing ppy as the C^N ligands, showed red-shifted emission compared to the previous two LCs centered at λ_{PL} = 517 nm, with Φ_{PL} of 51% and 45% and τ_{PL} = 1.4 µs and 1.6 µs, respectively. As the functionalisation of the acac ligand had little effect on the emission properties of the complexes in solution, the photophysical properties of **LC14**, **LC15**, **LC16** and **LC17** were very similar to those exhibited by the corresponding reference complexes [Ir(ppy)$_2$(acac)] and [Ir(dFppy)$_2$(acac)]. Each of **LC14**, **LC15**, **LC16** and **LC17** exhibited a smectic A mesophase with melting points between 150 °C and 170 °C. However, due to the unsymmetrical nature of **LC16** and **LC17**, the mesophase of these two complexes were found to be enantiotropic.

1.3.1.3 Luminescent gels

Macroscopically, gels consist of viscoelastic solid-like materials comprised of an elastic cross-linked network and a solvent trapped within the 3D matrix of the gel network by physical or chemical forces.[112, 113] Traditional gel chemistry is dominated by polymers formed through covalent bonds. Of more recent interest are fibrous gel networks, called "supramolecular gels", that can be constructed from small molecules that are interlinked through non-covalent interactions such as hydrogen bonding, π-π-interactions, metal coordination or host-guest inclusion.[114] Gels have been used in diverse applications such as tissue engineering and wound healing, drug delivery, templating self-assembled morphologies, molecular electronics and sensing.[115] Metal introduction in gel networks has been motivated as a way of tuning their properties with examples of gels containing metallo-porphyrins, ferrocene, platinum, ruthenium, gold and copper complexes having been described in the literature.[116] In this section of the review we summarize the recent developments in phosphorescent gels based on cyclometalated Ir(III) complexes.

By combining the blue-emitting 1,8-naphtalimide-based gelator **G1** with the orange-emitting iridium complex **G2** (**Figure 16a**), Yi and co-workers[117] reported a white-emitting two-components supramolecular gel. **G1** exhibited an excellent ability to gelate a series of polar or apolar organic solvents (e.g., cyclohexane, ethyl acetate, acetonitrile, acetone, methanol, propanol and dimethyl sulfoxide). Scanning electron microscopy (SEM) images of the xerogels of **G1** showed the formation of interweaving fibres (**Figure 16b**). **G1** could also efficiently form gel networks in acetonitrile in the presence of the iridium complex **G2** in a molar ratio **G1**:**G2** = 3:1. This xerogel had almost the same fiber framework as that of the neat **G1** xerogel, with the iridium complex **G2** assembled into nanoparticles of 20 – 50 nm dispersed into the gel fibres. **G1** exhibited a blue fluorescence at λ_{PL} = 430 nm with a Φ_{PL} of 26.7% in MeCN, while after gelation its emission was slightly red-shifted at λ_{PL} = 440 nm. The iridium complex **G2**, on the other hand, exhibited a structured orange emission at λ_{PL} = 533, 570 nm with a Φ_{PL} of 2.2%. Upon photoexcitation of **G1** in MeCN, inefficient energy transfer (with efficiency of approximately 0.5 - 5%) to the iridium complex **G2** was promoted. However, due to the close proximity of the chromophores **G1** and **G2** in the gel fibers, the efficiency of the energy transfer increased up to 60 – 70%, leading to white light emission from the gel network of composition **G1**:**G2** = 3:1 (CIE coordinates, x: 0.31, y: 0.39, **Figure 16c**).

It had previously been reported that Ir(III) complexes functionalised with carbonyl units can react with cysteine to give non-emissive complexes.[118] Addition of cysteine to complex **G2** in MeCN resulted in a red-shift of the emission of the iridium complex from 533 nm to 579 nm with a dramatic decrease in intensity due to the formation of the thiazolidine species. When cysteine (from 0 to 40 equiv.) was added to the white-emitting gel **G1**:**G2**, the gradual quenching of the orange emission of **G2** gave rise to a pronounced

colour change of the gel from white to blue. As a result, the emission properties exhibited by gel **G1**:**G2** can be exploited for the detection of cysteine.

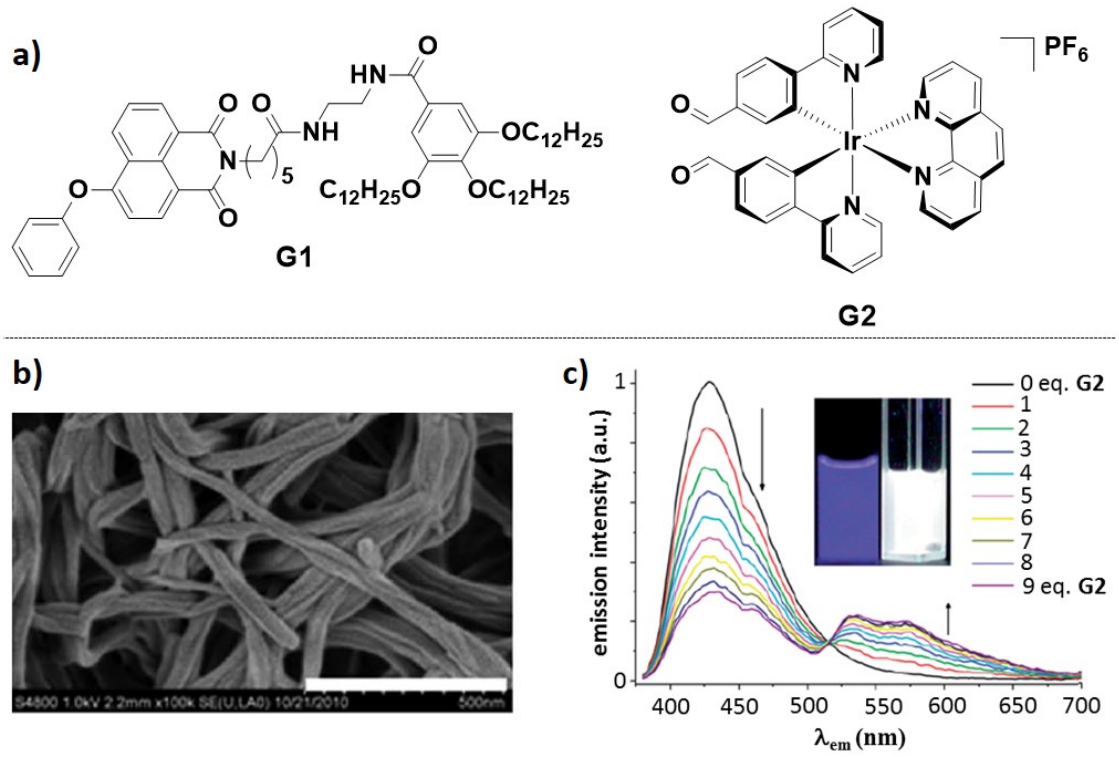

Figure 16. **a)** chemical structures of gelator **G1** (left) and the iridium complex **G2** (right). **b)** SEM images of xerogel **G1** in acetonitrile at 298 K. **c)** Emission spectral changes of **G1** as a result of the addition of **G2** from 0.1 to 9 equivalents. Insets are images of the blue emitting **G1** and white emitting gel **G1**:**G2**. Images **b)** and **c)** are adapted from ref. [117] with permission from The Royal Society of Chemistry.

Szerb, Donnio and co-workers[119] reported that cationic Ir(III) complexes of composition $[Ir(ppy)_2(bpy)]^+X^-$ spontaneously self-assembled into ordered aqueous gel phases when containing aliphatic carboxylate counterions, X^-, of the type of RCO_2^- (R: CH_3, C_2H_5, C_5H_{11}, C_7H_{15}, **Figure 17a**). When dissolved in water at a concentration of 2.5 wt%, complexes **G3**, **G4** and **G5** formed gel networks (**Figure 17b**), exhibiting similar blue-shifted emissions, respectively, at λ_{PL} = 540 nm, λ_{PL} = 538 nm and λ_{PL} = 536 nm with modestly higher Φ_{PL} of 15%, 15% and 17% compared to the corresponding isotropic solutions at lower concentration (1 wt% in degassed aqueous solution, **G3**: λ_{PL} = 564 nm, Φ_{PL}: 9%, **G4**: λ_{PL} = 554 nm, Φ_{PL}: 11%, **G5** λ_{PL} = 540 nm, Φ_{PL}: 16%). By contrast, due to the long C_7H_{15} aliphatic chain present on the counterion of **G6**, the complex was found to be poorly soluble in water and it formed only turbid suspensions when dissolved in aqueous solution. The aggregation process of **G3**-**G5** into gels was investigated by wide-

and small-angle x-ray scattering (WAXS and SAXS) and small-angle neutron scattering (SANS) measurements. At concentrations higher than 1.8 wt%, the gelification of **G3**-**G5** occurred with close packing of supramolecular columns, sheathed in their solvation shells into 2D-rectangular lattices surrounded by their counterions. The overall organisation of the gels **G3**-**G5** is classified as a lamellar-columnar phase (**Figure 17c**).

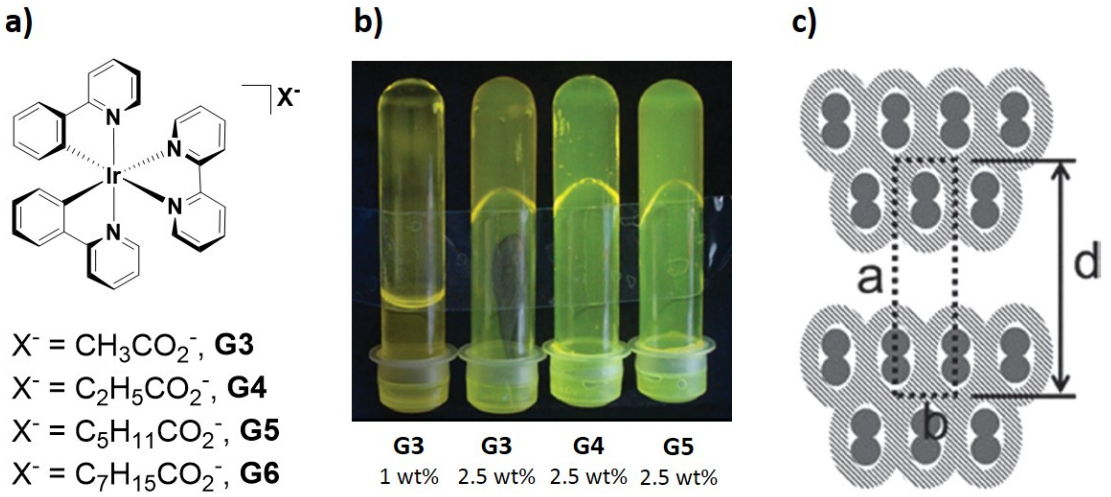

Figure 17. **a)** Chemical structures of complexes **G3**-**G6**; **b)** images from left to right of anisotropic solution of **G3** at concentration of 1 wt%, gel of **G3**, **G4** and **G5** at concentration of 2.5 wt%; **c)** schematic representation of the proposed organization of the Ir(III) complexes in the gel phase. Strand (solid gray) associated laterally into double rows incorporating water and counterions (dashed gray). Images **b)** and **c)** are adapted with permission. Copyright 2013, Wiley-VCH.[119]

The quasi-spherical shape of octahedral Ir(III) complexes is intrinsically unfavorable for face-to-face stacking and linearly polarised emission and therefore the number of emissive Ir(III) liquid crystals and gels reported to date are still limited. This contrasts, for example, with cyclometalated Pt(II) complexes that have square planar geometries and interact through both π-π and Pt-Pt bounding interactions, thus exhibiting good alignment with high polarisation ratio.[120] As a result, the number of reports of luminescent liquid crystals and gels to date based on Ir(III) complexes are much fewer in number than those based on Pt(II) chromophores.

1.3.1.4 Surfactant-based structures

The term surfactant defines molecules soluble in both organic solvents and water. They generally consist of a polar headgroup and an apolar tail that confer amphiphilic behaviour

to the systems.[55] One of the characteristic features of surfactants is their ability to self-assemble, under certain conditions, into well-defined aggregate structures such as micelles or highly symmetric volume phases through amphiphilic interactions.[121] Recent advances in nanoscience and colloidal technology have strongly driven the development of colloidal structures with integrated multifunctional properties.[46] In this context, iridium-based surfactants, when opportunely designed, have shown the ability to self-assemble into colloidal structures, giving rise to amphiphilic networks with enhanced photophysical properties.

De Cola and co-workers[122] reported the first examples of iridium and ruthenium metallo-surfactants assembled in micellar systems. Both the Ir(III) complex **MS1** [Ir(dFppy)$_2$(alk-bpy)]Cl and the Ru(II) complex **MS2** [Ru(bpy)$_2$(alk-bpy)]$_2$Cl (**Figure 18a**) contain a 2,2′-bipyridine ligand functionalised at the 4,4′-positions with seventeen methylene units (alk-bpy) as the hydrophobic part of the structure.

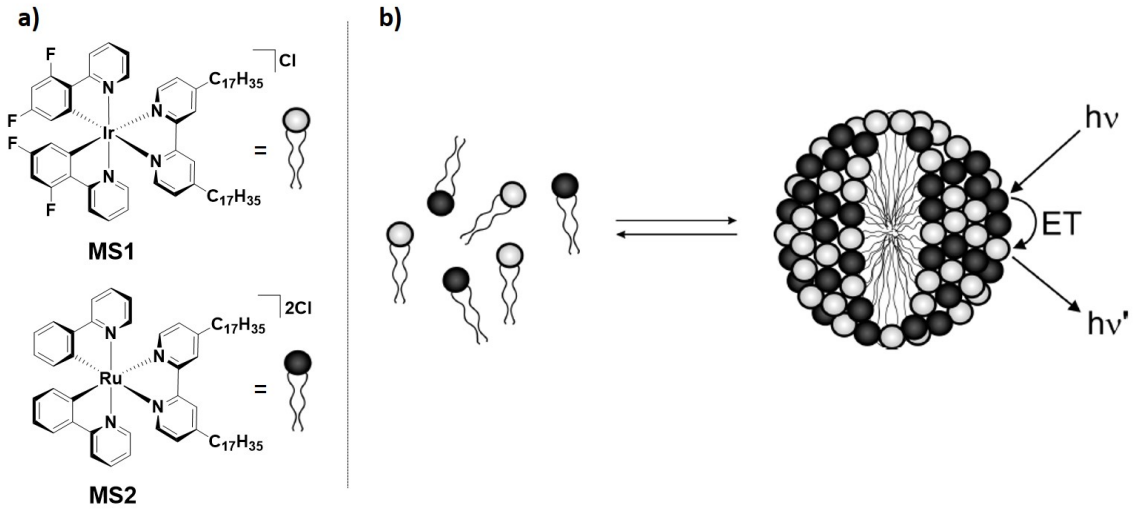

Figure 18. **a)** Chemical structure of the metallo-surfactants **MS1** and **MS2**. **b)** self-aggregation of **MS1** and **MS2** into mix micelle and schematic illustration of ET from donor Ir to acceptor Ru. Image **b)** is adapted with permission from ref. [122]. Copyright 2008, American Chemical Society.

The photophysical properties of **MS1** and **MS2** in water below their critical micelle concentrations (CMC), respectively, of 5 µM and 3 µM, resembled those of the reference complexes [Ir(dFppy)$_2$(bpy)]Cl, **3b** (**Figure 5**) and [Ru(bpy)$_3$]Cl$_2$. **MS1** exhibited, as a monomeric species, a broad emission at λ_{PL} = 635 nm with a Φ_{PL} of 3.0% and a τ_{PL} of 360 ns. At a concentration of 0.15 mM (above the CMC limit), the emission intensity of **MS1** was almost unchanged (Φ_{PL} = 3.3%) but its emission lifetime became bi-exponential in nature, with a short component due to the non-aggregated form of τ_{PL} = 400 ns, and a longer component of τ_{PL} = 860 ns that arises from the self-assembled species. Similarly, the emission intensity of **MS2** at a concentration of 0.01 mM was slightly enhanced (Φ_{PL}

= 4.5%) with longer bi-exponential lifetime decay components of τ_{PL} = 175 ns and 475 ns compared to the emission properties of **MS2** in its monomeric form (Φ_{PL} = 2.5%, τ_{PL} = 160 ns). The enhanced emissions with long lifetime components in both **MS1** and **MS2** observed at concentrations higher than their CMC are attributed to their micellar aggregation that reduce the non-radiative vibrational modes of the complexes as a function of their closer packing. When **MS1** and **MS2** were mixed in a 1:1 ratio at 0.025 mM each, the complexes aggregated into mixed micellar system, and when excited at 350 nm, only the characteristic emission of the ruthenium complex **MS2** was observed at 645 nm. Thus, efficient Förster energy transfer (ET) from the iridium donor to the ruthenium acceptor was promoted in the assembled mixed micelles (**Figure 18b**); ET was not observed when the two complexes were mixed at a concentration below their CMC.

The Ir(III) complex **MS3** (**Figure 19a**) was designed similarly to **MS1**, to have a polar charged iridium head and long aliphatic tail appended to the ligands with the complex of composition $[Ir(ppy)_2(N\hat{}N)]PF_6$, where N^N is 2,2'-bipyridine functionalised with six apolar long aliphatic chains, bis-[4,4′-bis(3,4,5-trydodecyloxybenzoyloxymethyl)-2,2′-bipyridyl)].[123] As observed for **MS1**, **MS3** exhibited high tendency to aggregate in water through interactions between the hydrophobic chains, resulting in a blue-shifted emission at λ_{PL} = 565 nm with higher Φ_{PL} of 25.6% and longer bi-exponential emission decays of 210 ns, 700 ns compared to the emission exhibited in THF, where no aggregation was observed (λ_{PL} = 605 nm, Φ_{PL} = 4.5%, τ_{PL} = 113 ns).

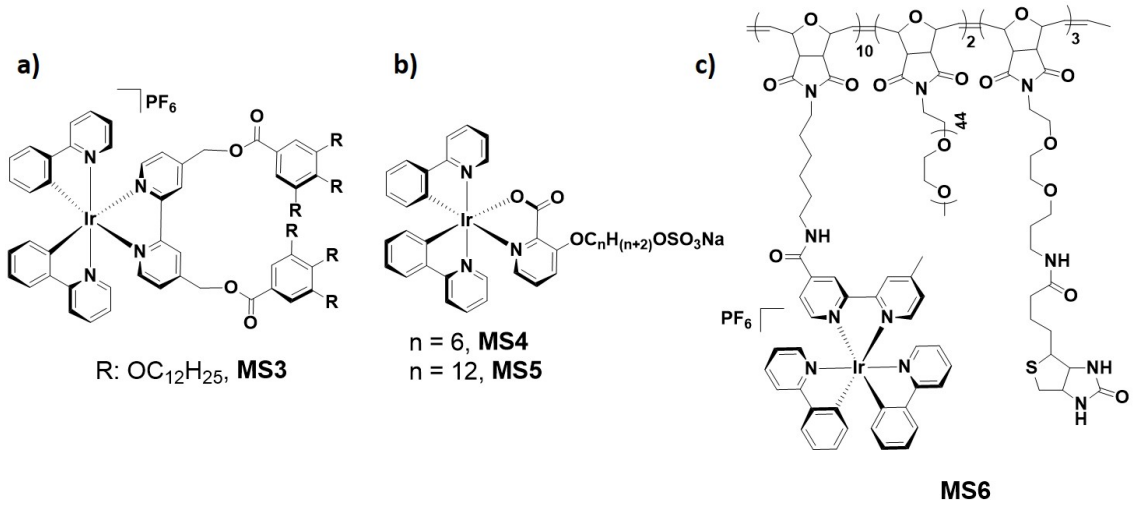

Figure 19. Chemical structures of **a) MS3**; b) **MS4** and **MS5** and **c)** copolymer **MS6**.

In contrast to **MS1** and **MS3** that consist of a neutral hydrophobic tail attached to the ancillary ligand and a cationic Ir(III) complex as the headgroup, **MS4** and **MS5** (**Figure 19b**) are characterised by a reverse design strategy where the Ir(III) core, $[Ir(ppy)_2(alk\text{-}pic)]$, is neutral and the picolinate ligand (alk-pic) is substituted with long alkyl chains

bearing a terminal mono-anionic sulfate group and sodium as counter cation.[124] At a low concentration of 0.01 mM in water, complexes **MS4** and **MS5** both exhibited weak emission centered respectively at λ_{PL} = 650 nm and λ_{PL} = 646 nm with $\Phi_{PL} < 0.1\%$ accompanied by very short emission lifetimes $\tau_{PL} < 20$ ns. At higher concentrations between 1 mM and 0.1 mM both **MS4** and **MS5** showed at first good solubility in water giving clear solutions, followed by a visible formation of colloidal samples within 2h. Compared to the mononuclear species, the colloidal samples of **MS4** and **MS5** exhibited enhanced and blue-shifted emissions, respectively, at λ_{PL} = 509 nm and λ_{PL} = 531 nm with Φ_{PL} of ca. 1% and bi-exponential τ_{PL} of 111 ns and 261 ns for **MS4** and 24 ns and 87 ns for **MS5**. The size, morphology and stability of the aggregates were determined by dynamic light scattering (DLS) and scanning electron microscopy (SEM), both of which evidenced the formation of particles with average radii of 300 – 1300 nm. In addition, zeta potential analyses showed that **MS4** and **MS5** at a concentration of 1.9 mM both have highly negative surfaces towards the water phase (-37 and -57 mV, respectively). Therefore, the surfactant molecules gave rise to aggregates where the neutral and hydrophobic iridium complexes were preferentially inside the colloidal structure while the anionic sulfate moieties faced the solvent. Consequently, the protection of the iridium chromophores inside the colloidal systems accounted for the enhanced emission properties of **MS4** and **MS5** observed at high concentration.

Luminescent mesoporous silicas were prepared by assembling the neutral iridium complex *fac*-[Ir(ppy)$_3$] with two structure-directing agents (SDA), the cationic cetyltrimethyl ammonium bromide (CTAB) and the non-ionic poly(ethylene glycol)-block-poly(propylene glycol)-block-poly(ethylene glycol) (P123).[125] The Ir(III) complex was firstly trapped into the micelles formed by the SDAs. The micelles were then used as templates to form mesoporous silicas. XRD and nitrogen sorption measurements provided evidence for the preferential inclusion of the Ir(III) luminophore into the hydrophobic channels of the mesostructures, without any substantial changes in the hexagonal symmetry of the silica. The resulting hybrid material showed a blue-shifted iridium-based emission at λ_{PL} = 509 nm with higher Φ_{PL} of 72% and longer bi-exponential τ_{PL} of 576 ns and 1077 ns compared to the emission observed for *fac*-[Ir(ppy)$_3$] as a pristine powder (λ_{PL} = 534 nm, Φ_{PL} = 12%, τ_{PL} = 38 ns) where aggregation-caused quenching is prevalent.

Phosphorescent materials based on templated synthesis of mesoporous silica using micellar solution of the Ir(III) metallosurfactant [Ir(dFptrBz)$_2$(hd-ppy)]Cl (dFptrBz is 1-benzyl-4-(2,4-difluorophenyl)-1H-1,2,3-triazole and hd-bpy is 4,4′-diheptadecyl-2,2′-bipyridine), **MS7** in CTAB were also investigated by Stucchi de Camargo, De Cola and co-workers[126] (**Figure 20**). **MS7** exhibited a broad emission at approximately λ_{PL} = 500 nm with a Φ_{PL} of 85% and a τ_{PL} = 1043 ns in degassed EtOH-H_2O (1:1 v/v) at a concentration of 10^{-5} M. Micellar solutions of **MS7**:CTAB (1:8000 ratio) also exhibited a broad emission at λ_{PL} = 500 nm with lower Φ_{PL} of 42% and a τ_{PL} = 1040 ns. Due to the rigidification

of the system and/or more restricted access of oxygen inside the pores of the host silica material, **MS7**:TEOS exhibited an emission at λ_{PL} = 460, 500 nm with a Φ_{PL} of 45% and significantly longer bi-exponential lifetime of τ_{PL} = 1037 ns, 4200 ns compared to the micellar solution **MS7**:CTAB.

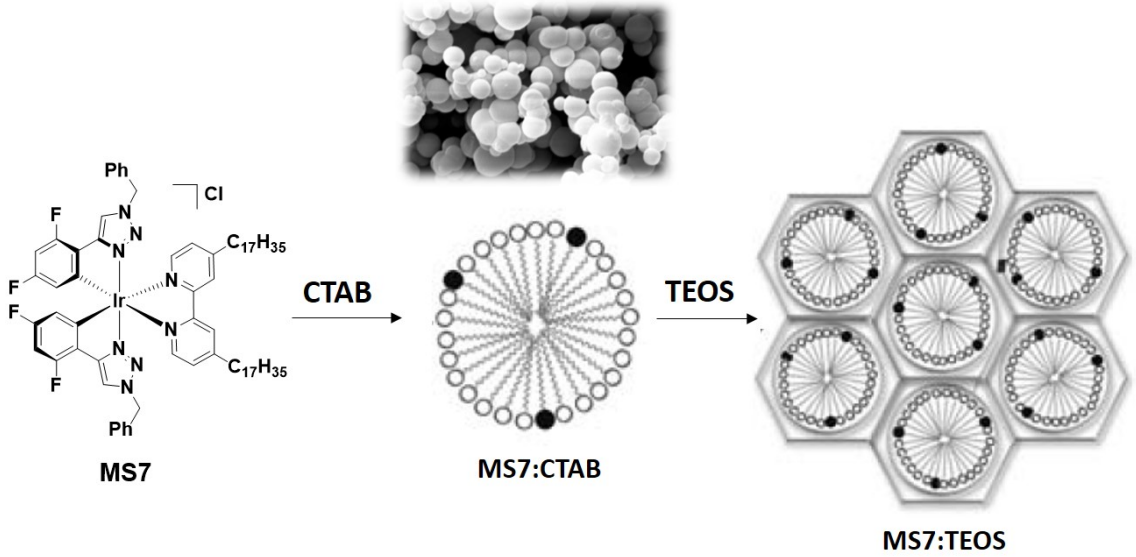

Figure 20. Chemical structure of **MS7** and representation of the micellar system **MS7**:CTAB and the silica material **MS7**:TEOS. Inset is a SEM micrograph image of **MS7**:CTAB (1:1500 ratio). Adapted from ref. [126] with permission from The Royal Society of Chemistry.

A different type of micellar system was reported by Mauzeroll, Sleiman and co-workers.[127] Through a ring-opening metathesis polymerisation (ROMP), a tri-block polymer, **MS6** (**Figure 19c**) containing an iridium complex with a core structure of composition of $[Ir(ppy)_2(bpy)]^+$ as the luminescent unit, oligoethylene glycol, and biotin as biorecognition unit for binding streptavidin (**Figure 19c**) was prepared. As the Ir(III) blocks are hydrophobic and the PEG-based block is water soluble, the self-assembly of the polymer into a micellar system was possible upon addition of water to an acetonitrile solution of the polymer. Atomic force microscopy (AFM) evidenced the formation of nanoparticles with an average diameter of 20 – 50 nm, where the iridium complexes were located in the core of the micelles, while the biotin recognition units were situated at the surface. As observed for **MS1**-**MS5**, the emission of the iridium complex in **MS6** was blue-shifted at λ_{PL} = 562 nm with slightly higher Φ_{PL} of 34% compared to its monomeric emission in MeCN (λ_{PL} = 579 nm, Φ_{PL} = 28%). Copolymer **MS6** was used for bio-detection[128] and for electrogenerated chemiluminescence.[127]

Two examples of supramolecular polymers incorporating Ir(III) core structures $[Ir(C\hat{}N)_2$

(pic)][129] and [Ir(dFC^N)$_2$(pic)][130] (pic is a picolinate ligand, and C^N and dFC^N are 2-phenylpyridinato- and 2-(2,4-difluorophenyl)pyridinato- derived cyclometalating ligands) used in OLEDs were reported by Huang, Zhu and co-workers. These systems take advantage of the efficient assembly between both the bis(dibenzo-24-crown-8)-functionalized Ir(III) complexes-based monomers with the bis(dibenzylammonium)-tethered co-monomer. The formation of the polymeric assemblies was evidenced by ^{1}H NMR spectroscopy and viscosity measurements. Atomic Force Microscopy (AFM) measurements revealed that the assemblies exhibited a high tendency to form homogeneous film morphologies. The supramolecular polymer incorporating the complex [Ir(C^N)$_2$(pic)] exhibited in neat film a structured emission at λ_{PL} = 416, 562, 604 nm with a Φ_{PL} of 17%. OLEDs fabricated with this polymer showed a turn-on voltage of 6.6 V, a luminous efficiency of 14.6 cd·A^{-1} at a luminance of 450 cd·m^{-2} and an EQE$_{max}$ of 6.9%. The polymer incorporating the complex [Ir(dFC^N)$_2$(pic)] exhibited in neat film sky-blue structured phosphorescence with λ_{PL} = 476, 497 nm and a high Φ_{PL} of 78%. OLEDs fabricated with this polymer showed a turn-on voltage of 5.6 V, luminous efficiency of 6.89 cd·A^{-1} at a current density of 2.1 mA·cm^{-1} and an EQE$_{max}$ of 3.96%.

1.3.1.5 Hydrogen bonding- and π-π-directing supramolecular networks

Hydrogen bonding and aromatic π-π-stacking interactions are particularly powerful building motifs employed in crystal engineering. Relevant examples of hydrogen bonding-directing supramolecular assembly of iridium(III) chromophore were reported by Talarico, Ghedini and co-workers[131] (**Figure 21**). The Ir(III) complexes [Ir(ppy)$_2$(en)]X (en = ethylenediamine), with X$^-$: ClO4$^-$ (**H1**), PF_6^- (**H2**), Cl$^-$ (**H3**) and BH_4^- (**H4**), assembled into different supramolecular networks depending on the nature of the counterions and the crystallisation conditions. Two different types of crystalline materials classified as "non-channelled" and "channelled" were obtained. Non-channelled structures primarily involved intermolecular interactions between the NH_2 functionalities of the en ligand and the counterions (**Figure 21a**). These types of frameworks were obtained from complexes **H1** and **H2** when crystallised through diffusion of Et_2O into methanol solutions, and from **H4** when crystallised through diffusion of water into an acetone solution. More interesting from a supramolecular point of view are the 3D-channelled networks exhibited by **H2** and **H3** when both crystallised through vapour diffusion of water into their methanol or acetone solutions, respectively. These 3D-networks assembled by multiple N-H···F intermolecular interactions, that formed two types of hexagonal channels along the crystallographic *c* axis (**Figure 21b**): (i) empty hydrophilic channels where PF_6^- or Cl$^-$ ions and en ligands were projected inwards and (ii) hydrophobic channels, defined by the ppy ligand, accommodating templating solvent molecules. The complexes **H1**-**H4** exhibited identical photophysical properties in deoxygenated acetone solution (λ_{PL} = 502 nm, Φ_{PL} = 68%, τ_{PL} = 1.6 µs). In the crystalline state, on the other hand, their photophysical properties strongly

depended upon their supramolecular organisations. Compared to the acetone emissions, non-channelled networks exhibited red-shifted emissions between 517 nm and 520 nm with lower Φ_{PL} of approximately 20%. Channelled networks also exhibited red-shifted emissions between 518 nm and 526 nm, but the emissions of these crystals were weak with Φ_{PL} ranging between 1 and 4%. The high degrees of inter-chromic interactions in the crystal networks accounted for the red-shifted emissions and the low Φ_{PL} observed for **H1**-**H4** in their crystalline states.

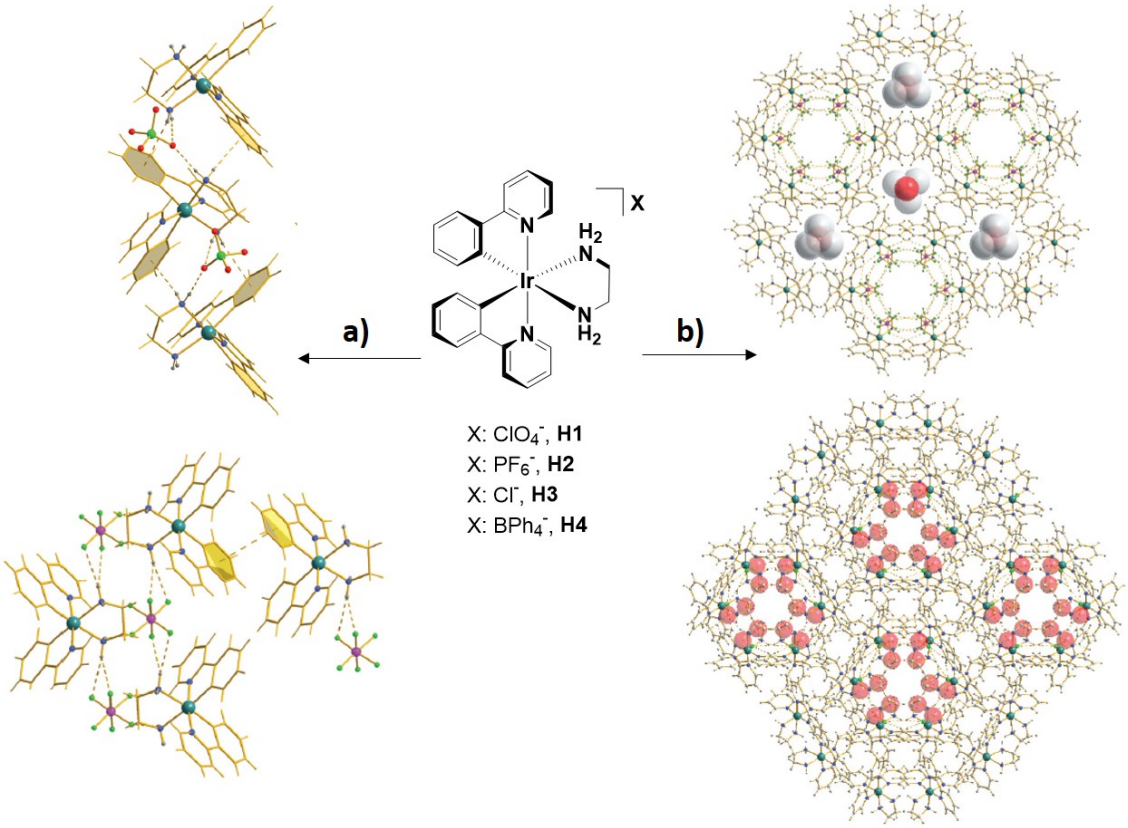

Figure 21. Chemical structure of the Iridium complexes **H1**-**H4**; **a)** illustration of the 1D motif in **H1** along the *c* crystallographic axis (top) and **H2** along the *a* crystallographic axis (bottom). **b)** illustration of the crystal packing of **H2** (top) and **H3** (bottom) showing the channeled networks along the *c* crystallographic axis. van der Walls radii (red and white balls) for the crystallisation solvent molecules are showed. Adapted from ref. [131] with permission from The Royal Society of Chemistry.

Donato, Zysman-Colman and co-workers reported two iridium complexes of the composition of $[Ir(dFphtl)_2(btl)]PF_6$ (**H5**) and $[Ir(dFphtl)_2(btl)]Cl$ (**H6**) (dFphtl is 1-benzyl-4-(2,4-difluorophenylato)-1H-1,2,3-triazole and btl is 1,1′-dibenzyl-4,4′-bis-1H-1,2,3-triazolyl) that exhibit the formation of 1D-networks dictated by the hydrogen bonding motifs involving the triazole units (**Figure 22**).[132, 133] Both **H5** and **H6** crystallised in the triclinic

space group $P\bar{1}$ and exhibited similar H-bonding motifs. The btl ligands formed C-H hydrogen bonds to the anions PF_6^- in **H5** and Cl^- in **H6** and a molecule of water, while the dFphtl triazole C-H groups acted as C-H hydrogen bond donors, forming C-N···N bonds to one of the nitrogen atom of the btl ligand (**Figure 22b**). Complexes **H5** and **H6** were not photostable at room temperature neither in solution nor in the solid state.[132, 134] However, at 77 K in 2-MeTHF glass state **H6** exhibited a weak emission at λ_{PL} = 393, 419 nm.

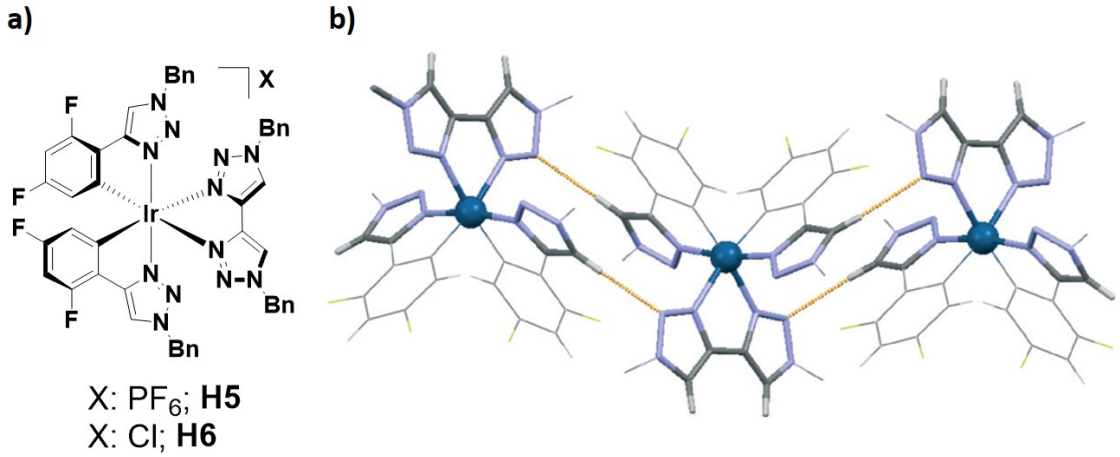

Figure 22. **a)** Chemical structures of complexes **H5** and **H6** and **b)** view of the X-ray structure of **H5** showing the C-N···N hydrogen bonds propagating parallel to the crystallographic *c*-axis. Image **b)** is adapted from ref. [133] with permission from The Royal Society of Chemistry.

Holdt and co-workers have shown that homoleptic octahedral Ni(II) and Fe(III) complexes bearing the 1,12-diazaperylene (dap) ligand and PF_6^- or BF_4^- as the counterion in $[M(dap)_3]^{2+}$ are able to form supramolecular assemblies in their crystalline state with honeycomb structures via π-π-stacking interaction.[135] Homoleptic tetrahedral Cu(I) complexes of 2,11-alkylated dap ligand are similarly able to form supramolecular columnar assemblies through π-π-interactions.[136] The work has been subsequently extended to investigate the self-assembly in the solid state of heteroleptic diazaperylene Ir(III) complexes $[Ir(C\hat{}N)_2(dap)]PF_6$ (where C^N are isophenylisoquinoline, benzoquinoline, 1-phenylpyrazole and 2-(thiophen-2-yl)-pyridine).[137] Among this family of complexes, $[Ir(piq)_2(dap)]PF_6$ (where piq is isophenylisoquinoline, **H7**) gave a three-dimensional assembly in the crystalline state (**Figure 23a**). Complex **H7** indeed exhibited π-π-stacking interactions involving both the dap and piq ligands, leading to the formation of rectangles consisting of four cationic complexes, assembled together through both π-π and CH-π interactions (**Figure 23b**). This particular crystal packing gave rise channels of 6.4 Å in height and 3.3 Å in width along the crystallographic *c*-axis (**Figure 23c**). Complex **H7** however was non emissive

both in solution and in the crystalline state.

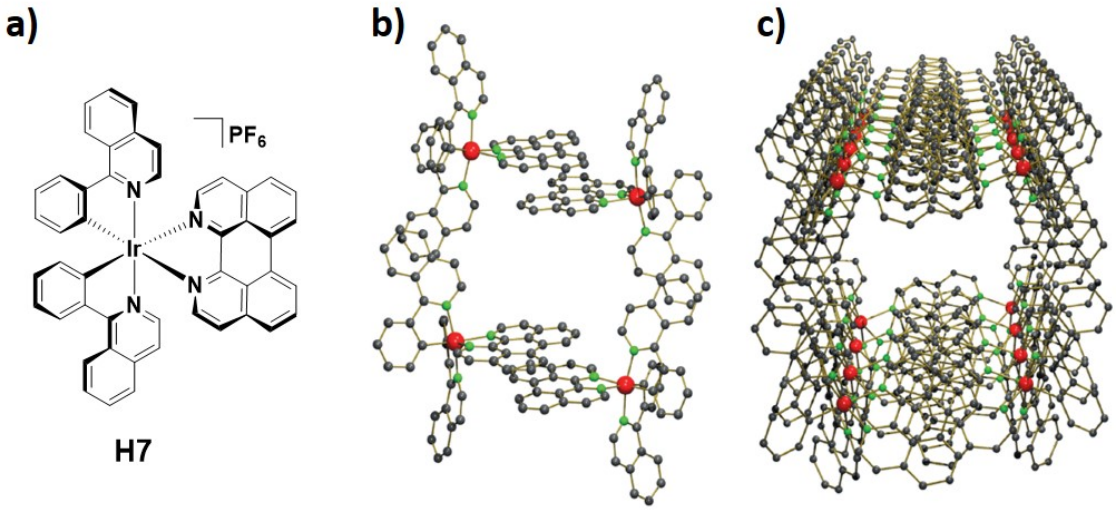

Figure 23. **a)** chemical structure of **H7**; **b)** illustration of the molecular rectangle exhibited by the x-ray structure of **H7** by π-π stacking aggregation; **c)** illustration of the channels exhibited by the x-ray structure of **H7**. Hydrogen and counterions are omitted for clarity. Images **b)** and **c)** are adapted from ref. [137] with permission from The Royal Society of Chemistry.

1.3.2 Coordination-driven self-assembly

Coordination-driven self-assembly, which is based on the formation of metal-ligand bonds, has proven to be a powerful method to prepare supramolecular well-defined nanostructures of varying shapes, sizes and functional properties, featuring considerable synthetic advantages such as facile and rapid construction of the final products and high yields.[138–140] In this section, the use of Ir(III) complexes as luminescent scaffolds in coordination-driven self-assembly are highlighted by describing the recent examples of luminescent coordination polymers, metal-organic frameworks (MOFs), discrete structures, capsules and cages.

1.3.2.1 Coordination polymers and metal-organic frameworks

Coordination polymers (CPs) and metal-organic frameworks (MOFs) are highly crystalline and porous materials constructed from metal ions or clusters usually bound to carboxylate or nitrogen capped organic linkers to form extended one-dimensional (1D), two-dimensional (2D) and three-dimensional (3D) networks.[141, 142] Because of the high surface area and

structural tunability, Ir(III)-based CPs and MOFs have been primarily used as functional materials for gas storage and purification, sensing and catalysis.

Lin and co-workers[143] reported the first examples of the incorporation of two Ir(III) complexes of the form of *fac*-[Ir(ppy-c)$_3$] (ppy-c is 3-(pyridin-2-yl)benzoic acid in **L1** and 4-(pyridin-2-yl)benzoic acid in **L2**, **Figure 24**), into Zn-based coordination polymers. Reaction of $Zn(NO_3)\cdot 6H_2O$ with **L1** and **L2** in DMF/H_2O at 90 °C for 24 h afforded, respectively, single crystals of $[Zn_4(\mu_4\text{-}O)(\mathbf{L1})_2]\cdot 6DMF\cdot H_2O$, **P1** (**Figure 24a**) and $[Zn_3(\mathbf{L2})_2(DMF)(H_2O)_3]\cdot 2DMF\cdot 3H_2O$, **P2** (**Figure 24b**).

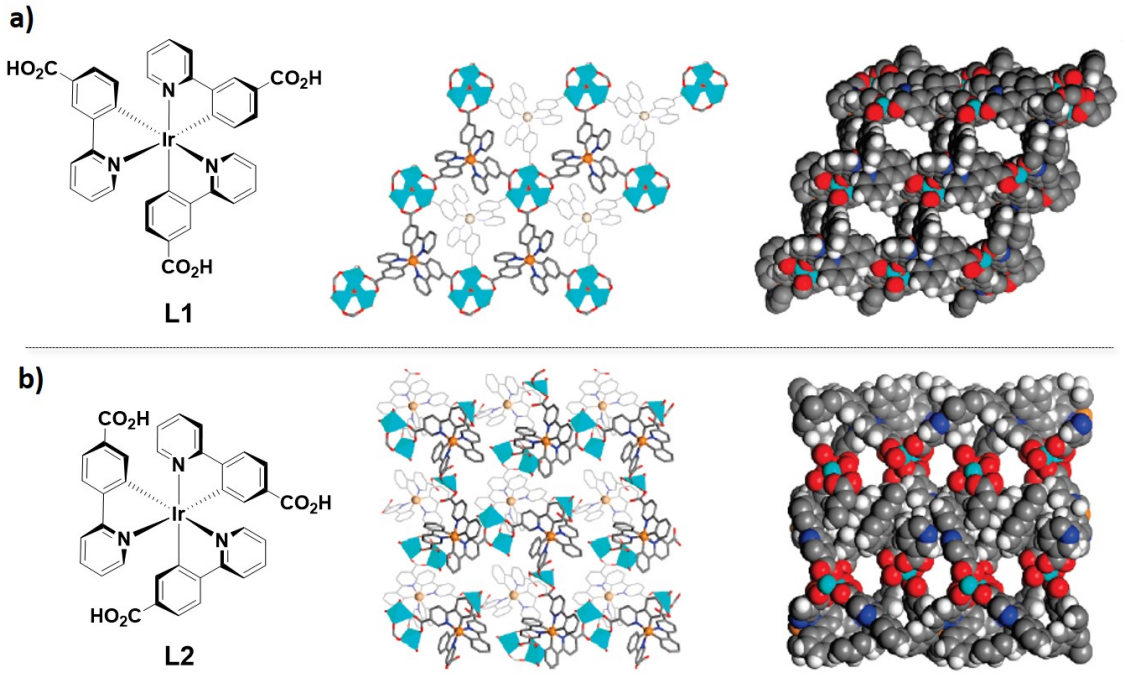

Figure 24. From left to right: **a)** chemical structure of metalloligand **L1**; a top view of the 2D bilayer of the x-ray structure of **P1** and space-filling model of the x-ray structure of **P1**. **b)** chemical structure of metalloligand **L2**; a top view of the 2D bilayer of the x-ray structure of **P2** and space-filling model of the x-ray structure of **P2**. Adapted with permission from ref. [143]. Copyright 2010, American Chemical Society.

P1 crystallised in a trigonal R$\overline{3}$ space group where the carboxylate groups from six adjacent **L1** ligands coordinate to four Zn centres to form 2D-bilayers $[Zn_4(\mu_4\text{-}O)(\mathbf{L1})_2]$. The crystal packing of the 2D layers along the crystallographic *c*-axis created open channels of dimensions of 7.9 Å x 4.3 Å (**Figure 24a**). By contrast, **P2** crystallised in the triclinic P$\overline{1}$ space group where both the carboxylate groups coordinate to the Zn to generate both mononuclear and dinuclear complexes where in the latter case three carboxylate groups bridge the two Zn centres, forming 2D-bilayers that packed along the *a*-axis. The largest

channels of **P2** were of 4 Å x 3 Å run along the *b*-axis (**Figure 24b**). **P1** exhibited high N_2 uptake at 77 K and CO_2 uptake at 273 K. However, due to its smaller porosity no N_2 or CO_2 uptake was observed for **P2**. The solid-state emission of **P1** was red-shifted at λ_{PL} = 540 nm compared to that of **L1** (λ_{PL} = 520 nm), while the emission of **P2** was blue-shifted at λ_{PL} = 550 nm compared to that of **L2** (λ_{PL} = 575 nm). Both **P1** and **P2** were sensitive to O_2 via the expected efficient and reversible luminescence quenching of the Ir(III) phosphors. When polymers **P1** and **P2** and metalloligands **L1** and **L2** were subjected to a gradual increase in O_2 partial pressure (from 0.05 to 1.0 atm), their luminescence intensity gradually decreased and, after addition of 1.0 atm of O_2, the quenching efficiencies of **P1**, **P2**, **L1** and **L2** were, respectively, 59% and 41%, 16% and 8%. As oxygen can be trapped within the pores of **P1** and **P2** and thus in persistent close contact with the Ir(III) luminophores, the emission quenching efficiencies of **P1** and **P2** were correspondingly higher than those of **L1** and **L2**.

Four Ir(III) coordination polymers $[Zn(\mathbf{L3})_2]\cdot 3DMF\cdot 5H_2O$ (**P3a**), $[Cd(\mathbf{L3})_2(H_2O)_2]\cdot 3DMF\cdot 6H_2O$ (**P3b**), $[Co(\mathbf{L3})_2(H_2O)_2]\cdot 2DMF\cdot 8H_2O$ (**P3c**) and $[Ni(\mathbf{L3})_2(H_2O)_2]\cdot 3DMF\cdot 6H_2O$ (**P3d**) were formed by using $[Ir(ppy)_2(H_2dcbpy)]PF_6$ (H_2dcbpy is 4,4′-dicarboxy-2,2′-bipyridine) as the bridging metalloligand (**L3**, **Figure 25a**) and Zn^{2+}, Cd^{2+}, Co^{2+} and Ni^{2+} as metal ions.[144] **P3a** exhibited an orthorhombic geometry ($Pna2_1$ space group) that consisted of **L3** ligand coordinated to the Zn centre through the carboxylate groups in a 1:2 ratio, with DMF and water molecules trapped in the cavities of the extended structure in the solid state. This particular packing generated channels of rectangular shape (**Figure 25b**).

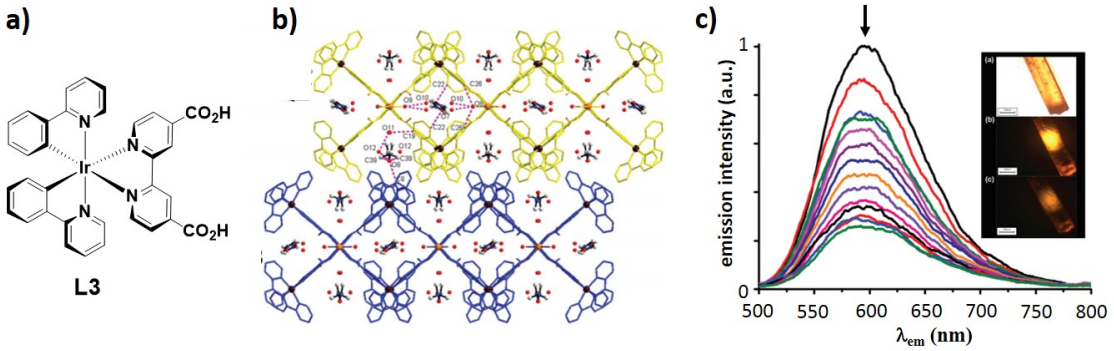

Figure 25. **a)** Chemical structure of **L3**; **b)** illustration of two layers (in yellow and blue) of the 3D cadmium-bridged structure of **P3b** with open channels. **c)** Emission quenching of **P3b** upon addition of an increased amount of O_2. Insets are images of the emissions from the crystal **P3b**, with 100% N_2, and with 100% O_2. Images **b)** and **c)** are adapted from ref. [144] with permission from The Royal Society of Chemistry.

Similarly, polymers **P3b**, **P3c**, **P3d** gave rise to 1D-chains with metal(II) ions in distorted orthorhombic geometries (Pnma space group) where Cd(II), Co(II) and Ni(II)

were each, respectively, bound to six oxygen atoms, four of which were from four carboxylate groups of **L3** and two of which were from water molecules (**Figure 25b**). **P3a**, **P3b**, **P3c**, **P3d** each exhibited CT emission from single crystals at λ_{PL} = 613 nm, λ_{PL} = 595 nm, λ_{PL} = 587 nm and λ_{PL} = 600 nm, respectively with Φ_{PL} values of 27.4%, 19.3%, 0.1% and 0.2%, respectively (λ_{PL} = 613 nm and Φ_{PL} of 17.8% for **L3** in the solid state). As reported for **P1** and **P2**, polymers **P3a**, **P3b**, **P3c** and **P3d** also exhibited reversible oxygen-sensing properties. Indeed, at 1 atm of O_2 the emission quenching efficiencies from their single crystals were, respectively, 46%, 74%, 57% and 52%. The emission spectra and photos in **Figure 25c** show the emission quenching of **P3b** upon gradual addition of oxygen.

In a subsequent report, the same group developed an electrochemical method to produce the Ir(III)-Zn(II) coordination polymer [Zn(**L3**)$_2$]·3DMF·5H_2O (**P3a**) with greater control over the crystal growing process. With this improved synthetic method, polymer **P3a** exhibited higher crystal stability and enhanced oxygen sensing performance.[145] Indeed, when electrochemically produced, **P3a** exhibited a high selectivity towards the absorption of O_2 with an emission quenching efficiency as high as 95%. Once oxygen was trapped within the pores of **P3a**, the gradual addition of glucose to the crystals of **P3a** restored its emission at λ_{PL} = 596 nm upon excitation at 405 nm. As the consumption of oxygen due to the combustion reaction between glucose and O_2 was linearly correlated to the reduction of the emission quenching of **P3a**, quantitative detection of glucose within the concentration range of 0.05 – 6.0 mM was also possible.

Three luminescent coordination polymers were synthesised by assembling metalloligand **L3** with Mg(II) ions, respectively, in H_2O, DMF and DEF (DEF is N,N-diethylformamide) to form [Mg(**L3**)$_2$]·3.5H_2O (**P3e**), [Mg(**L3**)$_2$(DMF)$_2$]·3.5H_2O (**P3f**) and [Mg(**L3**)$_2$(DEF)(H_2O)] ·3H_2O (**P3g**).[146] Single crystal x-ray diffraction analyses revealed that the three coordination polymers were allomeric and formed similar 1D chain structures in which the Mg atoms coordinated in an octahedral geometry to four carboxylate oxygen atoms from four **L3** ligands and two oxygen atoms from solvent molecules (**Figure 26**). Polymers **P3e**, **P3f** and **P3g** all exhibited in the solid state broad emission centered at λ_{PL} = 544 nm, λ_{PL} = 554 nm and λ_{PL} = 570 nm, respectively, with Φ_{PL} of 14.6%, 18.1% and 2.4% and τ_{PL} of 7.7 µs, 13.3 µs and 7.7 µs, respectively. Therefore, the different electron-donating abilities of the solvents, which increases in the order H_2O < DMF < DEF, exerted a strong influence on the emission energies of the polymers.

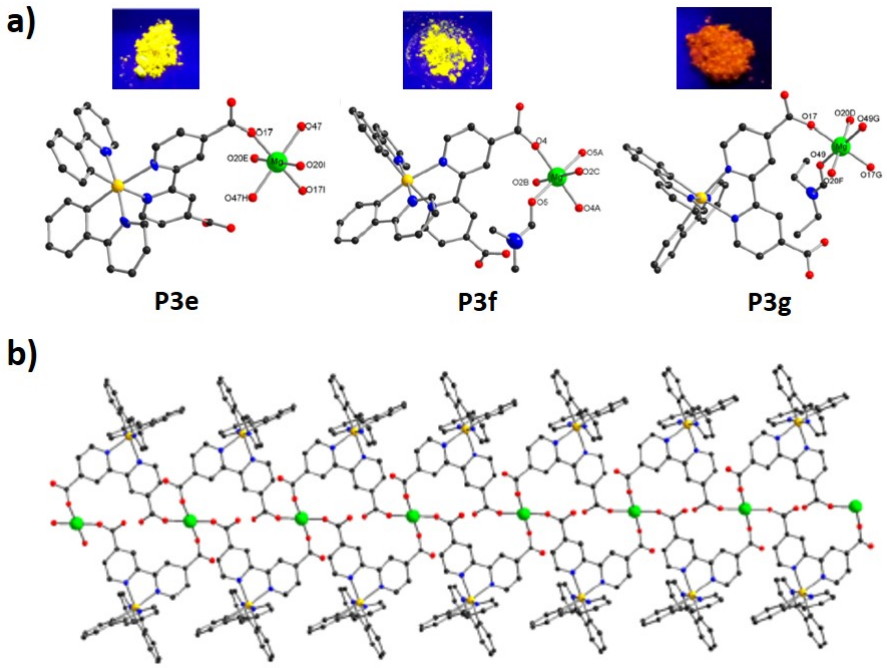

Figure 26. **a)** view of the coordination environments of the Mg(II) ions in **P3e**, **P3f** and **P3g**. Insets are images of the powder emissions upon UV irradiation. **b)** View of the 1D chains exhibited by the coordination polymers. Adapted with permission from ref. [146]. Copyright 2016, American Chemical Society.

Metalloligand **L3** was also used in heteronuclear Ir(III)-Ln(III) coordination polymers as a light-harvesting antenna to sensitise Ln(III)-based near-infrared (NIR) luminescence from Gd^{3+}, Yb^{3+}, Er^{3+} and Nd^{3+} ions.[147] The polymers Ir-Gd, Ir-Yb, Ir-Er and Ir-Nd are all isostructural and each crystallised in a triclinic $P\bar{1}$ space group where one Ln(III) center is seven-coordinate by five carboxylate oxygen atoms from five **L3** ligands and two hydroxylic groups from NaOH added to prepare to polymers, generating a pentagonal bipyramid coordination geometry. In the reference Ir-Gd polymer, as the Gd^{3+} ions cannot accept energy from the Ir excited state because of the absence of energy levels below 3200 cm^{-1}, the solid-state emission of Ir-Gd showed the characteristic ^{3}MLCT/^{3}LLCT emission of the Ir(III) luminophore at λ_{PL} = 610 nm with a τ_{PL} of 8.1 µs (**L3** emits in the solid state at λ_{PL} = 592 nm with a τ_{PL} of 7.8 µs). For the other three luminescent polymers Ir-Ln (Ln: Yb, Er, Nb), the Ir-based emission centred at 610 nm was largely quenched, indicating that Dexter d → f energy transfer from the Ir(III) units to the Ln^{3+} ions was efficiently promoted. The fastest energy transfer rate was observed for the Ir-Nd polymer, with a calculated quenching rate constant (k_q) of 6.8 x 10^6 s^{-1}, while for Ir-Yb and Ir-Er, k_q of 5.0 x 10^5 s^{-1} and 6.0 x 10^6 s^{-1} were, respectively, obtained.

A related example of a Ir(III)-Ln(III) discrete structure was reported by Zheng and co-workers[148] by microwave reaction between the iridium complex [Ir(ppy)$_2$(dppH)], **L4**

(dppH is 2-pyridyl phosphonic acid) and $Dy(CF_3SO_3)_3$ in MeOH at 100 °C. The composition of the resultant structure, **P4**, was identified to be $[Dy(\mathbf{L4})_6](CF_3SO_3)]\cdot 8H_2O$ by x-ray diffraction (**Figure 27**). The assembly **P4** exhibited a broad emission in the solid state centred at λ_{PL} = 531 nm, which is slightly blue-shifted compared to the emission in the solid-state of the iridium complex **L4** (λ_{PL} = 538 nm). Given that the emission of the Ir(III) complex was not quenched, energy transfer from Ir(III) to Dy(III) did not take place. **P4** exhibited field-induced slow magnetisation relaxation originating from both the Ir(III) and Dy(III) components.

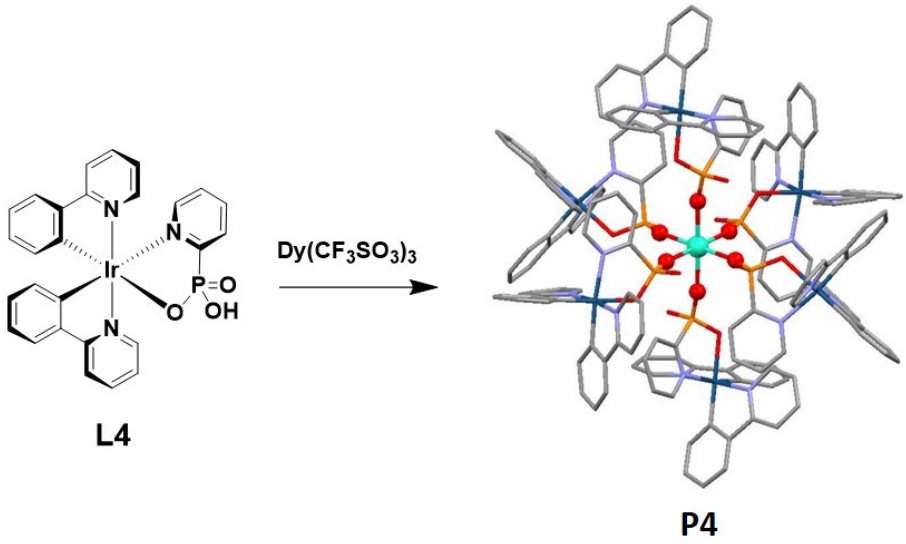

Figure 27. Chemical structure of complex **L4** and X-ray structure of the Ir(III)-Dy(III) assembly **P4**. The red balls illustrate the octahedral coordination around the Dy ion (in light-blue).[148]

Crystallisation of PPN**3a** (**Figure 5a**, PPN is bis(triphenylphosphine) iminium cation) in the presence of excess of the Ln ions Gd, Nd, Eu led to the formation of assemblies based on Ir-CN-Ln bonding, which generated in the solid state either $Ir_2Ln_2(\mu\text{-CN})_4$ square assemblies or linear trinuclear species with Ir-CN-Ln-NC-Ir cores.[149] In the Ir-Eu and Ir-Nd assemblies the vibronic emission of PPN**3a** in the solid state at λ_{PL} = 484, 507 nm was substantially quenched due to energy transfer to the lower-lying f-f states on these Ln ions. By contrast, similar to that observed for the Ir-Gd polymer previously described,[146] in the $Ir_2Gd_2(\mu\text{-CN})_4$ complex the Gd cannot accept the energy from the Ir chromophore and therefore no energy transfer was promoted.

A heterogeneous coordination polymer, **P3h**, based on the assembly between metalloligand **L3** and Y^{3+} ions (**Figure 28**) was used as a catalyst for the photochemical reduction of CO_2.[146] Similar to the Ir(III)-Ln(III) polymers previously described, **P3h** crystallises in a triclinic $P\bar{1}$ space group where the Y atom is seven-coordinate with a coordination

sphere consisting of five carboxylate oxygen atoms from five **L3** ligands and two hydroxyl groups from NaOH added to prepare the polymers, generating a pentagonal bipyramid coordination geometry (**Figure 28a**). The neighboring Y centres are alternatively linked via two hydroxide ions from NaOH and two carboxylate groups from two **L3** ligands, giving rise to a 1D-$[Y(OH)_2(CO_2)_2]\infty$ chain structure (**Figure 28b**). Neighboring chain structures pack together through non-bonding Ir···Y interactions, forming the 3D supramolecular frameworks illustrated in **Figure 28c**. Energy transfer from the Ir to Y centres was not possible due to the mismatching of their respective energy levels. Indeed, **P3h** displayed in the crystal state a strong Ir-based emission centred at λ_{PL} = 592 nm, with a bi-exponential emission decay with the longest component of τ_{PL} = 29.0 µs. The emission decay of **P3h** was found to be almost four times longer than that exhibited by **L3** (τ_{PL} = 7.8 µs). **P3h** exhibited remarkable photocatalytic activity for CO_2 reduction under visible-light irradiation (λ_{ex} = 475 nm). The quantum yield of $HCOO^-$ production was 1.2% with a high turnover frequency (TF) of 118.8 µmol (g of cat.)$^{-1}$ h^{-1}.

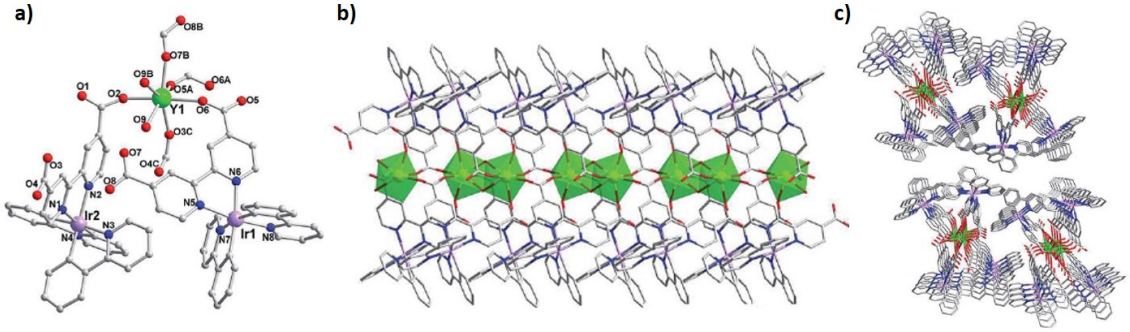

Figure 28. x-ray structure of **P3h** illustrating: **a)** pentagonal bipyramid coordination geometry of the Y(III) ions; **b)** view of 1D-chain structures and **c)** view of 3D networks. Adapted from ref. [146] with permission from The Royal Society of Chemistry.

The detection of nitroaromatic explosives on ppm scale is evidently of great importance for national security and defence. Luo and co-workers reported a highly luminescent heteronuclear MOF of composition $[Zn(\mathbf{L3})_2]\cdot 3DMF\cdot 5H_2O$ (**MOF1**).[150] **MOF1** crystallised in the non-centrosymmetric space group $Pna2_1$ where the Zn centre adopts a tetrahedral geometry coordinated to four carboxylate O atoms from four **L3** ligands thereby forming a 3D porous network. **MOF1** exhibited an Ir-based emission that was red-shifted at λ_{PL} = 602 nm with an enhanced Φ_{PL} of 23.6% and a longer τ_{PL} of 14.3 µs compared to that observed for **L3**. Similar to the behavior of polymers **P3a**, **P3b**, **P3c** and **P3e**, **P3f** and **P3g**, the enhanced emission of **MOF1** compared to **L3** is attribute to the enhanced rigidity and symmetry experienced by the Ir(III) luminophores in the coordination frameworks, which reduces non-radiative decay modes. **MOF1** exhibited good sensing abilities towards nitroaromatic compounds. Remarkably, when aromatic compounds with high nitro content

such as TNT (trinitrotoluene) were diffused into the crystal at a concentration of 625 ppm, the emission of **MOF1** was quenched by 60%-70% via electron transfer from the Ir(III) luminophores to the nitroaromatic acceptors.

Lin and co-workers[151] successfully incorporated three iridium-based water-oxidation catalysts, [Ir(Cp*)(dcppy)Cl] (**L5**), [Ir(Cp*)(dcbpy)Cl]Cl (**L6**) and [Ir(dcbpy)$_2$(OH$_2$)$_2$]OTf (**L7**) (**Figure 29a**) (where Cp* is pentamethylcyclopentadienyl, dcppy is 2-phenylpyridine-5,4′-dicarboxylic acid, dcbpy is 2,2′-bipyridine-5,5′-dicarboxylic acid and OTf is trifluoromethyl sulfonate) into the octahedral $Zr_6O_4(OH)_4(bpdc)_6$ framework UiO-67 (bpdc is para-biphenyldicarboxylate), forming, respectively, **MOF2**, **MOF3** and **MOF4** (**Figure 29a**).

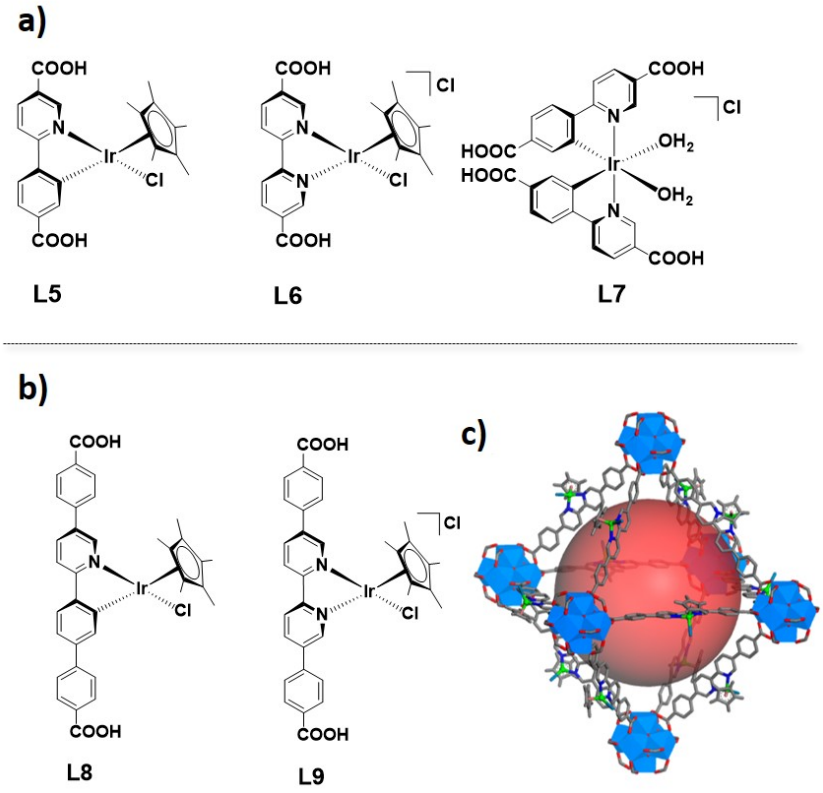

Figure 29. **a)** Chemical structures of the Ir(III) metalloligands **L5**, **L6** and **L7**. **b)** Chemical structures of the extended Ir(III) metalloligands **L8** and **L9**. **c)** Structure model for **MOF6** showing the octahedral cage of 1 nm in diameter. Zr, blue polyhedron; Ir, green balls; Cl, dark green, C, grey; N, blue. The red ball in the middle represents the cage cavity. Image **c)** is adapted with permission from ref. [152]. Copyright 2012, American Chemical Society.

When these materials were tested as photocatalysts for water oxidation by using cerium ammonium nitrate (CAN) as the oxidant, turnover frequencies (TOFs) of 4.8, 1.9 and 0.4 h^{-1} for **MOF2**, **MOF3** and **MOF4** were, respectively, reported. Higher TOFs of

7.5 and 94.5 h^{-1} were, however, observed when the Ir(III) complexes bearing elongated linear bridging ligands **L8** and **L9** (**Figure 29b**) were, respectively, incorporated into the octahedral zirconium frameworks (**MOF5** and **MOF6**).[152] The higher TOFs of **MOF5** and **MOF6** compared to **MOF2-MOF4** were attributed to the extended networks generated with wider channel sizes where the hydrated Ce^{4+} ions can freely diffuse without steric hindrance, thus promoting overall higher catalytic efficiency.

In a subsequent work, Pt nanoparticles of 2-3 nm and 5-6 nm in diameter were loaded into MOFs constructed with the metalloligands **L10** and **L11** (respectively in **Figure 30a** and **30b**) and the $Zr_6(\mu_3O)_4(\mu_3OH)_4(carboxylate)_12$ secondary units (**Pt-MOF7** and **Pt-MOF8**, respectively).[153]

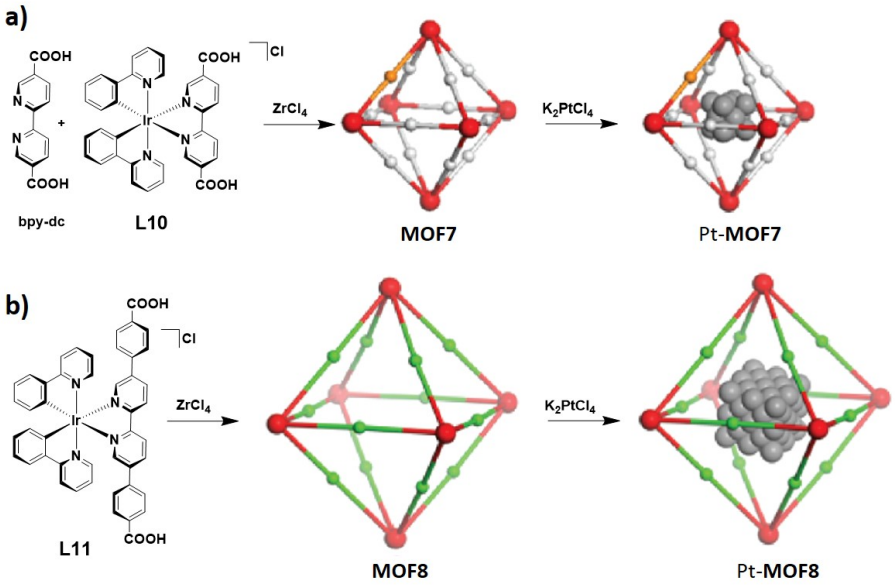

Figure 30. Schematic representation of the formation of: **a) Pt-MOF7** and **b) Pt-MOF8**. Red balls are Zr atoms, white linkers are bpy-dc, yellow linkers are **L10**, green linkers are **L11** and in grey are Pt nanoparticles. Adapted with permission from ref. [153]. Copyright 2012, American Chemical Society.

The resulting **Pt-MOF7** and **Pt-MOF8** MOFs were used as efficient photocatalysts for hydrogen evolution from water by synergistic photoexcitation of the MOF frameworks and electron-injection into the Pt-nanoparticles. The larger channels of **Pt-MOF8**, resulting from the use of the elongated ancillary ligand on **L11**, promoted enhanced catalytic efficiency of **Pt-MOF8** compared to **Pt-MOF7** under visible light irradiation, with triethylamine (TEA) serving as a sacrificial reducing agent. Over 48h, **Pt-MOF8** and **Pt-MOF7** exhibited, respectively, TONs of 2400 and 7000 h^{-1}. The MOF materials proved to be very stable and could be collected back after catalytic experiments and recycled for use at least three further times without loss of activity.

A supramolecular system composed of the iridium complex [Ir(ppy)$_2$(pytl-βCD)]Cl (pytl-βCD is 1-substituted-1H-1,2,3-triazol-4-yl)pyridine functionalised with a β-cyclodextrin unit) as the photosensitiser, viologen functionalised with two adamantyl moieties as the electron-relay and cyclodextrin coated platinum nanoparticles as the catalyst, was also tested for photoinduced hydrogen evolution from water.[154] The system was designed to assemble through adamantane – cyclodextrin non-covalent interactions and therefore to give rise to photoinduced electron transfer from the iridium chromophore to the Pt nanoparticle via the viologen bridge (**Figure 31**). Interestingly, with ethylendiaminetetra-acetic acid (EDTA) serving as a sacrificial donor, this supramolecular system could produce almost 32 µmoles (approximately 0.75 ml) of H_2 per hour from 10 ml of H_2O, which was a higher yield than the analogous supramolecular system involving a ruthenium chromophore in Ru-bpy/viologen/Pt.[155]

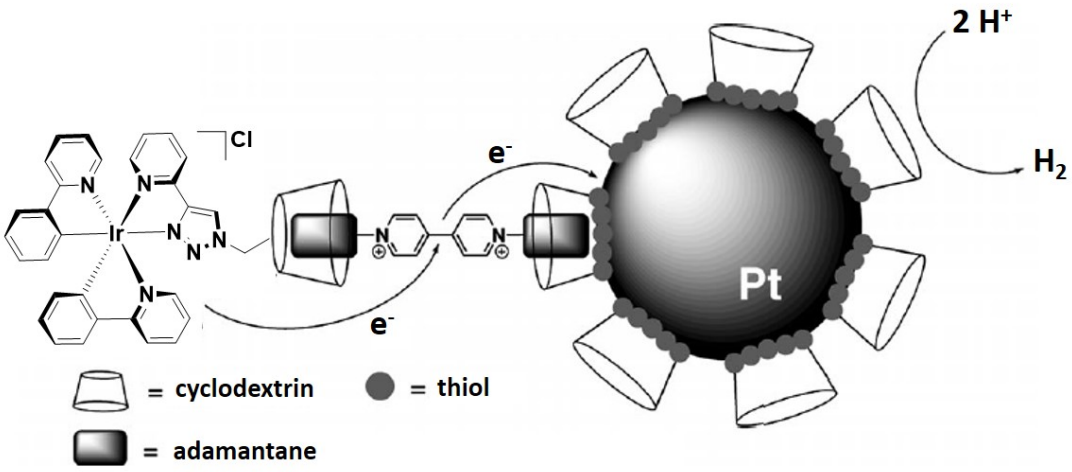

Figure 31. Illustration of the supramolecular assembly Ir/viologen/Pt used for photoproduction of H_2. Adapted with permission. Copyright 2012, Wiley-VCH.[154]

Two Ir(III) metalloligands containing six carboxylic acid groups appended at the 4,4′-positions of both the ppy and bpy ligands in the homoleptic complex *fac*-[Ir(dc-ppy)$_3$] (**L12**) (dc-ppy is 2-(3-carboxyphenyl)isonicotinic acid) and the heteroleptic complex [Ir(dc-ppy)$_2$(dc-bpyH)] (**L13**, **Figure 32a,b**), have been recently assembled with [Ni(cyclam)](ClO$_4$)$_2$ (cyclam is 1,4,8,11-tetraazacyclotetradecane), forming two networks of cubic topologies (**MOF9** and **MOF10**).[156] **MOF9** and **MOF10** both crystallised in trigonal space groups (R-3 and R-3c, respectively) where the Ni(II) cations are in octahedral coordination environments bound to four nitrogen atoms of the cyclam ligand and to two carboxylate groups from two **L12** and **L13** metalloligands, respectively, along the z-axis. As illustrated in **Figure 32c**, the crystal packing of **MOF9** and **MOF10** gave rise to two sets of interlocked primitive cubic networks. The materials exhibited small pore sizes and therefore poor ability to absorb CO_2 and N_2. For example, at 298 K and 1 atm, the sorption

capacity of **MOF9** for CO_2 was 13.2 $cm^3 \cdot g^{-1}$, while that of **MOF10** was 29.6 $cm^3 \cdot g^{-1}$. The luminescence properties of **MOF9** and **MOF10** were not investigated.

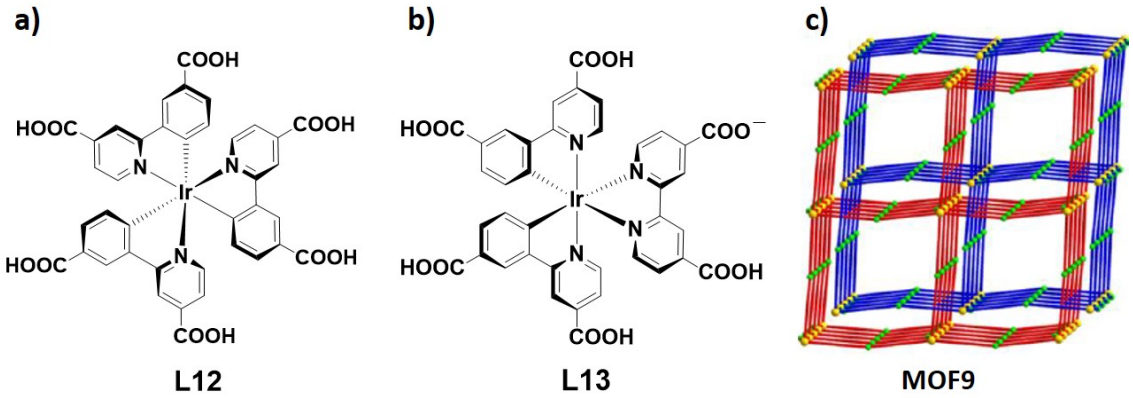

Figure 32. **a)** Chemical structure of **L12**; **b)** chemical structure of **L13** and **c)** illustration of the interlocked cubic topology exhibited by the crystal structures of **MOF9** and **MOF10**. Image **c)** is adapted with permission. Copyright 2017, Wiley-VCH.[156]

An example of a heterometallic paddlewheel structure (**P5**) was reported by Hosseini and co-workers[157] by assembling an Ir(III) dipyrrin derivative bearing an appended carboxylic acid (**L14**) with Cu(II) ions (**Figure 33**).

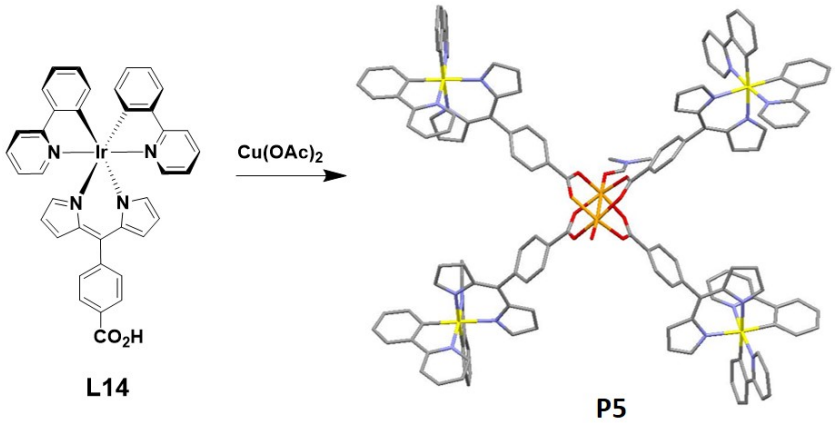

Figure 33. Formation of the paddlewheel structure **P5** by reacting the iridium complex **L14** with Cu(II) ions. The x-ray structure of **P5** is shown (carbon, oxygen, copper and iridium atoms are shown respectively in grey, red, orange and yellow).

Single crystals of **P5** suitable for x-ray diffraction were obtained by slow diffusion of a MeOH solution of $Cu(OAc)_2$ into a DMF solution of **L14**, leading to the formation after two weeks of dark red crystals of composition of $[(\mathbf{L14})_4Cu_2(DMF)(H_2O)]$. **P5** crystallised

in a in a triclinic $P\bar{1}$ space group where two Cu(II) cations form the paddlewheel motif bridged by the carboxylate groups of four **L14** molecules, and one DMF molecule and one water molecule occupy the remaining two axial positions (**Figure 33**). Complex **L14** exhibited a weak emission at λ_{PL} = 710 nm in degassed CH_2Cl_2. However, complex **P5** was rather insoluble or unstable in common organic solvents and therefore, its emission properties could not be investigated.

More recently the same group reported two homochiral heterometallic coordination networks involving cyclometalated Ir(III) chiral metallotectons.[158, 159] Enantiopure Δ- and racemic *rac*-Ir(III) complexes, Δ-, *rac*-**L15** and Δ-, *rac*-**L16**, of composition of Δ-, rac-$[Ir(C\hat{}N)_2$(py-alk-bpy)$]PF_6$ (where C^N is ppy in **L15** and dFppy in **L16** and py-alk-bpy is 5,5′-bis(pyridine-4-ylethynyl)-2,2′-bipyridine) were assembled, respectively, with Cu(I)[158] and Cd(II)[159] ions (**Figure 34a** and **34b**, respectively). When an EtOH solution of $[Cu(NCMe)_4]BF_4$ was left to slowly diffuse into an MeCN solution of *rac*-**L15**, single crystals suitable for x-ray diffraction were obtained. The structural investigation of these crystals revealed the formation of a grid-type network (**Figure 34a**), where Cu(II) ions, formed during the crystallisation process from oxidation of Cu(I) under ambient conditions, adopted a slightly distorted octahedral geometry, with four pyridyl units of four **L15** molecules occupying the square base of the octahedron and two BF_4^- ions occupying the axial positions. Interestingly, each grid was intrinsically chiral as only one enantiomer of **L15** was present. However, consecutive homochiral sheets were packed with alternation of Δ-**L15** and Λ-**L15** leading thus to achiral crystal. No single crystals were obtained when the enantiopure Δ-**L15** was used in the assembly. Metalloligand *rac*-**L15** exhibited a mixed ^{3}MLCT/^{3}LLCT emission in the solid state at λ_{PL} = 677 nm with a Φ_{PL} of 3%, while no emission could be detected from the grid-type network.

Diffusion of an EtOH solution of CdI_2 through an EtOH/$Cl_2CHCHCl_2$ buffer layer containing two drops of trifluoroethanol and 4,4,4-trifluorobutanol into a solution of either Δ- and *rac*-**L16** in 1,1,2,2-tetrachloroethane led to the slow formation of orange single crystals. X-ray analyses of the crystals obtained by the assembly of both complexes Δ-**L16** and *rac*-**L16** and CdI_2 demonstrated the formation identical structures. These resembled infinite 1D networks where the Cd centers adopted a trigonal bipyramidal coordination geometry with the two terminal pyridine moieties of Δ-**L16** and *rac*-**L16** occupying the apical positions, and three iodine atoms located at the trigonal base (**Figure 34b**). In the case of the network involving *rac*-**L16**, consecutive homochiral planes of opposite chirality were packed in a parallel fashion, resulting in the formation of non-chiral crystals. By contrast, the assembly of enantiopure Δ-**L16** with CdI_2 resulted in the formation of a chiral 1D network. Metalloligand *rac*-**L16** exhibited structured emission in both degassed THF and in the solid state with two maxima at λ_{PL} = 570, 605 nm, but with divergent Φ_{PL} of 19% (τ_{PL} of 1.47 μs) and 2%, respectively; no lifetime data were reported in the solid state. The racemic and enantiopure Ir(III)-Cd(II) coordination networks exhibited

structured emission in the solid state with two emission maxima red-shifted at $\lambda_{PL} = 575$, 620 nm and with lower $\Phi_{PL} < 1\%$ compared to *rac*-**L16**. The red-shifted emissions of the Ir-Cd networks are attributed to the lowering of their LUMO energy levels as a result of the binding of the Lewis-acidic Cd(II) ions to the pyridine moieties of **L16**.

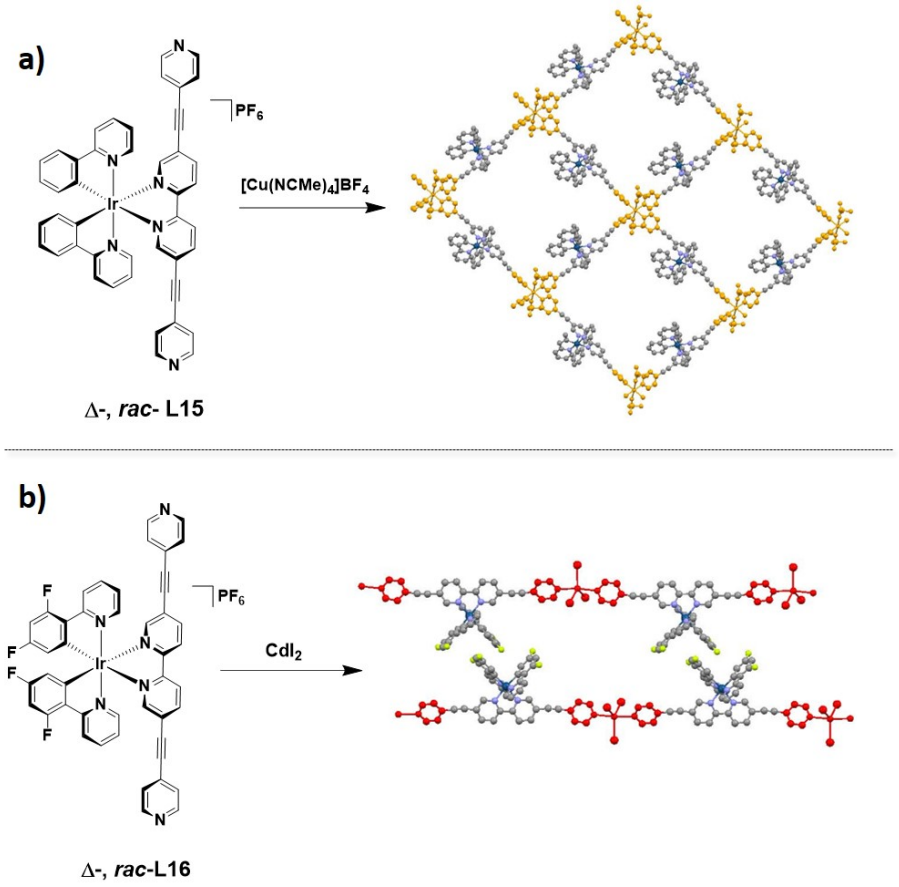

Figure 34. **a)** Self-assembly between metalloligands Δ-, *rac*-**L15** and Cu(I) ions yielding the Ir-Cu grid-type network. In orange is illustrated the coordination around the Cu(I) ions. **b)** Self-assembly between metalloligands Δ-, *rac*-**L16** and Cd(II) ions yielding the Ir-Cd linear network. In red is illustrated the coordination around the Cd(II) ions.

1.3.2.2 Macrocycles, capsules and cages

In the previous section, we documented extended structures incorporating iridium metalloligands. Here, we summarise discrete cage-like structure incorporating iridium.

A luminescent tetranuclear square-like macrocycle was reported by Baranoff and co-workers.[160] This macrocycle (**M1**, **Figure 35a**) was synthetised in one step by reacting the dimeric complex $[Ir(ppy)_2Cl]_2$ with two equivalents of tetrabutyl ammonium cyanide (TBACN) in the presence of a small excess of AgOTf in CH_2Cl_2. The geometry of **M1** was identified by x-ray diffraction (**Figure 35a**). **M1** could be defined as a cyclic tetramer where the four Ir(III) centres and the bridging ambidentate cyano ligands form a chiral structure. Interestingly, while each iridium unit could be either the Λ- or Δ-isomer, giving a total of nine possible optical isomers, only two isomers were observed in the crystal structure, namely the [-Δ-Λ-Δ-Λ] and the mirror image [-Λ-Δ-Λ-Δ]. **M1** exhibited a bright green structured luminescence with maxima at 496 nm and 521 nm in degassed MeCN, with a Φ_{PL} of 66% and a bi-exponential τ_{PL} of 40 ns, 2320 ns. The emission of **M1** was red-shifted and slightly quenched when compared to the reference $TBA[Ir(ppy)_2(CN)_2]$, which likewise showed structured emission in degassed MeCN at λ_{PL} = 470, 502 nm, with Φ_{PL} of 79%. Solution-processed OLEDs fabricated by using **M1** as the emitter achieving a maximum external quantum efficiency (EQE) of 10.2% (λ_{max} = 497 nm).

Shiu and co-workers[161] reported the self-assembly of the Ir(III) complex $[Ir(ppy)_2(4\text{-}pyCO_2H)_2]NO_3$ (4-$pyCO_2H$ is 4-pyridine carboxylic acid), **L17** with the Arrhenius base $Mg(OH)_2$ in the presence of KPF_6, yielding quantitatively the cage structure of composition $[(\mathbf{L17})_3(Mg(OH_2)_3)_2]K_2(PF_6)_3$, **C1** (**Figure 35b**). The x-ray crystal structure of **C1** comprised of a cationic coordination cage exhibiting a large trigonal bipyramidal geometry that encapsulated the quintuple ionic aggregate $K_2(PF_6)_3^-$ formed in solution from KPF_6 (**Figure 35b**). The neutralisation of **C1** with KOH and $Mg(OH)_2$ in MeOH or EtOH promoted the degradation of the coordination cage and the subsequent formation of a zig-zag coordination polymer of composition $[(\mathbf{L17})_4MgK_2]_n$, which was itself also characterised by x-ray diffraction. The emission properties of the coordination cage **C1** and the related coordination polymer were not investigated.

Lusby and co-workers[162] reported the first example of a 3D luminescent Ir(III) capsule of composition of $[(Ir(ppy)_2)_6(tcb)_4](OTf)_6$ (tbc is 1,3,5-tricyanobenzene) (**C2**, **Figure 35c**). To eliminate the problem of mixed stereoisomer formation during the self-assembly, the *rac*-$[Ir(ppy)_2Cl]_2$ dimer was firstly resolved into its enantiopure Λ,Λ- and Δ,Δ-stereoisomers through chromatographic resolution of serine-based complexes, the amino acid acting as a chiral ancillary ligand thereby forming a diastereomeric mixture of products. The synthetic protocol for preparing the enantiopure iridium dimer and complexes will be further discussed in the following chapter. Reaction of either Λ,Λ- and Δ,Δ-$[Ir(ppy)_2Cl]_2$ with tcb quantitatively yielded the enantiopure Λ_6- and Δ_6-**C2**. Vapor diffusion of benzene

into a saturated CH_2Cl_2 solution of Δ_6-**C2** afforded suitable crystals for x-ray diffraction. Within the crystal structure of Δ_6-**C2** a triflate anion is encapsulated within the octahedral cavity of **C2** (**Figure 35c**). Interestingly, despite the weak emission ($\Phi_{PL} < 1\%$) observed for the bis(benzonitrile) reference complex $[Ir(ppy)_2(NCPh)_2]OTf$ at $\lambda_{PL} = 525$ nm, a broad and red-shifted emission at 575 nm with an unusually enhanced Φ_{PL} of 4% was detected for **C2** in deareated tetrachloroethane. The capsule exhibited an affinity for the encapsulation of perfluorinated anions following the sequence: $PF_6^- > OTf^- \sim CF_3BF_3^- > BF_4^-$.

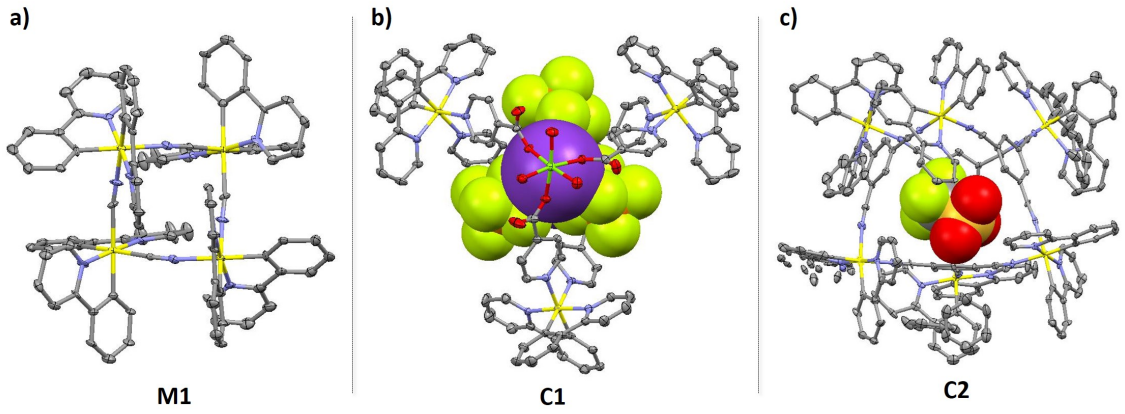

Figure 35. X-ray crystal structures of: **a) M1** and **b) C1** and **c) C2**. C, N and Ir atoms are respectively shown in grey, blue and yellow. The guests $K_2(PF_6)_3$ in **b)** and OTf molecule in **c)** are illustrated in space-fill mode.

Duan and co-workers recently reported the multicomponent self-assembly of two pentanuclears Ir(III)-Zn(II)[163] (**C3a**) and Ir(III)-Co(II)[164] (**C3b)** heterometal-organic polyhedrons. Polyhedron **C3a** was obtained by the reaction of *fac*-tris(4-(2-pyridinyl)phenylpyridinato)iridium (**L18**) and 2-formylpyridine, via a subcomponent self-assembly in the presence of $Zn(BF_4)_2{\cdot}6H_2O$ in acetonitrile under nitrogen (**Figure 36a**). Similarly, polyhedron **C3b** was formed by mixing **L18** with 2-formylpyridine in the presence of $Co(ClO_4){\cdot}6H_2O$ in a 2:6:3 ratio in acetonitrile (**Figure 37a**). Suitable single crystals for x-ray diffraction of both **C3a** and **C3b** were obtained through slow vapor diffusion of diethyl ether into MeCN solutions of the polyhedrons. X-ray crystallography analyses revealed the formation of discrete cages of composition of Ir_2M_3 (where M is Zn in **C3a** and Co in **C3b**) that exhibited a trigonal bipyramidal geometry. In both structures, the three M atoms form the equatorial plane and the two iridium atoms occupied the axial positions.

In Nature, carbon anhydrases (CAs) are common enzymes that contain active Zn^{2+} sites that are coordinated by three histidine residues and a water or hydroxide molecule and catalyse the reversible hydration of CO_2 to CO_3^{2-}.[165] Interestingly, **C3a** exhibits an adequate hydrophobic cavity and coordination geometry around the Zn atoms to mimic

the active site of natural CAs. Vapor diffusion of diethyl ether into a MeCN solution of **C3a** under a CO_2 atmosphere, yielded single crystals suitable for x-ray diffraction. The crystallographic analyses revealed that CO_2 was converted into CO_3^{2-} and encapsulated into the cavity of **C3a** (**C3a**$\supset CO_3^{2-}$, **Figure 36b**). **C3a**$\supset CO_3^{2-}$ exhibited the same polyhedral structure as **C3a** with each of the three Zn atoms coordinating to one mono-dentate oxygen atom from CO_3^{2-} forming a [$Zn_3(\mu_3$-CO_3^{2-})] core, which was protected inside the cavity of the polyhedron. Similarly, **C3a** was found to be able to capture SO_2 and convert it into SO_3^{-}. The x-ray crystal structure of **C3a** encapsulating SO_3^{-} (**C3a**$\supset SO_3^{2-}$, **Figure 36b**) was also obtained. The formation of the host-guest systems **C3a**$\supset CO_3^{2-}$ and **C3a**$\supset SO_3^{2-}$ was observed not only in the solid state but also in MeCN solution by ^{1}H NMR spectroscopy and ESI-MS spectrometry. Emission spectroscopy provided further evidence of the encapsulation of CO_3^{2-} within **C3a**. The weak Ir(III)-centred emission exhibited by **C3a** at 508 nm was gradually quenched within 18 minutes as a result of the formation of **C3a**$\supset CO_3^{2-}$ upon pumping gaseous CO_2 into the MeCN solution of **C3a**.

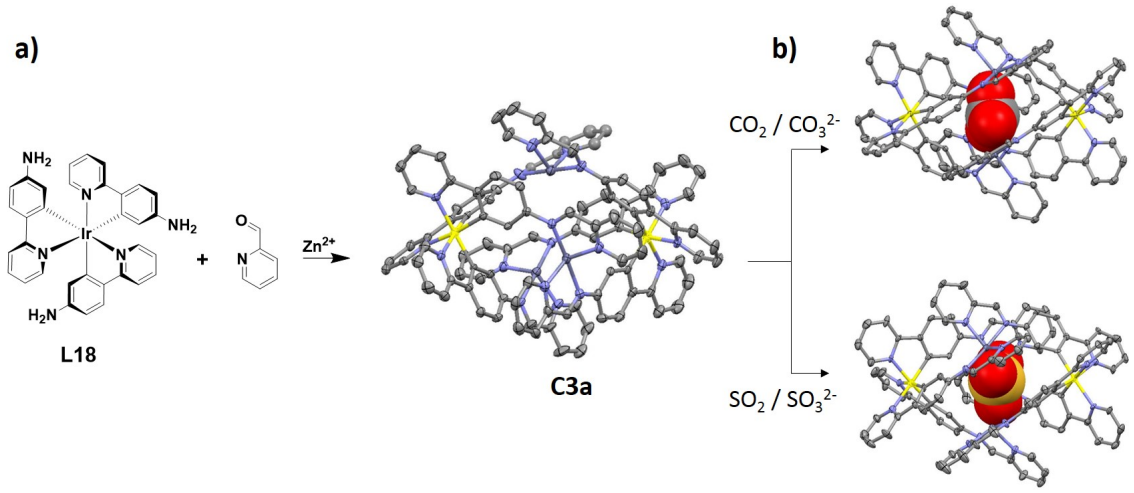

Figure 36. **a)** formation of polyhedron **C3a** from the assembly of **L18**. **b)** x-ray structures of **C3a** encapsulating CO_3^{2-} and SO_3^{2-} shown with space-fill representations.

When treatment of capsule **C3b** with one equivalent of carbonate dianions in MeCN solution, the formation of the host-guest assembly **C3b**$\supset CO_3^{2-}$ was observed both by x-ray diffraction (**Figure 37**) and ESI-MS spectrometry. Interestingly, the empty cage **C3b** was able to convert in high yield (86-96%) 2-aylpyridines to their α-trichloromethylated products when the system was photoirradiated with a 26 W fluorescent lamp (**Figure 37b**). However, when **C3b**$\supset CO_3^{2-}$ or only the single components **L18** or $Co(ClO_4)\cdot 6H_2O$ were tested as photocatalysts, no conversion was observed (**Figure 37c**). These results unequivocally demonstrate that in order to photocatalyze the conversion of 2-aylpyridines, it is necessary to combine the photoactivity of the Ir(III) chromophores with the coordinatively unsaturated Co(II) centres. **C3b** offers a rigid platform to keep the Ir(III) complexes in close

proximity to the Co(II) metal ions, increasing the effective reaction concentration within the local micro-environment, and thus promoting high photoconversion of the substrates.

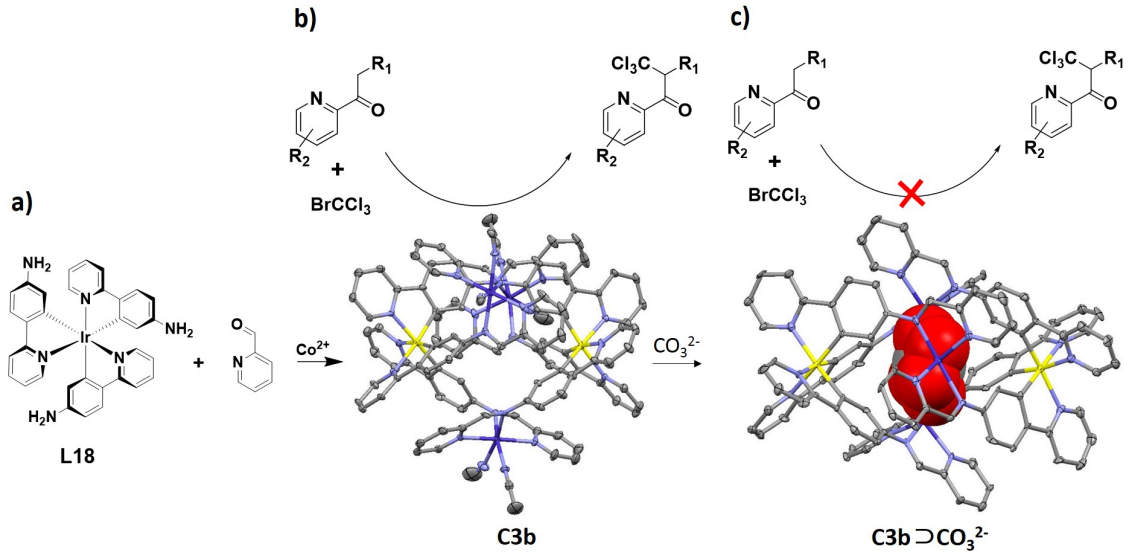

Figure 37. **a)** Synthesis and x-ray crystal structure of polyhedral **C3b**. **b)** illustration of the photocatalysed α-trichloromethylation of acylpyridine promoted by **C3b** (1 wt%). **c)** no photoreaction occurred when CO_3^{2-} ions was encapsulated into the cavity of **C3b**.

Hardie, our group and co-workers[166] reported the assembly of CTV-type ligands (CTV is cyclotriveratrylene), (±)-tris(isonicotinoyl)-cyclotriguaiacylene (**L19**), or (±)-tris(4-pyridyl-methyl)-cyclotriguaiacylene (**L20**), with $[Ir(ppy)_2(NC)_2]^+$, forming metallo-cryptophane cages of compositions of $[(Ir(ppy)_3)_3(\mathbf{L19})_2](BF_4)_3$ (**C4**) and $[(Ir(ppy)_3)_3(\mathbf{L20})_2](BF_4)_3$ (**C5**, **Figure 38a**). The geometry of **C4** was revealed by x-ray crystallography (**Figure 36b**). The cage has three pseudo-octahedrally coordinated Ir(III) centres, each bearing two ppy ligands and two pyridyl groups from two **L19** ligands in a *cis*-arrangements. The two **L19** ligands are bridged between three Ir(III) centres, acting as vertices. Interestingly, despite iridium-centred Λ- and Δ-enantiomers and the M and P enantiomers of the CTV ligands that were present in the reaction mixture, and thus twelve possible stereoisomeric cages, the cage exhibited homochiral self-sorting, and only the enantiomeric MM-ΛΛΛ and PP-ΔΔΔ cages were observed, both in the x-ray structure of **C4** and by NMR in solution after several months, where the self-sorting was found to be very slow. The self-sorting in solution was found to be accelerated by the presence of R-camphor or S-camphor as chiral guests.

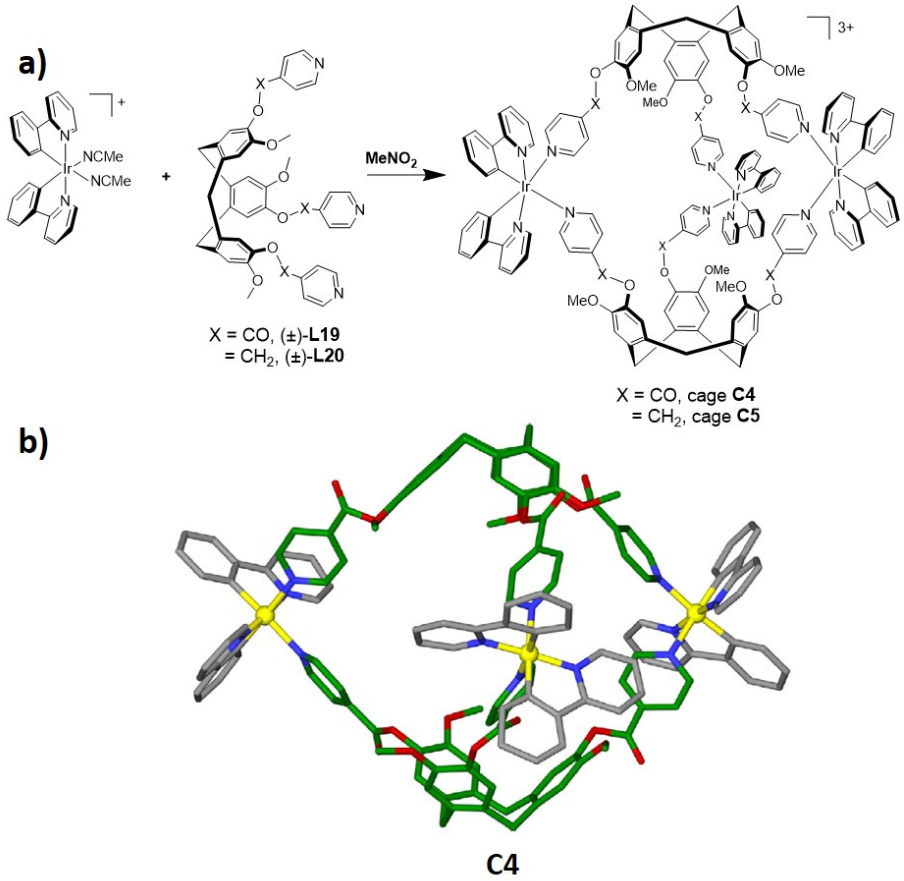

Figure 38. **a)** Chemicals structures of ligands **L19** and **L20** and cages **C4** and **C5**. **b)** X-ray structure of cage **C4**.[166]

Cages **C4** and **C5** are emissive in solution, as bulk powders and in PMMA-doped films (**Figure 39a,b**). The emission of **C4** in the powder was red-shifted (λ_{PL} = 648 nm) compared to that in CH_2Cl_2 (λ_{PL} = 604 nm). In both media low Φ_{PL} of 1% and short bi-exponential emission decays were observed. Due to the increased conjugation into the CTV scaffold as a result of the carbonyl linker to the distal pyridine, **C4** exhibited red-shifted emission compared to **C5** but with similar though red-shifted photophysical behavior compared to the monomeric $[Ir(ppy)_2(4\text{-}pyCO_2Et)_2]^+$ (4-$pyCO_2Et$ = 4-ethyl isonicotinate) (λ_{PL} = 560 nm; Φ_{PL} = 2%). As a result of the reduction of non-radiative vibrational motion in PMMA-doped thin films, the emission of **C4** was blue-shifted and more structured at λ_{PL} = 514 nm with an enhanced emission and longer photoluminescence decays (Φ_{PL} = 5.5%, τ_{PL} = 634 ns, 2319 ns) compared to the emission in CH_2Cl_2. The photoluminescence of **C5** in CH_2Cl_2 was found to be structured and blue-shifted at λ_{PL} = 516 nm with higher Φ_{PL} of 15% and longer τ_{PL} = 523, 887 ns compared to **C4**. Unlike that observed for **C4**, the emissions of **C5** as a powder and in PMMA-doped films were similar to that in CH_2Cl_2 (in powder: λ_{PL} = 519 nm, Φ_{PL} = 1.6%, τ_{PL} = 141, 1175 ns; in thin film: λ_{PL} = 515 nm, Φ_{PL} = 10%, τ_{PL} = 688, 3042 ns).

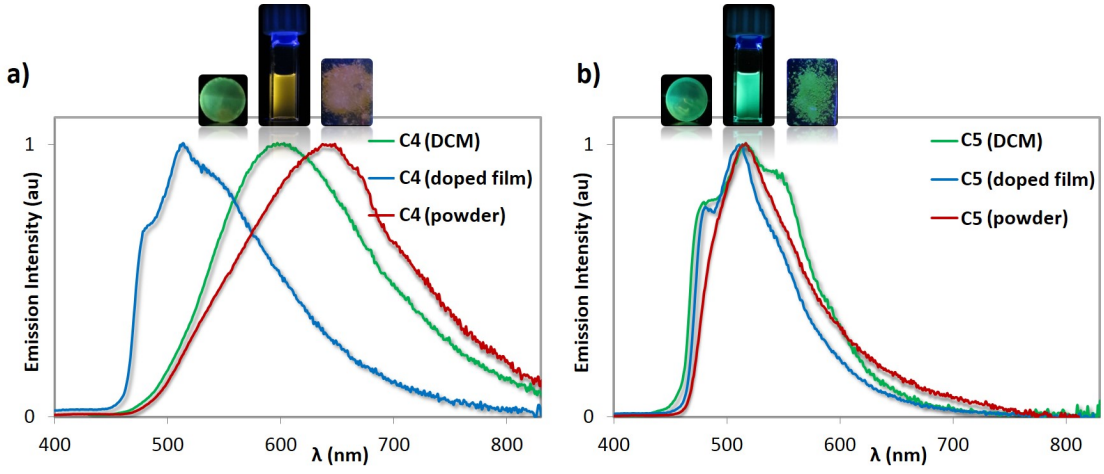

Figure 39. Normalised photoluminescence spectra of **a) C4** and **b) C5**. Green lines are deaerated CH_2Cl_2 solutions, light-blue lines are PMMA-doped films with 5wt% of cages spin-coated on a quartz substrate; red lines are bulk powders. Insets are images of the samples under UV irradiation.[166]

By functionalising the three arms of the CTV core with three bipyridines instead of pyridines as in the preceding example, we also reported emissive polynuclear systems composed of cationic Ir(III) complexes bearing core fragments of $[Ir(ppy)_2]^+$ and/or $[Ir(dFppy)_2]^+$ coordinated to the CTV through the bpy ligands (**Figure 40**).[167]

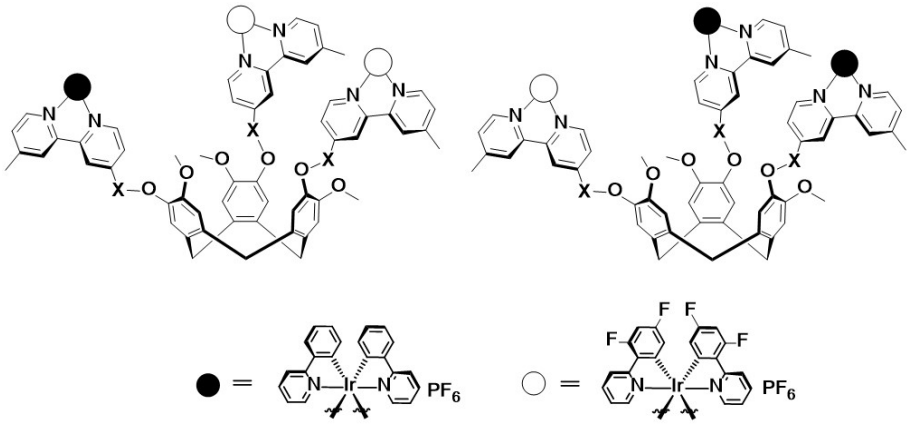

Figure 40. Illustration of the chemical structures of the multimetallic Ir(III)-luminophoric complexes.[167]

The photophysical properties of the complexes were investigated both in MeCN solution and in PMMA-doped films by steady-state and time-resolved emission spectroscopy while their electrochemical properties were investigated by cyclic voltammetry (CV) and differential pulse voltammetry (DPV). Interestingly, we observed that in mixed systems containing both the $[Ir(ppy)_2]^+$ and the $[Ir(dFppy)_2]^+$ luminescent units closely linked

to a single CTV core, the Ir(III) chromophores behaved as isolated centres, with no optoelectronic communication between them. This is an unusual behaviour for multimetallic Ir(III)-chromophoric complexes, since energy transfer between metal centres is commonly observed.

1.3.3 Encapsulation of Ir(III) chromophores

Several studies have demonstrated that the photophysical properties of luminescent Ir(III) metal complexes emitting from CT states strongly depend on the local environment.[117, 122] In this context, the encapsulation of iridium complexes into the cavities of photoactive cages, capsules or MOFs has been demonstrated to be an efficient approach to tuning of the emission properties of the assembly as a function of host-guest energy transfer.

Umakoshi and co-workers[168] encapsulated $[Ir(ppy)_2(bpy)]Cl$ (**L21**) within a hexameric resorcinarene hydrogen-bonded capsule (**Figure 40a**) and observed that the capsule provided a hydrophobic environment and also effectively hampered non-radiative decay, thereby inducing a change in the emission of **L21** from orange (λ_{PL} = 609 nm) to yellow (λ_{PL} = 582 nm) while enhancing both the Φ_{PL} and the τ_{PL} of the encapsulated iridium guest in degassed chloroform (encapsulated **L21**: Φ_{PL} = 32%, τ_{PL} = 860 ns; free **L21**: Φ_{PL} = 20%, τ_{PL} = 420 ns) (**Figure 40b**).

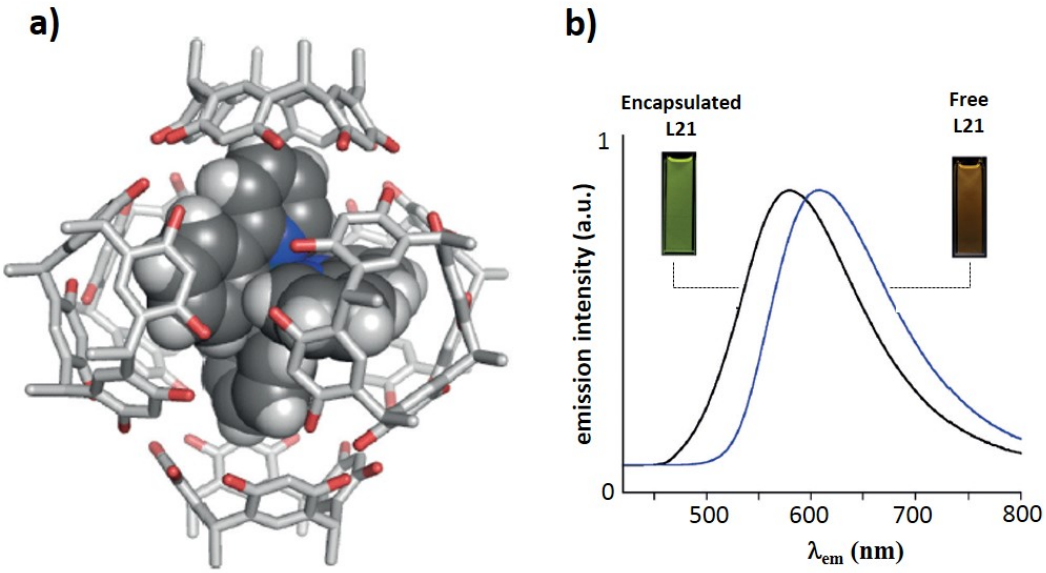

Figure 40. **a)** Molecular model of the resorcinarene capsule encapsulating **L21** (space-fill representation). **b)** normalised emission spectra of free **L21** (blue line) and encapsulated **L21** (black line) collected at 298 K in $CHCl_3$ (λ_{ex} = 400 nm). Image **b)** is adapted with permission. Copyright 2016, Wiley-VCH.[168]

Similarly, the emission of the Ir(III) complex $[Ir(ppy\text{-}CHO)_2(bpy)]^+$ (**L22**, where ppy-CHO is 4-(2-pyridylbenzaldehyde), **Figure 41a**) was remarkably enhanced and blue-shifted upon its encapsulation into the cavity of the cucurbituril [Q10] host (**Figure 41b,c**).[169] Indeed, in aqueous buffer solution (pH 4.7), complex **L22** exhibited a weak emission at 593 nm, which was enhanced 80-fold and blue-shifted to 543 nm after its encapsulation (**Figure 41b**). The temperature had a strong effect on the binding equilibrium; at 40 °C the host-guest assembly was found to be partially dissociated and thus its emission intensity and emission lifetime were, respectively, lower and shorter compared to those collected at 6 °C (at 40 °C: τ_{PL} = 100, 1750 ns; at 6 °C: τ_{PL} = 230, 3260 ns).

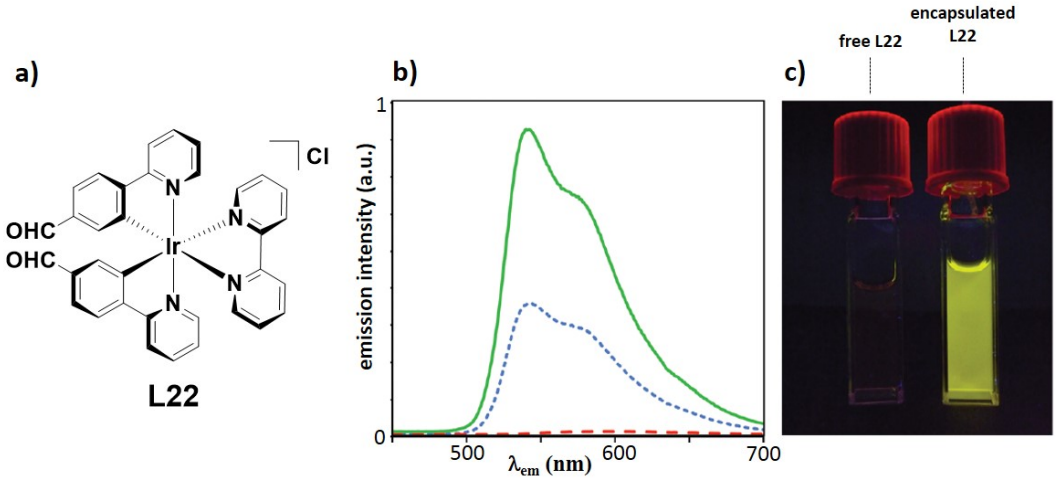

Figure 41. **a)** chemical structure of **L22**. **b)** Emission spectra in aqueous buffer solution (pH 4.7) at 22 °C of **L22** (dashed red line), with added [Q10] in 1:1 molar ratio (dotted blue line) and with excess of [Q10] (solid green line). **c)** Emission from free **L22** (left) and **L22** encapsulated into [Q10] host (right). Adapted from ref. [169] with permission from The Royal Society of Chemistry.

The introduction of Ir(III) luminophores into the nanospace of inorganic host materials have also been explored. Wada and co-workers[170] introduced mixtures of the homoleptic *fac*- and *mer*-$[Ir(ppy)_3]$ (**L23**) and *fac*- and *mer*-$[Ir(dFppy)_3]$ (**L24**), into the cavity of a zeolite (**Figure 42**). Depending on the Ir(III) species introduced into the zeolite, different emission colours were observed from the solid materials. Structured blue emission at λ_{PL} = 465, 488 nm was observed when **L24** was encapsulated, while green emission at λ_{PL} = 524 nm was observed from the zeolite encapsulating **L23** (**Figure 42**). These emission profiles were consistent with those exhibited by the free complexes **L23** (λ_{PL} = 510 nm) and **L24** (λ_{PL} = 468, 482 nm) in MeCN.

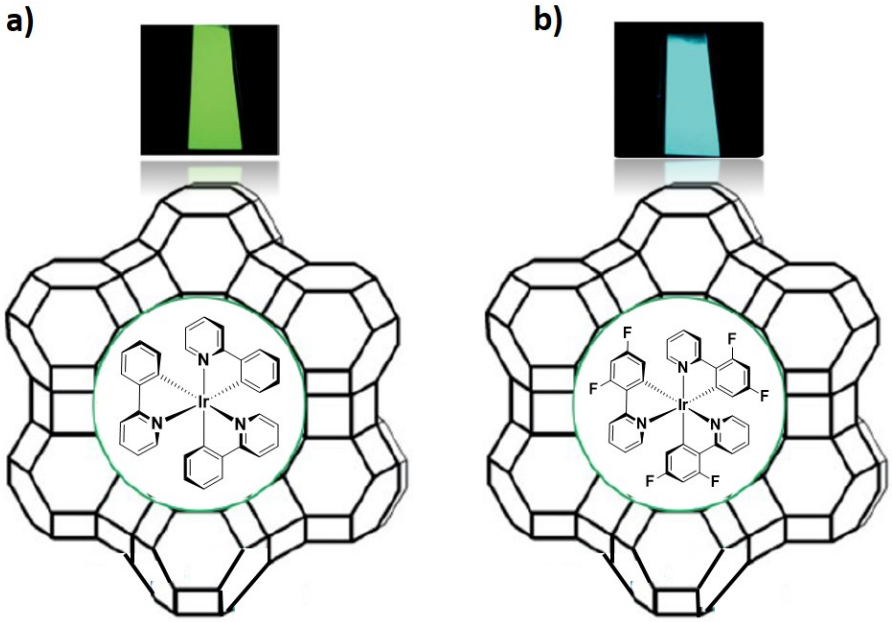

Figure 42. Illustration of the encapsulation of the Ir(III) chromophores [Ir(ppy)$_3$], **a)** and [Ir(dFppy)$_3$], **b)** into the cavity of the zeolite cage. Insets are images of their emission colours. Adapted with permission. Copyright 2012, Wiley-VCH.[170]

In a subsequent work, the same group investigated the photoinduced electron transfer (PeT) processes from **L23**⊃Zeolite to propyl viologen sulfonate (PVS) in solution by using 1,1′-ethylene-2,2′-bipyridilynium ($2DQ^{2+}$), also incorporated into the zeolite cage, as an electron-relay molecule.[171] Their results demonstrated that upon photoirradiation, electron transfer from **L23** to $2DQ^{2+}$ occurred in the zeolite framework, forming the $2DQ^{\cdot+}$ radical cation and the $\mathbf{L23}^{\cdot-}$ radical anion. $2DQ^{\cdot+}$ transferred subsequently the electron to PVS is solution through a dark reaction, forming the $PVS^{\cdot-}$ radical anion. The regeneration of **L23** in its ground state was achieved through the addition of triethanolamine as a sacrificial reductant. The encapsulation of both **L23** and $2DQ^{\cdot+}$ in the cavity of the zeolite was found to be pivotal for promoting the PeT. Indeed, when the free species **L23**, $2DQ^{2+}$ and PVS were irradiated in solution, no PeT was observed.

A Periodic Mesoporous Organosilica derivative (PMO) bearing high density of the homoleptic Ir(III) complex [Ir(ppy)$_3$] (**4b** in **Figure 5**) on the pore surface was investigated by Inagaki and co-workers.[172, 173] The PMO material was prepared by the polycondensation reaction between the ppy-bridge alkoxysilane precursor, 2-(4-triethoxysilylphenyl)-5-triethoxysilylpyridine and the cationic surfactant octadecyltrimethylammonium chloride (C_{18}TMACl). The subsequent cyclometalation reaction of [Ir(ppy)$_2$Cl]$_2$ with the ppy ligands of PMO in an ethylene glycol solution in the presence of K_2CO_3 at 120 °C for 24 h yielded the PMO material with the Ir(III) complex [Ir(ppy)$_3$] included in its pores (Ir-PMO). Ir-PMO exhibited a broad phosphorescence at λ_{PL} = 550 nm with a Φ_{PL} of 3% and a

bi-exponential emission lifetime of τ_{PL} = 250 ns, 1000 ns. These emission properties are characteristic for the meridional isomer *mer*-[Ir(ppy)$_3$], which is typically formed when cyclometalation reactions are conducted at relatively low temperature (< 140 °C).[174] Ir-PMO also acted as a light-harvesting antennae as the energy absorbed by the PMO framework upon photoexcitation at 300 nm was efficiently transferred to the Ir(III) complex following a Förster mechanism. Indeed, the emission of *mer*-[Ir(ppy)$_3$] in Ir-PMO was enhanced when excited at 300 nm (instead of at 380 nm) and the characteristic emission of the PMO framework at λ_{PL} = 420 nm was completely quenched. The phosphorescence properties of PMO derivatives functionalised with the heteroleptic Ir(III) complex [Ir(ppy)$_2$(bpy)]Cl (**4b** in **Figure 5**) were also investigated.[175] Depending on the amount of **4b** loaded into the pores of the PMO, the emission properties of **4b**-PMO in the solid state were found to differ only slightly. With a low, medium and high **4b** loading, respectively, of 3.47 µmol·g^{-1}, 20.4 µmol·g^{-1} and 59.9 µmol·g^{-1}, **4b**-PMO exhibited broad emission, respectively, at λ_{PL} = 527 nm, λ_{PL} = 530 nm and λ_{PL} = 535 nm with Φ_{PL} of 13%, 14% and 13% and τ_{PL} of 405 ns, 462 ns and 438 ns. In MeCN the emission of **4b**-PMO was red-shifted at λ_{PL} = 560 nm with Φ_{PL} of 7.0% and τ_{PL} of 784 ns. When a MeCN solution of tetracene was gradually added (from 0 to 0.4 mM) to a MeCN solution of **4b**-PMO, the emission intensity of **4b**-PMO at λ_{PL} = 527 nm was correspondingly quenched together with a shortenning of its emission lifetime from 784 ns to 107 ns. Förster energy transfer was therefore promoted from **4b**-PMO donor to the tetracene acceptor upon photoexcitation at 340 nm.

By encapsulating the yellow-emitting [Ir(ppy)$_2$(bpy)]PF$_6$ (**L25**) chromophore into the cavities of the blue-emitting fluorescent MOF [(CH$_3$)$_2$NH$_2$]$_{15}$[(Cd$_2$Cl)$_3$(TATPT)$_4$]·12DMF·18H$_2$O (MOF-H, TATPT is a hexadentate carboxylate triazine ligand, 2,4,6-tris(2,5-dicarboxyphenylamino)-1,3,5-triazine), an efficient white-emitting assembly was obtained as reported by Li and co-workers.[176] The Ir(III) complex **L25** exhibited an adequate molecular size of approximately of 10 x 11 Å^2 to be encapsulated into the aperture of the pore windows of MOF-H (11 x 11 Å^2). **L25** showed a broad emission at λ_{PL} = 570 nm in degassed DMF, while MOF-H exhibited bright blue emission at λ_{PL} = 425 nm attributed to the emissive TATPT linker. When complex **L25** was loaded into the pores of MOF-H at various concentrations from 0.52 wt% to 8.8 wt%, the host-guest MOF-H⊃**L25** exhibited two emission maxima with various intensities at λ_{PL} = 425 nm and λ_{PL} = 530 nm (**Figure 43a**), attributed, respectively, to the emissions of MOF-H and **L25** without energy transfer between the two. Due to the rigid confinement of **L25** into the cavities of MOF-H, the emission of **L25** in MOF-H⊃**L25** was blue-shifted by ca. 40 nm compared to that observed for the free complex in solution. Interestingly, at a concentration of 3.5 wt% of **L25**, MOF-H⊃**L25** exhibited pure white light emission with a high Φ_{PL} of 20.4% corresponding to CIE coordinates of x: 0.31, y: 0.33 (**Figure 43b,c**). A WOLED (white organic-light emitting diode) of CIE coordinates of x: 0.30, y: 0.35 using this material and an InGaAsN ultraviolet chip were both successfully fabricated.

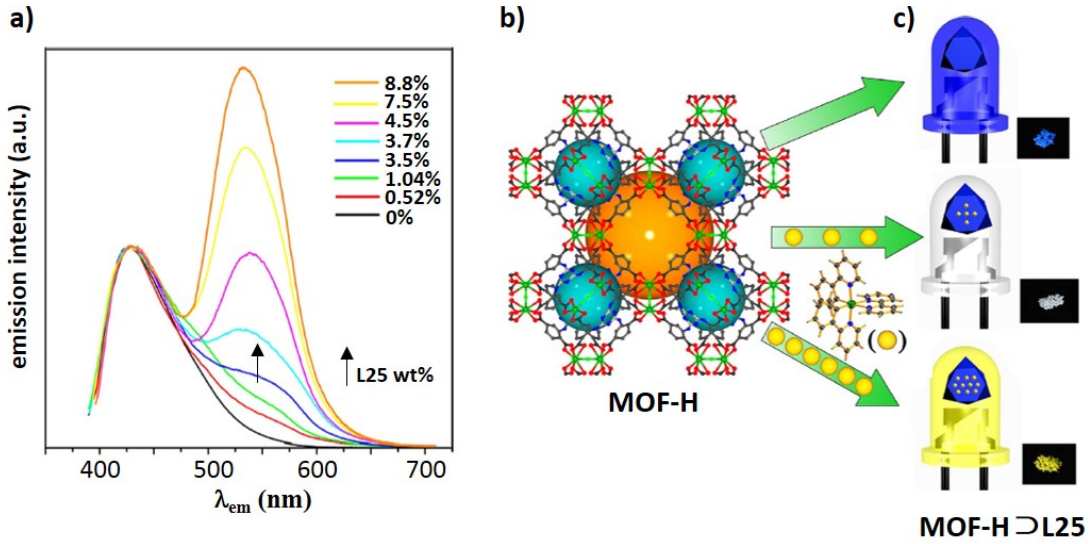

Figure 43. **a)** Emission spectra of MOF-H and MOF-H⊃**L25** with different concentrations of **L25** (from 0.52 wt% to 8.8 wt%, λ_{ex} = 370 nm, 298 K); **b)** ball and stick representation of the 3D structure of MOF-H (orange and cyan spheres represent the void spaces); **c)** illustration of the blue, white and yellow emissions exhibited by MOF-H⊃**L25** with a concentration of **L25** respectively of 0%, 3.5% and 8.8 wt%. Adapted from ref. [176], Springer Nature.

1.4 Phosphorescent ruthenium(II) cages

In contrast to the remarkable emission properties exhibited by cyclometalated Ir(III) complexes and Ir-based supramolecular assemblies, Ru(II) polypyridine complexes and assemblies are generally poorly emissive. Many examples have nevertheless been reported where ruthenium(II) complexes have been incorporated into polymers[177–181], networks,[182, 183] metal-organic frameworks[184–187] and discrete 2D metallamacrocycles.[188–192] Recently, examples of 3D phosphorescent supramolecular cages incorporating Ru(II) complexes as structural components or as metalloligand scaffolds have also been reported. These cage structures are summarised below. This discussion does not include non-emissive Ru(II) cages.[193–199]

Cook and co-workers[200] recently reported a Ru_4L_6-type octahedron, **C6**, by assembling the tpt ligand **L21** (tpt is 2,4,6-tris(pyridin-4-yl-1,3,5-triazine)) with the complex cis-bis(2,2′-bipyridine)ruthenium(II) (**Figure 44**).

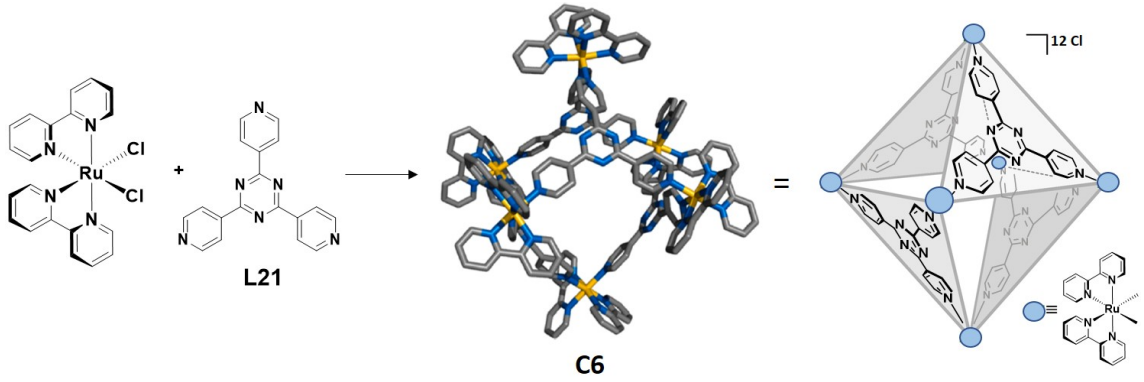

Figure 44. Coordination driven self-assembly of cage **C6**. The simulated structure of **C6** is illustrated. The x-ray structure of **C6** is taken with permission from ref. [200]. Copyright 2017, American Chemical Society.

The photophysical properties of cage **C6** were investigated in MeCN both at room temperature and at 77 K. **C6** exhibited a broad emission centred at $\lambda_{PL} = 577$ nm at room temperature, with a very low $\Phi_{PL} < 0.1\%$ and bi-exponential excited state lifetime of τ_{PL} of 2, 790 ns. This emission was red-shifted and partially quenched compared to the room temperature emission of $[Ru(bpy)_3](Cl)_2$ ($\lambda_{PL} = 613$ nm, $\Phi_{PL} = 5\%$, $\tau_{PL} = 821$ ns). Surprisingly, the 77 K emission of **C6** was also red-shifted at $\lambda_{PL} = 689$ nm compared to the emission observed at room temperature. Although population of the ^{3}ML(bpy$_\pi$*)CT state was the origin of the room temperature emission of **C6**, thermal population of this higher energy excited state no longer occurred at 77 K. Instead, the lower energy ^{3}ML(TPT$_\pi$*)CT was primarily populated at low temperature and accounted for the

red-shifted emission observed for **C6** at 77 K. The electrochemical properties of **C6** were investigated by cyclic voltammetry in MeCN. Multiple oxidation waves, corresponding to multiple Ru(III)/(II) redox couples were observed, with the first occurring at E^{ox} = 0.56 V (versus $Ag/AgNO_3$), which was significantly cathodically shifted compared to the same redox couple in $[Ru(bpy)_3](Cl)_2$ at 1.05 V. The remaining oxidation waves of **C6** ranged from E^{ox} = 0.61 V to 1.08 V. **C6** exhibited a single reduction wave at E^{red} = -1.29 V corresponding to the reduction of the bpy ligand, which was anodically shifted compared to the reduction of bpy in $[Ru(bpy)_3](Cl)_2$ located at -1.64 V, ostensibly a function of the presence of the electron-poor tpt ligand, which contributes to a reduction of the electron density on the Ru centre. Cage **C6** is therefore both a more powerful excited state photoreductant (E^{ox*}: -1.59 V vs -0.97 V) and a more powerful excited state photooxidant (E^{red*}: 0 .86 V vs 0.38 V) than $[Ru(bpy)_3](Cl)_2$. Stern-Volmer quenching studies were performed to probe the efficiency of **C6** as a photoreductant using cobaltocenium hexafluorophosphate as the quencher. However, identical bimolecular rate constants (k_q) of 1.2 x 10^8 s^{-1} were calculated for the energy transfer from both **C6** and $[Ru(bpy)_3](Cl)_2$ donors to the cobaltocenium hexafluorophosphate acceptor, an indication that the same percentage of effective quenching collisions for both chromophores in the presence of cobaltocenium hexafluorophosphate.

A nanosized Pd-Ru heteronuclear metal-organic cage was reported by Su and co-workers.[201] As illustrated in **Figure 45a**, the combination of the spatially triangular C_3-symmetric racemic metalloligand *rac*-**L22** bearing three terminal 3-pyridine units with coplanar squared D_4-symmetric naked Pd(II) ions gave rise to the formation of a $[Pd_6(rac\text{-}\mathbf{L22})_8]^{28+}$ cage, *rac*-**C7**, through N(pyridine)-Pd coordination. Cage *rac*-**C7** was characterized by ^{1}H- and ^{1}H DOSY-NMR spectroscopy and high-resolution electrospray ionization time-of-flight mass spectrometry (ESI-TOF-MS). Furthermore, single crystals of *rac*-**C7** were obtained by co-crystallising *rac*-**C7** with the heavy coordinating molecule $[Ir(ppy)_2(dc\text{-}bpyH)](NO_3)$, $\mathbf{Ir}_a$ (ppy is 2-phenylpyridinato, dc-bpyH is 2,2′-bipyridine-4,4′-dicarboxylic acid), yielding red crystals of the composition of $[rac\text{-}\mathbf{C7}(\mathbf{Ir}_a)_4](NO_3)_{24}$, with the $\mathbf{Ir}_a$ molecules situated outside the structure of cage *rac*-**C7**.

rac-**C7** exhibited a truncated-octahedral geometry with eight *rac*-**L22** metalloligands occupying the eight faces of the cage, six PdN_4 planes truncating the six vertices of the octahedron, and twelve rhombic windows alongside each octahedral edge (**Figure 45a**). The overall cage size is 3.1 x 3.4 x 3.4 nm^3, possessing six Pd vertices with separation of approximately 29 Å and a large cavity of 5350 $Å^3$. Cage *rac*-**C7** was capable of encapsulating neutral non-polar aromatic compounds such as phenanthrene, pyrene and anthracene in a 1:1 mixture of DMSO-d_6/D_2O as a function of the hydrophobic character of its cavity. Molecular dynamic simulations of *rac*-**C7**⊃phenanthrene revealed that a maximum of seven phenanthrene molecules could reside within the cavity of the coordinating cage while an additional seventeen phenanthrene molecules could be accommodated in the "doorway" of twelve cage windows, allowing as many as twenty-four phenanthrene guests to be trapped

(**Figure 45b**). In addition, *rac*-**C7** also exhibited the ability to encapsulate and protect against UV-light radiation three common light-curing agents widely used in inks and paints: 2,2-dimethoxy-2-phenylacetophenone (DMPA), 1-hydroxycyclohexyl phenyl ketone (HCPK) and 2-hydroxy-2-methylpropiophenone (HMPP). While these free molecules showed photolysis when photoirradiated at 365 nm for 12 h, no photolysis of the guest molecules was observed after photoirradiation at 365 nm of *rac*-**C7**⊃DMPA, *rac*-**C7**⊃HCPK and *rac*-**C7**⊃HMPP for 120 h.

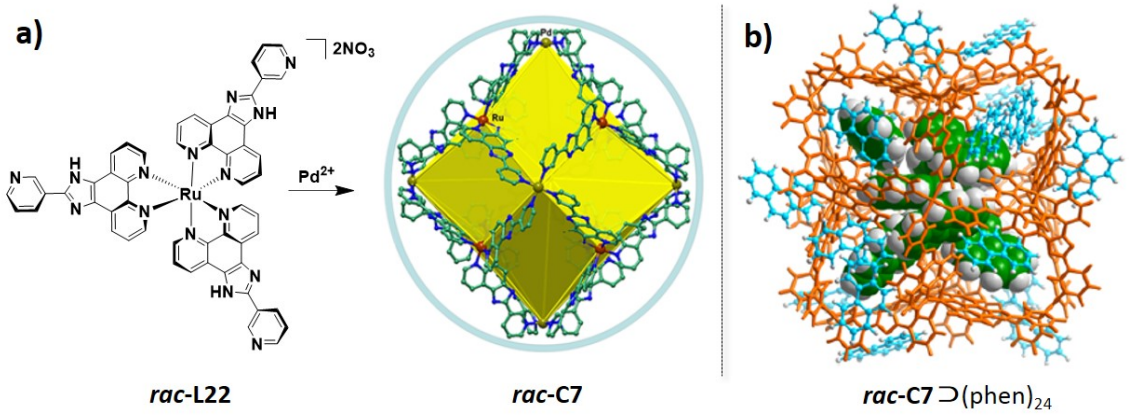

Figure 45. **a)** Preparation of cage *rac*-**C7** from metalloligand *rac*-**L22** and Pd(II). The X-ray structure of *rac*-**C7** is shown highlighting in yellow its cavity. **b)** molecular dynamics simulation of *rac*-**C7**⊃phenanthrene, showing *rac*-**C7** encapsulating phenanthrene guests in its cavity (space-filling mode) and in its windows (stick mode in light blue). Adapted with permission. Copyright 2014, American Chemical Society.[201]

Enantiopure metalloligands Λ- and Δ-**L22** were also prepared in three steps following chiral resolution of *rac*-$[Ru(phen)_3]^{2+}$ with $K_2[Sb_2[(+)\text{-tartrate}]_2]\cdot 3H_2O$, oxidation of Λ- and Δ-$[Ru(phen)_3]^{2+}$ to yield Λ- and Δ-$[Ru(phendione)_3]^{2+}$, which were finally reacted with 3-pyridinecarboxaldehyde in the presence of ammonium acetate in acetic acid. When Λ- and Δ-**L22** were assembled with Pd^{2+} ions, enantiopure cages of composition Λ_8- and Δ_8-**C7** were, respectively, obtained.[202] The enantiopurity and absolute configuration of metalloligands Λ-, Δ-**L22** and metallocages Λ-, Δ-**C7** were, respectively, confirmed by CD spectroscopy and established by x-ray single crystal analyses. The single crystals of Λ-, Δ-**C7** were grown from their MeCN solutions in the presence of R-BINOL and S-BINOL, respectively. Both Λ-, Δ-**C7** crystallised in the chiral space group $I422$ (D_4 symmetry) (**Figure 46a**). In Δ-**C7**, eight Δ-**L22** metalloligands are assembled with six Pd^{2+} ions to form $[Pd_6(\mathbf{C7})_8]^{28+}$ with **L22** in the $\Delta,\Delta,\Delta,\Delta,\Delta,\Delta,\Delta,\Delta$-homochiral configuration, and eight S-BINOL molecules captured in the cage window pockets. Similarly, Λ-**C7** integrated eight **L22** metalloligands with the $\Lambda,\Lambda,\Lambda,\Lambda,\Lambda,\Lambda,\Lambda,\Lambda$-homochiral configuration and co-crystallised with eight R-BINOL molecules likewise assembled in the cage window pockets.

The stereoselective inclusion of chiral molecules of C_2 symmetry such as BINOL, 3-bromo-BINOL, 6-bromo-BINOL and 1,1′-spirobiindane-7,7′-diol, and chiral molecules characterised by a chiral carbon centre such as Naproxen, 1-(1-naphtyl)ethanol and benzoin into the cavity of cages Λ- and Δ-**C7** were examined by ^{1}H NMR enantiodifferentiation experiments in a DMSO-d_6:D_2O = 1:5 mixture at 298 K. Homochiral cages Λ- and Δ-**C7** exhibited poor stereoselectivity towards the chiral compounds Naproxen, 1-(1-naphtyl)ethanol and benzoin (encapsulating R- and S-enantiomers with a ratio of ca. 50:50). However, through the same separation process, a pair R- and S-BINOL atropisomers were successfully resolved, with the ee values reaching approximately 34% and 36%, respectively, with Δ-**C7** (encapsulating R-/S-BINOL with a ratio of 67/33) and Λ-**C7** (encapsulating R-/S-BINOL with a ratio of 32/68). Relatively low enantioseparation results were obtained for R- and S-(3-bromo-BINOL) with a ee value of approximately 8%. The chiral resolution was greatly improved for the chiral discrimination of R- and S-(6-bromo-BINOL) enantiomers. Indeed, by using Δ-**C7** the resolved product contained 77% of the R-isomer and 23% of the S-isomer, giving an ee of approximately 54%, while an ee of 62% was obtained by using Λ-**C7**, with the product dominant in S-isomer. Similarly, Δ-**C7** showed preferable stereoselectivity towards R-(1,1′-spirobiindane-7,7′-diol) with ee value of approximately 34%, while Λ-**C7** incorporated primarily the S-isomer with ee value of 44%. In general, Δ-**C7** showed a preferable selectivity towards the encapsulation of the R-isomers, while Λ-**C7** preferred the encapsulation of the S-isomer for all chiral guests.

In a subsequent work the same group reported the use of the cage *rac*-**C7** as a molecular flask to promote cavity-directed photodimerization of 2-naphtol and 3-bromo-2-naphtol, forming racemic mixtures of S- and R-[4-(2-hydroxy-1-naphtyl)-1,2-naphtoquinone] and of its 3-bromo derivative (**Figure 46b**). Importantly, when the photodimerization reaction of 3-bromo-2-naphtol was conducted in the cavity of the enantiopure cages Λ- and Δ-**C7** (5 mol% loading of cages), an enantiomeric excess of 58% ee (product R/S ratio: 79/21) and 54% ee (product R/S ratio: 23/77) was respectively obtained, albeit with low isolated yields of 9%. Although examples of self-assembled cages as molecular flasks to induce photochemical transformations of encapsulated guests have been previously reported,[203] with relevant examples involving [2+2] photodimerization of olefins,[204] [2+2] cross-photodimerization,[205, 206] cyclisation of α-diketones,[207] and photochemical oxidations of alkanes and alkynes,[208] this work showed for the first time that chiral photoactive cages can be efficiently used also to promote regio- and enantio-selective photo-transformations of bound guests.

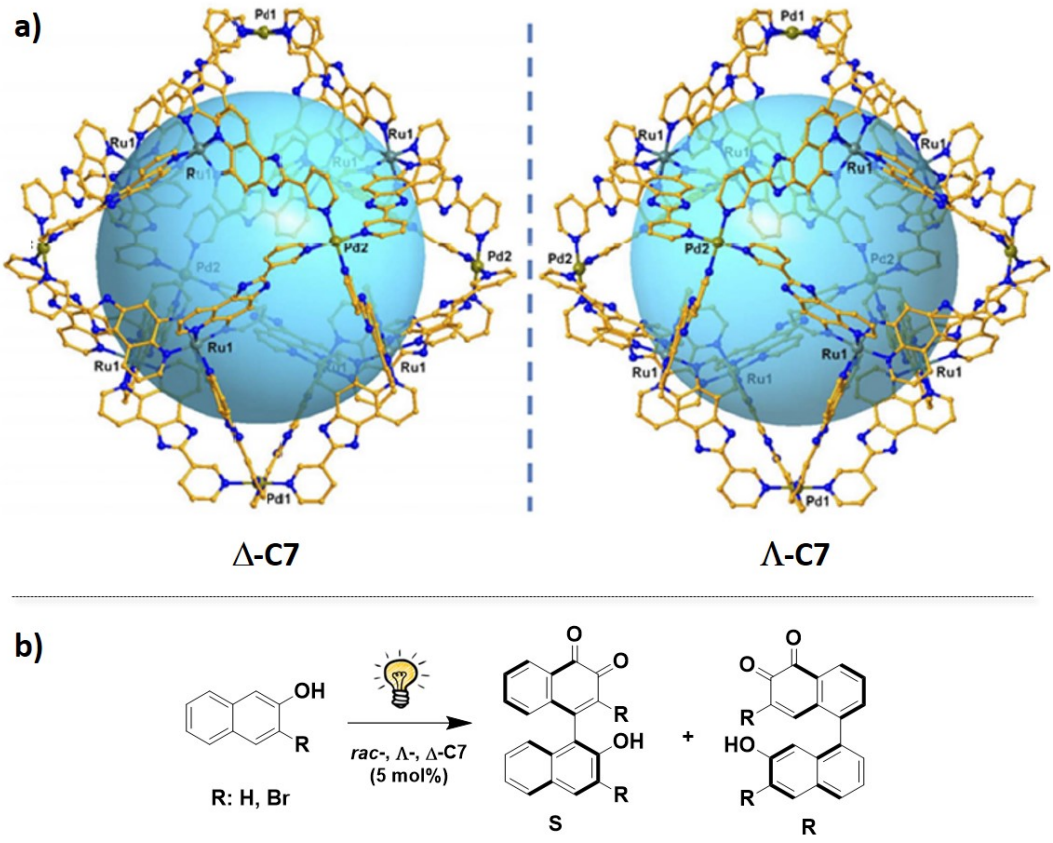

Figure 46. **a)** X-ray structure of enantiopure cage Δ-**C7** (left) and Λ-**C7** (right). The blue sphere illustrates the cavity of the cage. **b)** photoinduced dimerization of 2-naphtol and 3-bromo-2-naphtol in the presence of cage *rac*-, Λ- and Δ-**C7**. The system was irradiated with 8W blue LED light (λ_{ex} = 453 nm) in air in MeCN:H_2O = 1:1.[202]

During the last decade, research into solar fuels has greatly accelerated, mostly in the area photocatalytic water splitting to generate clean hydrogen energy.[209] Remarkable progress has been made since the development of intramolecular photochemical molecular devices (PMDs) by integrating chromophoric photosensitizers, catalytic centers and electron relay components into a single component photocatalyst.[210] For example, many photoactive multimetallic PMDs[211] including trinuclear Ru-Pt-Pd, Ru-Pt_2[212] and Ru-Rh-Ru[213, 214] or tetranuclear Ru2-Ru-Pt[215] and Ru-Pt_3[216] complexes have been developed as photocatalysts for hydrogen production, achieving up to 870 turn-over number (TON) after 46 h.[213, 214] Cage *rac*-**C7** represents a fascinating example of a highly organized structure composed by eight Ru^{2+} photocenters and six catalytically active Pd^{2+} centers that, linked through a phenanthroline (phen) bridging ligand and a benzimidazole-pyridine (biim-py) peripheral unit, mimic the composition of PMDs (**Figure 45**).[217]

The metalloligand *rac*-**L22** and cage *rac*-**C7** exhibited similar emission spectra with maxima at ca. 610 nm, which corresponds for both *rac*-**L22** and *rac*-**C7** the emissions from $Ru(phen)_3$-centred triplet ^{3}MLCT states. However, compared to that of *rac*-**L22**,

the emission intensity of *rac*-**C7** was reduced by about 32% due to intramolecular charge transfer from $Ru(phen)_3$ to $Pd(pyridine)_4$ moieties. Both DFT calculations and ultrafast transient absorption spectroscopy elucidated the electronic structure of *rac*-**C7**. The photoexcitation of the $[Ru(phen)_3]^{2+}$ chromophore at 400 nm populates ^{1}MLCT state, followed by intersystem crossing (ISC) to populate ^{3}MLCT state involving the phenanthroline. The subsequent excited state relaxation occurs via an intraligand charge transfer (ILCT) process from phen to biim-py, and finally, a much slower process of ligand-to-metal charge transfer (LMCT) takes place from biim-py to the Pd catalytic center. Interestingly, the photocatalytic hydrogen production exhibited by cage *rac*-**C7** in a closed gas circulation and evacuation system upon irradiation with visible light ($\lambda_{ex} > 420$ nm) was found to be efficient. Indeed, under optimised conditions (100 mL DMSO solution with 22 µM *rac*-**C7**, 0.34 M H_2O and 0.75 M triethanolamine), the highest reaction rate for H_2 production was found to be 380 µmol·h^{-1} with a turnover number of 635 after 48 h. The efficiency of H_2 production by using *rac*-**C7** as a photocatalyst is comparable to those observed for H_2 production with photoactive multimetallic PMDs.[211]

Beves and co-workers[218] designed the Ru(II) complexes **L23** and **L24** featuring a $[Ru(tpy)_2]^{2+}$ core (tpy is 2,2′,6′,2″-terpyridine) decorated at the 4'-position with a 3,5-disubstited benzene containing 4-pyridyl groups capable of binding to square-planar Pd metal centres (**Figure 47**). Reaction of **L23** with two equivalents of $[Pd(dppp)](OTf)_2$ (dppp is 1,3-diphenylphosphino-propane) in nitromethane at room temperature immediately afforded a single major species in solution, the composition and purity of which were ascertained to be $[(Pd(dppp))_8(\mathbf{L23})_4](PF_6)_{24}$ (**C8** in **Figure 47a**) by ESI-MS spectrometry and ^{1}H- and ^{31}P-NMR spectroscopies. The analogous reaction of complex **L24**, which features alkyne spacers between the phenyl and pendant pyridyl rings, and $[Pd(dppp)](OTf)_2$ gave rise to a trimeric, rather than a tetrameric structure as observed for the assembly of **L23**, of the composition of $[(Pd(dppp))_6(Ru_7)_3](PF_6)_{18}$ (**C9** in **Figure 47b**). The simulated structure of **C9** is illustrated in **Figure 47b**. Slow diffusion of toluene into a nitromethane solution of cage **C8** gave red crystals suitable for x-ray diffraction. **C8** crystallised in the $P\bar{1}$ space group and exhibits a box-like structure of dimensions of approximately 21 x 21 x 32 Å, with Pd(II) centers located at each end of the box forming almost perfect squares (Pd-Pd-Pd angles of 86.0°-92.8° and Pd···Pd distances of 13.2-13.4 Å). The center of the cage is occupied by $[Ru(tpy)_2]$ units with alternating Ru···Ru distances of 11.82 Å and 8.78 Å. Preliminary investigation of the photophysical properties of **C8** and **C9** revealed that their emissions are similar to those of the corresponding metalloligands **L23** and **L24**. All the species exhibited weak emissions at $\lambda_{PL} = 640$ nm from ^{3}MLCT states centered on the $[Ru(tpy)_2]$ chromophores with very short mono-exponential excited state lifetimes of 1.59 ns, 2.04 ns, 1.95 ns and 2.53 ns, respectively, for **L23**, **C8**, **L24** and **C9**. The photophysical properties of **L23**, **C8**, **L24** and **C9** are also comparable to those previously reported for the related $[Ru(4'\text{-tolyl-tpy})(\text{bis-tpy})]^{2+}$ complex[219] (tolyl-tpy is 4′-(p-tolyl)-2,2′;6′,2″-terpyridine, bis-tpy is 1,4-di-[(2,2′;6′,2″-terpyridin)-4′-yl]benzene.

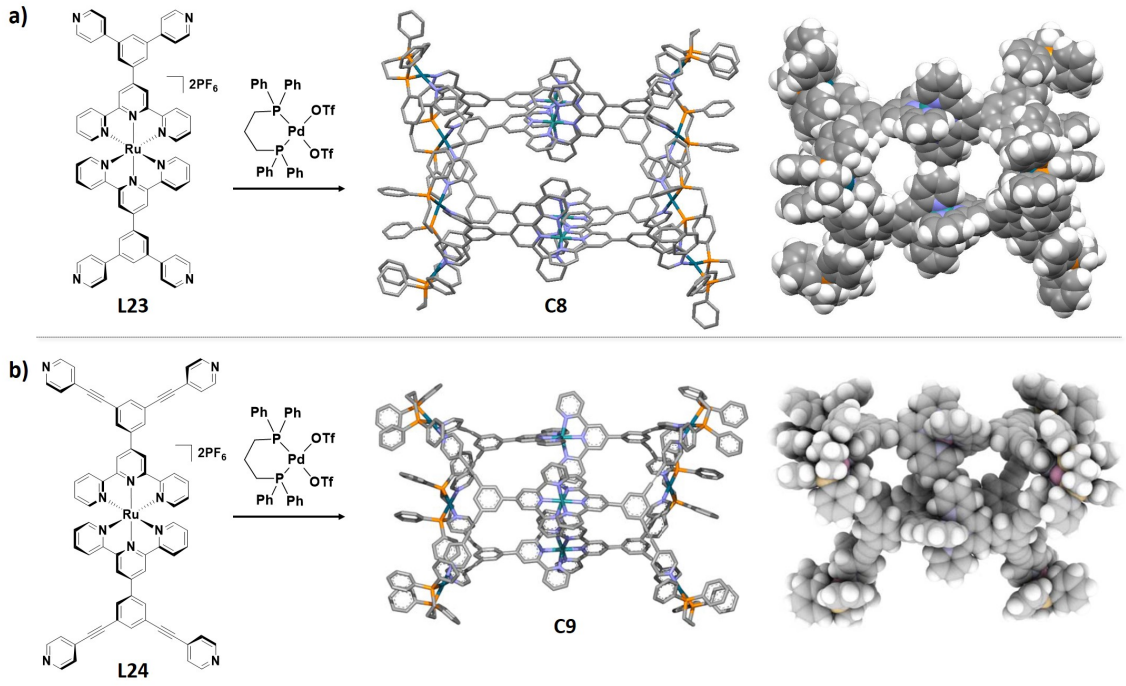

Figure 47. **a)** Self-assembly between the Ru metalloligand **L23** and $[Pd(dppp)](OTf)_2$ to yield cage **C8**. The x-ray structure of **C8** is illustrated in capped sticks (left) and spacefill (right) modes. **b)** Self-assembly between the Ru metalloligand **L24** and $[Pd(dppp)](OTf)_2$ to yield cage **C9**. The simulated structure of **C9** is illustrated. Adapted from ref. [218] with permission from The Royal Society of Chemistry.

As exemplified by cages **C7**, **C8** and **C9** the assembly of Ru metalloligands with Pd^{2+} ions often results in inhibition or complete quenching of the luminescence properties of the ruthenium chromophores, which is the result of the population of low-lying dark-states involving the Pd centres. This problem can be avoided by electronically isolating the requisite metal complexes from the ligand frameworks and Pd(II) metal ions. In this context, there have been a few reports in the literature of functionalised cages generated from ligands appended at their exohedral faces with photoactive Ru(II) complexes.

Crowley and co-workers[220, 221] recently reported $[Pd_2L_4]^{4+}$ metallo-supramolecular cages constructed from a tripyridyl 1,2,3-triazole backbone exo-functionalized with the Ru(II) complexes $[Ru(bpy)_2(az\text{-}py)](PF_6)_2$ and $[Ru(bpy)_2(az\text{-}bpy)](PF_6)_2$ (az-py is 3-(1-methyl-1H-1,2,3-trazol-4-yl)pyridine and az-bpy is 5-(1-methyl-1H-1,2,3-triazol-4-yl)-2,2′-bipyridine). DFT calculations, absorption, emission and raman spectroscopies and cyclic voltammetry evidenced minimal electronic communication between the Pd_2L_4 cage unit and the exo-appended Ru(II) chromophores. Similarly, Casini, Kuhn and co-workers[222] reported a Pd_2L_4 cage exo-functionalised with the Ru(II) complex $[Ru(bpy)_2(bpy\text{-}alk\text{-}CO_2H)](PF_6)_2$ (bpy-alk-CO_2H is 3-(4-methyl-[2,2′-bipyridin]-4-yl)propanoic acid). As a result of the isolation of the Ru(II) chromophoric units from the Pd^{2+} ions, this ruthenium

cage exhibited a strong orange phosphorescence at λ_{PL} = 640 nm with a high Φ_{PL} of 66%, which is comparable to the Φ_{PL} of 88% they obtained for the mononuclear ruthenium complex. To the best of our knowledge this represent the highest Φ_{PL} reported for supramolecular coordination cages.

1.5 Summary of the introduction

The self-assembly of Ir(III) luminophores into supramolecular materials clearly offers possibilities for tuning the physical and optoelectronic properties of Ir(III) complexes and opens up opportunities for exploiting these materials in many applications, ranging from catalysis to electroluminescent devices. Iridium-based soft materials generally exhibit highly organised structures with enhanced emission when compared to their mononuclear counterparts. Three-dimensional iridium-based polymers and MOFs are still in their infancy. However, it appears clear that the combination of the luminescent properties of Ir(III) chromophores and the large channel sizes exhibited by these classes of porous materials is of great interest for sensing and for solar-driven chemical transformations. Photoactive coordination cages and capsules incorporating Ir(III) and Ru(II) chromophores are promising candidates as photoactive containers capable of photophysically interacting with guest molecules. Heterometallic cage compounds composed of Ir(III) or Ru(II) chromophores and Pd^{2+} metal ions generally show red-shifted emissions with lower Φ_{PL} and shorter τ_{PL} compared to the corresponding phosphorescent metalloligands. The quenching of the cage emissions is generally due to the population of non-emissive charge transfer states involving both the photoactive metalloligands and the Pd^{2+} ions used as structural components. On the other hand, when the phosphorescent metal complexes are electronically isolated from the ligand frameworks, the photophysical properties of the luminescent complexes are generally maintained also in the assembled structures. Stability, ligand design and control of the luminescent properties of the materials in the solid state are the major challenges to meet in order to expand the use and number of supramolecular Ir(III) and Ru(II) cages. The relatively small number of examples included in Chapter 1 shows, however, that the field is relatively new, with most of the articles published only in the last decade. However, given the demonstrated functionality of these systems, their importance is sure to grow rapidly.

Chapter 2

Chiral Iridium(III) Complexes in Light-Emitting Electrochemical Cells: Exploring the Impact of Stereochemistry on the Solid-State Photophysical Properties

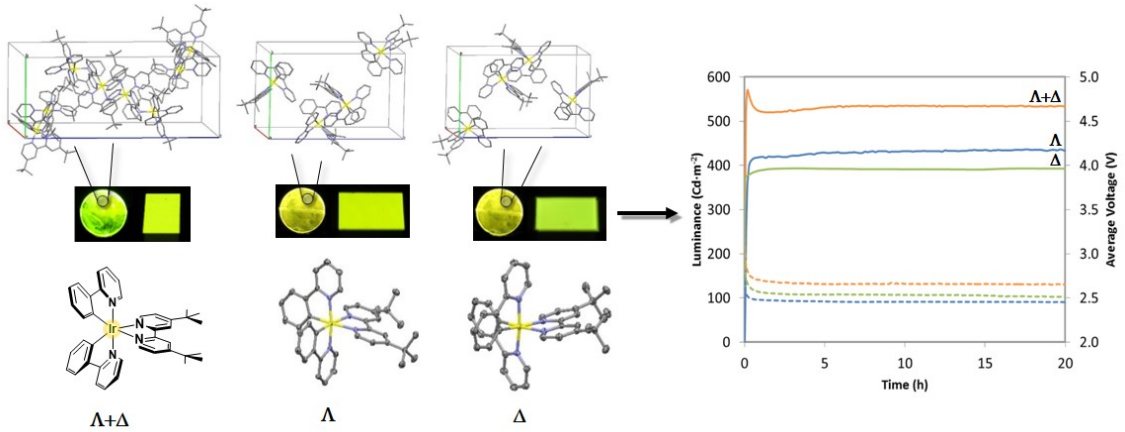

2.1 Introduction

2.1.1 The expansion of solid-state lighting

The development of luminescent materials has revolutionised human society, increased global productivity and improved the quality of life in dramatic fashion. Phosphorescent materials hold great promise in artificial lighting,[223–225] in photocatalysis to drive chemical transformations of compounds of industrial relevance,[226] and in sensing for the detection of a variety of analytes from nitroaromatic explosives[227] to biological targets.[228, 229]

The diffusion of artificial lighting is one of the greatest achievements of the past century,[230] but even today, about twenty percent of world electricity consumption is devoted to the use of environmentally damaging, poorly efficient lighting technologies such as mercury vapour lamps and halogen lamps, which cover most of today's market.[231, 232] Due to the increased industrial growth and world population, energy demand is increasing exponentially; thus, cheap and more efficient energy technologies must play an important role in the evolution of world energy supply in the short-term future.[233–235]

Solid-State Lighting (SSL), in which selected luminescent materials are stimulated to produce visible light under the action of an electrical field (electroluminescence) in suitably engineered devices, are more than ten times as efficient as incandescent lighting.[236–238] This is because, unlike for traditional lighting devices where visible light is essentially a by-product of other processes such as heating and discharging, in SSL devices the primary products are photons. As a result, SSL creates visible lighting with reduced heat generation, less energy dissipation and thus high efficiency.[239–241] There are two main families of SSL devices, namely Light-Emitting Diodes (LEDs) and Organic Light-Emitting Diodes (OLEDs).[242, 243] LED technology is based on inorganic semiconductors made from combination of different elements, *e.g.*, In, Ga, P, N, and provides highly efficient and convenient light point sources of different colors.[244] LEDs are extensively used for screen back-lighting, automotive applications, traffic signaling and advertising.[245] An OLED device, on the other hand, is a flat, multilayer, thin film architecture in which the core of the technology is the layer containing the luminescent material, typically a polymer, a small fluorescent molecule or a phosphorescent transition-metal complex embedded in a charge transporting matrix.[246–248] OLEDs are more recent than LEDs and have found prominent use as displays in cellphones and in prototype televisions.[1, 249] The working principles of OLEDs are quite simple: through application of an electric current, holes and electrons are injected at opposite electrodes of the device and they migrate through the cell toward the emitting layer by hopping processes. Hole-electron recombination in the emitting layer promotes the formation of excitons (bound electron-hole pairs) that quickly relax back to the ground state by emitting light.[1, 248] Depending on the nature of the

compounds employed within the emitting layer, singlet or triplet excitons can be formed upon the action of an electric field. Fluorescent materials can only populate singlet excited states and form only singlet excitons.[250] By contrast, due the heavy atom-induced spin-orbit coupling, phosphors such as iridium(III), platinum(II) and ruthenium(II) complexes populate triplet states via intersystem crossing and therefore can harvest both singlet and triplet excitons for the emission of light.[251] As a consequence, according to spin statistics, exciton-based electroluminescence from fluorophores cannot exceed a maximum Internal Quantum Efficiency (IQE) of 25%,[252] whereas the IQE of phosphors can yield up to the theoretical limit of 100%.[253] As a result, the interest on organometallic based emitters for SSL is in rapid expansion and devices based on this class of materials already cover an important segment of todays' market.[251]

State-of-the-art OLEDs consist however of a complex multilayer stacks employing often more than 15 individual layers.[254] Such a multilayer stack can only be prepared by vacuum sublimation techniques that imply the exclusive use of thermally stable non-ionic materials.[14, 255] Moreover, the high manufacturing costs of OLEDs associated with the stack multilayer preparation and evaporation processes are major limitations that have prevented significant expansion of this technology in the lighting market to date.[254]

Light-Emitting Electrochemical Cells (LEECs) have been recently targeted as a promising and potentially lower cost-alternative SSL technology to OLEDs.[254] LEEC technology has indeed a much simpler architecture than OLEDs, which consists of a ionic luminescent material in a ionic environment generally sandwiched between two air-inert aluminium electrodes. LEECs can be easily processed from solution, they do not rely on air-sensitive charge-injection and charge-transporting layers and hence require less stringent packaging procedures.

2.1.2 Chapter outline

Iridium(III) ionic transition-metal complexes (iTMCs) are by far the most widely investigated class of emitter employed in LEECs.[254, 256–258] In this type of electroluminescent device, iTMCs along with their associated counterions play several key roles, including the following: facilitating charge injection from the electrodes; charge transport through the device; and, after electron and hole recombination, emission of light.[254, 256] Ionic cyclometalated iridium(III) complexes are the most popular emitters used in LEECs as they generally possess relatively short-lived triplet excited states (τ_{PL}), high photoluminescence quantum yields (Φ_{PL}), and a huge variety of chemically stable complexes covering emissions over the entire visible spectrum,[11, 12, 259, 260] all pivotal properties for emitters in electroluminescence devices.[261]

Octahedral iridium complexes bearing at least two bidentate ligands exhibit intrinsic

metal-centred stereochemistry.[262–264] During the prototypical synthesis of cationic bis-cyclometalated iridium(III) complexes of the form $[Ir(C\hat{}N)_2(N\hat{}N)]^+$, the two stereoisomers (Λ, Δ) are formed as a racemic mixture. Generally, in order to obtain enantiopure metal complexes, chiral resolution of the racemic mixtures is required to isolate the pure Λ and Δ enantiomers.[263, 265–269] This can be achieved by purification by liquid chromatography using either a chiral stationary phase[265, 270–272] or a chiral anion in the eluent (cation-exchange chromatography).[273, 274] More recently, the concept of auxiliary-mediated asymmetric synthesis by using tailored chiral bidentate ligands, such as simple amino acids,[158, 162] salicyloxazolines, salicylthiazolines,[262, 263, 275] or prolines[276] have been reported. Such auxiliaries can transfer their chiral information to an octahedral-metal centre and can be subsequently removed tracelessly with retention of the metal-centred absolute configuration. Despite the hundreds of examples of cationic iridium complexes as emitters in LEECs since the first example of their use in 2004,[257] and the importance packing that the emissive layer plays in these LEEC devices, there have been no reports that has probed the importance of the metal-centred stereochemistry on the performance of the device.

With this in mind we decided to investigate two families of iridium(III) complexes of the form of $[Ir(C\hat{}N)_2(dtBubpy)]PF_6$ (where C^N is ppy = 2-phenylpyridinato in **Ir1**, mesppy = 2-phenyl-4-mesytilpyridinato in **Ir2**, and dtBubpy is 4,4′-di*tert*-butyl-2,2′-bipyridine, **Figure 48**) in both their Λ- and Δ-enantiopure and racemic configurations.

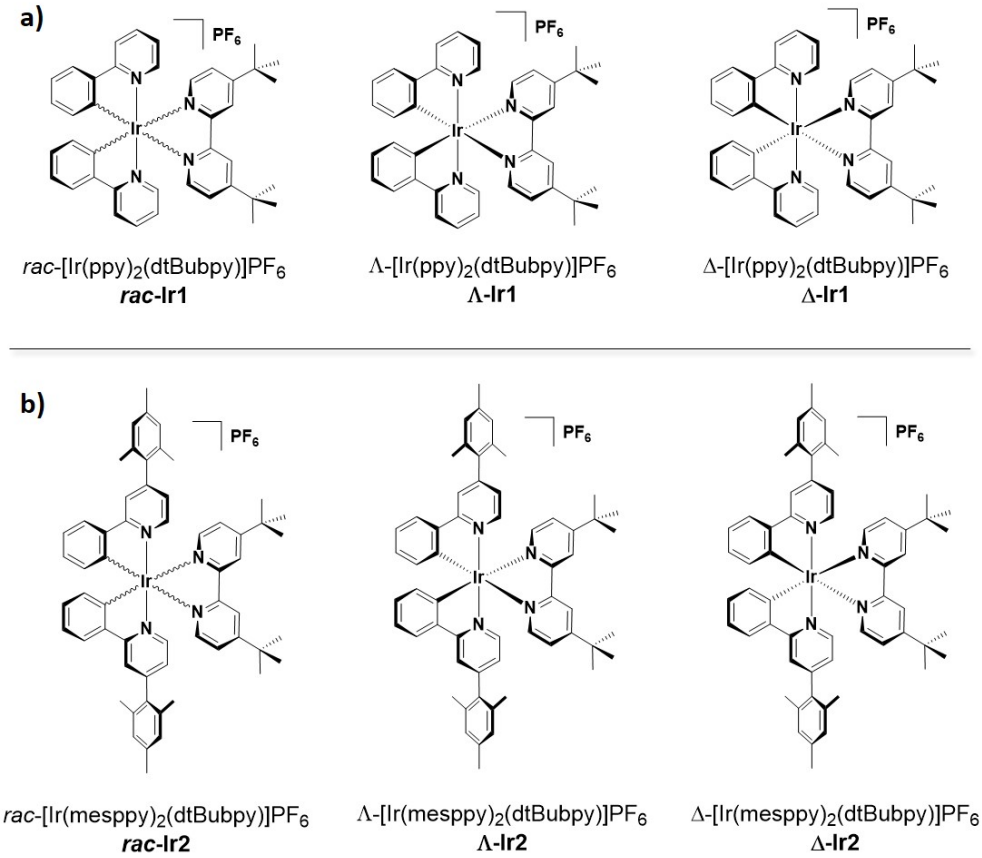

Figure 48.Chemical structures of the two families of complexes: **a)** ***rac*-Ir1**, **Λ-Ir1** and **Δ-Ir1** and **b)** ***rac*-Ir2**, **Λ-Ir2** and **Δ-Ir2**.

We targeted the family of $[Ir(ppy)_2(dtBubpy)]PF_6$ complexes given the historic and well-studied behavior of ***rac*-Ir1** and the potential for its use as a simple archetype to evaluate the effect of the enantiopurity (**Λ-Ir1** and **Δ-Ir1**, **Figure 48a**) on the solid-state photophysical and LEEC device properties.[257] We extended our study to the family of $[Ir(mesppy)_2(dtBubpy)]PF_6$ complexes (**Figure 48b**) as mesityl substitution at the 4-position of the pyridine ring of fluorinated analogue dFppy (2-(4,6- difluorophenyl)pyridinato) C^N ligand had been previously shown by Bryce and co-workers for $[Ir(dFmesppy)_2(pic)]$ (where pic is 2-piconilate and dFmesppy is (2-(4,6-difluorophenyl)-4-mesitylpyridinato),[277] and our group and co-workers for $[Ir(dFmesppy)_2(dppe)]PF_6$ (where dppe is 1,2-bis(diphenylphosphino)ethene)[278] to (1) improve solubility of the complex in organic solvents, which impacts positively homogeneous film deposition;[279] (2) promote reduced intermolecular interaction due to the bulky mesityl group and therefore reduced quenching phenomena, giving rise to increased Φ_{PL} in the solid state;[277, 278] (3) negligibly impact the emission energy, as the mesityl moiety is disposed in a nearly orthogonal and locked conformation with respect to the plane of the pyridine ring[280] and (4) positive impact on devices performance.[277] By contrast, in the crystalline state of $[Ir(dFmesppy)_2(dtBubpy)]PF_6$, π-stacking intermolecular interactions between mesityl

rings on adjacent complexes are present, and as a consequence, the Φ_{PL} is reduced in neat film compared to MeCN solution or PMMA doped thin film.[280]

The syntheses, crystal structures, and solid-state photophysical properties of ***rac*-**, Λ- and Δ-**Ir1**, and ***rac*-**, Λ- and Δ-**Ir2** are reported in this chapter. LEEC devices have also been fabricated using both the enantiopure Λ and Δ complexes (Λ-, Δ-**Ir1** and Λ-, Δ-**Ir2**, **Figure 48**) as well as the racemic analogues of both families (***rac*-Ir1** and ***rac*-Ir2**, **Figure 48**), and the effect of the stereochemistry of the iridium complexes on the devices performances have been tested.

2.2 Synthesis and characterisation

2.2.1 Synthesis of racemic and enantiopure complexes

The syntheses of the C^N ligands and the racemic heteroleptic iridium complexes (***rac*-Ir1** and ***rac*-Ir2**) are shown in **Scheme 1**.

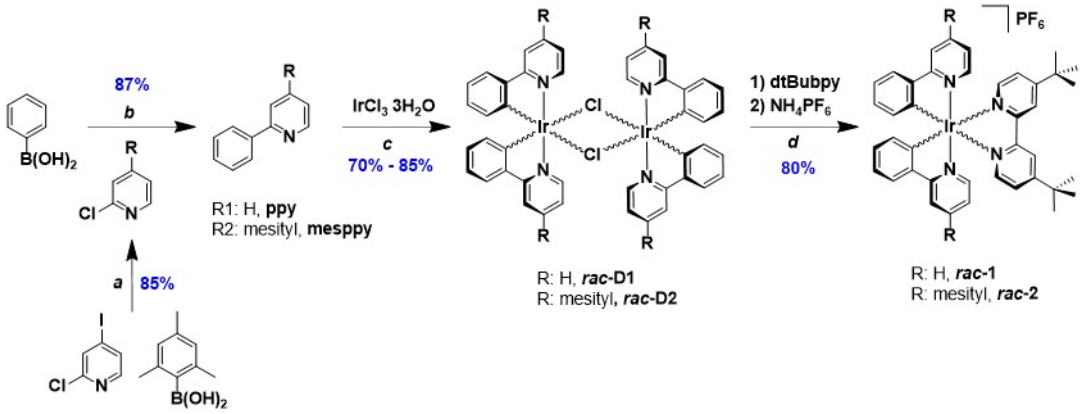

Scheme 1. Synthesis of ligands **ppy** and **mesppy** and racemic complexes ***rac*-Ir1** and ***rac*-Ir2**. Reagents and conditions. [a] 2.0 equiv. K_2CO_3, 5 mol% $Pd(PPh_3)_4$, N_2, 1,4-dioxane/H_2O (4:1 v/v), 105 °C, 56 h; [b] 2.0 equiv. K_2CO_3, 5 mol% $Pd(PPh_3)_4$, N_2, 1,2-dimethoxyethane/H_2O (4:1 v/v), 130 °C, 19 h; [c] 2-$EtOC_2H_4OH$/H_2O (4:1 v/v), 110 °C, N_2, 19 h. [d(1)] CH_2Cl_2/MeOH (2:1 v/v), 55 °C, 19 h, N_2; [d(2)] Excess solid NH_4PF_6.

Ligand ppy is commercially available and it was used as supplied. Ligand mesppy was prepared in high yield via Suzuki–Miyaura[281, 282] palladium-catalysed cross-coupling reactions following the protocols reported in the experimental section. The ppy and mesppy C^N ligands were complexed with $IrCl_3 \cdot 3H_2O$ and the resulting racemic μ-dichloro-bridged iridium dimers *rac*-$[Ir(ppy)_2Cl]_2$, ***rac*-D1** and $[Ir(mesppy)_2Cl]_2$, ***rac*-D2** were formed in good yield under standard conditions.[283] As reported in the experimental section (chapter

6), the racemic complexes ***rac*-Ir1** and ***rac*-Ir2** were isolated in high yield through cleavage of dimers ***rac*-D1** and ***rac*-D2**, respectively, with dtBubpy and subsequent anion metathesis with aqueous NH_4PF_6.

Following a previously reported protocol by Lusby and co-workers,[162] treatment of ***rac*-D1** and ***rac*-D2** with L-serine afforded the diastereomers Δ-[Ir(ppy)$_2$(L-serine)] and Λ-[Ir(ppy)$_2$(L-serine)] (respectively, **Δ-Lser1** and **Λ-Lser1** in **Scheme 2**) and Δ-[Ir(mesppy)$_2$(L-serine)] and Λ-[Ir(mesppy)$_2$(L-serine)] (respectively, **Δ-Lser2** and **Λ-Lser2** in **Scheme 2**).

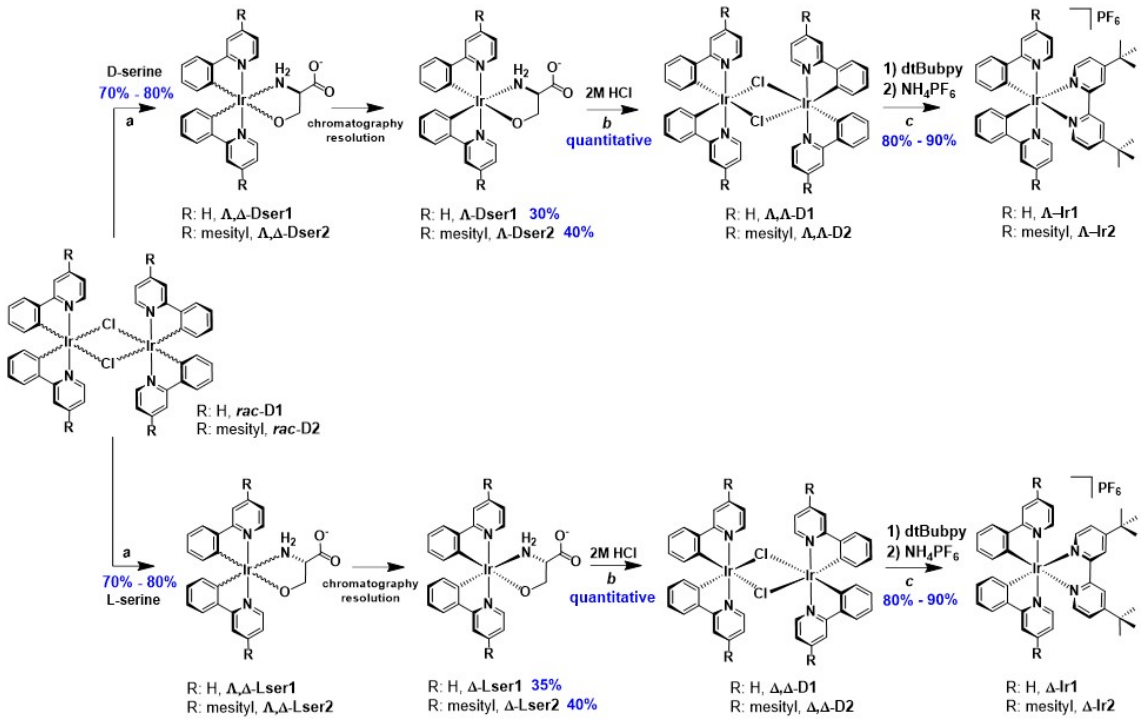

Scheme 2. Synthesis of enantiopure complexes **Λ, Δ-Ir1** and **Λ, Δ-Ir2**. Reagents and conditions: [a] CH_2Cl_2/MeOH (2:1 v/v), 1.2 equiv. C_2H_5ONa, 55 °C, 19 h, N_2; [b] MeOH/2M HCl_{aq} (2:1 v/v), 20 °C, 30 min; [c(1)] CH_2Cl_2/MeOH (2:1 v/v), 55 °C, 19 h, N_2; [c(2)] Excess solid NH_4PF_6. Yields for the enantioseparation step are isolated yields following chromatography resolution (maximum yield for each diastereomer = 50%).

By chromatographic purification on silica gel, we were able to obtain analytically pure only the first eluting diastereomers Δ-[Ir(C^N)$_2$(L-serine)] (**Δ-Lser1** and **Δ-Lser2**); the second lower mobility distereomers corresponding to Λ-[Ir(ppy)$_2$(L-serine)] and Λ-[Ir(mesppy)$_2$(L-serine)] were found to be contaminated respectively with traces of the **Δ-LSer1** and **Δ-LSer2**. Fortunately, following chromatographic resolution of the corresponding D-serine complexes, we obtained the analytically pure Λ-[Ir(C^N)$_2$(D-serine)] complexes as the first eluting bands (**Λ-DSer1** and **Λ-DSer2** in **Scheme 2**). The crude

^{1}H NMR spectra of ***rac*, Δ-Lser1** and Λ-**Dser1** and ***rac*, Δ-Lser2** and Λ-**Dser2** are reported in the appendix in **S43**,**S44**. Addition of a solution of 1M HCl to the Λ-, Δ-[Ir(C^N)$_2$(serine)] complexes yielded the enantiopure Λ,Λ- and Δ,Δ-[Ir(C^N)$_2$Cl]$_2$ dimers (**Λ,Λ-D1**, **Δ,Δ-D1** and **Λ,Λ-D2**, **Δ,Δ-D2**, **Scheme 2**). Finally, the enantiomers Λ-**Ir1** and Δ-**Ir1** were obtained, respectively, upon reaction of Λ,Λ- and Δ,Δ-[Ir(ppy)$_2$Cl]$_2$ dimers with dtBubpy following standard conditions, while the enantiomers Λ-**Ir2** and Δ-**Ir2** were obtained, respectively, by reacting the Λ,Λ- and Δ,Δ-[Ir(mesppy)$_2$Cl]$_2$ dimers with dtBubpy. The presence of the mesityl substituent in Λ-**Ir2** and Δ-**Ir2** facilitated the chromatographic resolution of the Λ- and Δ-serine complexes and consequently, Λ-**Ir2** and Δ-**Ir2** were obtained in slightly higher yields (ca. 40%) compared to Λ-**Ir1** and Δ-**Ir1** (ca. 30%). All complexes were purified by column chromatography and isolated as the PF_6^- salts following an anion metathesis reaction using NH_4PF_6.

The purity of the complexes was confirmed by ^{1}H- and ^{13}C-NMR, HRMS and melting point analyses (^{1}H-NMR spectra are illustrated in **Figure S46a,b** and **Figure S48a,b** in the appendix). The degree of enantiopurity and absolute configuration of Λ-**Ir1**, Δ-**Ir1**, Λ-**Ir2** and Δ-**Ir2** was confirmed by circular dichroism (CD) spectroscopy and X-ray crystal structure analyses, respectively. In addition, X-ray single crystal structures of the enantiopure Λ,Λ- and Δ,Δ-[Ir(ppy)$_2$Cl]$_2$ and Λ,Λ- and Δ,Δ-[Ir(mesppy)$_2$Cl]$_2$ dimers (**Λ,Λ-** and **Δ,Δ-D1** and **Λ,Λ-** and **Δ,Δ-D2**) and the racemic mixtures ***rac*-Ir1** and ***rac*-Ir2** were also obtained (^{1}H- and ^{13}C-NMR and HRMS spectra are reported in the appendix).

2.2.2 Crystal structures

The X-ray structures of the enantiopure dimers Λ,Λ- and Δ,Δ-[Ir(ppy)$_2$Cl]$_2$ (**Λ,Λ-D1** and **Δ,Δ-D1**) and Λ,Λ- and Δ,Δ-[Ir(mesppy)$_2$Cl]$_2$ (**Λ,Λ-D2** and **Δ,Δ-D2**) are shown in **Figure 49**, while the X-ray structures of the enantiopure complexes Λ-**Ir1**, Δ-**Ir1**, Λ-**Ir2** and Δ-**Ir2** are shown in **Figure 50**. The absolute configuration of the metal centres has been unambiguously determined by X-ray crystallography as Λ for the dimers **Λ,Λ-D1** and **Λ,Λ-D2** and the complexes Λ-**Ir1** and Λ-**Ir2**, and as Δ for the dimers **Δ,Δ-D1** and **Δ,Δ-D2** and the complexes Δ-**Ir1** and Δ-**Ir2**. Additionally, the enantiopurity of the complexes has been confirmed by CD spectroscopy (**Figure 50**).

In a similar manner to other [Ir(C^N)$_2$(N^N)]PF_6 complexes,[280, 284] in the structures of ***rac*-**, Λ- and Δ-**Ir1** and ***rac*-**, Λ- and Δ-**Ir2** the iridium center adopts a distorted-octahedral geometry with the two nitrogen atoms of the C^N ligands mutually trans to each other, and the two nitrogen atoms of the dtBubpy ligand disposed trans with respect to the carbon atoms of the C^N ligands. For all complexes both the Ir–C and Ir–N bond lengths, respectively of ca. 2.02 - 2.16 Å and 2.01 - 2.10 Å and the N-Ir-C and N-Ir-N bond angles respectively of ca. 80° and 76° fall in the range expected for [Ir(C^N)$_2$(N^N)]$^+$ complexes.[280, 284] Those complexes bearing mesppy as cyclometalating ligand (***rac*-**, Λ-

and **Δ-Ir2**), all display a nearly orthogonal orientation of the mesityl with respect to the pyridinato fragment. As expected, identical geometries are obtained between the two pairs of enantiomers (see geometrical parameters of complexes ***rac*-**, **Λ-** and **Δ-Ir1** and ***rac*-**, **Λ-** and **Δ-Ir2** in the appendix).

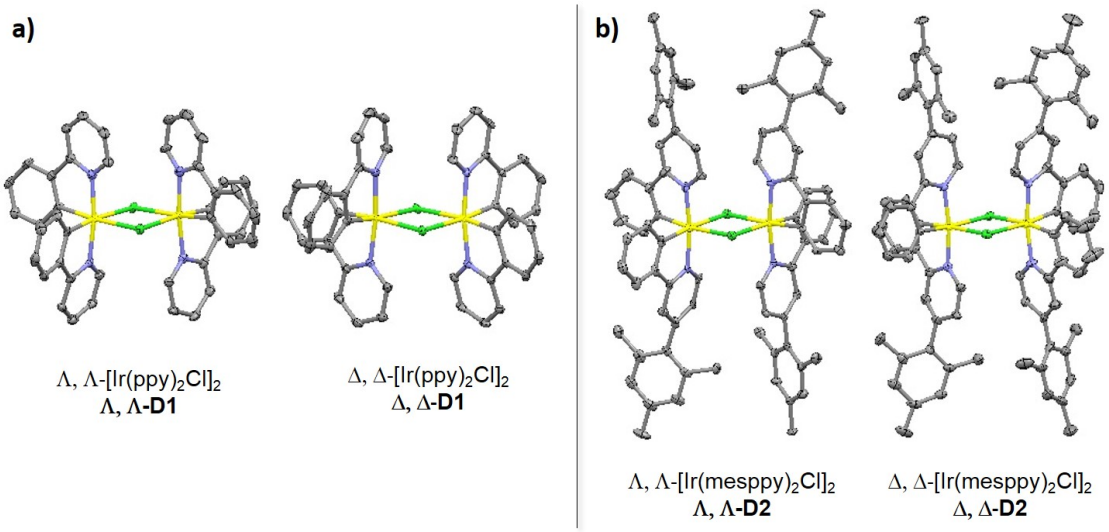

Figure 49. X-ray structures of enantiopure dimers; **a)** Λ,Λ- and Δ,Δ-$[Ir(ppy)_2Cl]_2$ (**Λ,Λ-** and **Δ,Δ-D1**); **b)** Λ,Λ- and Δ,Δ-$[Ir(mesppy)_2Cl]_2$ (**Λ,Λ-** and **Δ,Δ-D2**).

Figure 50 illustrates the crystallographic unit cells of ***rac*-Ir1**, **Λ-Ir1** and **Δ-Ir1**. The racemic complex ***rac*-Ir1** crystallises in the centrosymmetric space group $P2_1/n$ upon Et_2O diffusion into a 1,2-dichloroethane solution (**Figure 50a**). Both Λ- and Δ-$[Ir(ppy)_2(dtBubpy)]PF_6$ enantiomers **Λ-Ir1** and **Δ-Ir1** crystallise in the Sohncke space group $P2_12_12_1$ upon Et_2O diffusion into CH_2Cl_2 solutions (**Figure 51b,c**, respectively). The racemic mixture ***rac*-Ir1** shows a unit cell populated by equal amounts of both Λ and Δ enantiomers, where the molecules pack such that layers of molecules of the same enantiomer form in the (1 0 0) plane, and where molecules of the same enantiomer show a slightly longer shortest Ir···Ir distance than molecules of different enantiomers [7.9098(9) Å and 7.8973(9) Å, respectively]. A similar trend can be observed for the family of $[Ir(mesppy)_2(dtBubpy)]PF_6$ complexes (**Figure 52**). The racemate ***rac*-Ir2** crystallised in the centrosymmetric space group $I2/a$, and the two enantiomers **Λ-Ir2** and **Δ-Ir2** crystallised in the Sohncke space group $P2_1$ giving rise again to two unit cells related by inversion through the origin (**Figure 52b,c**). In contrast to the layered packing mode seen in ***rac*-Ir1**, the packing in the structure of racemic ***rac*-Ir2** shows a motif of alternating adjacent Λ and Δ enantiomers (**Figure 52a**). Again, the shortest Ir···Ir distance for molecules of the same enantiomer is greater than that for molecules of differing enantiomers, although in this case, the difference is more pronounced [11.8361(13) Å and 9.8691(7) Å, respectively].

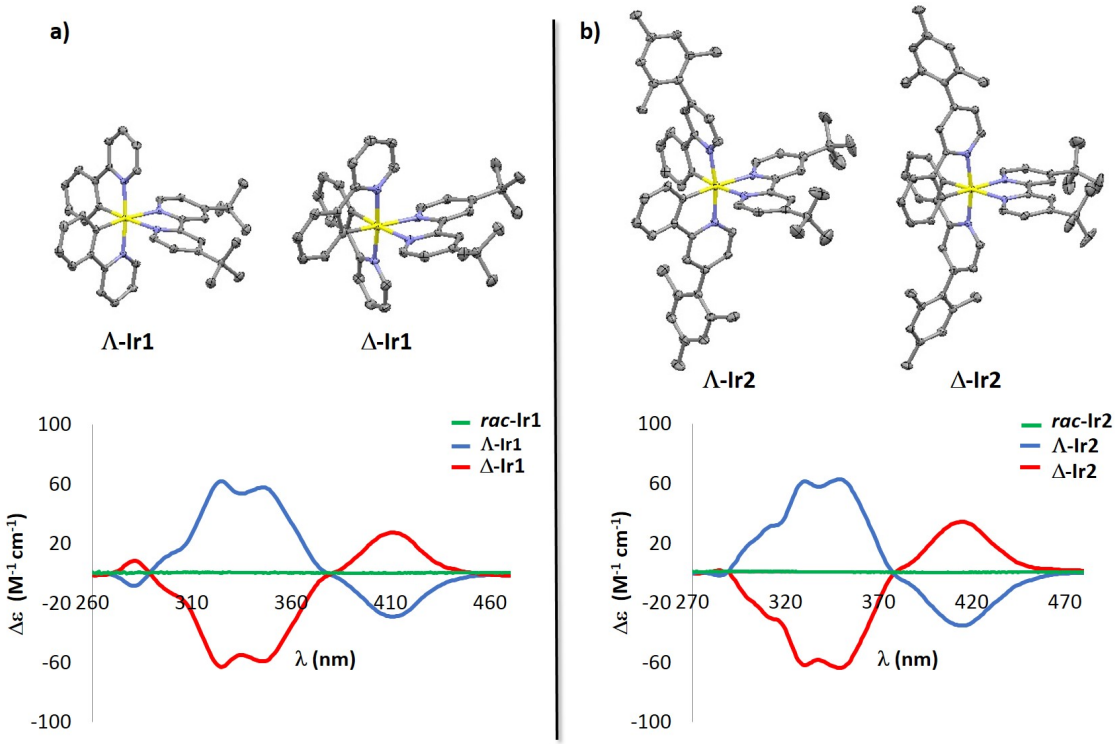

Figure 50. Molecular structures and CD spectra of **(a)** Λ-[Ir(ppy)$_2$(dtBubpy)]PF$_6$, **Λ-Ir1** and Δ-[Ir(ppy)$_2$(dtBubpy)]PF$_6$, **Δ-Ir1**, and **(b)** Λ-[Ir(mesppy)$_2$(dtBubpy)]PF$_6$, **Λ-Ir2** and Δ-[Ir(mesppy)$_2$(dtBubpy)]PF$_6$, **Δ-Ir2**. Hydrogen atoms, PF_6^- counterions, additional independent molecules of complex and solvent molecules have been omitted for clarity. CD spectra were collected in CH_2Cl_2 at 298 K at a concentration of 1 x 10^{-5} M. Green lines: CD spectra of **(a)** ***rac*-Ir1** and **(b)** ***rac*-Ir2**; light-blue lines: CD spectra of **(a)** **Λ-Ir1** and **(b)** **Λ-Ir2**; red lines: CD spectra of **(a)** **Δ-Ir1** and **(b)** **Δ-Ir2**.

The molecular packing in the solid state in all the complexes ***rac*-**, **Λ-** and **Δ-Ir1** and ***rac*-**, **Λ-** and **Δ-Ir2** is built up from a variety of weak interactions. None of the complexes, in either enantiopure or racemic structures, show strong intermolecular interactions, such as π-π stacking, in contrast to previously reported fluorinated analogue complexes.[280] The three structures of ***rac*-**, **Λ-** and **Δ-Ir1** all show very few intermolecular interactions between complex cations but more interactions between cation and anion. In the racemic ***rac*-Ir1**, edge-to-face CH···π interactions are seen [H···centroid distance 2.83 Å, C···centroid distance 3.684(14) Å], forming loosely interacting molecular dimers. These are linked together through weak CH···F hydrogen bonds to the PF_6^- anions [H···F distances 2.36 - 2.51 Å; C···F distances 3.122(13) - 3.386(14) Å], forming bilayer sheets in the (101) plane. The structure does pack with space available for included solvent molecules in channels running along the *b*-axis; however, probably due to solvent loss on handling the crystals, no solvent could be located in these channels. In contrast, both the enantiopure complexes **Λ-Ir1** and **Δ-Ir1** do not show the CH···π interaction, but they do show a similar formation of a weakly hydrogen-bonded bilayers, mediated by PF_6^- anions [H···F distances: **Λ-Ir1**

2.31 - 2.45 Å, **Δ-Ir1** 2.29 - 2.55 Å; C···F distances: **Λ-Ir1** 3.019(9) - 3.401(12) Å, **Δ-Ir1** 3.005(9) - 3.436(10) Å], in the (001) plane. These two structures also show narrow solvent channels, again running along the *b*-axis, containing the included dichloromethane solvent. None of the structures of ***rac*-**, **Λ-** and **Δ-Ir1** show any significant interactions between bilayer sheets. The three structures of ***rac*-**, **Λ-** and **Δ-Ir2** in turn show a different set of intermolecular interactions. In the racemic ***rac*-Ir2**, edge-to-face CH···π interactions are seen [H···centroid distance 2.88 Å, C···centroid distance 3.429(3) Å], forming loosely interacting molecular dimers. These are linked together through weak CH···F hydrogen bonds to the PF_6^- anions [H···F distances 2.50 - 2.53 Å; C···F distances 3.268(3) - 3.451(2) Å], forming double chains running along the *a*-axis. Like ***rac*-Ir1**, ***rac*-Ir2** does not contain solvent; however, it does not contain sufficient contiguous void space to contain solvent molecules, either. The total free space of 233 $Å^3$ arises from a combination of a number of smaller voids, likely arising from packing inefficiencies, scattered throughout the structure. The intermolecular interactions in enantiopure **Λ-Ir2** and **Δ-Ir2** are, in contrast, different to those seen in any of the structures of ***rac*-**, **Λ-** and **Δ-Ir1** and in racemic ***rac*-Ir2**. The cationic complexes form a network of multiple CH···π interactions [H···centroid distances: **Λ-Ir2** 2.68 - 2.94 Å, **Δ-Ir2** 2.67 - 2.94 Å; C···centroid distances: **Λ-Ir2** 3.447(9) - 3.861(11) Å, **Δ-Ir2** 3.443(5) - 3.855(7) Å], leading to the formation of two-dimensional sheets in the (001) plane. Surprisingly, the PF_6^- anions in **Λ-Ir2** and **Δ-Ir2** do not form any weak hydrogen bonds to the cations, but rather, they bond to the diethyl ether solvent molecules via further weak CH···π interactions to the cations. As was the case in ***rac*-Ir2**, **Λ-Ir2** and **Δ-Ir2**, both **Λ-Ir2** and **Δ-Ir2** show small packing inefficiencies, despite included solvent molecules, leading to some residual void space (**Λ-Ir2**: 56 $Å^3$, **Δ-Ir2**: 42 $Å^3$). The presence of the intermolecular interactions within the structures, as well as the size and shape of the complex cations themselves give rise to a range of short Ir···Ir distances in ***rac*-**, **Λ-**, **Δ-Ir1** and ***rac*-**, **Λ-**, **Δ-Ir2**, the distances for ***rac*-**, **Λ-**, **Δ-Ir2** being greater than those for ***rac*-**, **Λ-**, **Δ-Ir1**. In the case of both complexes, the enantiopure structures show almost identical separations: 8.4281(5) and 8.3944(7) Å for **Λ-Ir1** and **Δ-Ir1**, and 10.6642(8) Å for both **Λ-Ir2** and **Δ-Ir2**. In both the racemic complexes ***rac*-Ir1** and ***rac*-Ir2**, the Ir···Ir distance for the Λ-form and Δ-form is shorter than the distances seen in the enantiopure complexes; 7.8973(9) Å for **Λ-Ir1** and 9.8691(7) Å for **Λ-Ir2**. However, when the shortest Ir···Ir distance between complexes of the same stereochemistry within the racemic structure is considered, in ***rac*-Ir1** this distance is still shorter than the equivalent contact in **Λ-Ir1** or **Δ-Ir1**, at 7.9098(9) Å, but in **Λ-Ir1** this distance is the longest Ir···Ir separation seen in any of the six structures, at 11.8361(13) Å.

As expected, the solid-state interactions in the crystal packing of both pairs of enantiomers of both families **Λ-** and **Δ-Ir1** and **Λ-** and **Δ-Ir2** are identical and as a result, very similar solid-state photophysical properties are observed between the two enantiomers **Λ-Ir1**, **Δ-Ir1** and **Λ-Ir2**, **Δ-Ir2**. By contrast, the different crystal packing found for each of the two racemates ***rac*-Ir1** and ***rac*-Ir2** promote divergent solid-state properties compared

to their enantiopure analogues (**Table 1**).

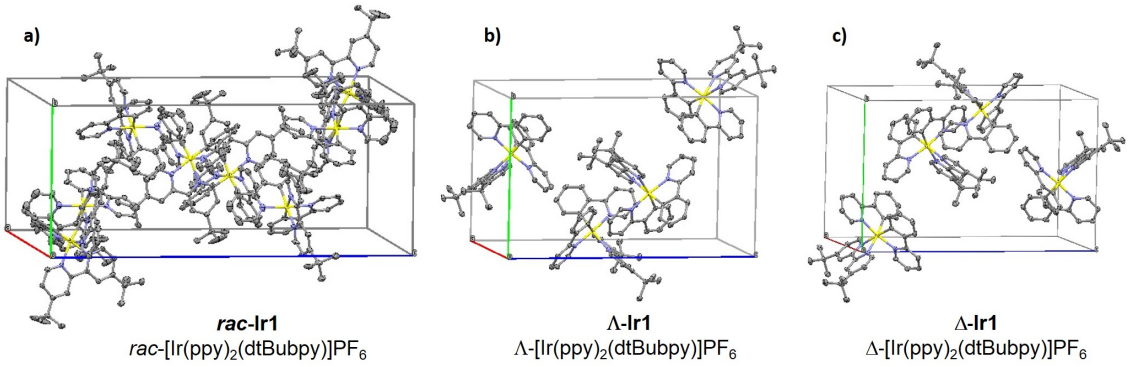

Figure 51. Views of the unit cells (whole molecules shown only) of **(a)** *rac*-[Ir(ppy)$_2$(dtBubpy)]PF$_6$, ***rac*-Ir1**; **(b)** Λ-[Ir(ppy)$_2$(dtBubpy)]PF$_6$, **Λ-Ir1**; and **(c)** Δ-[Ir(ppy)$_2$(dtBubpy)]PF$_6$, **Δ-Ir1**. Hydrogen atoms, PF_6^- counterions, and solvent molecules are omitted for clarity.

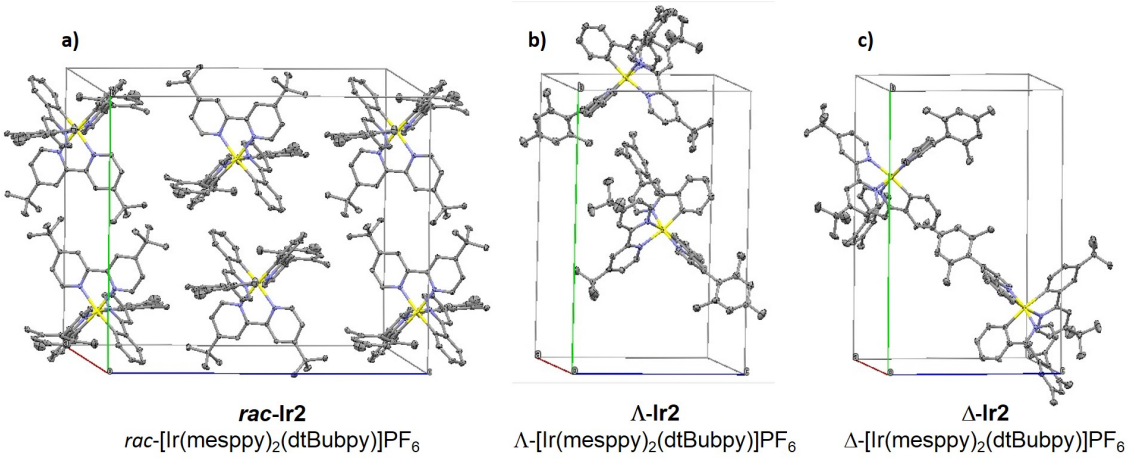

Figure 52. Views of the unit cells (whole molecules shown only) of **(a)** *rac*-[Ir(mesppy)$_2$(dtBubpy)]PF$_6$, ***rac*-Ir2**; **(b)** Λ-[Ir(mesppy)$_2$(dtBubpy)]PF$_6$, **Λ-Ir2**; and **(c)** Δ-[Ir(mesppy)$_2$(dtBubpy)]PF$_6$, **Δ-Ir2**. Hydrogen atoms, PF_6^- counterions, and solvent molecules are omitted for clarity.

2.3 Photophysical investigation

The optoelectronic properties of ***rac*-Ir1**, **Λ-Ir1** and **Δ-Ir1** and ***rac*-Ir2**, **Λ-Ir2** and **Δ-Ir2** have been investigated in CH_2Cl_2 solution and as spin-coated neat thin films and are summarised in **Table 1**. Upon excitation with unpolarised light, the absorption spectra

of ***rac*-Ir1**, Λ**-Ir1** and Δ**-Ir1** match with that previously reported for ***rac*-Ir1**.[285] As expected, no differences in the absorption properties between enantiopure and racemic analogues of both families of complexes **Ir1** and **Ir2** are observed (**Figure 53**).

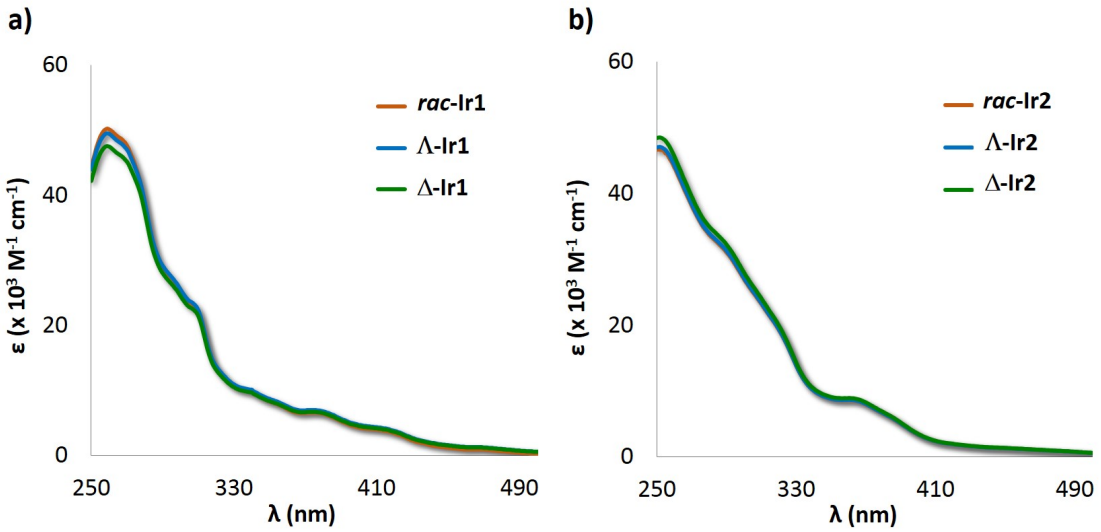

Figure 53. UV-Visible spectra of **(a)** ***rac*-Ir1** (orange line), Λ**-Ir1** (light-blue line) and Δ**-Ir1** (green line) and **(b)** ***rac*-Ir2** (orange line), Λ**-Ir2** (light-blue line) and Δ**-Ir2** (green line) collected in CH_2Cl_2 at 298 K.

The absorption spectra of all the complexes in CH_2Cl_2 are characterised by intense bands between 260 nm and 320 nm and broad lower intensity bands between 340 nm and 420 nm. Similar to many other cationic iridium complexes of the form $[Ir(C\hat{}N)_2(N\hat{}N)]^+$ found in the literature,[259, 280, 284, 285] the higher energetic bands can be attributed to the spin-allowed $^1\pi \rightarrow \pi^*$ ligand centered (^{1}LC) transitions localised on the C$\hat{}$N ligands, while the broad bands at wavelengths longer than 340 nm can be assigned to a mixture of spin-allowed and spin-forbidden metal-to-ligand charge transfer transitions (^{1}MLCT/^{3}MLCT). Indeed, as previously reported and predicted by TD-DFT calculations,[259, 284, 286] spin-forbidden transitions directly to the triplet state are accessible in iridium(III) complexes due to the large spin–orbit coupling exhibited by the heavy iridium atom. The presence of the mesityl moiety in ***rac*-**, Λ- and Δ**-Ir2** leads to slightly enhanced molar absorptivities in the UV region of the spectrum, the transition of which is assigned as ^{1}LC in nature, while also introducing an absorbing band at around 340–380 nm.

In CH_2Cl_2 solution, the emission properties of the enantiomers Λ**-Ir1**, Δ**-Ir1** and Λ**-Ir2**, Δ**-Ir2** match, respectively, those of their racemic analogues ***rac*-Ir1** and ***rac*-Ir2**, as would be expected (**Table 1**, **Figure 54**); the photophysical properties of ***rac*-Ir1** in CH_2Cl_2 solution also match those previously reported.[285] All complexes exhibited broad

emissions upon photoexcitation into the $^1\pi \rightarrow \pi^*$ bands at 360 nm, which implicates great ^{3}MLCT character. The solution emission maxima of ***rac*-**, Λ- and **Δ-Ir2** are not affected by the presence of the mesityl group, which is disposed in a nearly orthogonal and locked conformation with respect to the plane of the pyridine ring (**Figure 54b**). Thus, for ***rac*-**, Λ- and **Δ-Ir1** and ***rac*-**, Λ- and **Δ-Ir2**, the same yellow emissions at λ_{PL} = 577 nm are observed with similar Φ_{PL} values of 34 - 35% for ***rac*-**, Λ- and **Δ-Ir1** and 40 - 41% for ***rac*-**, Λ- and **Δ-Ir2**. The monoexponetial τ_{PL} of ***rac*-**, Λ- and **Δ-Ir1** in CH_2Cl_2 are slightly longer (***rac*-Ir1**: τ_{PL} = 877 ns; Λ- and **Δ-Ir1**: τ_{PL} = 811 ns) than those of ***rac*-**, Λ- and **Δ-Ir2** (***rac*-Ir2**: τ_{PL} = 757 ns; Λ- and **Δ-Ir2**: τ_{PL} = 765 ns) (**Table 1**).

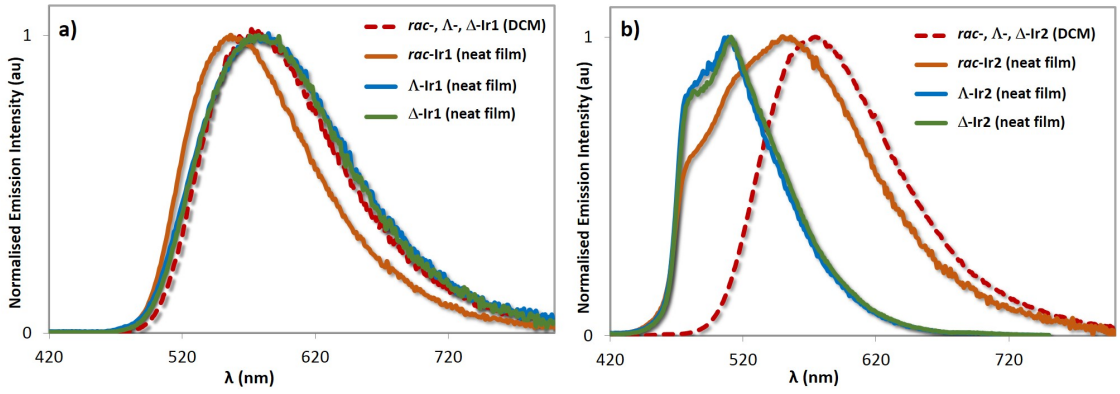

Figure 54. Dotted red lines: normalised photoluminescence spectra of **(a)** ***rac*-Ir1**, **Λ-Ir1** and **Δ-Ir1** and **(b)** ***rac*-Ir2**, **Λ-Ir2** and **Δ-Ir2** collected in degassed CH_2Cl_2 at 298 K; solid orange lines: normalised photoluminescence spectra of **(a)** ***rac*-Ir1** and **(b)** ***rac*-Ir2**; solid light-blue lines: normalised photoluminescence spectra of **(a) Λ-Ir1** and **(b) Λ-Ir2**; solid green lines: normalised photoluminescence spectra of **(a) Δ-Ir1** and **(b) Δ-Ir2**. All of the solid-state measurements were collected at 298 K on films formed by spin-coating deposition on pristine quartz substrate.

Differences of the emission properties between enantiomerically pure and racemic materials arise in the solid state. At this stage it is important to mention that each complex ***rac*-Ir1**, **Λ-Ir1**, **Δ-Ir1** and ***rac*-Ir2**, **Λ-Ir2** and **Δ-Ir2** was synthesised twice in order to confirm batch-to-batch reproducibility. Each of the complexes ***rac*-Ir1**, **Λ-Ir1**, **Δ-Ir1** and ***rac*-Ir2**, **Λ-Ir2** and **Δ-Ir2** was dissolved in 2-methoxyethanol (HPLC grade at a concentration of 5 mM) and the solutions were spin-coated (at 2000 rpm for 1 minute) onto quartz substrates forming four thin films per complex. The emission properties of the complexes were then evaluated from four films ensuring measurement reproducibility and statistically relevant analysis. A detailed explanation about the protocols followed for sample preparation and photophysical measurements, including instrumental errors affecting the measurements are given in the experimental section (Chapter 6).

As shown in **Figure 54a**, the neat film emission of the racemate ***rac*-Ir1** is blue-shifted

(λ_{PL} = 560 nm) compared to the emission of the Λ and Δ enantiomers **Λ-Ir1** and **Δ-Ir1**, both of which emit at λ_{PL} = 582 nm. The racemate ***rac*-Ir1** showed a higher Φ_{PL} of 38.0% coupled with a longer biexponential emission lifetime (τ_{PL} = 455 ns, 779 ns) compared to **Λ-Ir1** and **Δ-Ir1**, both of which showed nearly identical photophysical properties and multiexponential decay kinetics (for **Λ-Ir1**: Φ_{PL} = 31.3% and τ_{PL} = 58 ns, 157 ns, 644 ns; for **Δ-Ir1**: Φ_{PL} = 29.8% and τ_{PL} = 42 ns, 173 ns, 622 ns, **Table 1**). Divergent solid-state photophysical properties between the racemate ***rac*-Ir2** and the enantiomers **Λ-Ir2** and **Δ-Ir2** are also observed (**Table 1**). Indeed, the broad emission profile at ca. 550 nm of the racemate ***rac*-Ir2** is distinct compared to the more structured and blue-shifted emission (λ_{PL} = 480 and 511 nm) present for the enantiomers **Λ-Ir2** and **Δ-Ir2** (**Figure 54b**). Furthermore, the Φ_{PL} of 18.2% for ***rac*-Ir2** in the solid-state is considerably lower than that for **Λ-Ir2** (Φ_{PL} = 39.8%) and **Δ-Ir2** (Φ_{PL} = 40.7%). The multiexponential emission lifetime for ***rac*-Ir2** of 25, 211, 672 ns is significantly shorter than the biexponential emission lifetime behaviour determined for **Λ-Ir2** (τ_{PL} = 405 ns, 923 ns) and **Δ-Ir2** (τ_{PL} = 411 ns, 940 ns). The solid-state lifetime decays are illustrated in the appendix.

Table 1. Relevant photophysical data for ***rac*-**, Λ- and **Δ-Ir1** and ***rac*-**, Λ- and **Δ-Ir2**

	λ_{PL} (nm)[a,b]		Φ_{PL} (%)[d]		τ_{PL} (ns)[a]	
	DCM[a]	film[b,c]	DCM[d]	film[c,e]	DCM	film[c,f]
***rac*-Ir1**	577	560	35	38.1	877	455 (0.30), 779 (0.70)
Λ-Ir1	577	582	34	31.3	811	58 (0.05), 322 (0.35), 693 (0.70)
Δ-Ir1	577	582	34	29.8	811	42 (0.04), 291 (0.29), 698 (0.60)
***rac*-Ir2**	577	478 (0.6), 516 (0.9), 550 (1.0)	40	18.2	757	25 (0.06), 211 (0.42), 672 (0.52)
Λ-Ir2	577	480 (0.8), 511 (1.0)	41	39.8	765	405 (0.47), 923 (0.53)
Δ-Ir2	577	479 (0.8), 511 (1.0)	41	40.7	765	411 (0.47), 940 (0.53)

[a]Measurements in degassed CH_2Cl_2 at 298 K (λ_{exc} = 360 nm). [b]Principal emission peaks listed with values in parentheses indicating relative intensity (λ_{exc} = 378 nm). [c]Thin films formed by spin-coating on a pristine quartz substrate. [d]Φ_{PL} measurements were carried out in degassed CH_2Cl_2 under nitrogen (λ_{exc} = 360 nm) using quinine sulfate as the external reference (Φ_{PL} = 54.6% in 0.5 M H_2SO_4 at 298 K).[287] [e]Values obtained using an integrating sphere. [f]Values in parentheses are pre-exponential weighting factor, in relative % intensity, of the emission decay kinetics (λ_{exc} = 378 nm).

From the emission properties of both families of complexes **Ir1** and **Ir2**, the species that emits at higher energy (***rac*-Ir1** for family **Ir1** and both enantiomers **Λ-Ir2** and **Δ-Ir2** for family **Ir2**) also show the highest Φ_{PL} and the longest average $\tau_{\mathbf{PL}}$. However, no consistent correlation between these properties and the crystal packing of these materials has been observed. Indeed, for both families of complexes, the racemates ***rac*-Ir1** and ***rac*-Ir2** show the shortest Ir···Ir intermolecular distances (7.8973(9) Å for ***rac*-Ir1** and 9.8691(7) Å for ***rac*-Ir2**) compared to the corresponding enantiopure analogues **Λ-Ir1**, **Δ-Ir1** and **Λ-Ir2** and **Δ-Ir2** (respectively, 8.4281(5) and 8.3944(7) Å for **Λ-Ir1** and **Δ-Ir1** and 10.6642(8) Å for both **Λ-Ir2** and **Δ-Ir2**). While for ***rac*-Ir1**, a slightly blue-shifted emission with higher Φ_{PL} is observed compared to **Λ-Ir1** and **Δ-Ir1**, the opposite behavior is noted for the racemate ***rac*-Ir2**, where its emission is red-shifted and lower in intensity compared to both enantiomers **Λ-Ir2** and **Δ-Ir2** (**Table 1**). It is worth pointing out that the neat films of ***rac*-**, **Λ-** and **Δ-Ir1** and ***rac*-**, **Λ-** and **Δ-Ir2** were prepared by spin-coating deposition from a 2-methoxyethanol solution of the samples and therefore differences in the packing found in the single crystals and the amorphous films may account for the differences observed between the two families of complexes.

2.4 Light-Emitting Electrochemical Cells

Double-layer LEEC devices have been prepared using the racemic and the Λ and Δ enantiomers from both families of complexes. Devices were prepared on cleaned patterned glass-ITO (indium tin oxide) substrates elaborated with a spin-coated, thin layer (80 nm) of poly(3,4-ethylenedioxythiophene):polystyrenesulfonate (PEDOT:PSS). On top of this a 100 nm thick complex:ionic liquid (IL) (4:1 molar ratio) film has been deposited from an acetonitrile solution (20 mg·mL^{-1}), where the IL employed is 1-butyl-3-methylimidazolium hexafluorophosphate, BMIM-PF_6. The IL was added to reduce the turn-on time of the LEEC due to the increase in the concentration of ionic species and the ionic mobility.[288, 289] The substrates were annealed under an N_2 atmosphere at 100 °C over 1 h. Thermal evaporation of a 70 nm thick aluminum electrode under a base pressure of 2 x 10^{-6} mbar completes the device. LEECs fabricated with the complexes ***rac*-**, **Λ-** and **Δ-Ir1** and ***rac*-**, **Λ-** and **Δ-Ir2** will be referred as LEECs ***rac*-**, **Λ-** and **Δ-Ir1** and ***rac*-**, **Λ-** and **Δ-Ir2**, respectively. For each device configuration at least two substrates (from two freshly prepared batches of the same complex) each containing 4 individual cells were evaluated ensuring a statistically relevant analysis. The luminance and voltage vs time dependence of the LEECs ***rac*-**, **Λ-** and **Δ-Ir1** and ***rac*-**, **Λ-** and **Δ-Ir2** are shown in **Figure 55a,b**. Performance metrics for these devices are summarised in **Table 2**.

Both families present different characteristics under pulsed-current density driving but

all devices exhibit the typical LEEC behavior: the luminance increases until a maximum is reached and then starts to decrease while the operating voltage rapidly decays at the beginning of operation, reaching a minimum at values in the range of 2.4-2.7 V, indicating that the barrier for electron and hole injection is effectively removed by the ion migration. Interestingly, once this state is achieved, the voltage follows different behaviour depending on the family of complexes incorporated in the device. The LEECs ***rac*-**, **Λ-** and **Δ-Ir1** show a constant steady-state voltage whereas the LEECs ***rac*-**, **Λ-** and **Δ-Ir2** show a slow increase of the voltage. This increase of the layer resistance could be an indication of chemical degradation under operation.[290] The turn-on time (t_{on}) of the devices, defined as the time to reach 100 cd·m^{-2} luminance, is near instantaneous (<2 s) except for LEECs ***rac*-** and **Λ-Ir1**, where turn-on times vary from 80 to 200 s, respectively. The time required to reach 100 cd·m^{-2} luminance is likewise strongly complex-dependent. Despite containing less mobile complexes due to their larger size, LEECs ***rac*-**, **Λ-** and **Δ-Ir2** show faster response than LEECs ***rac*-**, **Λ-** and **Δ-Ir1**. This behaviour is attributed to the presence of the mesityl substituents, which induce a more efficient electronic communication and more rapid charge hoping and recombination kinetics, resulting in faster turn-on time for the devices fabricated using complexes ***rac*-**, **Λ-** and **Δ-Ir2**.

Table 2. LEECs performances data under pulsed-current operation (average current density 50 A·m^{-2}, 1000 Hz, 50% duty cycle, block wave)

	$\mathbf{lum_{max}}$ (cd·m^{-2})[a]	$\mathbf{t_{on}}$ (s)[b]	$\mathbf{t_{1/2}}$ (h)[c]	$\mathbf{EQE_{max}}$ (%)[d]	$\lambda_{\mathbf{EL,max}}$ (nm)	CIE[e]
***rac*-Ir1**	571	800	> 1300	3.5	575	(0.4898, 0.5021)
Λ-Ir1	435	200	> 700	2.8	573	(0.4809, 0.5095)
Δ-Ir1	394	< 2	> 400	2.6	574	(0.4820, 0.5091)
***rac*-Ir2**	224	< 2	0.6	1.4	572	(0.4715, 0.5166)
Λ-Ir2	398	< 2	5.2	2.5	574	(0.4718, 0.5120)
Δ-Ir2	432	< 2	22	2.7	568	(0.4568, 0.5293)

[a]Maximum luminance reached. [b]Time to reach 100 cd·m^{-2} luminance. [c]Time to reach one-half of the maximum luminance. [d]Maximum external quantum efficiency reached. [e]The Commission Internationale de l'*Éclairage* (CIE) color coordinates.

The lifetime ($t_{1/2}$), defined as the time to reach one-half of the maximum luminance, is used to evaluate the device stability. The LEECs fabricated with ***rac*-**, Λ- and **Δ-Ir1** are more stable with significantly higher lifetime compared to the LEECs based on the family ***rac*-**, Λ- and **Δ-Ir2**. At this point, it is worth highlighting that the $t_{1/2}$ could not be determined during the lifetime test of the LEECs ***rac*-**, Λ- and **Δ-Ir1**. However, an estimated lifetime value can be determined by extrapolation, thereby obtaining $t_{1/2}$ longer than 1300 h for device ***rac*-Ir1**, 700 h for **Λ-Ir1**, and 400 h for **Δ-Ir1** (**Figure 55a)**. A direct comparison with previous LEECs reported for complex ***rac*-Ir1** is complicated due to the driving mode used in this work. Pulsed current driving is well-known to improve the device stability with respect to traditional constant-voltage driving. The lifetime found here for the LEEC ***rac*-Ir1** is in the same range to other very stable and efficient orange LEECs with lifetimes ranging from 2000 to 3000 h.[291, 292] In the case of devices ***rac*-**, Λ- and **Δ-Ir2**, the lifetime follows the opposite trend. The lifetime for ***rac*-Ir2** is less than 1 h, for **Λ-Ir2** it is 5.2 h, and **Δ-Ir2** it is 22 h (**Figure 55b**). The lifetime differences observed here could be understood by the device response and voltage behaviour described above. On the one hand, the faster response of LEECs ***rac*-**, Λ- and **Δ-Ir2** leads to a faster growth of the doped regions, which increase the exciton-quenching efficiency over time. On the other hand, the increase of the voltage over time of devices ***rac*-**, Λ- and **Δ-Ir2** is an indication of material degradation during device operation. Hence, both characteristics negatively influence the lifetime of LEECs ***rac*-**, Λ- and **Δ-Ir2**.

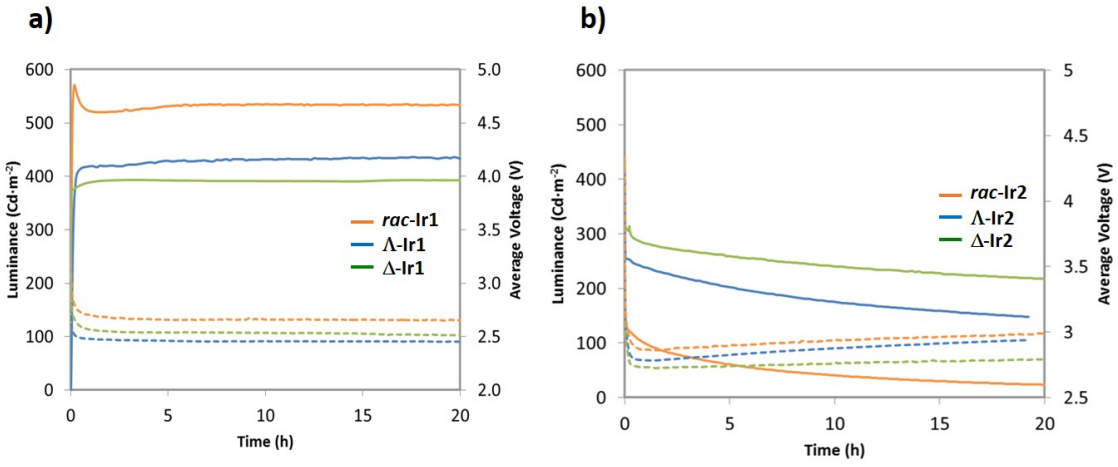

Figure 55. Time-dependent luminance (solid line) and operating voltage (dashed line) data of LEECs driven under pulsed-current operation with an average current density of 50 $A{\cdot}m^{-2}$ (1000 Hz, 50% duty cycle, block wave) using complexes **(a)** ***rac*-**, Λ- and **Δ-Ir1** and **(b) (a)** ***rac*-**, Λ- and **Δ-Ir1** as emitters.

A LEEC device was previously prepared by using $[Ir(ppyPh)_2(dtBubpy)]PF_6$ as the emitter (ppyPh = 2-(3- phenylphenyl)pyridinato) where this iridium complex is function-

alised with a phenyl ring at the 5-position of the phenyl ring of the C^N ligands.[293] Employing this Ir complex resulted in a very bright and stable device (lum_{max} = 1090 cd·m^{-2} and $t_{1/2}$ = 437 h). Thus, the regiochemistry of aryl substitution on the C^N ligands has a dramatic effect on the overall device performance.

Interestingly, the LEECs employing the Λ and Δ enantiomers show different device luminance and device efficiency (EQE) compared to the LEEC using the respective racemic mixtures. LEEC ***rac*-Ir1** shows a maximum luminance of 570 cd·m^{-2}, which corresponds to an EQE of 3.5%. LEECs **Λ-Ir1** and **Δ-Ir1**, by contrast, exhibit lower performance in both cases (for **Λ-Ir1**; lum_{max}: 435 cd·m^{-2} and EQE: 2.8%; **Δ-Ir1**: lum_{max}: 394 cd·m^{-2} and EQE: 2.6%). In the case of LEEC ***rac*-Ir2**, the maximum luminance is 224 cd·m^{-2}, which corresponds to an EQE 1.4%, while LEECs **Λ-Ir2** and **Δ-Ir2** show considerable improvement in performance compared to ***rac*-Ir2**. Specifically, the maximum luminance and EQE were respectively 398 cd·m^{-2} and 2.5% for LEEC **Λ-Ir2** and 432 cd·m^{-2} and 2.7% for LEEC **Δ-Ir2**. The efficiency trend for each family of complexes is in line with the Φ_{PL} obtained for the thin films (**Table 1**) described above. Indeed, for both the photoluminescence and electroluminescence measurements the racemic mixture ***rac*-Ir1** exhibited an enhanced emission intensity when comparing to the two enantiomers **Λ-Ir1** and **Δ-Ir1**, while the enantiomers **Λ-Ir2** and **Δ-Ir2** exhibited enhanced emission intensities when comparing to the racemate ***rac*-Ir2**. Surprisingly, despite the two pairs of enantiomers of each family of complexes **Λ-Ir1** and **Δ-Ir1** and **Λ-Ir2** and **Δ-Ir2** exhibited between themselves almost identical photophysical properties in thin films (**Table 2**), their LEEC device performances were somehow different. For example, LEEC device fabricated with **Λ-Ir1** exhibited a lum_{max} of 435 cd·m^{-2} with a lifetime of > 700 h, while LEEC device fabricated with **Δ-Ir1** exhibited a reduced lum_{max} of 394 cd·m^{-2} with a shorter lifetime of > 400 h. LEEC device fabricated with **Δ-Ir2** exhibited a lum_{max} of 432 cd·m^{-2} with a lifetime of 22 h, whereas LEEC device fabricated with **Λ-Ir2** exhibited a reduced lum_{max} of 398 cd·m^{-2} with a shorter lifetime of 5.2 h. The differences observed when compared the device performances between **Λ-Ir1** and **Δ-Ir1** and **Λ-Ir2** and **Δ-Ir2** are surprising considering that the two pairs of enantiomers were expected to exhibit similar device efficiency. However, As the Φ_{PL} values in the neat film were somewhat comparable for each pair of enantiomers and significantly different for the racemic mixture, the differences observed should be related to different packing and aggregation in the thin film when comparing pure enantiomers with racemic mixture, despite the addition of IL in the emissive layer of the EL device. However, this effect is rather dependent on the family studied. On the one hand, in view of the lower Φ_{PL} of ***rac*-Ir2**, the presence of the mesityl groups induces in thin film the complex to aggregate more in the racemic mixture compared to the enantiopure compounds (**Λ-Ir2** and **Δ-Ir2**). On the other hand, for the family ***rac*-**, **Λ-** and **Δ-Ir1**, the enantiopure compounds (**Λ-** and **Δ-Ir1**) show in thin film a higher predisposition to aggregate, suggested by their lower Φ_{PL}. These observations are also supported by the differences in the photoluminescence emission discussed above (**Figure 54** and **Table 1**),

where the complex Λ- and Δ-**Ir1** as well as ***rac*-Ir2** show a red shifted emission with respect to ***rac*-Ir1** and Λ- and Δ-**Ir2**, respectively.

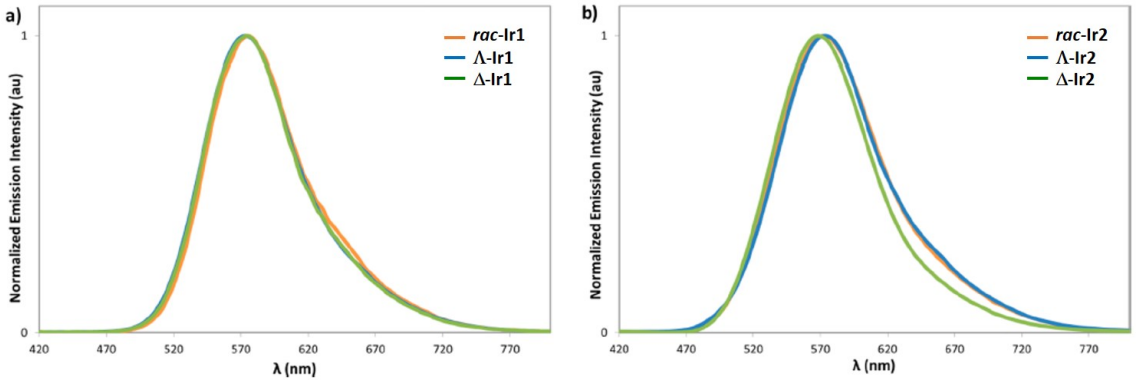

Figure 56. Electroluminescence spectra of LEECs **(a)** ***rac*-Ir1**, Λ-**Ir1** and Δ-**Ir1** and **(b)** ***rac*-Ir2**, Λ-**Ir2** and Δ-**Ir2**.

The electroluminescence (EL) spectra are depicted in **Figure 56**. The Commission Internationale de l'*É*clairage (CIE) color coordinates (see **Table 2**) of the compounds were determined from the respective electroluminescence spectra. The CIE color coordinates of compounds ***rac*-Ir1**, Λ-**Ir1** and Δ-**Ir1** are (0.4898, 0.5021), (0.4809, 0.5095), and (0.4820, 0.5091). For the family **Ir2**, the CIE color coordinates are (0.4715, 0.5166) for ***rac*-Ir2**, (0.4718, 0.5122) for Λ-**Ir2**, and (0.4568, 0.5293) for Δ-**Ir2**. All CIE coordinates correspond to orange emission. The EL spectra of LEECs ***rac*-Ir1**, Λ-**Ir1** and Δ-**Ir1** exhibit a single band with maxima emission wavelength of 575, 573, and 574 nm, respectively. A single band is also observed for LEECs ***rac*-Ir2**, Λ-**Ir2** and Δ-**Ir2**, where the maximum emission wavelengths are respectively at 572 nm, 574 nm, and 568 nm. Hence, all six complexes exhibit similar maximum EL peak, which is red-shifted with respect to the PL emission peak, except for complex Λ-**Ir1** and Δ-**Ir1**, which are slightly blue-shifted. Incorporation of the mesityl group does not significantly impact the emission colour in the device, which is a behaviour distinct to that observed in the neat film PL where mesityl substitution promotes a significant blue-shifting in the neat film (**Figure 54**).

2.5 Conclusions

In this chapter we have reported the preparation, the crystal structures, and the photophysical properties in neat thin film of two families of iridium(III) complexes of the form of $[Ir(C^{\wedge}N)_2(dtBubpy)]PF_6$ in both their racemic and Λ, Δ enantiopure isomers. For both families of complexes, mirrored crystal unit cells and similar solid-state photophysical properties exist between the Λ and Δ enantiomers. However, the photophysical properties

of the enantiomers are different compared to the racemic analogues. LEEC devices have been fabricated using the Λ and Δ enantiomers as well as the racemic analogues of both families, and reflecting the different photophysical properties in the solid state, different device performance have been achieved. Depending on the particular iridium complex family evaluated, we see positive and negative effects when employing enantiopure complexes in LEECs. Among the family of complexes ***rac-***, **Λ-** and **Δ-**[Ir(ppy)$_2$(dtBubpy)]PF$_6$ (***rac-***, **Λ-** and **Δ-Ir1**), the racemate ***rac*-Ir1** exhibited the highest solid-state Φ_{PL} and the best LEEC performances while, by contrast, among the family of complexes ***rac-***, **Λ-** and **Δ-**[Ir(mesppy)$_2$(dtBubpy)]PF$_6$ (***rac-***, **Λ-** and **Δ-Ir2**), the highest solid-state Φ_{PL}, LEEC luminance and EQE are exhibited by the enantiomers **Λ-** and **Δ-Ir2**. The change in the solid-state photoluminescent properties and device behaviour are attributed to differences in solid-state film morphology due to different packing of the two complex families. In this context, the investigation of the thin film morphology by atomic force microscopy with and without the addition of ionic liquid could provide important insight into the quality of the films and the solid-state packing of the complexes, and may help to understand the differences observed in the photoluminescence and electroluminescence properties between enantiopure and racemic emitters. This study reveals the importance and the complexity that enantiopurity plays on the performance of LEEC devices.

Chapter 3

Phosphorescent Iridium(III) and Ruthenium(II) Supramolecular Cages

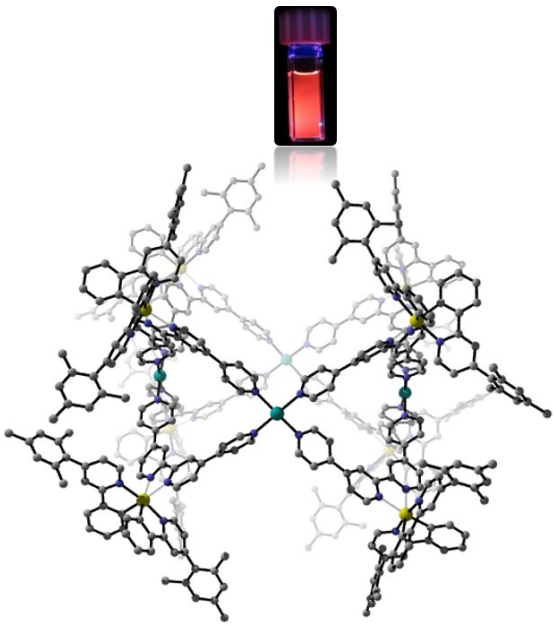

$[Ir_8Pd_4]^{16+}$

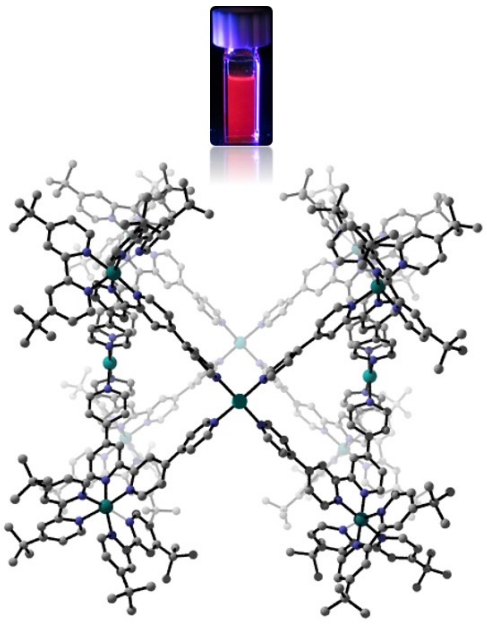

$[Ru_8Pd_4]^{24+}$

3.1 Introduction

Coordination cages, also referred to as metallosupramolecular cages, are 3-D assemblies of metal ions and bridging ligands that exhibit nano-sized structures.[138, 294] During the past two decades coordination-driven self-assembly has rapidly matured as a powerful approach for the construction of discrete 2-D metallomacrocycles and 3-D metallocages and capsules with well-defined shapes, geometries and cavities.[294, 295] In this context, the groups of Lehn,[296] Stang,[140, 297] Fujita,[298, 299] Raymond,[300, 301] Newkome[302, 303] and others[304–307] have succesfully pioneered a number of methodologies to construct numerous metallosupramolecular architectures. They have shown that the relatively strong and highly directional metal-ligands bonds can program the coordination-driven self-assembly process towards defined shapes and topology of the resultant structures, frequently in high yields and short reaction times. As introduced in the first chapter, the self-assembly between palladium(II) or platinum(II) metal ions and ligands containing specifically positioned distal pyridine moieties, first demonstrated by Fujita and co-workers,[308] is one of the most popular and successful strategies to prepare molecular cages and capsules.[309, 310] The first example of a molecular cage was a small $[M_6L_4]^{12+}$ tetrahedron[308] where M is either Pd(II) or Pt(II) metal ions located at each vertex of the tetrahedron and L is a bridging ligand, specifically the elctron-poor 2,4,6-tris(pyridin-4-yl-1,3,5-triazine) (tpt), spanning each of the six edges. More recently, by assembling bis-pyridyl bridging ligands characterised by extended curvatures with Pd^{2+} ions, large $[Pd_{12}L_{24}]^{24+}$,[53] $[Pd_{24}L_{48}]^{48+}$[298] and huge $[Pd_{30}L_{60}]^{60+}$[52] "nanospheres" have been rationally designed (**Figure 57**). Such cages represent a fascinating synthetic challenge as they illustrate how, with careful control of the bridging ligand geometry and the type of metal ion, remarkably elaborate and highly symmetric structures can be successfully formed by self-assembly from simple components.

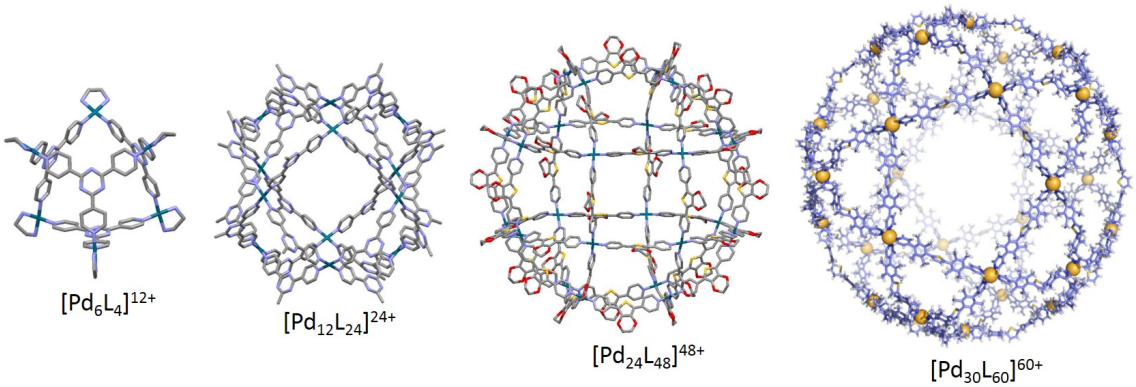

Figure 57. X-ray structures of cage $[Pd_6L_4]^{12+}$ and nanospheres $[Pd_{12}L_{24}]^{24+}$, $[Pd_{24}L_{48}]^{48+}$ and $[Pd_{30}L_{60}]^{60+}$, respectively from left to right.

As the field of coordination cage assembly has matured, the focus has more recently shifted increasingly towards the design of cages with defined function and the investigation of their properties.[311, 312] Small guest molecules have been shown to be selectively sequestrated inside the cavities of these cages and their host-guest interactions have been exploited in diverse applications such as "artificial enzyme" catalysis,[139, 313] for hazardous chemical capture and reactive intermediate stabilization,[314, 315] for drug delivery and release,[316, 317] as well as in molecular sensing[318, 319] and biology.[320] The functional properties of these cages are frequently derived from the incorporation of functional groups into the organic building blocks.[65, 311] For example, Stang and co-workers have successfully introduced various functional moieties, such as ferrocene,[321] crown-ether[322] and dendrons[323] at the vertex of building blocks, which enabled the construction of a series of functional metallomacrocycles. Lutzen and co-workers[324] introduced 2,2′-dihydroxy-1,1′-binaphtyl (BINOL) as chiral units into molecular cages of composition $[Pd_4L_8]^{8+}$, $[Pd_6L_{12}]^{12+}$ and $[Pd_{12}L_{24}]^{24+}$. Yoshizawa and co-workers[325] introduced electro- and magneto-chemical dihydrophenazine derivatives that can form stable radical cations by single-electron oxidation under ambient conditions into cage compounds of the composition of $[Pd_2L_4]^{4+}$. Clever and co-workers[326] have also reported a series of $[Pd_2L_4]^{4+}$ coordination cages, but featuring endohedral functionalities consisting of two electron-withdrawing substituents (CO_2R and/or CN) attached to an electron-rich backbone via a double bond that behave as push-pull molecular rotors.

A recent area of considerable interest is the design and development of photoactive cages and capsules in which at least one component, either the metal ion or the bridging ligand, is luminescent.[64, 65] Incorporation of fluorescent emitters such as porphyrins[66] and BODIPYs[318] and π-conjugated organic compounds[327, 328] into the ligand backbone of cages and macrocycles have been explored to give rise to fluorescent cages and macrocycles. As discussed in the first chapter, supramolecular cages incorporating phosphorescent iridium(III) and ruthenium(II) complexes have also started to become increasingly popular, but as yet much less studied compared to fluorescent cages. Importantly, phosphorescent cages provide both a high concentration of phosphors in fixed dispositions and known orientations, and restricted shape and size to govern the photophysics of the host-guest interactions. This immediately generates many interesting possibilities for applications such as sensing and photocatalysis involving bound guests that can photophysically interact with the emitting hosts.

3.1.1 Chapter outline

This chapter discusses the preparation, characterisation and photophysical properties of phosphorescent iridium(III) and ruthenium(II) supramolecular cages of the general composition of $[M_8Pd_4]^{n+}$ (M is either Ir or Ru). The iridium cages are formed through

the self-assembly of Pd^{2+} ions with racemic and enantiopure iridium metalloligands of the composition of $[Ir(C^{\wedge}N)_2(qpy)]^+$ (where C^N is mesppy: 2-phenyl-4-mesitylpyridinato in ***rac-***, **Λ-** and **Δ-Ir3** and dFmesppy: 2-(4,6- difluorophenyl)-4-mesitylpyridinato in ***rac-***, **Λ-** and **Δ-Ir4**, and qpy is 4,4′:2′,2″:4″,4‴-quaterpyridine) through N_{py}-Pd coordination, while the ruthenium cages are formed by reacting Pd^{2+} ions with the racemic ruthenium metalloligand $[Ru(dtBubpy)_2(qpy)]^{2+}$, **Ru1**. The chemical structures of the Ir and Ru metalloligands are illustrated in **Figure 58**. The first part of this chapter describes the self-assembly and photophysical properties of cages based on the iridium metalloligands ***rac-***, **Λ-** and **Δ-Ir3** and ***rac-***, **Λ-** and **Δ-Ir4**, whereas the self-assembly of the ruthenium complex **Ru1** with Pd^{2+} ions is described afterwards.

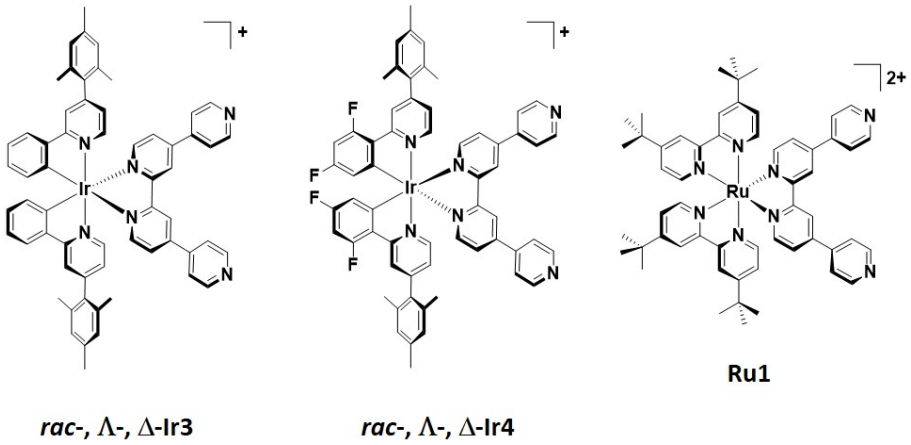

Figure 58. Chemical structures of the iridium metalloligands ***rac-***, **Λ-** and **Δ-Ir3** and ***rac-***, **Λ-** and **Δ-Ir4** and ruthenium metalloligand **Ru1** used for self-assembly.

3.2 Homochiral Emissive Λ_8- and Δ_8-$[Ir_8Pd_4]^{16+}$ Supramolecular Cages

3.2.1 Synthesis of racemic and enantiopure $[Ir(C^{\wedge}N)_2(qpy)]BF_4$ complexes

The synthesis of the mesppy C^N ligand and racemic dimer ***rac*-D2** follows that illustrated in **Scheme 1** (chapter 2). The fluorinated dFmesppy C^N ligand was prepared by reacting 2-chloro-4-(2,4,6-trimethylphenyl)pyridine with 2,4-difluorphenyl boronic acid *via* Suzuki–Miyaura palladium-catalysed cross-coupling reaction.[278] The racemic iridium dimer $[Ir(dFmesppy)_2Cl]_2$, ***rac*-D3**, was subsequently prepared by reacting the C^N ligand dFmesppy with $[Ir(COD)(Cl)]_2$ precursor (COD is 1,5-cyclooctadiene), following the preparation reported in the experimental section. The synthesis of the qpy ligand was

adapted from a previously reported protocol,[329] and consists of an Pd/C-catalysed oxidative homocoupling of 4,4′-bipyridine. Each family of metalloligands **Ir3** and **Ir4** is easily accessed in racemic form (***rac*-Ir3** and ***rac*-Ir4**) by reacting the racemic dimers ***rac*-D2** and ***rac*-D3**, respectively, with qpy in 2-methoxyethanol at 110°C for 19 h. Following the protocol illustrated in **Scheme 2** (chepter 2) for the preparation of the enantiopure dimers **Λ,Λ-D2** and **Δ,Δ-D2**, we also resolved the racemic dimer ***rac*-D3** into the enantiomerically pure Λ,Λ-, and Δ,Δ-$[Ir(dFmesppy)_2Cl]_2$ diatereomers (**Λ,Λ-D3** and **Δ,Δ-D3**), by using L- and D-serine as chiral auxiliaries (the NMR characterisation of the serine complexes is reported in the appendix, **Figure S45**). The x-ray structures of the enantiopure dimers **Λ,Λ-D3** and **Δ,Δ-D3** were obtained and are illustrated in **Figure 59**.

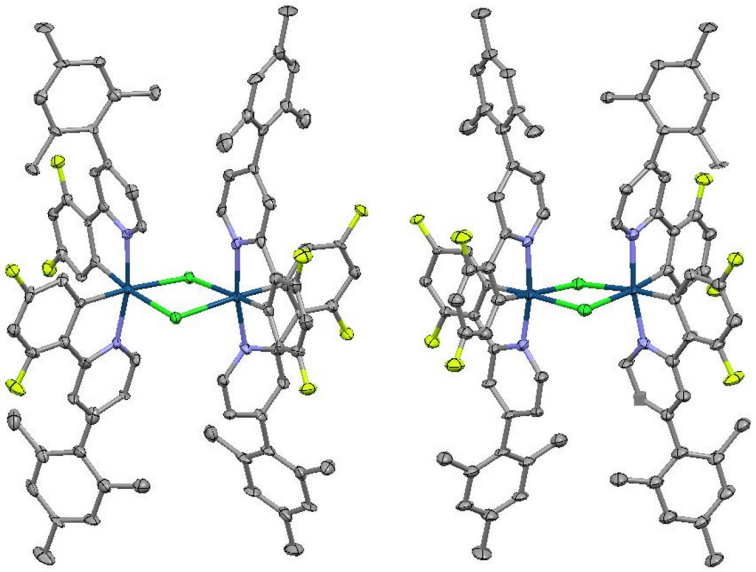

Figure 59. X-ray crystal structures of Λ,Λ-$[Ir(dFmesppy)_2Cl]_2$ (**Λ,Λ-D3**), left and Δ,Δ-$[Ir(dFmesppy)_2Cl]_2$ (**Δ,Δ-D3**), right. Ellipsoids are drawn at the 50% probability level. Solvent molecules and hydrogen atoms are omitted for clarity.

The reaction of the enantiopure dimers Λ,Λ-, and Δ,Δ-$[Ir(mesppy)_2Cl]_2$, **Λ,Λ-D2** and **Δ,Δ-D2** with qpy afforded respectively the enantiopure complexes Λ- and Δ-$[Ir(mesppy)_2(qpy)]BF_4$ (**Λ-** and **Δ-Ir3**), while the reaction of Λ,Λ-, and Δ,Δ-$[Ir(dFmesppy)_2Cl]_2$, **Λ,Λ-D3** and **Δ,Δ-D3** (**Figure 60**) with qpy yielded complexes Λ- and Δ-$[Ir(dFmesppy)_2(qpy)]BF_4$ (**Λ-** and **Δ-Ir4**) (**Figure 58**). The enantiomeric excess of the bulk samples of **Λ-** and **Δ-Ir3** and **Λ-** and **Δ-Ir4** was confirmed by CD spectroscopy (**Figure 60a-d**). The presence of fluorine atoms in ***rac*-**, **Λ-** and **Δ-Ir4** provides a useful tag for monitoring both the self-assembly process and the purity of the cage by ^{19}F NMR spectroscopy and, by virtue of their electronwithdrawing nature, for promoting a blue-shift in the absorption and emission

spectra concomitant with a stabilisation of the HOMO of the complexes, which are located on the C^N ligand. An exhaustive discussion about the energetics and x-ray structures of the iridium complexes **Ir3** and **Ir4** will be given in the following chapter.

3.2.2 Self-assembly of *rac*-, Λ_8- and Δ_8-$[Ir_8Pd_4]^{16+}$ cages

The self-assembly of ***rac***-, **Λ-** and **Δ-Ir3** and ***rac***-, **Λ-** and **Δ-Ir4** with Pd^{2+} ions was firstly investigated by NMR spectroscopy. When any of the Ir metalloligands ***rac***-, **Λ-** and **Δ-Ir3** and ***rac***-, **Λ-** and **Δ-Ir4** and $[Pd(NCMe)_4][BF_4]_2$ were heated in a 2:1 ratio in dimethyl sulfoxide-d_6 (DMSO-d_6) at 85°C for 12 h, the proton resonances associated with the metalloligand broadened and experienced downfield shifts (Figures **S90-S92** and **S95** in the appendix). The broad ^{1}H NMR signals are indicative of the formation of very large assemblies, the tumbling motion of which is very slow on the NMR timescale. As expected, the proton resonances associated with the proton in *ortho*-position to the distal nitrogen of the qpy moiety (H_a, H_b, in **Figure S90** and **Figure S95** in the appendix) were most sensitive to the axial coordination of the pyridine ring to Pd. Evidence for the formation of a single species was confirmed by ^{1}H DOSY NMR spectroscopy with a single diffusion coefficient (D) in DMSO-d_6 of 5.2 x 10^{-11} $m^2{\cdot}s^{-1}$ and 4.9 x 10^{-11} $m^2{\cdot}s^{-1}$, respectively, for **IrC1** and **IrC2** (**Figure 4e,f**, and **Figures S93,94** and **S97,98**). These diffusion coefficients are indicative of much larger structures than either of the two metalloligands **Ir3** and **Ir4**, which show nearly identical diffusion coefficients in DMSO-d_6 of 1.3 x 10^{-10} $m^2{\cdot}s^{-1}$ and 1.2 x 10^{-10} $m^2{\cdot}s^{-1}$, respectively (**Figure 60e,f** and **Figures S93,94** and **S97,98**). The corresponding hydrodynamic radii (r_s) of **IrC1** and **IrC2** are calculated to be 19.8 Å and 20.0 Å, respectively (**Table S2** in the appendix). ^{19}F NMR spectroscopy further confirmed quantitative conversion from **Ir4** to **IrC2**, with the fluorine resonances associated with the dFppy ligand shifted downfield from -106.33 ppm and -108.52 ppm in **Ir4** to -106.09 ppm and -108.31 ppm in **IrC2** (**Figure 60f** and **Figure S96**). As the two doublets associated with the fluorine resonances of the dFppy ligands in **Ir4** are maintained in the ^{19}F NMR spectra of **IrC2**, the local C_2 symmetry present around the iridium centre in **Ir4** is maintained also in the cage. Furthermore, no differences in the ^{1}H, ^{1}H DOSY and ^{19}F NMR spectra were observed when the enantiopure metalloligands **Λ-** and **Δ-Ir3** or **Λ-** and **Δ-Ir4** were employed towards the self-assembly of the cages in lieu of the racemic analogues ***rac*-Ir3** and ***rac*-Ir4**.

The compositions of the assemblies **IrC1** and **IrC2** have been unequivocally established to be $[(\mathbf{Ir3})_8Pd_4][BF_4]_{16}$ and $[(\mathbf{Ir4})_8Pd_4][BF_4]_{16}$, respectively, by HR-MS-ESI spectrometry, showing isotopically resolved peaks for $[\mathbf{IrC1}\text{-}(BF_4)_n]^{n+}$ (n= 5–8). For example, each of the ESI-MS spectra of ***rac***-, **Λ-** and **Δ-IrC1** reveal peaks at m/z= 1953.5016, 1611.7369, 1370.5512 and 1187.5743, which are assigned to $[\mathbf{IrC1}\text{-}(BF_4)_4]^{4+}$, $[\mathbf{IrC1}\text{-}(BF_4)_5]^{5+}$, $[\mathbf{IrC1}\text{-}(BF_4)_6]^{6+}$, $[\mathbf{IrC1}\text{-}(BF_4)_7]^{7+}$ and $[\mathbf{IrC1}\text{-}(BF_4)_8]^{8+}$, respectively. Similarly, the charge states

$[$**IrC2**-$(BF_4)_n]^{n+}$ (n= 5–8), were likewise observed in the MS spectra of each of ***rac***-, Λ- and **Δ-IrC2** at m/z= 2067.2391, 1707.8640, 1451.5934 and 1259.2765, respectively. The isotopically resolved distributions of these spectra closely match the simulated spectra. The ESI-MS spectra of all the cages can be found in **Figure S100-S110** in the appendix. As representative examples, the 7+ charge state observed in the ESI-MS spectra of **Δ-IrC1** and **Δ-IrC2** are illustrated in **Figure 61**.

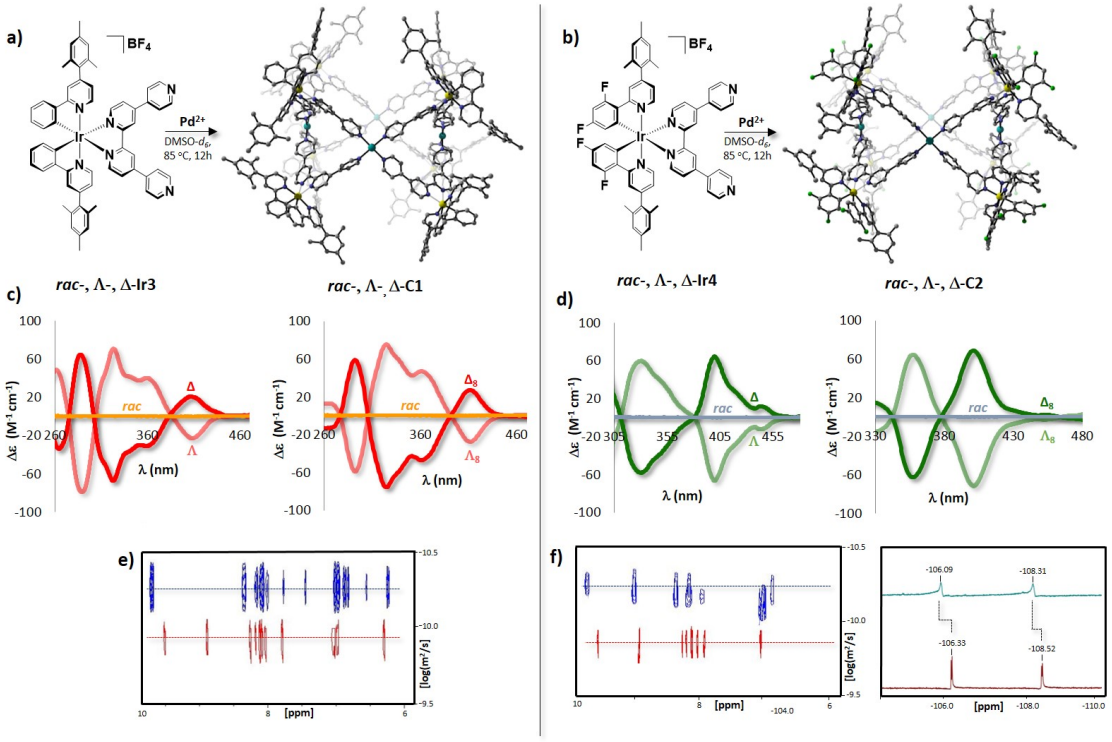

Figure 60. Self-assembly between the Ir metalloligands, and Pd^{2+} ions yielding: **a)** for ***rac***-, Λ- and **Δ-Ir3**; racemic ***rac*-IrC1**, and homochiral **Λ$_8$-IrC1** and **Δ$_8$-IrC1** cages, respectively (for clarity, only the calculated structure of **Λ-IrC1** obtained from **Λ-Ir3** is shown) and **b)** for ***rac***-, Λ- and **Δ-Ir4**; ***rac*-IrC2**, **Λ$_8$-IrC2** and **Δ$_8$-IrC2** cages (for clarity, only the calculated structure of **Λ-IrC2** obtained from **Λ-Ir4** is shown). **c)** CD spectra collected in CH_2Cl_2 at 298 K; light-red lines: **Λ-Ir3** (left), **Λ-IrC1** (right); red lines: **Δ-Ir3** (left) and **Δ-IrC1** (right); orange lines: ***rac*-Ir3** (left) and ***rac*-IrC1** (right). **d)** CD spectra collected in CH_2Cl_2 at 298 K; light-green lines: **Λ-Ir4** (left), **Λ-IrC2** (right); green lines: **Δ-Ir4** (left) and **Δ-IrC2** (right); light-blue lines: ***rac*-Ir4** (left) and ***rac*-IrC2** (right). The CD spectra of ***rac***-, Λ- and **Δ-Ir3** and ***rac***-, Λ- and **Δ-Ir4** were collected at a concentration of 5 x 10^{-5} M while the concentration of ***rac***-, Λ- and **Δ-IrC1** and ***rac***-, Λ- and **Δ-IrC2** was maintained at 1 x 10^{-5} M. **e)** ^{1}H DOSY NMR of **Δ-Ir3**, in red and **Δ-IrC1**, in blue. **f)** ^{1}H DOSY NMR of **Δ-Ir4**, in red and **Δ-IrC2**, in blue (left) and stacked ^{19}F NMR spectra of **Δ-Ir4** in red, and **Δ-IrC2** in blue (right). The geometries

of Λ-**IrC1** and Λ-**IrC2** have each been determined in vacuo at the HF/6-31G(d) level of theory.

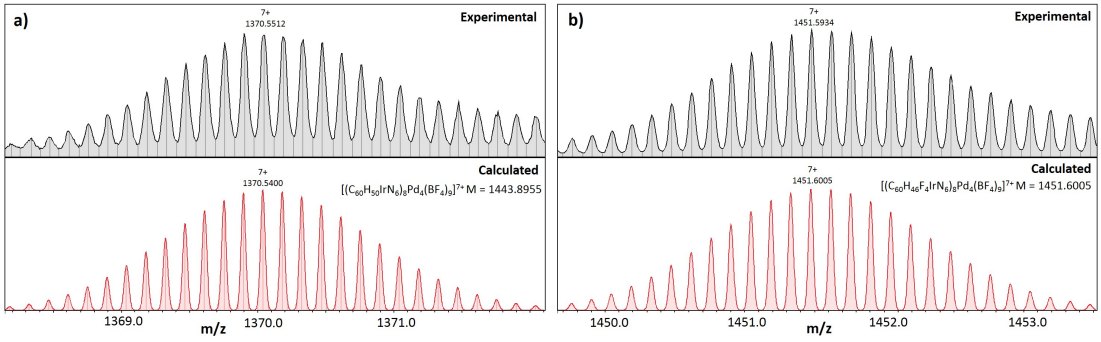

Figure 61. ESI-MS spectra of **(a)** [Δ-**IrC1**-$(BF_4)_7$]$^{7+}$ of Δ-**IrC1** and **(b)** [Δ-**IrC2**-$(BF_4)_7$]$^{7+}$ of Δ-**IrC2**. In blue are illustrated the experimental spectra while in red the simulation of the corresponding isotopic distribution patterns.

The CD spectra of Λ-**IrC1**, Δ-**IrC1**, Λ-**IrC2** and Δ-**IrC2** revealed that the Ir-centred stereochemistry of the eight metalloligands was mantained during the self-assembly and homochiral cages of compositions Λ_8- and Δ_8-[(**Ir3**)$_8$Pd$_4$][BF$_4$]$_{16}$ and Λ_8- and Δ_8-[(**Ir4**)$_8$Pd$_4$][BF$_4$]$_{16}$ were formed (**Figure 60c,d**). When ***rac*-Ir3** and ***rac*-Ir4** were employed as the metalloligands, racemic mixtures of composition *rac*-[(**Ir3**)$_8$Pd$_4$][BF$_4$]$_{16}$ and *rac*-[(**Ir4**)$_8$Pd$_4$][BF$_4$]$_{16}$ respectively, were formed (orange and light-blue lines in **Figure 60c,d**), although this did not enable us to determine if these complexes were racemic cages, or racemic mixtures of enantiopure cages. In order to ascertain the impact of the nature of the iridium centred stereochemistry on the assembly of the cages, we examined the self-assembly, in DMSO-d_6, of Pd^{2+} ions with one equivalent of one of the isostructural and enantiopure metalloligands, Λ-**Ir3** or Δ-**Ir3**, and one equivalent of Δ-**Ir4** (**Figure 62a**). The detailed experiment design is illustrated in **Figure 62** and further explained in the appendix. There are three possibilities by which similarly shaped components can self-assemble in structures: 1) random mixing,[330] 2) well-defined mixing,[331] or 3) self-sorting.[332] ESI-MS of a DMSO-d_6 solution containing either Λ-**Ir3** or Δ-**Ir3** (illustrated in red in **Figure 62a**) with Δ-**Ir4** (illustrated in green in **Figure 62a**) and [Pd(NCMe)$_4$][BF$_4$]$_2$ stirred at 85 °C for 12 h show a statistical mixture of cage species of composition [(Λ-**Ir3**/Δ-**Ir3**)$_n$(Δ-**Ir4**)$_m$Pd$_4$][BF$_4$]$_{16}$ (n+m=8), from Λ-**Ir3**/Δ-**Ir3**:Δ-**Ir4**=7:1 to Λ-**Ir3**/Δ-**Ir3**:Δ-**Ir4**=1:7, (**Figures 62b,c**), indicating that our cages do not assemble by self-sorting with respect to either the chirality or identity of the metalloligands. The 7+ charge states of the homonuclear and heteronuclear cage mixture observed by ESI-MS are illustrated in **Figure 62c,d** and in **Figure 63**. Similarly, mixing the preformed cages Λ-**IrC1** and Δ-**IrC1** with Δ-**IrC2** (**Figure 62a**) at 85 °C for 12 h resulted in a rapid exchange between ligands Λ-**Ir3**, Δ-**Ir3**, and Δ-**Ir4** (**Figure 62b,c** and **Figure 63f,g**). As illustrated in **Figures 62c**, the isotopically resolved distributions of the 7+ charge states, [(Λ-**IrC1**/Δ-**IrC1**)$_n$(Δ-

IrC2)$_m$(BF$_4$)$_7$]$^{7+}$ closely match the simulated spectra. The ESI-MS spectra of all the heteronuclear cages can be found in **Figure S109-S112** in the appendix. When homochiral cages of the same stereochemistry, **Δ-IrC1** and **Δ-IrC2**, are mixed at 85 °C in DMSO-d_6, the formation of homochiral heteronuclear cages are observed by CD spectroscopy with a CD spectrum intermediate for the mixed cage assemblies (**Figure 64**, dark-blue line). However, when homochiral cage **Λ-IrC1** is mixed with **Δ-IrC2** at 85 °C, which is of opposite stereochemistry, the formation of racemic heteronuclear cages which absorb in an almost equal amount l- and d-polarised light is promoted(**Figure 64**, light-blue line).

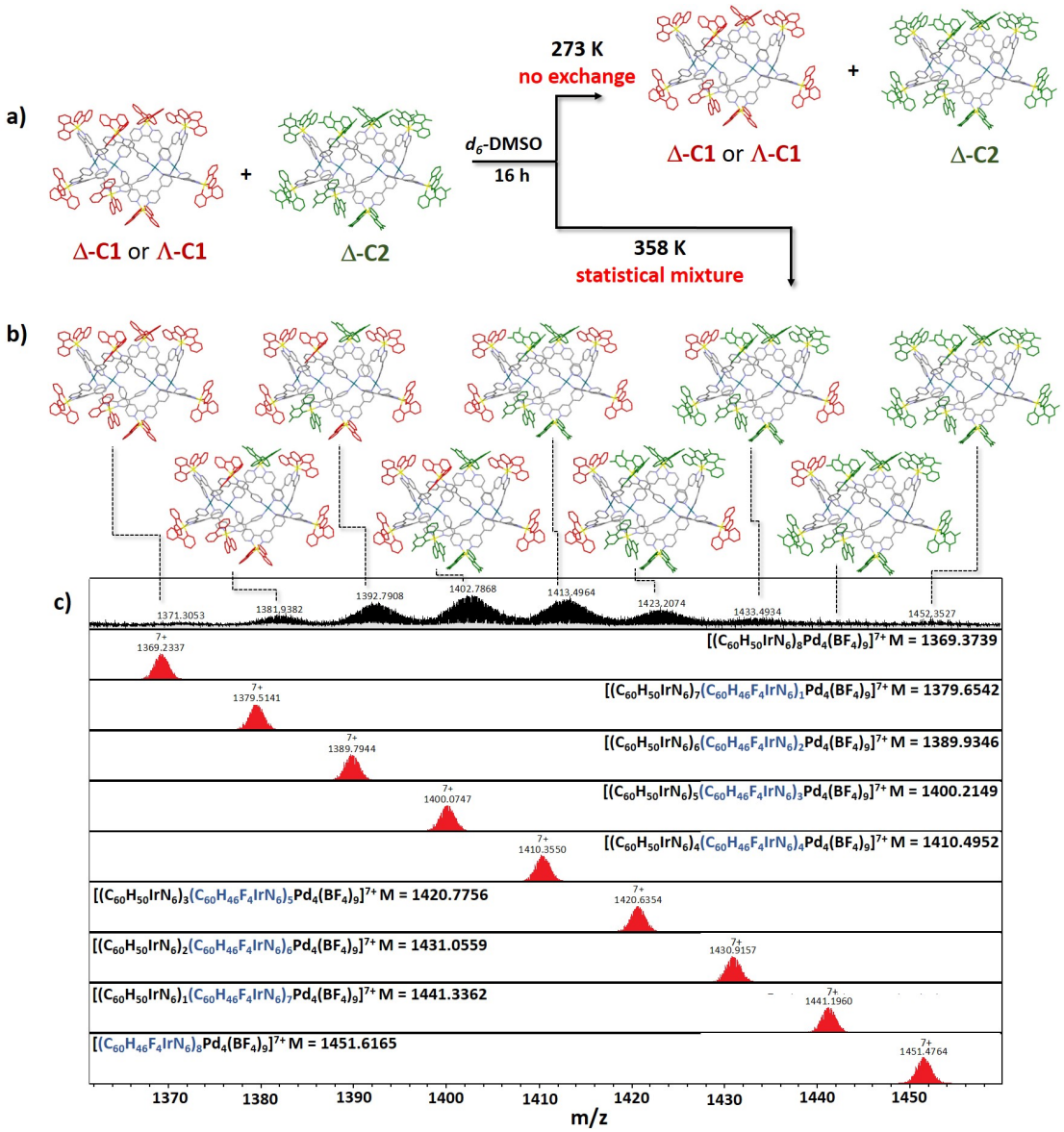

Figure 62. **a)** Schematic representation of the exchange experiments carried out by mixing **Δ-IrC1** or **Λ-IrC1** (ppy ligand in red) with **Δ-IrC2** (dFppy ligand in green). The mesityl substituents have been omitted for clarity. **b)** Illustration of the formation of statis-

tical mixture of cage species of compositions $[(\Lambda\text{-}/\Delta\text{-}\ \mathbf{Ir3})_n(\Delta\text{-}\mathbf{Ir4})_m\mathrm{Pd}_4][\mathrm{BF}_4]_{16}$ (n+m=8, from Λ-**Ir3**/Δ-**Ir3**:Δ-**Ir4**=7:1 to Λ-**Ir3**/Δ-**Ir3**:Δ-**Ir4**=1:7). **c)** ESI mass spectra of the 7+ charge states $[(\mathbf{Ir3})_n(\mathbf{Ir4})_m(\mathrm{BF}_4)_7]^{7+}$ (n+m=8, from **Ir3**:**Ir4**=7:1 to **Ir3**/:**Ir4**=1:7) of Δ-**IrC1**+Δ-**IrC2** heated at 85 °C for 12 h. In red are illustrated the simulated 7+ charge states of the heteroleptic cages. The same statistical distributions are observed for the 8+, 6+ and 5+ charge states.

This was expected considering that the chirality of the iridium core does not contribute directly to the overall self-assembly process. No metalloligand exchange is observed when either homochiral cage Λ-**IrC1**/Δ-**IrC1** is mixed with Δ-**IrC2** at room temperature, and the cages show a high degree of kinetic inertness (**Figures 63e** and **Figures S113, S114** in the appendix).

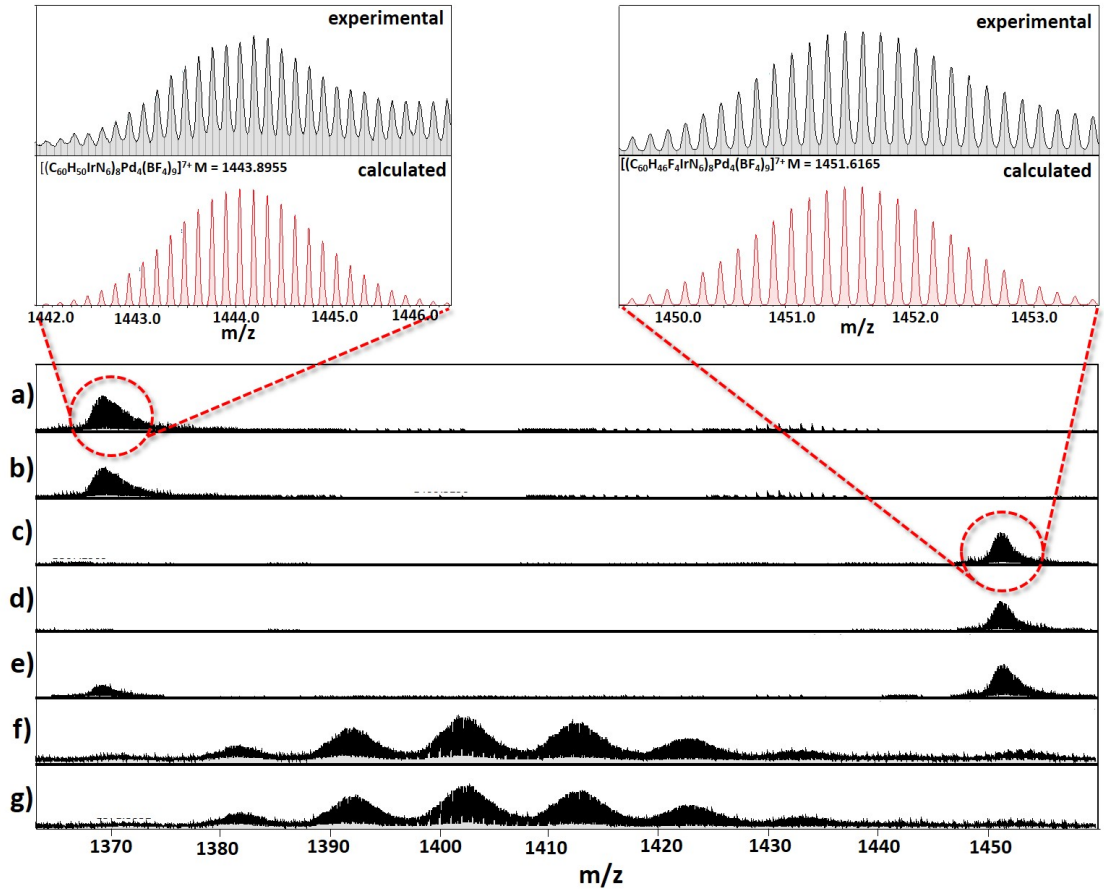

Figure 63. **a)** ESI mass spectrum of Δ-**IrC1** indicating the $[(\Delta\text{-}\mathbf{IrC1})\text{-}(\mathrm{BF}_4)_7]^{7+}$ charge state with its simulation; **b)** ESI mass spectrum of Λ-**IrC1** indicating the $[(\Lambda\text{-}\mathbf{IrC1})\text{-}(\mathrm{BF}_4)_7]^{7+}$ charge state; **c)** ESI mass spectrum of Δ-**IrC2** indicating the $[(\Delta\text{-}\mathbf{IrC2})\text{-}(\mathrm{BF}_4)_7]^{7+}$ charge state with its simulation; **d)** ESI mass spectrum ofΛ-**IrC2** indicating the $[(\Lambda\text{-}\mathbf{IrC2})\text{-}(\mathrm{BF}_4)_7]^{7+}$ charge state; **e)** ESI mass spectrum of a mixture of Δ-**IrC1** and

Δ-IrC2 mixed at 273 K; **f)** ESI mass spectrum of a mixture of **Δ-IrC1** and **Δ-IrC2** mixed at 358 K for 16 h; **g)** ESI mass spectrum of a mixture of **Λ-IrC1** and **Δ-IrC2** mixed at 358 K for 16 h.

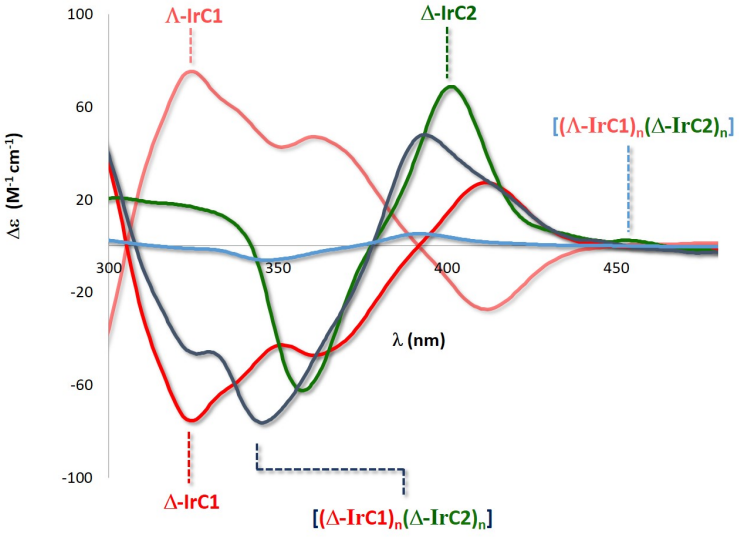

Figure 64. CD spectra of **Δ-IrC1** (red line), **Λ-IrC1** (light-red line), **Δ-IrC2** (green line) and mixed cages of compositions $[(\mathbf{\Delta\text{-}IrC1})_n(\mathbf{\Delta\text{-}IrC2})_n](BF_4)_{16}$ (dark-blue line) and $[(\mathbf{\Lambda\text{-}IrC1})_n(\mathbf{\Delta\text{-}IrC2})_n](BF_4)_{16}$ (light-blue line).

The structures of both **IrC1** and **IrC2** were modelled at the HF/6-31G(d) level of theory (**Figure 60a**), and were found to be very similar. They resemble metallamacrocyclic structures in which two ligands doubly bridge between adjacent Pd centres around the macrocycle, in a crown-like fashion.[333] Among supramolecular assemblies composed of ligands containing two or more pyridine units possessing divergent vectors and Pd^{2+} ions ions, the stoichiometry $[(L)_8Pd_4]$ is rare with only five examples of assemblies with this structural motif reported to date.[333–337] This relative stoichiometry is only possible when the angle between the coordinating 4-pyridyl units is inferior to 90°.[298] This is indeed the case for both metalloligands **Ir3** and **Ir4** which exhibit an angle between the distal 4-pyridyl units of the qpy ligand of approximately 78° determined by x-ray analysis (the detailed discussion of the x-ray structures of ***rac*-Ir3** and **rac-Ir4** is reported in the following chapter).

The calculated structure confirmed that the qpy vector of the metalloligands **Ir3** and **Ir4** is compatible to form the $[Ir_8Pd_4]^{16+}$ cages identified by mass spectrometry. The optimised cage exhibits a diameter of approximately 18.8 Å (corresponding to the Pd···Pd distance), an internal volume from the top to the bottom bounds of the structure of approximately 3480 $Å^3$, and a distance between neighbouring Ir atoms bridging the same Pd···Pd edge of approximately 13.7 Å. The radius around the metallamacrocyclic core across long axes of the structure, measures 21.5 Å and matches with the hydrodynamic

radii obtained by ^{1}H NMR DOSY analysis (r_s=19.8 Å). The cage structure can be seen to be approximately C_4 symmetric about the Pd_4 square. Unfortunately, while single crystals of cages **IrC1** and **IrC2** could be grown, and were examined by X-ray diffraction, all crystals investigated showed extremely weak diffraction, with even synchrotron radiation not showing diffraction above 1.6 Å. Attempted structure solutions have given the positions of the metal cations and poorly ordered parts of the ligands, the data not, as yet, being amenable to further refinement (**Figure 65**).

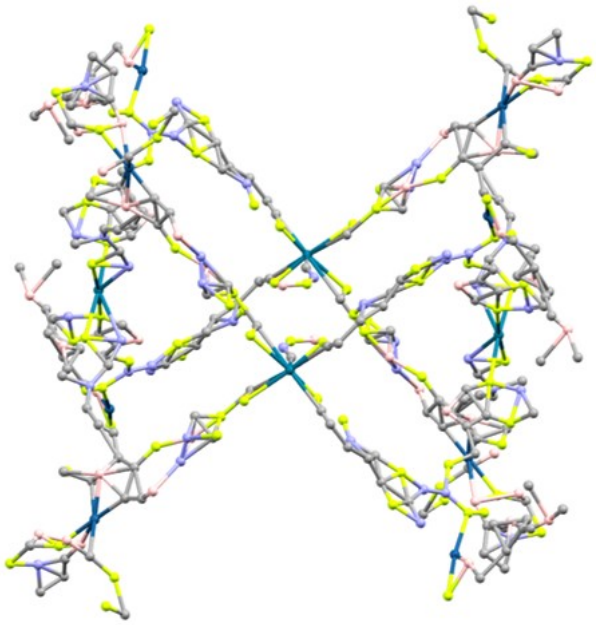

Figure 65. Attempted structure solution of cage **IrC1**.

3.2.3 Photophysical properties of Ir metalloligands and metallocages

In CH_2Cl_2, the photophysical properties of the racemic metalloligands ***rac*-Ir3** and ***rac*-Ir4** and of the racemic cages ***rac*-IrC1** and ***rac*-IrC2** are identical to those of the respective homochiral analogues **Λ-Ir3**/**Δ-Ir3**, **Λ-Ir4**/**Δ-Ir4**, **Λ-IrC1**/**Δ-IrC1**, and **Λ-IrC2**/**Δ-IrC2** (**Table 3**). The emission profiles of both families of cages **IrC1** and **IrC2** in CH_2Cl_2 are red-shifted, respectively, at 655 nm and 561 nm, relative to those of the corresponding metalloligands **Ir3** (λ_{max} = 620 nm) and **Ir4** (λ_{max} = 527 nm). Their Φ_{PL} and τ_{PL} are correspondingly lower and shorter, respectively (e.g., ***rac*-IrC1**: Φ_{PL} = 5%, τ_{PL} = 202 ns; ***rac*-IrC2**: Φ_{PL} = 10%, τ_{PL} = 825 ns), compared to those of **Ir3** and **Ir4** (e.g., ***rac*-Ir3**: Φ_{PL} = 14%, τ_{PL} = 300 ns; ***rac*-Ir4**: Φ_{PL}=34%, τ_{PL} = 1000 ns).

These features are reflected in the excited-state decay kinetics. Indeed, both families of homochiral and racemic coordination cages **IrC1** and **IrC2** exhibit slightly smaller radiative

rate constants (k_r, e.g., 2.47 x 10^5 s^{-1} for ***rac*-IrC1** and 1.21 x 10^5 s^{-1} for ***rac*-IrC2**), and slightly larger non-radiative rate constants (k_{nr}, e.g., 4.66 x 10^6 s^{-1} for ***rac*-IrC1** and 1.09 x 10^6 s^{-1} for ***rac*-IrC2**), relative to the corresponding metalloligands (e.g., ***rac*-Ir3**: k_r = 4.67 x 10^5 s^{-1}, k_{nr} = 2.45 x 10^6 s^{-1}; ***rac*-Ir4**: k_r = 3.40 x 10^5 s^{-1}, k_{nr} = 6.60 x ^{5} s^{-1}).

The presence of the electron-withdrawing fluorine atoms in **IrC2** induces a blue shift in the emission relative to the fluorine-free cage **IrC1**. Similar to that observed for **Ir3** and **Ir4**, the emission profiles of **IrC1** and **IrC2** are broad and unstructured, an indication that the nature of the emission remains unchanged and is from mixed metal-to-ligand and ligand-to-ligand charge transfer (^{3}MLCT/ ^{3}LLCT) states (**Figure 66** and **Figures S131, S132** in the appendix).

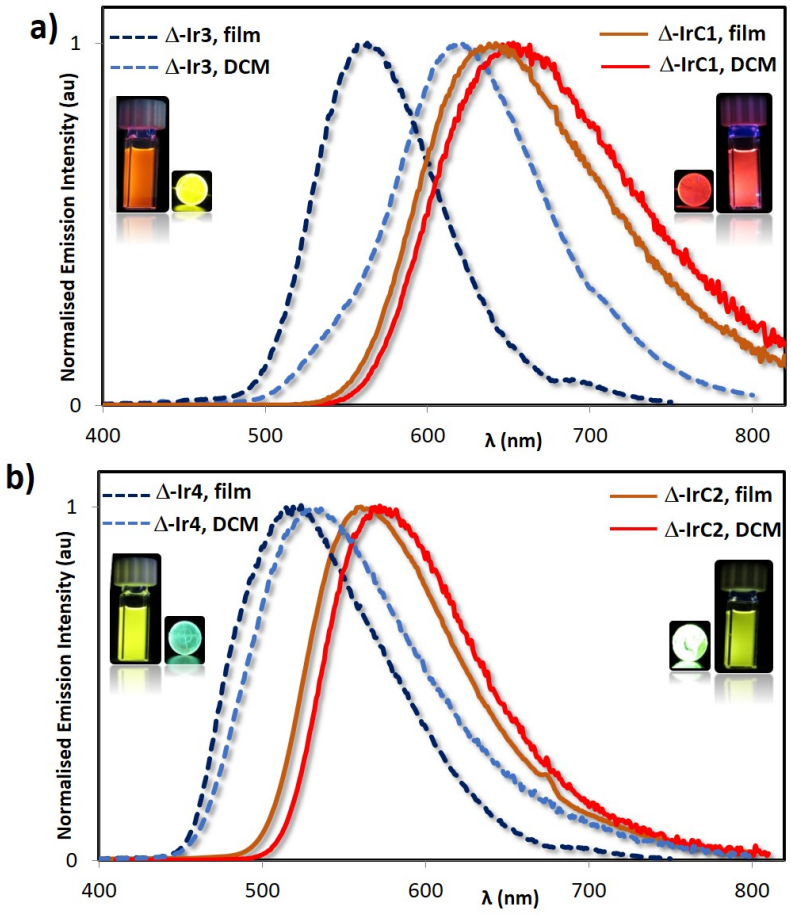

Figure 66. Normalised emission spectra of: **a) Δ-Ir3** and **Δ-IrC1** and **b) Δ-Ir4** and **Δ-IrC2**. Dotted dark-blue lines: PMMA-doped film with 5 wt% of metalloligands **Δ-Ir3** and **Δ-Ir4** spin-coated on quartz substrates; Dotted light-blue lines: deaerated CH_2Cl_2 solution of **Δ-Ir3** and **Δ-Ir4**; Solid orange lines: PMMA-doped film with 5 wt% of cages **Δ-IrC1** and **Δ-IrC2** spin-coated on quartz substrates; Solid red lines: deaerated CH_2Cl_2 solution of **Δ-IrC1** and **Δ-IrC2**.

Table 3. Relevant photophysical data for ***rac*-**, Λ- and **Δ-Ir3** and ***rac*-**, Λ- and **Δ-IrC1**, ***rac*-**, Λ- and **Δ-Ir4** and ***rac*-**, Λ- and **Δ-IrC2**

	λ_{PL} (nm)[a,b]		Φ_{PL} (%)[d]		τ_{PL} (ns)[a]	
	DCM[a]	film[b,c]	DCM[d]	film[c,e]	DCM	film[c,f]
***rac*-Ir3**	620	564	14	28.1	300	344 (0.14), 1045 (0.86)
Δ-Ir3	620	563	13	28.7	300	333 (0.13), 1038 (0.87)
Λ-Ir3	620	563	13	26.4	299	343 (0.12), 1044 (0.88)
***rac*-IrC1**	655	643	5	10.9	204	49 (0.12), 270 (0.68), 715 (0.20)
Δ-IrC1	655	643	5	10.3	202	47 (0.12), 269 (0.67), 707 (0.21)
Λ-IrC1	655	643	5	9.6	202	48 (0.12), 266 (0.67), 695 (0.21)
***rac*-Ir4**	565	518	34	41.2	1000	48 (0.09), 259 (0.21), 1195 (0.70)
Δ-Ir4	564	518	35	42.3	1001	46 (0.08), 246 (0.22), 1184 (0.70)
Λ-Ir4	565	519	31	40.9	1001	48 (0.08), 240 (0.22), 1189 (0.70)
***rac*-IrC2**	573	531	10	16.8	825	13 (0.14), 412 (0.17), 1125 (0.69)
Δ-IrC2	572	531	8	16.3	824	13 (0.14), 378 (0.14), 1101 (0.72)
Λ-IrC2	573	531	11	15.8	824	11 (0.13), 372 (0.14), 1117 (0.73)

[a]Measurements in degassed CH_2Cl_2 at 298 K (λ_{exc} = 360 nm). [b]Principal emission peaks listed with values in parentheses indicating relative intensity (λ_{exc} = 378 nm). [c]PMMA-doped thin films formed by spin-coating the samples (5 wt%) on a quartz substrate. [d]Φ_{PL} measurements were carried out in degassed CH_2Cl_2 under nitrogen (λ_{exc} = 360 nm) using quinine sulfate as the external reference (Φ_{PL} = 54.6% in 0.5 M H_2SO_4 at 298 K).[287] [e]Values obtained using an integrating sphere. [f]Values in parentheses are pre-exponential weighting factor, in relative % intensity, of the emission decay kinetics (λ_{exc} = 378 nm).

In order to mitigate non-radiative vibrational motion, we spin-coated 5 wt% of **Ir3**, **Ir4**, **IrC1** and **IrC2** in PMMA, which serves as an inert matrix. As a result of the less polar environment and the rigidification conferred by the PMMA host (PMMA = poly(-methyl methacrylate)), the emissions of **Ir3**, **Ir4**, **IrC1** and **IrC2** in the thin films were blue-shifted,

respectively at 564 nm, 518 nm, 643 nm and 531 nm (**Figure 66**, with enhanced Φ_{PL} and longer multi-exponential τ_{PL} (as representative examples: ***rac*-Ir3**: Φ_{PL} = 28%, τ_{PL} = 344, 1045 ns, ***rac*-Ir4**: Φ_{PL} = 41%, τ_{PL} = 48, 259, 1195 ns, ***rac*-IrC1**: Φ_{PL} = 11%, τ_{PL} = 49, 270, 715 ns, and ***rac*-IrC2**: Φ_{PL} = 17%, τ_{PL} = 13, 412, 1125 ns) relative to the photophysical behaviour in CH_2Cl_2 (**Table 3**).

The red-shifted emissions of the cages **IrC1** and **IrC2** in both CH_2Cl_2 and PMMA-doped films relative to those of the corresponding metalloligands can be interpreted as the result of coordination of the Lewis acidic Pd^{II} to the iridium complex. By acting as a Lewis acid, the Pd^{2+} ions lower the LUMO levels of complexes **Ir3** and **Ir4** located on the qpy ligand, giving rise to smaller optical gaps. The HOMO - LUMO energy levels of **Ir3** and **Ir4** predicted by DFT calculations will be discussed in the next chapter.

3.2.4 Host-guest chemistry

The calculated cage structures, ***rac*-**, Λ- and **Δ-IrC1** all show an internal pocket volume of approximately 3480 $Å^3$, which is sufficient to include large guest molecules, including mononuclear phosphorescent iridium complexes. As comprensively documented in the first chapter, the photophysical properties of luminescent iridium complexes emitting from CT states, strongly depend on the local environment. For example, as previously discussed, Umakoshi et al.[168] encapsulated the Ir(III) complex, $[Ir(ppy)_2(bpy)]Cl$, within a hexameric resorcinarene hydrogen-bonded capsule and observed that the capsule effectively hampers the non-radiative decay thereby enhancing both the Φ_{PL} and the τ_{PL} of the encapsulated iridium guest.

We targeted the encapsulation of blue-emitting Ir(III) guests within the confined cavity of our red-emitting cage **IrC1** to study the nature of the energy-transfer process between donor guest and acceptor host cage. Importantly, by modulating the degree of energy transfer between the donor and the acceptor as a function of the choice of medium or concentration, emission of white light can also be achieved.[71, 318] In the context of iridium phosphors, this approach has been investigated in multi-metallic covalently linked complexes,[338] soft salts,[71] or in MOFs containing emissive materials,[176] but still remains unexplored in photo-active host–guest assemblies. Preliminary ^1H NMR studies on the interactions between a selected range of small organic guest compounds and **Δ-IrC1** revealed that the cage interacts selectively with anionic guests in DMSO-d_6. Interactions can be observed with ammonium tetraphenyl borate or ammonium pyrenecarboxylate (see the ^1H NMR spectra in **Figures S115, S116** in the appendix), but no interaction is observed for neutral guest compounds, such as pyrene or pyrene carboxylic acid. A similar behaviour was observed for the interaction of guest molecules with a polycationic $[Pd_2L_4]^{12+}$ cage (in whihch L are acridinium panels connected by a meta-phenylene spacers).[168] Indeed, in the computed molecular electrostatic potential map of **IrC1** (**Figure 67**), all

regions are of positive potential, the most positive potential regions of **Δ-IrC1** being found in the pocket of the cage (in the closest proximity to the Pd^{2+} ions). Therefore, favourable interactions are expected with negatively charged guests.

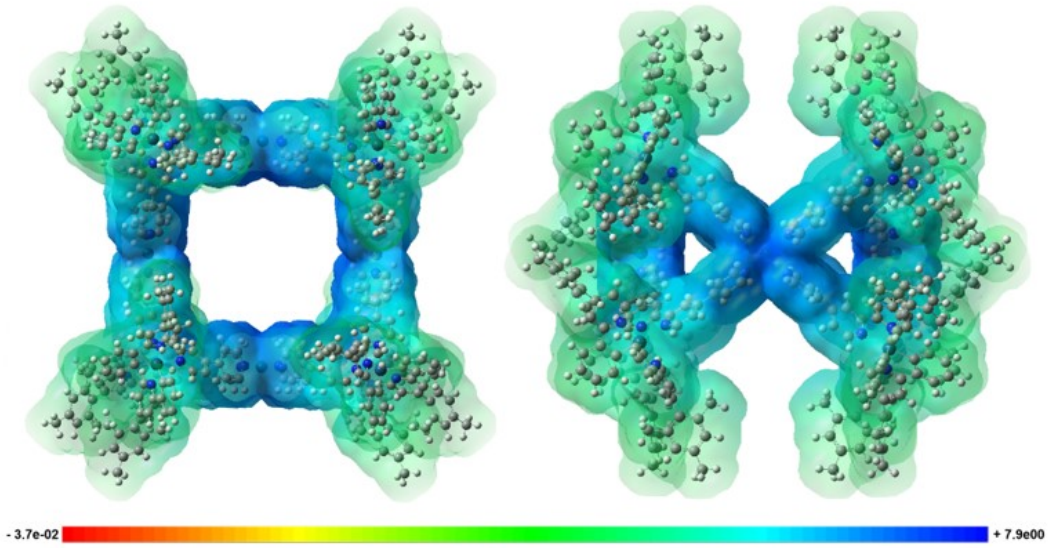

Figure 67. Molecular electrostatic potential [HF/6-31G(d)] map of **IrC1** with front (left) and central (right) views. The most positive potential regions are shown in deep blue.

We next turned our attention to investigate the interactions between the racemic blue-emitting anionic $[Ir(dFppy)_2(CN)_2]^-$ complex (**Ir5**)[339] with cage **IrC1** (**Figure 68a**). ^{1}H DOSY NMR analysis of a room-temperature solution containing one equivalent of **Δ-IrC1** and **Ir5** in DMSO-d_6 revealed a significant reduction of the diffusion coefficient of **Ir5** ($D_{(\mathbf{Ir5})}$ = 1.9 x 10^{-10} $m^2{\cdot}s^{-1}$) after mixing with cage **Δ-IrC1** to form the host– guest system **Δ-IrC1⊃Ir5** ($D_{(\mathbf{\Delta\text{-}IrC1\supset Ir5})}$ = 4.9–6.0 x 10^{-11} $m^2{\cdot}s^{-1}$, **Figure 68a**), with a diffusion coefficient similar to that of host **Δ-IrC1** ($D_{(\mathbf{\Delta\text{-}IrC1})}$ = 5.3 x 10^{-11} $m^2{\cdot}s^{-1}$). In addition, the ^{1}H NMR spectra of **Δ-IrC1⊃Ir5** revealed that the binding of **Ir5** with cage **Δ-IrC1** proceeds with significant broadening of the resonances associated with **Ir5** (**Figure S117-S120**, appendix), confirming its slow tumbling motion on the NMR timescale. A downfield shift and a significant broadening of the fluorine resonances of **Ir5** in **Δ-IrC1⊃Ir5** were also observed by ^{19}F NMR spectroscopy (**Figures S118, S119**, appendix). In contrast, when the cationic complex $[Ir(dFppy)_2(dmbpy)]PF_6$ (dmbpy = 4,4′-dimethyl-2,2′-bipyridine; **Ir6**) was mixed with **Δ-IrC1** in DMSO-d_6 at room temperature, no binding affinity was observed by ^{1}H, ^{19}F and ^{1}H DOSY NMR spectroscopy (**Figure 68b** and **Figures S122-S124**).

The potential host–guest complexes, **Δ-IrC1⊃Ir5** and **Δ-IrC1**+**Ir6**, were optimised at the HF/6-31G(d) level of theory in order to gain insights into the nature of the host–guest interactions. For the optimised **Δ-IrC1⊃Ir5** host–guest structure, the **Ir5** complex is located in the pocket of the cage (**Figure 68a**), in agreement with the electrostatic potential

map predictions for the cage. Its optimised structure reveals weak interactions between the cyano ligand of **Ir5** with one of the Pd^{2+} ions (3.2 Å) and several C-H units of **Δ-IrC1**. By contrast, any attempts to optimise a **Δ-IrC1⊃Ir6** host–guest structure did not lead to a stable complex. Indeed, both units fall apart during the optimisation process, stressing that no favourable interactions between **Ir6** and **Δ-IrC1** could be found, and that this holds both in the pocket and on the exterior surface of the cage.

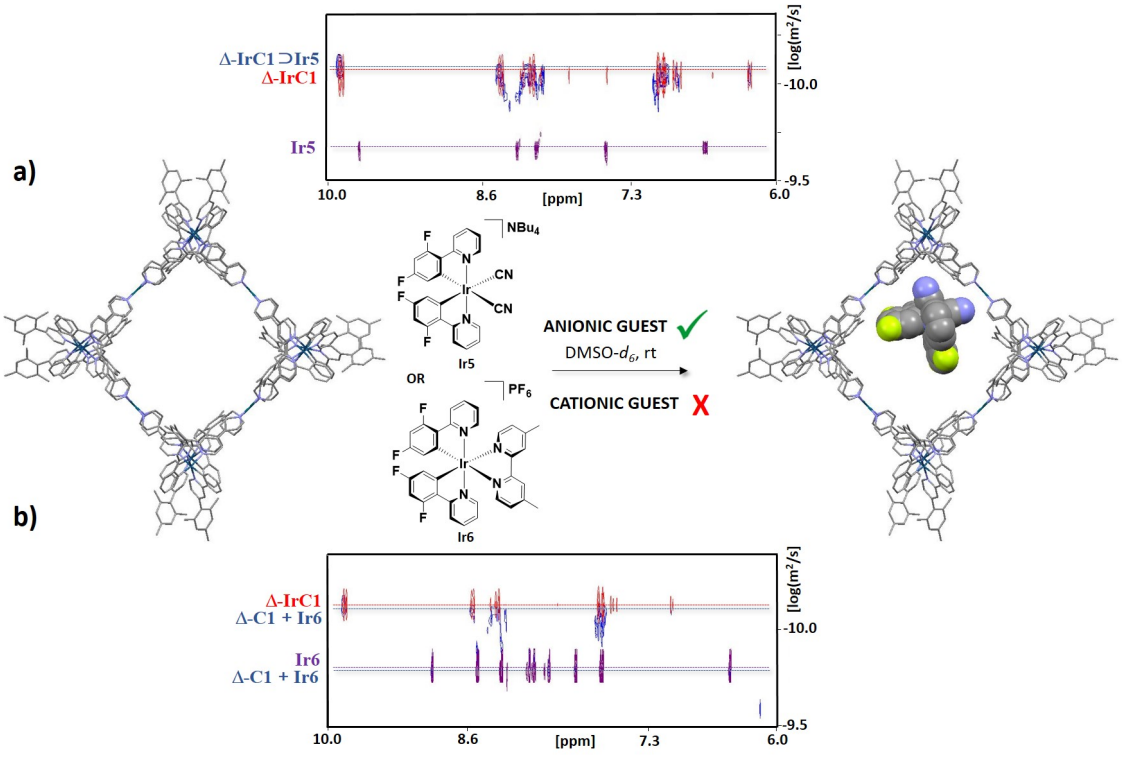

Figure 68. **a)** Representation of encapsulation in DMSO-d_6 at room temperature of complex the $NBu_4[Ir(dFppy)_2(CN)_2]$ (**Ir5**) within the cavity of cage **Δ-IrC1**; including (top) the ^{1}H DOSY NMR spectra of **Ir5** (in purple), **Δ-IrC1** (in red) and a 1:1 solution of **Ir5** and **Δ-IrC1** (**Δ-IrC1⊃Ir5**, in blue). The HF/6-31G(d) optimised host–guest structure **Δ-IrC1⊃Ir5** is shown. **b)** ^{1}H DOSY NMR spectra of $[Ir(dFppy)_2(dmbpy)]PF_6$ (**Ir6**) (in purple), **Δ-IrC1** (in red) and a 1:1 solution of **Ir6** and **Δ-IrC1** (**Δ-IrC1** + **Ir6**, in blue).

The anionic complex **Ir5** exhibits a blue ^{3}LC emission in DMSO, with two maxima at 458 and 483 nm and a shoulder at 515 nm (blue line in **Figure 69a**), a Φ_{PL} of 52%, and a τ_{PL} of 2915 ns. The same vibronic emission profile, with λ_{PL} at 460 nm and 485 nm, was observed in CH_2Cl_2, but with a higher Φ_{PL} of 80% and a longer τ_{PL} of 3280 ns.[339] Emission titration of cage **Δ-IrC1** (from 0 to 120 µM) into a 100 µM degassed solution of **Ir5** in DMSO at 298 K results in a gradual quenching of the blue emission of the donor **Ir5** together with a gradual enhancement of the emission of the red-emitting

cage **Δ-IrC1** at 666 nm, with an isosbestic point observed at 565 nm (**Figure 69a**). At a concentration of 110 µM of **Δ-IrC1** (titration 8 in **Figure 69a**), the emission of the **Ir5** was completely quenched and only emission from **Δ-IrC1** was observed. Upon photoexcitation of **Δ-IrC1⊃Ir5** at 360 nm, energy transfer from the blue-emitting **Ir5** to the red-emitting **Δ-IrC1** is therefore promoted. This emission titration data could be fitted to a 1:1 binding model using an iterative fitting procedure implemented within the OpenDataFit tool of the Supramolecular program (www.supramolecular.org) (**Figure S146**, appendix). The best fit of the binding model to the emission data afforded a value for the binding constant K_b of 3.9 x 10^6 ± 0.2 M^{-1} for the formation of **Δ-IrC1⊃Ir5** from **Δ-IrC1** and **Ir5**. This association constant is in the range reported for encapsulation of anionic guests into polycationic host cages.[340]

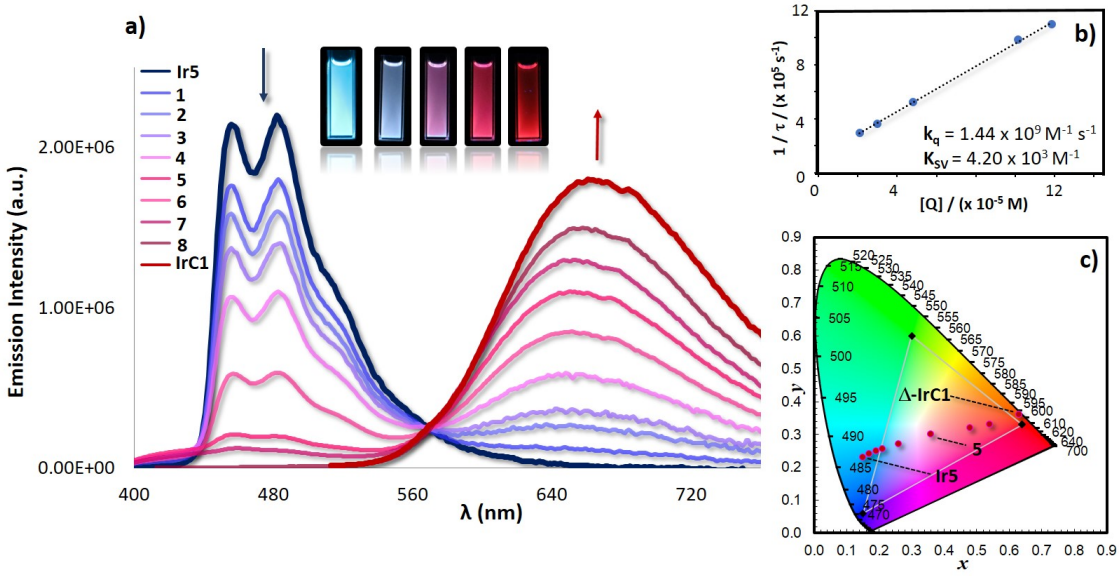

Figure 69. **a)** Emission titrations of **Δ-IrC1** (0 µM: **Ir5**; 2 µM: 1; 5 µM: 2; 10 µM: 3; 21 µM: 4; 30 µM: 5; 48 µM: 6; 78 µM: 7; 101 µM: 7; 120 µM: 8) into a 100 µM solution of **Ir5** at 298 K in degassed DMSO. Insets are images of the emissions of the assembly during the titration. **b)** Stern–Volmer plot of the quenching study between **Ir5** and **Δ-IrC1**. The emission lifetimes of **Ir5** were monitored at 480 nm ($\tau_{PL}{}^0$ = 2915 ns) upon photoexcitation at 378 nm. **c)** CIE diagram indicating the change of emission colours during the emission titration.

To study the energy transfer between anionic **Ir5** and **Δ-IrC1** in **Δ-IrC1⊃Ir5**, Stern–Volmer quenching analysis was carried out (**Table S5**, appendix). The emission lifetimes of **Ir5** (monitored at λ_{PL} = 480 nm in degassed DMSO, λ_{ex}= 378 nm) after addition of increasing amount of quencher **Δ-IrC1** were recorded (see the emission lifetime spectra in the appendix, **Figures S149-S156**). The concentration of **Ir5** was maintained constant at

100 µM, whereas the concentration of **Δ-IrC1** varied from 0 to 120 µM. Based on a bimolecular quenching model (eq. **2** in chapter 1), the reciprocal of the lifetime of **Ir5** is linearly correlated to the concentration of the quencher **Δ-IrC1** (**Figure 69b**). From this analysis, we calculated a quenching rate constant (k_q) of 1.44 x 10^9 $M^{-1}{\cdot}s^{-1}$ and a Stern–Volmer constant (K_{SV}) of 4.20 x 10^3 M^{-1}, suggesting that the energy transfer/quenching process in **Δ-IrC1⊃Ir5** is very efficient.[71, 341] Förster energy transfer is unlikely to be an efficient pathway for energy transfer due to the poor spectral overlap between the absorption of **Δ-IrC1** and the emission of **Ir5** (**Figure S148** in the appendix), therefore, Dexter energy transfer is the likely mechanism for the energy transfer in system.[71]

By contrast, emission titrations of **Δ-IrC1** (from 0 to 120 µM) into a 100 µM solution of the cationic **Ir6** complex at 298 K in DMSO did not show any evidence of quenching of the emission of **Ir6** to the **Δ-IrC1** cage (**Figure S156**, appendix); rather a superposition of the emission spectra of the two species was observed. These findings are consistent with our computational investigation of **Δ-IrC1⊃Ir6**, which did not lead to a stable complex. Therefore, both emission studies and host–guest simulations demonstrate that high binding affinity between the host and the guest is required to promote energy transfer.

The CIE (Commission Internationale de l'*É*clairage) diagram shown in **Figure 69c** illustrates the change in the emission colours observed during the emission titration. Titration 5 (**Figure 69a**) shows CIE coordinates of (0.36, 0.30), which are close to coordinates of the pure white light (x: 0.31, y: 0.33). However, the emission titration involving **Δ-IrC1⊃Ir5** does not lead to pure white light because the emission of **Ir5** is located at a too high energy.

In an effort to produce a pure white-light emitting assembly we decided to investigate also the energy transfer between the anionic guest $[Ir(ppy)_2(CN)_2]^-$ (**Ir7**),[73] and the host cage **Δ-IrC1**. As illustrated in **Figure 70a**, the vibronic ^{3}LC emission in DMSO of **Ir7** with maxima at 485 nm and 508 nm is red-shifted compared to **Ir5**, the result of the absence of electron-withdrawing fluorine atoms on the ppy ligand. Analogously to that observed for **Δ-IrC1⊃Ir5**, emission titration of cage **Δ-IrC1** (from 0 to 120 µM) into a 100 µM degassed solution of **Ir7** in DMSO at 298 K results in a gradual quenching of the blue-green emission of the donor **Ir7** together with a gradual enhancement of the emission of the red-emitting cage **Δ-IrC1** at 666 nm, with an isosbestic point observed at 571 nm (**Figure 70a**). Dexter energy transfer from the blue-emitting **Ir7** to the red-emitting **Δ-IrC1** in **Δ-IrC1⊃Ir7** is therefore promoted with calculated k_q of 1.53 x 10^9 $M^{-1}{\cdot}s^{-1}$ and K_{SV} of 3.12 x 10^4 M^{-1}. Unfortunately, as illustrated in the CIE diagram in **Figure 70b**, the emission of **Ir7** is now located at too low an energy to give pure white light in combination with cage **Δ-IrC1**. Titration 4 with CIE coordinates of (0.34, 0.42) exhibits the emission closest in colour to pure white light. The encapsulation of an emitting guest with emission energy intermediate between **Ir5** and **Ir7** into cage into **Δ-IrC1** would therefore be required to achieve a pure white light-emitting assembly.

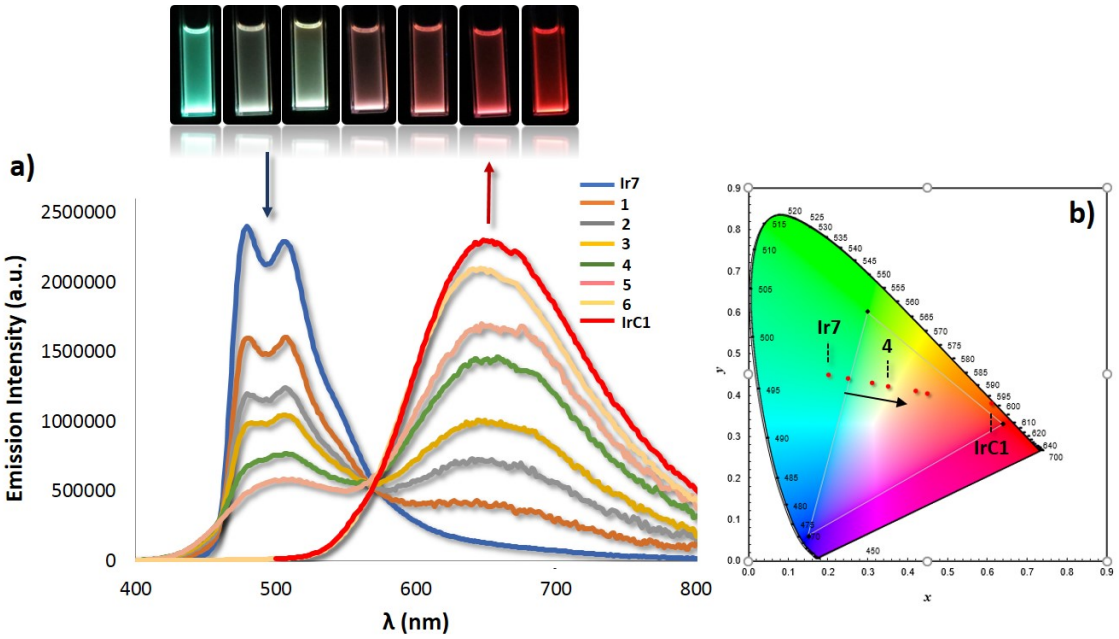

Figure 70. **a)** Emission titrations of **Δ-IrC1** (0 µM: **Ir7**; 10 µM: 1; 30 µM: 2; 50 µM: 3; 80 µM: 4; 100 µM: 5; 120 µM: 6) into a 100 µM solution of **Ir7** at 298 K in degassed DMSO. Insets are images of the emissions of the assembly during the titration. **b)** CIE diagram indicating the change of emission colours during the emission titration.

3.3 Phosphorescent Ruthenium(II) Supramolecular Cage

3.3.1 Synthesis and crystal structure of [Ru(dtBubpy)$_2$(qpy)]2PF$_6$

The synthetic method for preparing the racemic Ru(II) metalloligand [Ru(dtBubpy)$_2$(qpy)]2PF$_6$ (**Ru1**) is illustrated in **Scheme 3**.

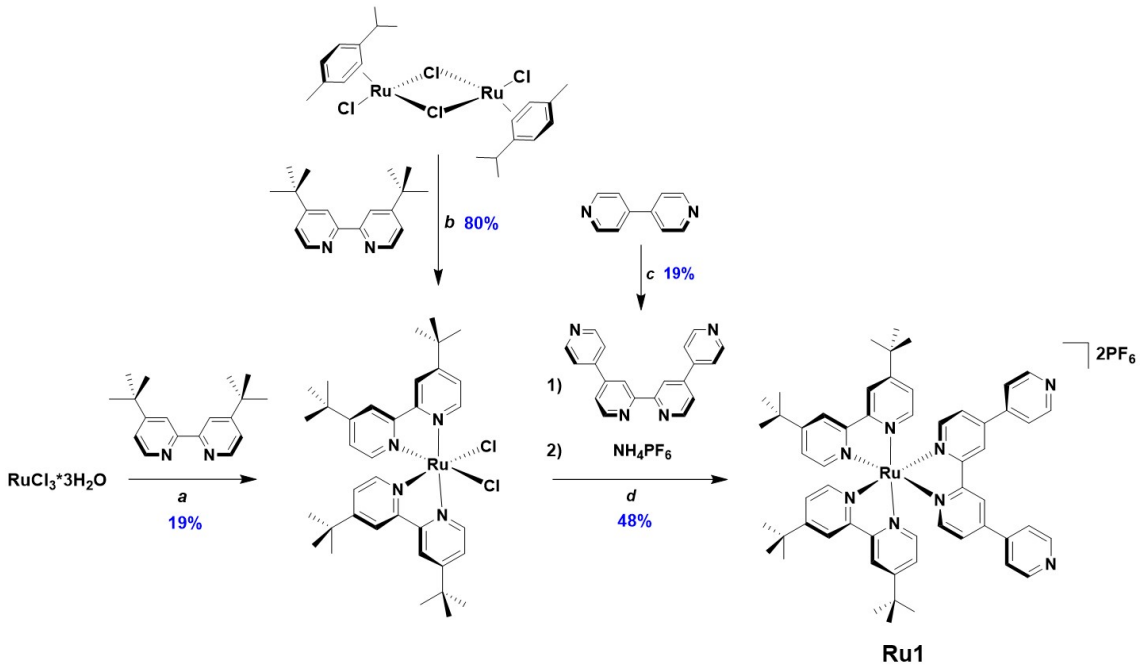

Scheme 3. Synthesis of complex **Ru1**. Reagents and conditions: [a] 4.0 equiv. LiCl, N_2, dark, DMF, 140 °C, 6 h; [b] DMF, 10 mol% Pd/C, 165 °C, 48 h; [c(1)] ethylene glycol, 160 °C, 1 h, N_2; [c(2)] Excess solid NH_4PF_6.

The precursor bis-(4,4′-di-*tert*-butyl-2,2′-bipyridine)-dichloro ruthenium(II), Ru(dtBubpy)$_2$Cl$_2$ could be obtained either by reacting RuCl$_3$·xH$_2$O (1.0 equiv.) or dichloro(p-cymene)ruthenium(II) dimer (1.0 equiv.) with 4,4′-di-*tert*-butyl-2,2′-dipyridyl (2.0 equiv.) following the conditions reported in **Scheme 3**. However, the reaction involving the dichloro(p-cymene)ruthenium(II) dimer afforded Ru(dtBubpy)$_2$Cl$_2$ with a higher yield of 80% compared to that with RuCl$_3$·xH$_2$O (yield: 19%). The subsequent reaction between Ru(dtBubpy)$_2$Cl$_2$ and qpy followed by an anion metathesis reaction using NH_4PF_6 afforded **Ru1** with a yield of approximately 50%. The purity of the complex was confirmed by ^{1}H, ^{13}C NMR spectroscopy, HR-MS and melting point analyses (^{1}H, ^{13}C NMR spectra and HR-MS spectra are reported in the appendix). In addition, crystals of **Ru1** suitable for x-ray diffraction were grown by vapour diffusion of diethyl ether into a CH_2Cl_2 solution of **Ru1**. The x-ray structure of **Ru1** is shown in **Figure 71**. **Ru1** is partially protonated at

both external pyridine nitrogen atoms of the qpy ligand, and the PF_6^- anion balancing this charge was disordered over two sites. When compared to the archetypal $[Ru(bpy)_3](PF_6)_2$ complex,[342] the global geometry of the molecule is not affected by the replacement of the *para* hydrogen atoms of the bpy ligand by 4,4′-di-*tert*-butyl moieties (in dtBubpy) and 4-pyridyl substituents (in qpy). Indeed, in both **Ru1** and $[Ru(bpy)_3](PF_6)_2$, the ruthenium centre adopts a distorted octahedral geometry with similar Ru-$N_{(bpy)}$ distances of around 2.062 -2.070 Å in **Ru1** and 2.062 Å in $[Ru(bpy)_3](PF_6)_2$ and $N_{(bpy)}$-Ru-$N_{(bpy)}$ angles of around 78.2 - 79.0° in **Ru1** and 78.6° in $[Ru(bpy)_3](PF_6)_2$. In **Ru1**, the angle between the distal 4-pyridyl units of the qpy ligand measures 69°.

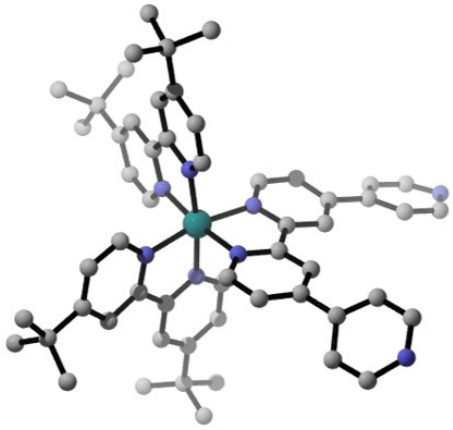

Figure 71. X-ray structure of **Ru1**. Hydrogen atoms, PF_6^- counterions and solvent molecules are omitted for clarity.

3.3.2 Self-assembly of $[Ru_8Pd_4]^{24+}$ cages

The self-assembly of **Ru1** with Pd^{2+} ions was carried out as previously described for the formation of the iridium cages **IrC1** and **IrC2** (**Figure 72a**). Two equivalents of **Ru1** were reacted with $[Pd(NCMe)_4](BF_4)_2$ in DMSO-d_6 at 85 °C for 12 h, while monitoring the formation of the assembly by NMR spectroscopy. As observed during the formation of the iridium cages **IrC1** and **IrC2**, the proton resonances associated with **Ru1** broadened and shifted downfield upon coordination to Pd^{2+} ions in the assembly **RuC1**. The downfield shift of the signals of **RuC1** compared to complex **Ru1**, is particularly evident for the pyridyl α- hydrogen atoms ($\Delta\delta$ = 0.23 ppm), and it is characteristic of metal-pyridine complexation. The broadness of the NMR signals of **RuC1** is indicative of the formation of a large structure, the motion of which is very slow on the NMR time scale. ^{1}H DOSY NMR spectroscopy clearly documents the formation of a single species in solution, the diffusion coefficient of which, measured in DMSO-d_6 was found to be D = 5.3 x 10^{-11} m^2/s. The magnitude of D correlates to the presence of a much larger structure than the metalloligand **Ru1**, which has a diffusion coefficient of 1.3 x 10^{-11} m^2/s in DMSO-d_6 (**Figure 72**). The

calculated hydrodynamic radius (r_s) of the cage is 19.7 Å (**Table S7**, appendix) and is similar to those calculated for the iridium cages **IrC1** and **IrC2** (r_s respectively of 19.8 Å and 20.0 Å).

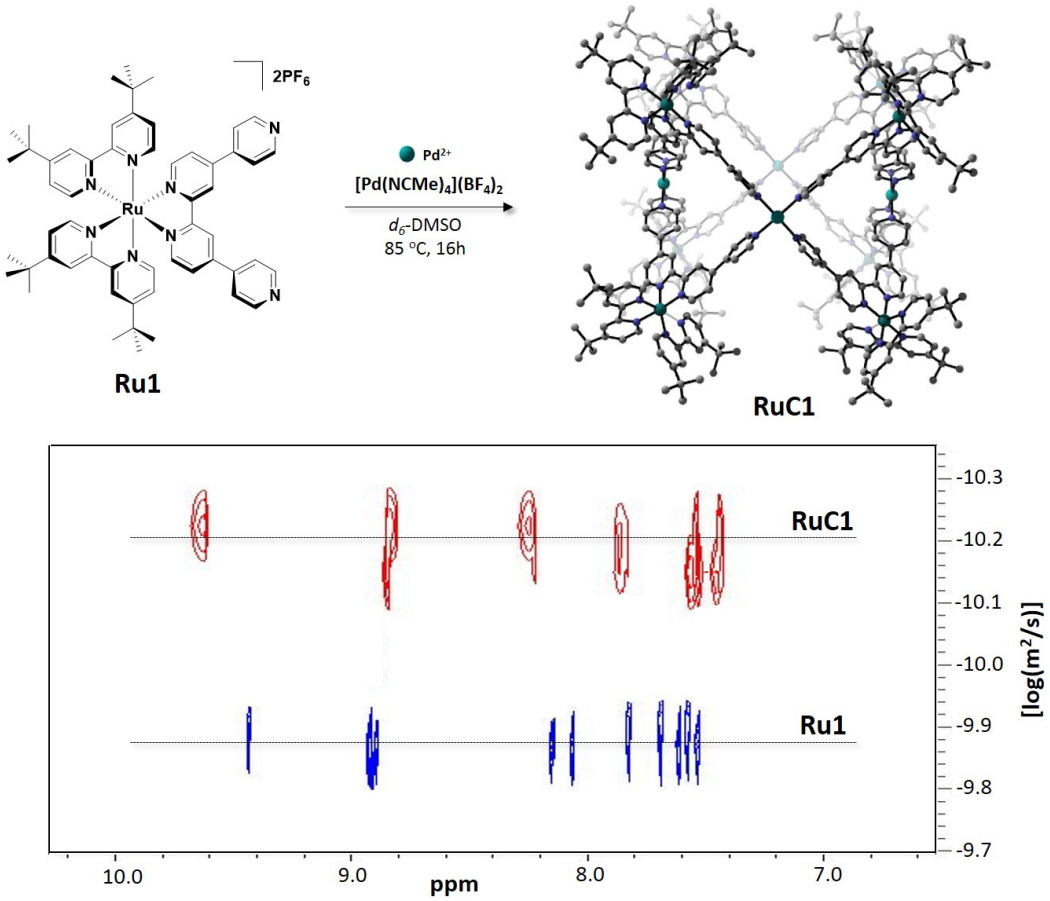

Figure 72. top: Self-assembly between **Ru1**, and Pd^{2+} ions yielding cage **RuC1**. The geometry of **RuC1** has been determined by X-ray diffraction. bottom: ^{1}H DOSY NMR of **Ru1**, in blue and **RuC1**, in red. The ^{1}H DOSY NMR spectra were collected in DMSO-d_6 at 298 K.

The structure of **RuC1** was unambiguously determined by X-ray crystallography (**Figure 73**). Crystals suitable for X-ray analysis were grown by the slow diffusion of a 1:1 mixture of ethyl acetate-hexane into a DMSO solution of **RuC1** (25 mM) over 40 days. The presence of **RuC1** was further corroborated by HR-ESI-MS spectrometry, showing the isotopically resolved peaks for $[(\mathbf{RuC1})\text{-}(BF_4)_n]^{n+}$ (n = 7 - 9) that match with the simulated spectra (**Figures S165-S168** in the appendix). The topology of **RuC1** resembles that reported by Klein *et al.*[333] and is very similar to the simulated structures of **IrC1** and **IrC2** wherein the macrocyclic structure is constructed such that two ligands doubly bridge adjacent Pd(II) centres about the macrocycle in a crown-like fashion, disposing the four palladium ions in a square arrangement. As previously illustrated, the angle between

the coordinating 4-pyridyl units is less than 90° and it is therefore appropriate to form a cage-type structure of composition Pd_4L_8.[298] It is interesting to note that the angle between the coordinating 4-pyridyl units of **RuC1** is smaller than that of the previously reported complex **Ir3**, which showed a coordinating angle of 78°. However, the assembly of both qpy-based complexes with Pd^{2+} ions gave rise to cages of the same Pd_4L_8 topology.

Cage **RuC1** exhibits a diagonal of ca. 39 Å (corresponding to the distance between furthest carbon atoms of opposite t-butyl groups, **Figures 74a**), leading to a radius of the metallamacrocyclic structure based on this diagonal of 19.2 Å and is similar to the hydrodynamic radii obtained by ^{1}H DOSY NMR analysis (r_s = 19.7 Å). The cage shows a distance between neighbouring ruthenium atoms bridging the same Pd···Pd edge of 15.0 Å, and a resulting internal volume of ca. 3700 Å^3, which is comparable with the internal volume of ca. 3480 Å^3 calculated for the simulated structures of the iridium cages **IrC1** and **IrC2**. Notably, **RuC1** represent one of the largest X-ray structure of a Ru(II) cage assembled with Pd(II) reported to date. Relevant examples of x-ray structures of other Ru(II) cages are illustrated in the first chapter.

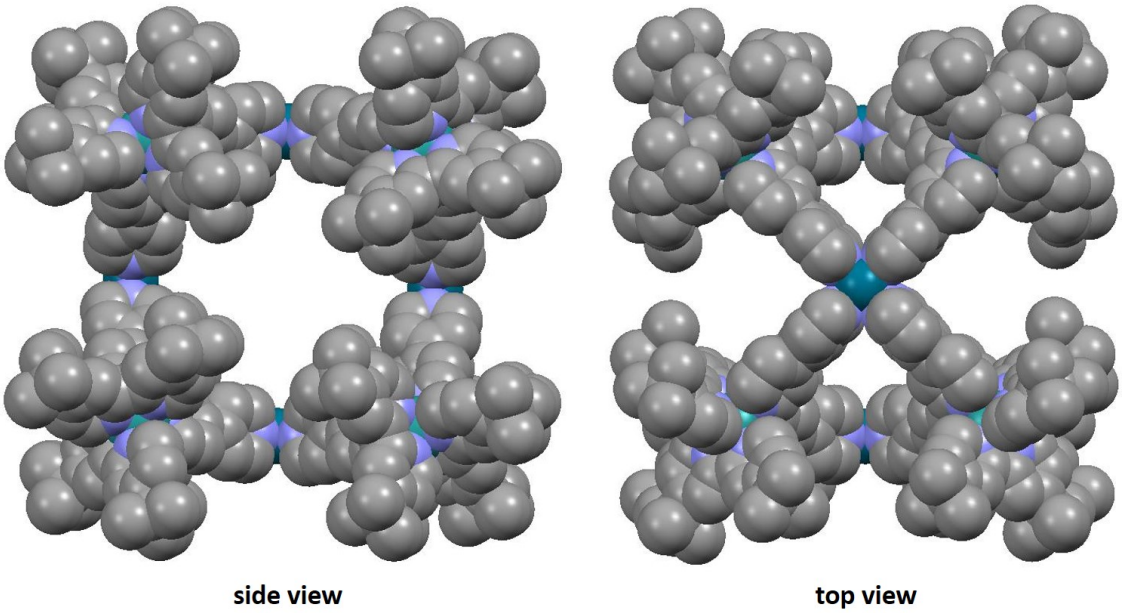

Figure 73. Single crystal X-ray crystal structure of cage **RuC1** viewed down to the crystallographic *a*- (left) and *c*-axes (right). Hydrogen atoms, solvent molecules and counterions have been omitted for clarity.

The nanostructure of cage **RuC1** was probed by Transmission Electron Microscopy (TEM) analysis upon deposition of **RuC1** (concentration of 1 x 10^{-6} M) onto carbon-coated copper grids (**Figure 74b**). The size of the nanostructures of RuPd observed by TEM are of around 4.0 - 4.2 nm, in good agreement with the diagonal distance of 3.9 nm observed for the X-ray structure (**Figure 73**).

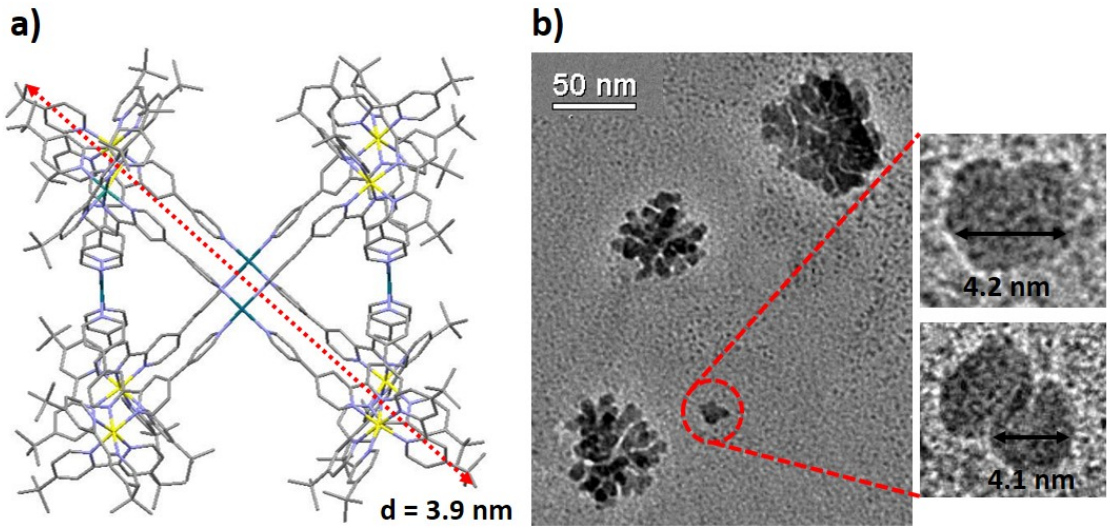

Figure 74. **a)** Illustration of the diagonal distance around the macrocyclic core across long axes of the X-ray structure of **RuC1**. **b)** TEM images of the nanostructures of RuPd.

3.3.3 Emission properties of Ru1 and RuC1

The emission properties of cage **RuC1** have been investigated in CH_2Cl_2 by steady-state and time-resolved photoluminescence spectroscopy and compared with those of the **Ru1** metalloligand (**Table 4**).

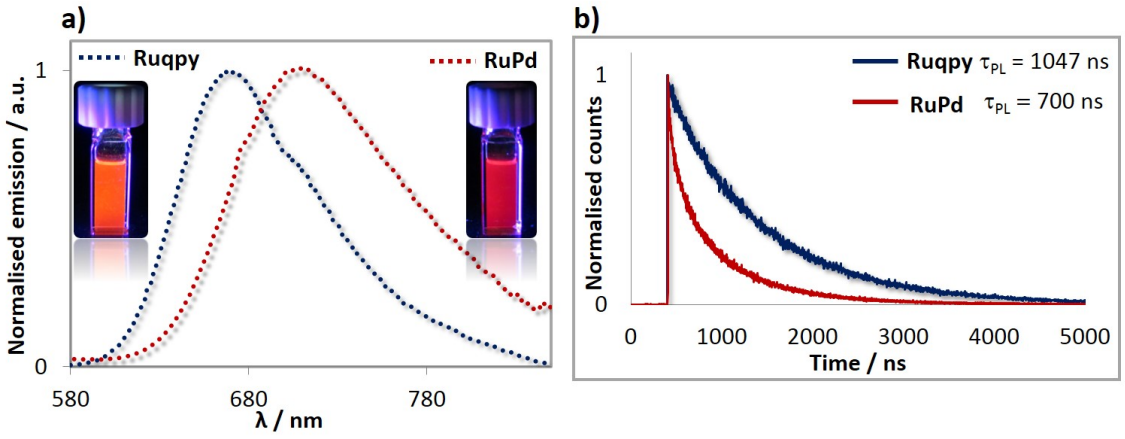

Figure 75. **a)** Normalised emission spectra of **Ru1** (dotted blue line) and **RuC1** (dotted red line) in degassed CH_2Cl_2 at 298 K (λ_{ex} = 360 nm). Photographs of the emissions of **Ru1** (left) and **RuC1** (right) are shown in the inset of the spectra. **b)** emission decays of **Ru1** (blue line) and **RuC1** (red line) in degassed CH_2Cl_2 at 298 K (λ_{ex} = 378 nm).

As described in the first chapter, most of the supramolecular assemblies incorporating Ru(II) metalloligands are either poorly or non-emissive, and examples of luminescent Ru(II)-based supramolecular architectures are extremely rare. However, cage **RuC1** in CH_2Cl_2 exhibit a broad photoluminescence at 710 nm with a Φ_{PL}, of 6.9%, which is red-shifted and comparable in intensity compared to that of **Ru1** (λ_{max} = 674 nm, Φ_{PL} = 7.3%) (**Figure 75a**). Notably, the Φ_{PL} of **RuC1** is one of the highest reported among ruthenium cages. The red-shifted emission of **RuC1** compared to **Ru1** is the result of coordination of the Lewis acidic Pd(II) ions to the Ru complex, which essentially stabilises the π_{qpy} orbital level involved in the emission, and thus lowers the energy of the triplet state. This is in agreement with the red-shifted emissions exhibited by the iridium cages **IrC1** and **IrC2** compared to the corresponding metalloligands **Ir3** and **Ir4**. A more detailed discussion about the energetic of the ruthenium metalloligand **Ru1** corroborated with TD-DFT calculations will be given in the following chapter.

Table 4. Relevant photophysical data for **Ru1** and **RuC1**

	λ_{PL} (nm)	Φ_{PL}(%)[b]	τ_{PL} (ns)[c]	k_r x 10^4 (s^{-1})	k_{nr} x 10^5 (s^{-1})
Ru1	674	7.3	1047	6.97	8.85
RuC1	710	6.9	700	9.86	13.3

[a]Measurements in degassed CH_2Cl_2 at 298 K (λ_{exc} = 360 nm). [b]Φ_{PL} measurements were carried out in degassed CH_2Cl_2 under nitrogen (λ_{exc} = 360 nm) using quinine sulfate as the external reference (Φ_{PL} = 54.6% in 0.5 M H_2SO_4 at 298 K).[287] [c](λ_{exc} = 378 nm)

Both **Ru1** and **RuC1** exhibit mono-exponential photoluminescence decay kinetics with lifetimes, τ_{PL}, of 1047 ns and 700 ns, respectively (**Figure 75b**). As a result, similar radiative rate constants, k_r, of 6.97 x 10^4 s^{-1} and 9.86 x 10^4 s^{-1}, and non-radiative rate constants, k_{nr}, of 8.85 x 10^5 s^{-1} and 13.30 x 10^5 s^{-1} have been calculated for **Ru1** and **RuC1**, respectively (**Table 4**). Thus, the Pd(II) ions do not adversely affect the photophysical properties of this metalloligand. This observation is rather unusual considering that the emissions of the vast majority of metal complexes assembled within cage structures are often partially or completely quenched by the presence of Pd(II) ions,[199, 218] likely due to the population of low-lying dark-states involving the donor and acceptor units. The computational investigation (**Figure 76**; more details are reported in the appendix) of **RuC1** reveals that these low-lying states are also present for **RuC1** (see exemplarily its HOMO and LUMO orbitals in **Figure 76**), which lead to an excited state from *d*-based Ru orbitals to the Pd units. The presence of these parasitic states explains the slightly lower Φ_{PL} value (along with its increased k_{nr} value) for **RuC1** as compared to **Ru1**. The fact that, in this specific case, the photoluminescence is not completely quenched in the cage indicates that the radiative process is fast enough to compete with internal decay to the lowest-lying dark states.

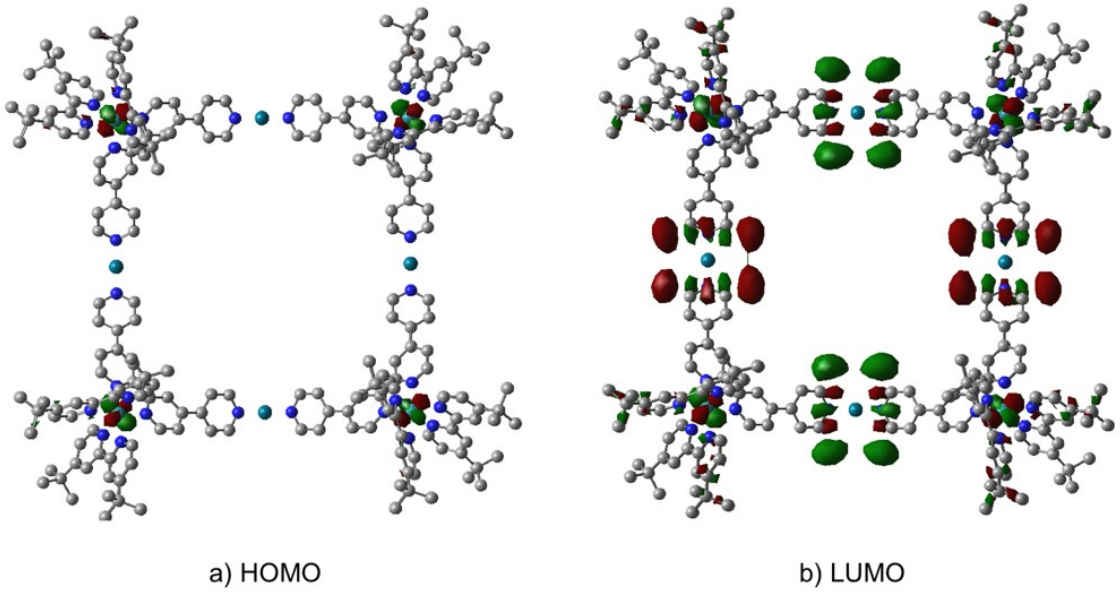

Figure 76. HOMO (a) and LUMO (b) orbitals (B3LYP/6-31G(d)) of the **RuC1** cage. Hydrogen atoms omitted for clarity.

3.4 Conclusions

Phosphorescent and supramolecular Pd_4L_8 metallocages have been prepared by self-assembly between Pd^{2+} ions and two families of metalloligands, *rac*-, Λ- and Δ-[Ir(C^N)$_2$(qpy)]BF_4 (C^N is either mesppy or dFmesppy) and *rac*-[Ir(dtBubpy)$_2$(qpy)]BF_4. The iridium cage **IrC1** selectively encapsulates anionic compounds. Strong binding and efficient energy transfer (k_q of approximately 1.5 x 10^9 $M^{-1}{\cdot}s^{-1}$) between either the anionic blue-emitting or light-blue/green-emitting complexes $[Ir(dFppy)_2(CN)_2]^-$ and $[Ir(ppy)_2(CN)_2]^-$ and the red-emitting cage **IrC1** has been observed. Examples of efficient energy transfer between luminescent guests and photoactive cages are rare. On the other hand, cages based on ruthenium(II) complexes are limited and generally poorly- or non-emissive. Our ruthenium cage **RuC1**, however, exhibited near infra-red emission with a photoluminescence quantum yield of 6.9%, which is remarkably high considering the emission maximum of 710 nm. We believe these cages are promising candidates as chiral photoactive containers capable of absorbing photons and transferring light energy to or from encapsulated guest acceptors and open up the possibility of promoting stereoselective photocatalytic transformations, examples of which at present are exceedingly rare.

Chapter 4

Exploring the Self-Assembly and Energy Transfer of Dynamic Supramolecular Iridium-, Ruthenium-Porphyrin Systems

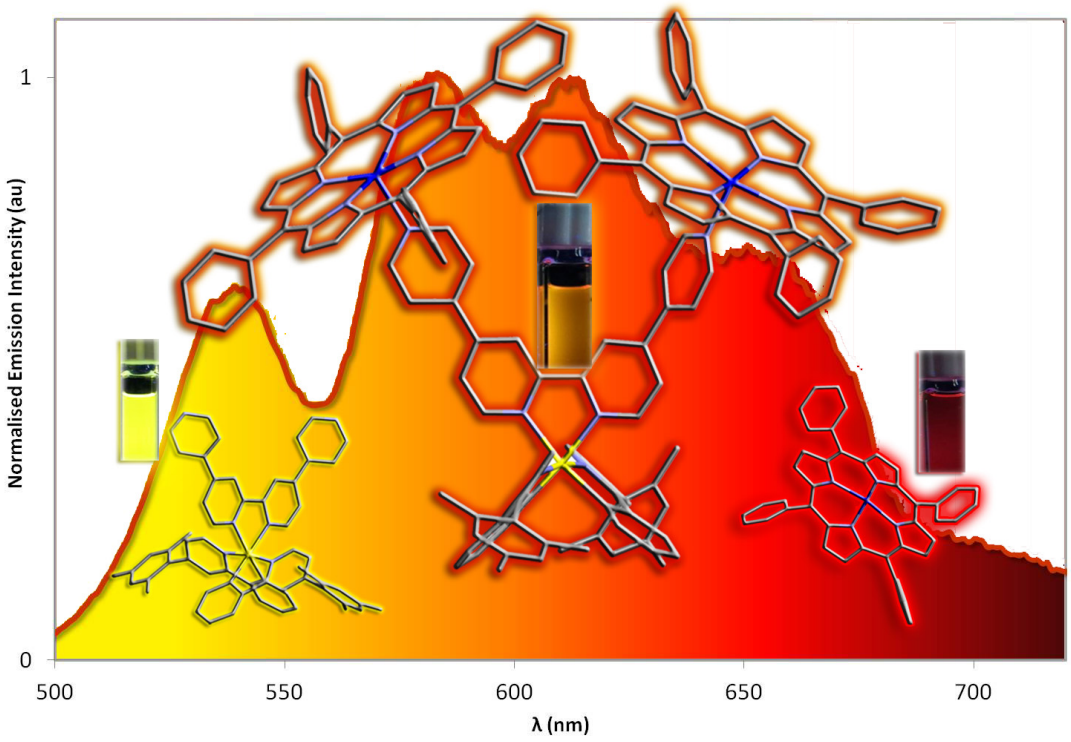

4.1 Introduction

As discussed in the first chapter, the self-assembly of iridium(III) or ruthenium(II) luminophores into supramolecular materials offers possibilities for modulating the physical and optoelectronic properties of the metal complexes and opens up opportunities for exploiting these materials in many applications, including sensing, catalysis and electroluminescent devices. The third chapter discussed the preparation, photophysical properties and potential applications of phosphorescent cages base on Ir(III) and Ru(II) chromophores. However, in recent years much effort has also been devoted to the preparation of artificial donor-acceptor systems based on combinations of multi-chromophoric arrays[343–349] in order to emulate light harvesting in plants. In nature, light-harvesting antennae are composed of different chromophoric units,[40, 43, 350] which are generally linked through non-covalent interactions[351–353] such as hydrogen bonding, salt bridges, metal-ligand coordination or hydrophobic interactions, and are capable of absorbing sunlight and channeling the energy in an efficient way to the reaction centre.

The association between photophysically-active Ru or Re complexes, and metalloporphyrins has been well-explored with the aim of emulating the efficient energy transfer exhibited by light-harvesting antennae in plants.[27, 354–357] As an example, Ziessel and co-workers[358] studied the electronic communication between zinc tetraarylporphyrin (ZnTAP) and a tris(2,2′-bipyridyl)ruthenium(II) complex, covalently connected through a trans-Pt(II)diacetylide fragment bearing tri-n-butylphosphine (trans-C≡CPt$(PBu_3)_2$-C≡C), (schematically [ZnTAP]-[Pt]-[Ru]). Their results demonstrated that a variety of intramolecular energy transfer processes are present although ultimately the ZnTAP acceptor becomes excited following an efficient Förster-type energy transfer (**Figure 77a**). The Pt(II)-diacetylide bridge facilitates strong electronic communication between the two chromophores without contributing to the overall photo-processeses.

There are only a few examples of multi-metallic dyads and triads composed of metalloporphyrins covalently linked to iridium(III) polypyridyl complexes. Soliman and co-workers[359] explored the energy transfer processes in a multi-chromophoric [ZnTAP]-[Pt]-[Ir] dyad where [ZnTAP] is zinc(II) tetraarylporphyrin, [Pt] is a trans-Pt(II)-diacetylide fragment bearing two tri-n-butylphosphine (trans-C≡CPt$(PBu_3)_2$-C≡C), and [Ir] is $[Ir(ppy)_2(bpy)]PF_6$. Surprisingly, despite the same trans-Pt(II)-diacetylide bridge between the ZnTAP and the Ir(III) complex as in Ziessel's compound, no electronic communication between the two units was observed for this system (**Figure 77b**).

Sauvage, Flamigni and co-workers[346] investigated multi-chromophoric triads consisting of zinc and gold tetraarylporphyrins covalently linked to a central iridium(III)-bis(terpyridyl) complex [Ir] (schematically, [ZnTAP]-[Ir]-[AuTAP], where [ZnTAP] is a zinc tetraarylporphyrin and [AuTAP] is a gold tetraarylporphyrin) (**Figure 78**). Through

a series of steady-state and time-resolved spectroscopic studies they showed that upon excitation of either [Ir] or [ZnTAP], efficient and ultrafast electron transfer ($k_{eT} > 5 \times 10^{10}$ s^{-1}) to the [AuTAP] occurred, leading to the formation of a long-lived charge-separated state $[ZnTAP]^{\cdot+}$-[Ir]-$[AuTAP]^{\cdot-}$ No energy transfer was detected for this system.

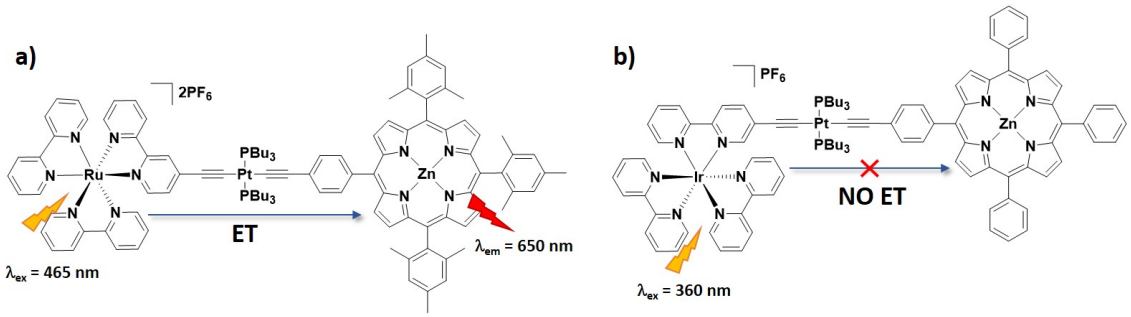

Figure 77. **a)** Energy Transfer (ET) in the multimetallic [ZnTAP]-[Pt]-[Ru] system.[358] **b)** Absence of ET in the multi-chromophoric [ZnTAP]-[Pt]-[Ir] dyad.[359]

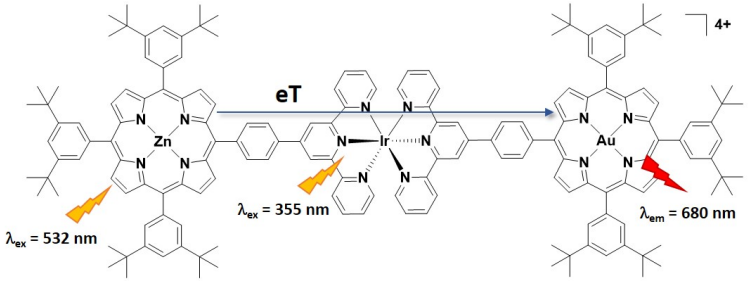

Figure 78.Chemical structure of the multi-chromophoric [ZnTAP]-[Ir]-[AuTAP] array and schematic representation of its electron transfer (eT) processes.

Although the electronic communication between metallo-porphyrins covalently linked to chromophoric organometallic complexes has been well-investigated,[27, 346, 354, 358] supramolecular systems involving metalloporphyrins and photophysically-active complexes remain largely unexplored. Kim and Shin[352] reported a non-covalently linked electron donor–acceptor dyad consisting of zinc tetratolylporphyrin (ZnTTP) and a ruthenium(II) tris-bipyridyl complex linked via axial coordination of the zinc and the distal pyridine moiety of the ruthenium complex (**Figure 79a**). Fluorescence of the porphyrin donor was significantly quenched after coordination with the ruthenium complex as a result of facile electron transfer to the ruthenium acceptor. Hammarstrom *et al.*[360] also observed electron transfer processes in a similar covalently linked dyad system (**Figure 79b**).

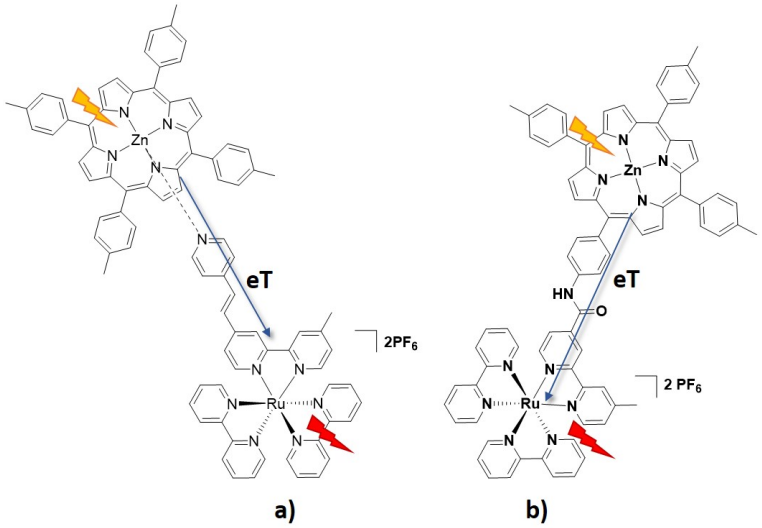

Figure 79. **a)** Schematic representation of electron transfer observed from ZnTTP to the ruthenium centre, which are non-covalently linked together, upon photoexcitation.[352] **b)** electron transfer from ZnTAP to the covalently-connected ruthenium centre.[360]

Many other examples of systems composed of metallo–porphyrins and ruthenium(II) polypyridine conjugates have been investigated.[358, 361, 362] In these systems, as a result of the formation of the charge-separated state following photoinduced electron transfer (PeT) from the porphyrin units to the ruthenium moieties, the phosphorescence of the ruthenium complexes is quenched and only weak porphyrin-centred luminescence is generally detected.

4.2 Experiment design

Herein we report dynamic supramolecular assemblies composed of the Ir(III) complexes **Ir3** and **Ir4** or the Ru(II) complex **Ru1** and zinc tetraphenylporphyrin (ZnTPP) (**Figure 80**). As only the racemic mixtures of the Ir(III) complexes have been investigated in this work, they will be referred from now on simply as **Ir2**, **Ir3**, **Ir4**, omitting the nature of their chiral configuration. In these systems, either one or two ZnTPP complexes can coordinate to one or both of the two distal pyridine rings of the qpy ligand of the Ir or Ru complexes **Ir3**, **Ir4** and **Ru1**, forming the assemblies shown in **Figure 80a,c**. As shown in the previous chapter, the iridium complexes **Ir3** and **Ir4** have different emission energies as a function of their C^N ligands. Thus, with this work we want to explore the electronic communication between the two Ir chromophoric units (as a function of their emission energies) and ZnTPP in the assemblies **IrZn1**, **IrZn2**, **IrZn3** and **IrZn4** (**Figure 80a**). On the other hand, the assembly **RuZn1** and **RuZn2** (**Figure 80c**) has an analogous non-covalent axial coordination between the distal pyridine units of qpy and Zn of ZnTPP compared to the supramolecular ZnTPP–Ru donor-acceptor dyad illustrated

in Figure **79a**. These multi-chromophoric systems are of particular interest as models of supramolecular dyes used in artificial photosynthesis and photoelectrochemical devices. In particular, the subsequent replacement of the dtBubpy ligands in **Ru1** with dcbpy (2,2′-bipyridine-4,4′-dicarboxylic acid) ligands would allow us to transfer this fundamental study of the electronic communication between the ruthenium complex and ZnTPP directly into DSSC application.[363] This design contributes to an improved absorption profile and therefore enhanced short circuit current by combining the absorption profiles of both ZnTPP and the ruthenium complex.[355, 364]

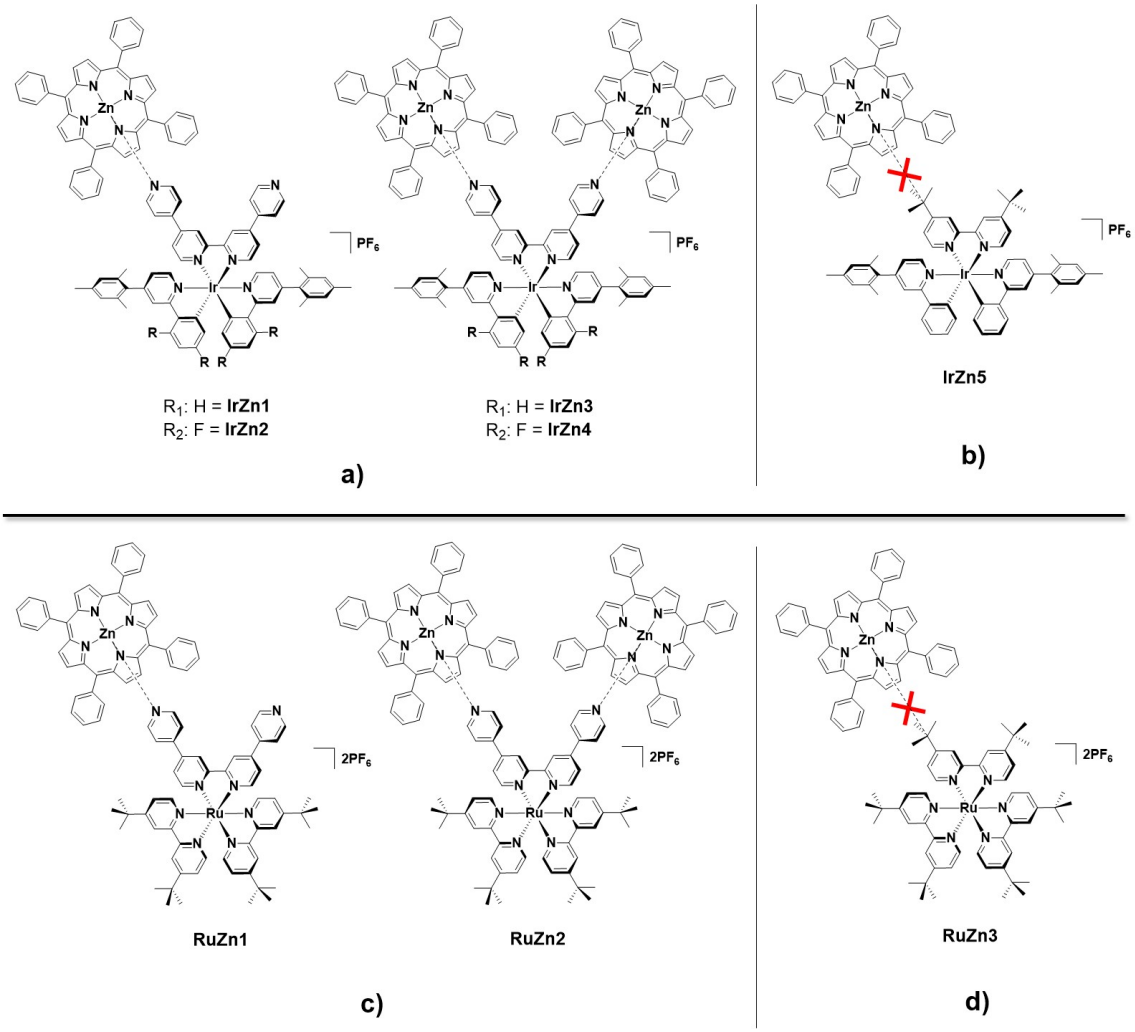

Figure 80. Chemical structures of **a)** the assemblies **IrZn1** (**Ir3**:ZnTPP 1:1 ratio), **IrZn2** (**Ir3**:ZnTPP 1:2 ratio), **IrZn3** (**Ir4**:ZnTPP 1:1 ratio) and **IrZn4** (**Ir4**:ZnTPP 1:2 ratio); **b)** complex **Ir2** mixed with ZnTPP (**IrZn5**) used as a control experiment; **c)** the assemblies **RuZn1** (**Ru1**:ZnTPP 1:1 ratio) and **RuZn2** (**Ru1**:ZnTPP 1:2 ratio); **d)** complex **Ru2** mixed with ZnTPP (**RuZn3**) used as a control experiment.

The use of $[Ir(mesppy)_2(dtBubpy)]PF_6$, **Ir2** and $[Ru(dtBubpy)_3]2PF_6$, **Ru2** provides

a useful negative control in the form of the "non-assembly" **IrZn5** and **RuZn3** (**Figure 80b,d**) to verify the presence/absence of electronic communication between **Ir3**, **Ir4** or **Ru1** and ZnTPP that is a direct result of axial coordination to Zn.

By combining one- and two-dimensional NMR spectroscopy (^{1}H NMR titrations, 2D COSY and HETCOR NMR, and low-temperature ^{1}H NMR spectra), detailed optoelectronic investigations (UV-Vis and Near InfraRed (NIR) absorption spectroscopy, steady-state and time-resolved emission studies, including streak camera measurements for the IrZn assemblies, and cyclic voltammetry experiments) and X-ray single crystal structure analysis for the assemblies **IrZn1** and **IrZn2**, the nature of the interaction and electronic communication between Ir or Ru and Zn in the assemblies **IrZn1**, **IrZn2**, **IrZn3**, **IrZn4**, **RuZn1** and **RuZn2** has been elucidated.

This chapter initially discusses the IrZn assemblies **IrZn1**, **IrZn2**, **IrZn3** and **IrZn4**. The RuZn systems **RuZn1** and **RuZn2** will be discussed afterwards.

4.3 Iridium-phorphyrin assemblies

4.3.1 Synthesis and solution structural elucidation

Assemblies **IrZn1**, **IrZn2** were rapidly obtained after mixing **Ir3** with one or two equivalents of ZnTPP, respectively, in CD_2Cl_2 at room temperature. The analogous assemblies **IrZn3**, **IrZn4** were formed upon mixing **Ir4** with one or two equivalents of ZnTPP (**Figure 80a**). The formation of the assemblies was monitored by ^{1}H NMR, 2D COSY, HMBC and HMQC and ^{19}F NMR experiments (NMR data are reported in the appendix). Crystal structures of **Ir3**, **Ir4**, **IrZn1**, **IrZn2** were obtained through X-ray single-crystal diffraction (*vide infra*), which confirmed the identity of the assemblies under study.

The assignment of all of the resonances in the ^{1}H NMR spectrum of **Ir3**, **IrZn1**, **IrZn2** (**Figure 81** and Figure **S190**, appendix) was carried out using 2D ^{1}H–^{1}H COSY, ^{1}H–^{13}C HMBC and ^{1}H–^{13}C HMQC NMR experiments. After mixing **Ir3** with one equivalent of ZnTPP in CD_2Cl_2 (**IrZn1**, **Figure 81h**), the proton resonances associated with **Ir3** experienced an upfield shift (**Figure 81c**). As expected, the proton resonances associated with the qpy moiety (H_a, H_b, H_c, H_d and H_e in **Figure 81h**) were most sensitive to the axial coordination of the pyridine ring to ZnTPP. After the addition of a second equivalent of ZnTPP, the qpy proton resonances experienced a further upfield (**Figure 81d**). The formation of **IrZn1** and **IrZn2** takes place essentially instantaneously after mixing **Ir3** with ZnTPP and, after their formation, no further changes in the ^{1}H NMR spectra were observed.

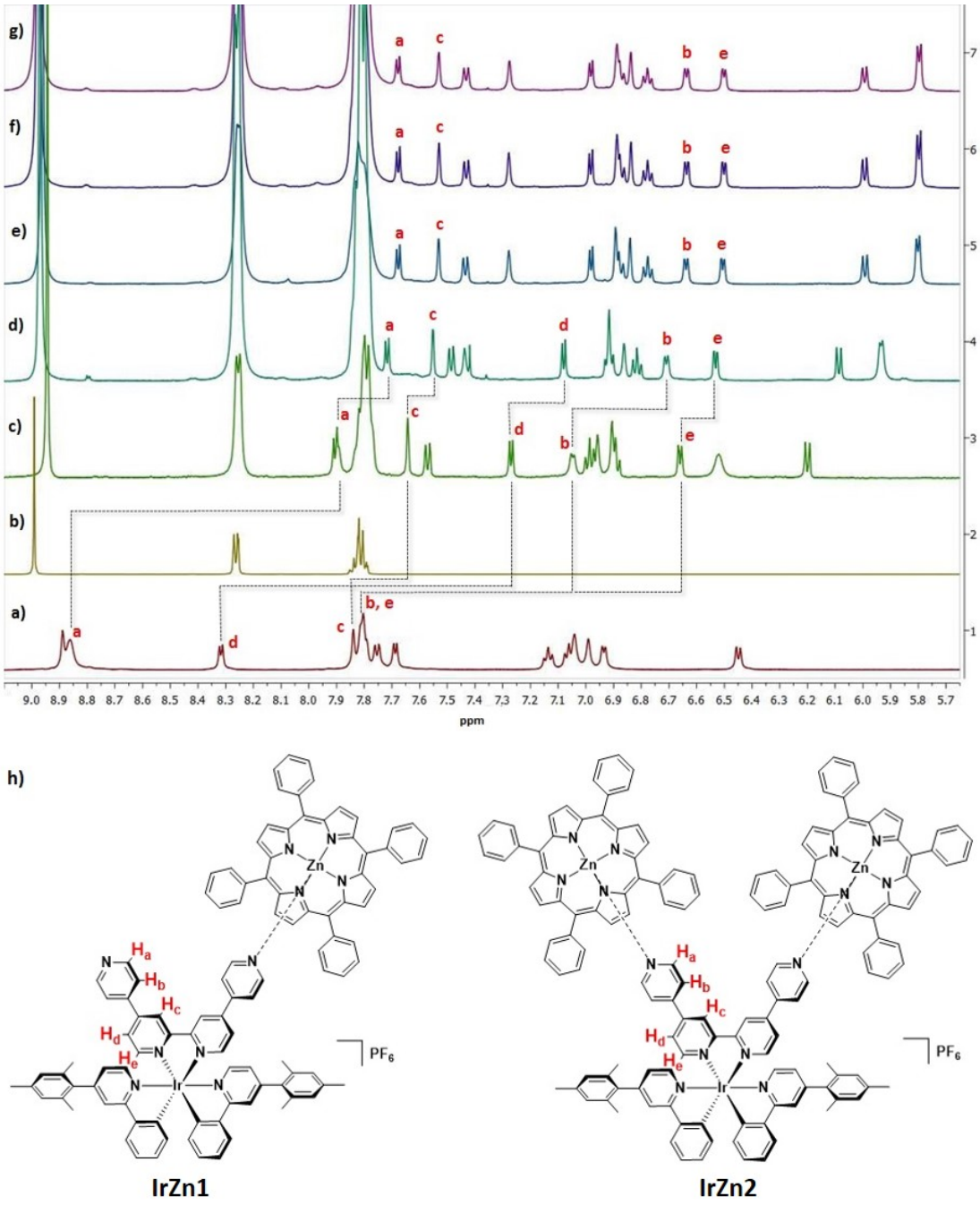

Figure 81. ^{1}H NMR spectra (CD_2Cl_2, 500 MHz) of: **a) Ir3** at a concentration of 3.09 mM (298 K); **b)** ZnTPP at a concentration of 1 mM (298 K); **c)** mixture of **Ir3** (1 equiv., 3.09 mM) and ZnTPP (1 equiv., 3.09 mM) (298 K), speciation (f): **IrZn1**/**IrZn2**: 0.7/0.3; **d)** mixture of **Ir3** (1 equiv., 3.09 mM) and ZnTPP (2 equiv., 6.18 mM) (298 K), speciation (f): **IrZn1**/**IrZn2** : 0.3/0.7; **e)** mixture of **Ir3** (1 equiv., 3.09 mM) and ZnTPP (1 equiv., 3.09 mM) (236 K); **f)** mixture of **Ir3** (1 equiv., 3.09 mM) and ZnTPP (2 equiv., 6.18 mM) (236 K); **g) Ir3** (1 equiv., 3.09 mM) mixed with 4 equivalents of ZnTPP (236 K). The spectral assignments correspond to the labelling scheme in **h)**.

This observation has been described[352, 365, 366] for many axial interactions between N-donor ligands and ZnTPP. The ^{1}H NMR spectrum of **IrZn1** (**Figure 81c**) is relatively simple, indicating a local C_2 symmetry around the iridium centre. This observation suggests that the exchange of bound and unbound ZnTPP is fast compared to the NMR chemical shift timescale and that the ^{1}H NMR spectrum observed reflects a mixed speciation of ZnTPP – both free ZnTPP and ZnTPP bound to **Ir3**. Titration of ZnTTP into a 3.09 mM solution of **Ir3** in CD_2Cl_2 results in the expected upfield shift of the resonance arising from H_a from δ 8.90 to δ 7.55 as the concentration of ZnTPP is increased from 0 to 8.95 mM.

Association constants for the 1:1 complex **IrZn1** and the 1:2 complex **IrZn2** were determined by standard NMR spectroscopic titration methods (see **Figure S191** in the appendix). Small aliquots of ZnTPP were added to a 3.09 mM solution of **Ir3** in CD_2Cl_2 such that the concentration of ZnTPP in the sample carried from 0 mM to 8.95 mM. A ^{1}H NMR spectrum was recorded on the solution after each addition and the variation of the chemical shift of H_a in **Ir3** with respect to ZnTPP concentration determined from this data. This data was then fitted to the sequential binding model shown below using an iterative fitting procedure implemented within the Gepasi program (**Figure 82**). This ^{1}H NMR titration data affords an equilibrium constant of 8000 ± 370 M^{-1} for the formation of **IrZn1** from **Ir3** and ZnTPP and 2000 ± 190 M^{-1} for the formation of **IrZn2** from **IrZn1** and ZnTPP. These data can then be used to construct speciation plots for complexes **IrZn1** and **IrZn2** as a function of the initial concentration and the stoichiometry of the mixture using the parameter scan mode implemented in Gepasi.[367, 368]

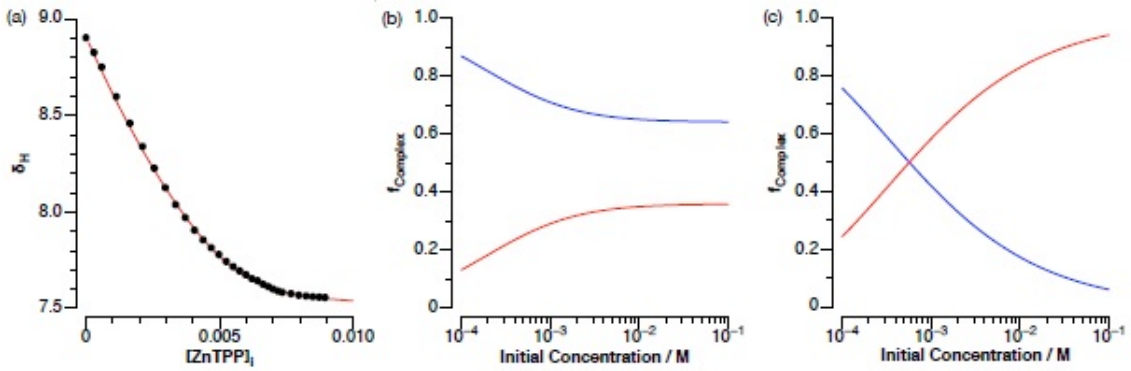

Figure 82. **(a)** the chemical shift changes observed in the ^{1}H NMR spectrum of a 3.09 mM solution of **Ir3** in CD_2Cl_2 upon addition of aliquots of ZnTPP (black points) that are fitted (red line) to a sequential binding model corresponding to the formation of **IrZn1** and **IrZn2**. Fractions of 1 : 1 complex **IrZn1** (blue lines) and 1 : 2 complex **IrZn2** (red lines) present in solution as a function of concentration when **(b)** $[ZnTPP]_{initial} = [\mathbf{Ir3}]_{initial}$ and **(c)** $[ZnTPP]_{initial} = 2$ x $[\mathbf{Ir3}]_{initial}$. As K_d is about 10^{-4} M^{-1}, a little amount of uncomplexed ZnTPP contributes to the spectra plotted in **Figure 82**.

For solutions containing 1 : 1 mixture of **Ir3** and ZnTPP initially, **IrZn1** is the dominant complex at concentrations between 100 µM and 100 mM. For solutions containing 1 : 2 mixture of **Ir3** and ZnTPP initially, **IrZn1** is the dominant complex at concentrations below 600 µM and **IrZn2** is the dominant complex between this concentration and 100 mM. The lower association constant for the binding of the second ZnTPP molecule to form **IrZn2** was expected, as the coordination of a second ZnTPP to **IrZn1** would be somewhat impeded as a result of the steric bulk of the already-bound ZnTPP. The association constants for the formation of **IrZn1** and **IrZn2** are in the range reported for coordination between zinc porphyrins and monotopic nitrogen ligands such as pyridine, with measured association constants ranging between $K_a = 10^2$ and 10^5 M^{-1}.[352, 365]

The low-temperature (236 K) ^{1}H NMR spectra of **IrZn1** (**Figure 81e**), **IrZn2** (**Figure 81f**) and of **Ir3** in the presence of 4 equivalents of ZnTPP (**Figure 81g**) are all similar. These results suggest that at 236 K similar speciation exists, regardless of the relative stoichiometry of **Ir3** and ZnTPP, due to the slowing of the interchange processes between ZnTPP and the two distal pyridine moieties of the qpy ligand. ^{1}H NMR DOSY experiments of **Ir3**, **IrZn1** and **IrZn2** in CD_2Cl_2 at room temperature were carried out in order to estimate the diffusion coefficients of the three entities in solution and the results are reported in the experimental section and in the appendix (**Figure S178, S185**). Although **IrZn1** and **IrZn2** possess higher molecular weights than **Ir3**, similar diffusion coefficients of ca. D = 1.35 x 10^{-9} $m^2 \cdot s^{-1}$ have been obtained for the three entities. These results corroborate the dynamic and weak N–Zn coordination for **IrZn1** and **IrZn2**. As expected, when **Ir2** was mixed with 2 equivalents of ZnTPP no change was observed in the ^{1}H NMR spectra (**Figure S194**, appendix), which clearly confirms that the upfield shifting of the protons in **IrZn1** and **IrZn2** compared to **Ir3** (**Figure 81**) results from N_{py}–Zn coordination.

Competitive displacement assay was also carried out by adding to CD_2Cl_2 solutions of the assemblies **IrZn1** and **IrZn2** the more basic 4-dimethylaminopyridine (DMAP). Following the addition of DMAP to **IrZn1** and **IrZn2**, coordination between ZnTPP with DMAP with concomitant release of **Ir3** was observed by ^{1}H NMR spectroscopy (**Figure S193** in the appendix). In addition, the crystal structure of the ZnTPP-DMAP adduct has been obtained and its x-ray structure matches with that previously reported.[369]

4.3.2 Crystal structures

Crystal structures of **Ir3**, **Ir4**, **IrZn1** and **IrZn2** (**Figure 83**) were obtained through single-crystal X-ray diffraction studies. The crystal structures of ZnTPP coordinated to diethyl ether was also obtained and are presented in the appendix (**Figure S196** in the appendix), along with crystallographic data for all complexes. Diffraction for assemblies **IrZn1** and **IrZn2** was very weak, but despite this, the structures of the two complexes could be unambiguously determined.

As for complexes ***rac-***, **Λ-** and **Δ-Ir1** and ***rac-***, **Λ-** and **Δ-Ir2** reported in chapter 2, in **Ir3**, **Ir4**, **IrZn1** and **IrZn2** the iridium center adopts a distorted octahedral geometry, with the two nitrogen atoms of the C^N ligands mutually trans while the two nitrogen atoms of the qpy ligand disposed trans with respect to the two Ir–C_{C^N} bonds. Notably, the geometries (bond lengths and angles) of **Ir3** do not differ markedly from those of **IrZn1** and **IrZn2**, indicating little perturbation of the local structure of iridium upon coordination of **Ir3** with ZnTPP.

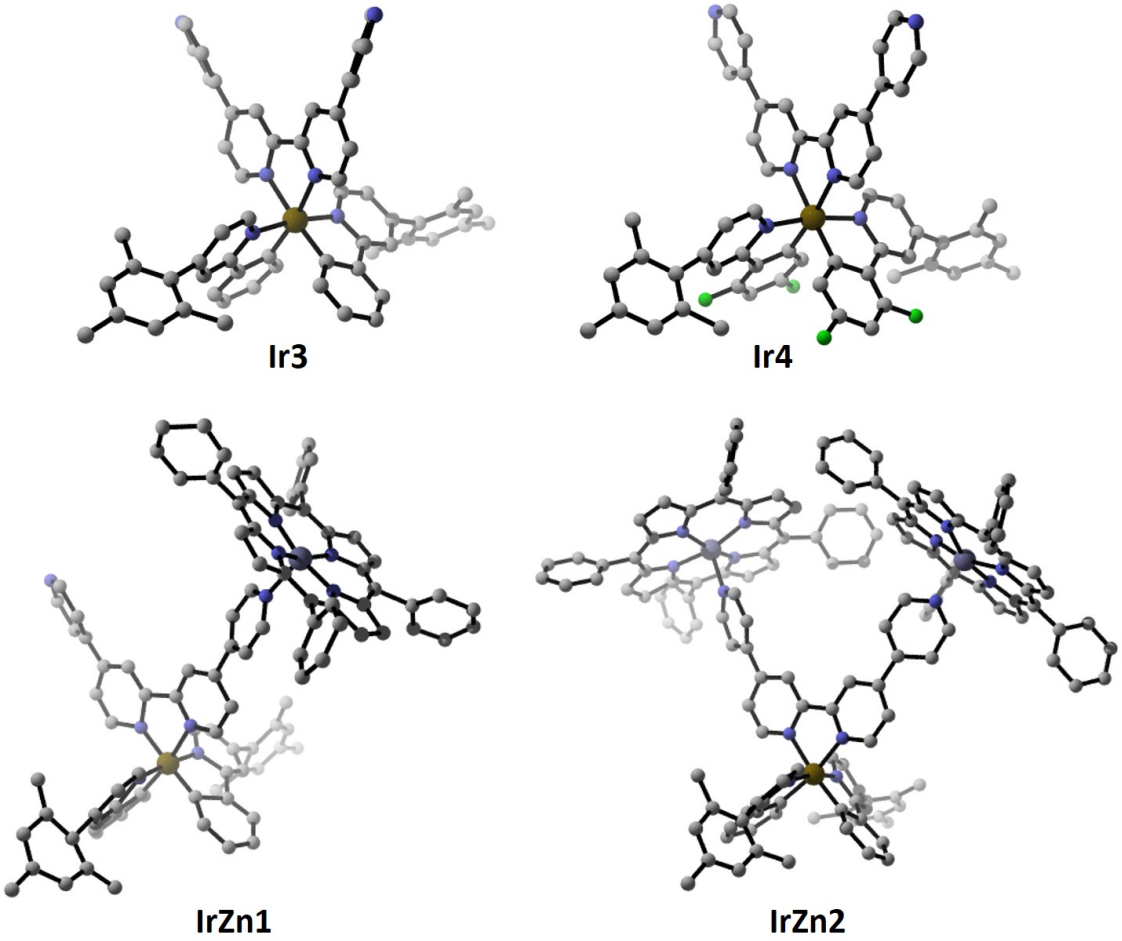

Figure 83. Views of the structures of **Ir3** and **Ir4** (top) and **IrZn1** and **IrZn2** (bottom), with PF_6^- anions, solvent molecules, minor disorder components and hydrogen atoms omitted for clarity.

For all three structures the Ir–N_{C^N} bonds are ca. 2.03 Å, the Ir–C_{C^N} bonds are ca. 2.00 Å, and the Ir–N_{N^N} bonds are ca. 2.12 Å, which are close to the values reported for other $[Ir(C^N)_2(N^N)]PF_6$ complexes.[11, 280, 284] In each complex, an orthogonal orientation of the mesityl ring with respect to the pyridine ring is observed (torsion angles of ca. 90.5°). This feature was also observed in the crystal structures of ***rac-***, **Λ-** and **Δ-Ir2** and of other mesityl-containing iridium complexes.[278, 280] The four pyridine rings

of the qpy moiety in each of **Ir3**, **Ir4**, **IrZn1** and **IrZn2** are not completely coplanar but instead adopt a torsion angle of approximately -40° between each of the two distal pyridine rings and the central bipyridyl moiety. In all the structures, the bond angles between the iridium centre and the qpy ligand (N_{qpy}–Ir–N_{qpy}) are essentially the same, ranging between 76.29(19) and 79.2(7)°. In **IrZn1** and **IrZn2**, the Zn–$N_{pyridyl}$ bond distances are approximately 2.15 Å, which are in agreement with the typical bond length values between N-donor ligands and ZnTPP.[369, 370] In **IrZn1** and **IrZn2** the qpy moieties show vector angles of, respectively, 74.16 and 64.68° (**Figure 84**) appropriate to accommodate either one or two ZnTPP molecules around one iridium complex resulting in Ir···Zn separations of 11.22 – 11.33 Å.

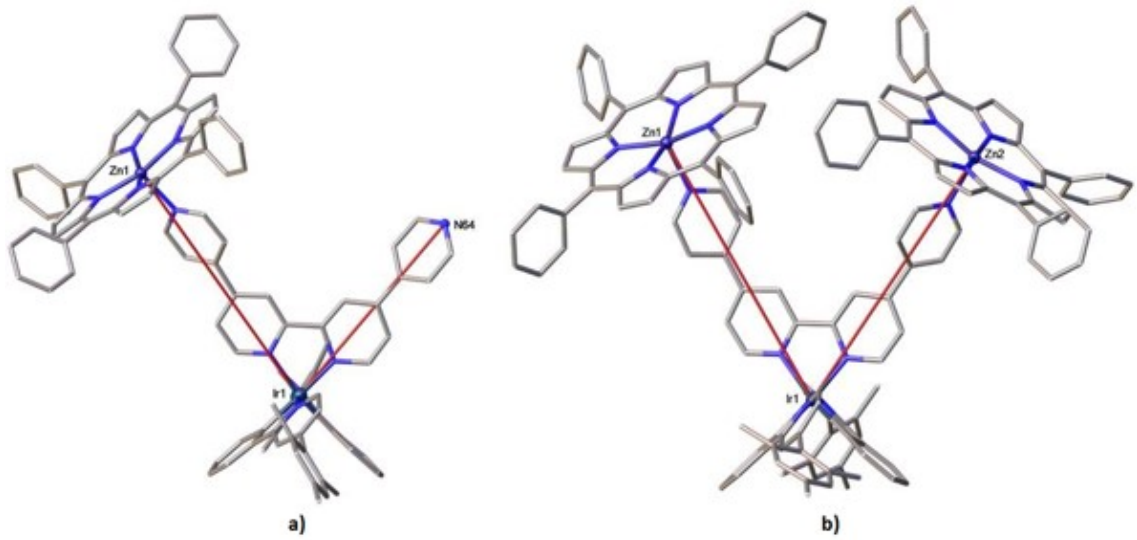

Figure 84. Views showing the relative orientation and positions of the ZnTPP and [Ir(C^N)$_2$] centres in **IrZn1 (a)** and **IrZn2 (b)**, with Ir···N or Ir···Zn vectors highlighted in red. Selected distances (Å) and angles (°): **IrZn1** Ir1···Zn1 11.33; Zn1-Ir1-N64 74.16. **IrZn2** Ir1···Zn1 11.22, Ir1···Zn1 11.24; Zn1-Ir1-Zn2 64.68.

4.4 Photophysical properties

4.4.1 Absorption

The optoelectronic properties of all compounds were investigated in CH_2Cl_2 solutions at varying concentrations between 5 x 10^{-4} M (above K_d) and 1 x 10^{-6} M (below K_d) at room temperature and the results are summarised in **Table 5, Table 6** and **Table S11**. In addition, DFT and TD-DFT calculations (see computational details in the appendix)

were performed to gain insights into the nature of the electronic transitions of the different complexes and assemblies. At a concentration of 1 x 10^{-6} M, less than 1% of ZnTPP is actually bound to the qpy ligand in **IrZn1**, **IrZn2**, **IrZn3** and **IrZn4** whereas at a concentration of 5 x 10^{-4} M ca. 90% of the ZnTPP is bound to the iridium complex. After mixing **Ir3** and ZnTPP in a 1:1 ratio at a concentration of 5 x 10^{-4} M, a speciation of **IrZn1** : **IrZn2** = 0.75 : 0.25 exists while after mixing **Ir3** (at a concentration of 5 x 10^{-4} M) with two equivalents of ZnTPP, a speciation of **IrZn1** : **IrZn2** = 0.55 : 0.45 is formed.

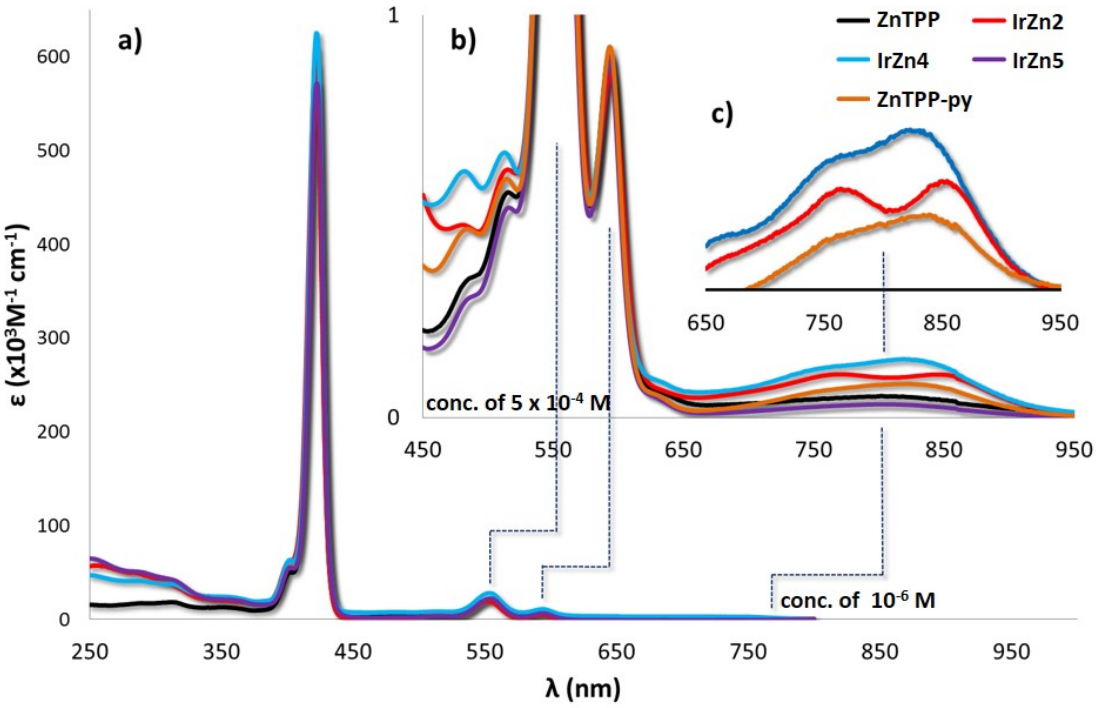

Figure 85. **(a)** UV-Vis absorption spectra of ZnTPP, **IrZn2**, **IrZn4** and **IrZn5** recorded in CH_2Cl_2 at 298 K at a concentration of approximately 10^{-6} M. **(b)** NIR-absorption spectra from 450 to 950 nm of ZnTPP, **IrZn2**, **IrZn4** and **IrZn5** and ZnTPP-pyridine recorded in CD_2Cl_2 at 298 K at a concentration of 5 x 10^{-4} M. **(c)** Expansion of the NIR-absorption spectra from 650 to 950 nm of ZnTPP, **IrZn4** and **IrZn5** and ZnTPP-pyridine after mathematical subtraction of the NIR-absorption of uncomplexed ZnTPP attributed to the formation of J-aggregates.

The UV-Visible (UV-Vis) and Near Infra-Red (NIR) absorption spectra of ZnTPP, **IrZn2**, **IrZn4** and **IrZn5** and ZnTPP coordinated to pyridine (ZnTPP-py, used as a reference assembly) are shown in **Figure 85a** while the UV-Vis absorption spectra of complexes **Ir2**, **Ir3** and **Ir4** are shown in **Figure 86**. The absorption spectra of all the iridium complexes are characterised by two intense bands between 260 nm and 330 nm and a broad, lower-intensity band at around 390 nm. These bands are well reproduced

by the TD-DFT calculations using the B3LYP exchange–correlation functional (see, for example, the UV-Vis spectra of **Ir3** and **Ir4** in **Figure S225** and **S228**, respectively in the appendix). In line with other cationic iridium complexes of the form $[Ir(C\hat{}N)_2(N\hat{}N)]^+$,[280, 284] the two higher energy bands are theoretically assigned to spin allowed $^1\pi \rightarrow \pi^*$ (^{1}LC transitions) localised on the C^N ligands, while the broad bands at wavelengths > 350 nm are due to several (^{1}MLCT/^{1}LLCT) transitions. This absorption band in **Ir4** is blue-shifted (λ_{max} ca. 360 nm) compared to **Ir3** due to presence of the electron- withdrawing fluorine atoms on the C^N ligands, which stabilise the highest occupied molecular orbital (HOMO) and consequently increase the band gap. The energy levels of the frontier orbitals of **Ir3** and **Ir4** obtained by DFT calculations are given in **Figure S226** in the appendix.

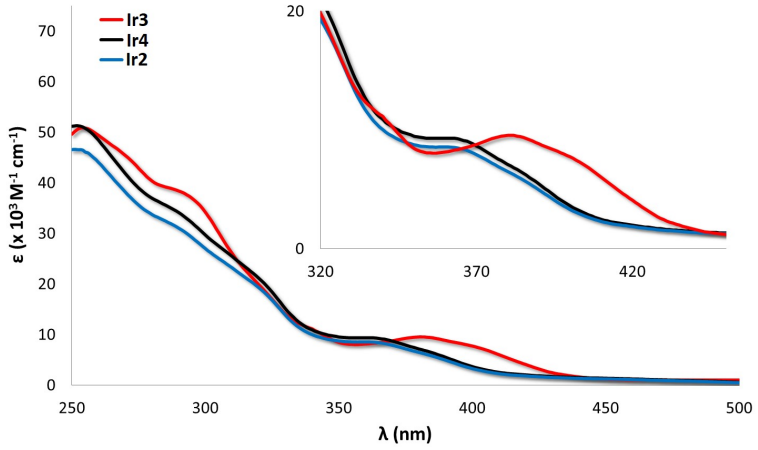

Figure 86. UV-Vis spectra of **Ir3** (in red), **Ir4** (in black) and **Ir2** (in blue) collected in CH_2Cl_2 at 298 K with a concentration on the order of 10^{-6} M.

The UV-Vis absorption spectrum of ZnTPP (**Figure 85a**) is characterised by two major bands. The intense absorption between 400 and 430 nm (Soret band) is due to a $^1\pi \rightarrow \pi^*$ transition (S_2) localised on the porphyrin moiety while the low intensity absorption band between 500 and 600 nm shows vibronic structures and originates from the $^1\pi \rightarrow \pi^*$ electronic excitation (S_1), the so-called Q-bands.[358, 371] As shown in **Figure S227** in the appendix, good agreement between the experimental UV-Vis spectrum of ZnTPP and its computed TD-DFT results is obtained. The absorption spectra of **IrZn2**, **IrZn4** and **IrZn5** collected at a concentration of approximately 10^{-6} M (association <1%) are very similar in profile to that of ZnTPP and show the sum of the absorptivities of the iridium complexes and ZnTPP, without any significant interactions between the two (**Figure 85a**).

NIR absorption spectroscopy of ZnTPP, **IrZn2**, **IrZn4** and **IrZn5** and ZnTPP-py collected in CH_2Cl_2 at a concentration of 5 x 10^{-4} M are shown in **Figure 85b**. For metallo-porphyrins, the presence of broad and weak absorption bands between 820 and 850 nm are generally ascribed to the formation of molecular aggregates, which can occur at a

concentration higher than 10^{-5} M.[372, 373] Indeed, in each of ZnTPP, ZnTPP-py, **IrZn2**, **IrZn4** and **IrZn5**, there is a weak and broad absorption band centred at approximately 800 nm. However, compared to ZnTPP, which shows a single broad and unstructured absorption band in the NIR, there are two distinct bands observed with enhanced absorptivity at 768 and 853 nm for **IrZn2** and 755 and 827 nm for **IrZn4**, respectively. This behavior matches the profile of ZnTPP-py, which was formed in situ upon addition of an excess pyridine to ZnTPP (**Figure 85b**). By contrast, for **IrZn5**, where no coordination between the chromophoric units takes place, the NIR absorption profile is very similar to that of ZnTPP. Importantly, for metallo-porphyrins spin-forbidden singlet–triplet transitions are possible and, as previously reported, the axial coordination between N-donor ligands and ZnTPP can easily perturb the lowest triplet excited states of ZnTPP.[374] From our experiments, the enhanced absorptivity in the NIR observed for **IrZn2** and **IrZn4** seems to be primarily due to perturbation the triplet state of ZnTPP, which is promoted by the axial coordination between the distal pyridines of **Ir3** and **Ir4** with ZnTPP; though porphyrin aggregation cannot be ruled out as contributing to this absorption band. In view of the TD-DFT results, the NIR absorption observed for **IrZn2** and **IrZn4** can tentatively be assigned to T_1 and T_2 (both located at 750 nm). Note that, within the computational approach employed, the triplet excitation energies have no intensity because spin–orbit coupling (SOC) was neglected. Notably, the absorption spectra shown in **Figure 85b** are the weighted superposition of the assemblies and free mononuclear complexes ZnTPP, **Ir3** and **Ir4**. **Figure 85c** shows the deconvoluted absorption spectra for **IrZn2**, **IrZn4** and ZnTPP-py after mathematical subtraction of the absorption spectrum of unbound ZnTPP. The remarkable enhancement of the NIR absorption in **IrZn2** and **IrZn4** showcases the sensitivity of the triplet excited-state of ZnTPP to the presence and nature of the axially bound ligand. As a result, upon coordination to ZnTPP, new CT singlet and triplet excited-states arise in the assemblies. A very low intensity $\pi_{\text{porphyrin}} \rightarrow \pi^*_{\text{bpy}}$ CT transition (S_1), which is predicted by TD-DFT to occur at 736 nm (using the CAM-B3LYP functional for this obviously long-range CT transition), might importantly contribute (along with the ZnTPP-based lowest triplet excited states) to the low-energy UV-Vis bands. These new bands significantly contribute to the observed enhancement of the NIR features of the assemblies.

4.4.2 Electrochemical properties

The ground-state electronic communication between the iridium and ZnTPP moieties in **IrZn1**, **IrZn2**, **IrZn3** and **IrZn4** has been investigated by cyclic voltammetry, the data of which is reported in **Table 5**. The cyclic voltammograms (CVs) of **Ir3**, ZnTPP, **IrZn1**, **IrZn2** are shown in **Figure 87a** as representative examples, while CVs of **Ir4**, **IrZn3**, **IrZn4** are reported in the appendix, **Figures S221, S222**). The CVs of **Ir2** and **IrZn5** as control experiments are reported in **Figure 87b**.

The CVs were recorded in deaerated CH_2Cl_2 solution containing n-NBu_4PF_6 as the supporting electrolyte and using Fc/Fc^+ as an internal standard at 298 K at a concentration of the iridium complexes of 1.46 x 10^{-3} M. At this concentration, for **IrZn1**, **IrZn2**, **IrZn3**, **IrZn4**, we can consider ZnTPP as completely bound to the pyridine moieties of **Ir3** and **Ir4**. After mixing **Ir3** and ZnTPP in a 1 : 1 ratio, a speciation of **IrZn1** : **IrZn2** = 0.70 : 0.30 exists, while after mixing **Ir3** with two equivalents of ZnTPP, a speciation of **IrZn1** : **IrZn2** = 0.40 : 0.60 is formed.

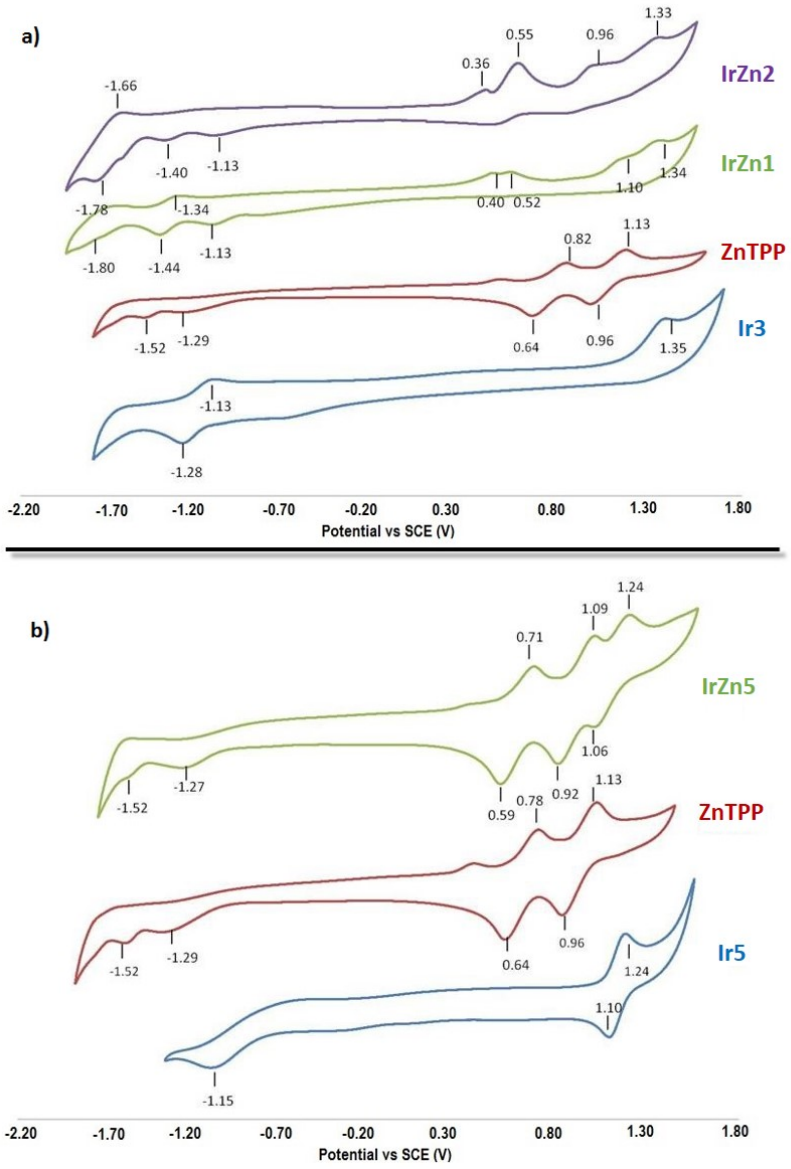

Figure 87. **(a)** CVs for **Ir3**, ZnTPP, **IrZn1** and **IrZn2** and **(b)** CVs for **Ir2**, ZnTPP and **IrZn5** recorded at 298 K in deaerated CH_2Cl_2 solution containing n-NBu_4PF_6 as the supporting electrolyte and using Fc/Fc^+ as an internal standard ($Fc/\ Fc^+$ = 0.46 V in CH_2Cl_2 with respect to SCE).[375]

In agreement with the previously reported electrochemistry,[376] ZnTPP exhibits two mono-electronic irreversible reduction processes that are ascribed to the formation of the porphyrin radical anion $[porph]^{\cdot-}$ and dianion species $[porph]^{2-}$ at E^{pc} = -1.29 V and -1.52 V, respectively. There are two mono-electronic reversible oxidation processes due to the formation of the porphyrin radical cation $[porph]^{\cdot+}$ and dication species $[porph]^{2+}$ at $E^{ox}_{1/2}$ = 0.73 V and 1.05 V, respectively (ZnTPP in **Figure 87**). Similar to the CVs of other cationic heteroleptic Ir(III) complexes,[259] **Ir3** exhibits one quasi-reversible reduction wave at $E^{red}_{1/2}$ = -1.21 V attributed to the first reduction of the qpy ligand (note that the LUMO is located on this ligand, as shown in **Figure S226** in the appendix) and one irreversible oxidation at E^{pa} = 1.35 V assigned to the Ir(III)/Ir(IV) redox couple with significant contribution from the C^N ligands (**Ir3** in **Figure 87a**, see also the HOMO in **Figure S226**).

Table 5. Relevant electrochemical data for ZnTPP, **Ir3**, **IrZn1**, **IrZn2**, **Ir4**, **IrZn3**, **IrZn4**, **Ir2**, **IrZn5**, ZnTPP-py

	E^{ox} (V)	E^{ox} (V)	E^{ox} (V)	E^{red} (V)	E^{red} (V)	E^{red} (V)	$E_{0,0}$ (eV)[c]
ZnTPP	0.73[a]	1.05[a]	-	-	-1.29[b]	-1.52[b]	2.19
Ir3	-	-	1.35[b]	-1.20[a]	-	-	2.21[d]
IrZn1	0.40[b]	1.10[b]	1.34[b]	-1.13[b]	-1.39[b]	-1.80[b]	-
IrZn2	0.36[b]	0.96[b]	1.33[b]	-1.13[b]	-1.40[b]	-1.72[b]	-
Ir4	-	-	1.46[b]	-1.26[b]	-1.45[b]	-	2.55
IrZn3	0.68[b]	-	1.41[b]	-1.25[b]	-1.43[b]	-	
IrZn4	0.67[b]	-	1.40[b]	-1.19[b]	-1.29[b]	-	
Ir2	-	-	1.17[a]	-1.15[b]	-	-	2.55
IrZn5	0.65[a]	1.01[a]	1.15[a]	-1.27[b]	-1.52[b]	-	-
ZnTPP-py	0.37[a]	0.69[a]	-	-	-1.31[a]	-1.73[a]	-

CV traces recorded in CH_2Cl_2 solution with 0.1 M n-NBu_4PF_6 at 298 K at 50 mV·s^{-1}. Values are in V vs. SCE (Fc/Fc^+ vs. SCE = 0.46 V). [a]$E_{1/2} = (E_{pa} + E_{pc})/2$ and result from one-electron processes. [b]Irreversible oxidation and reduction peak potentials. [c]$E_{0,0}$ estimated from the intersection point of the absorption and emission spectra at 298 K in CH_2Cl_2. [d]$E_{0,0}$ estimated from 10% of the onset of the absorption spectra at 298 K in CH_2Cl_2.

For the assemblies **IrZn1** and **IrZn2**, the oxidation potentials localised on the iridium complex are only slightly cathodically shifted compared to **Ir3** (E^{pa} = 1.35 V for **Ir3** vs. E^{pa} = 1.34 V for **IrZn1** and E^{pa} = 1.33 V for **IrZn2**). However, remarkable changes are observed for the redox processes localised on ZnTPP. Indeed, compared to ZnTPP, the

Zn-centred oxidation waves of both **IrZn1** and **IrZn2** exhibit a cathodic shift ($E^{ox}_{1/2}$ = 0.40 V for **IrZn1**, $E^{ox}_{1/2}$ = 0.36 V for **IrZn2** vs. $E^{ox}_{1/2}$ = 0.73 V for ZnTPP) and their first reduction processes are likewise cathodically shifted ($E^{red}_{1/2}$ = -1.39 V for **IrZn1**, $E^{red}_{1/2}$ = -1.40 V for **IrZn2** vs. E^{pc} = -1.29 V for ZnTPP). This behavior mirrors the electrochemistry of ZnTPP coordinated with N-donor electron-donating ligands,[366, 376, 377] making the ZnTPP more easily oxidised and less easily reduced. The CV of ZnTPP coordinated with pyridine (ZnTPP-py) (**Figure S222**, appendix) corroborates the observed trends in the CVs for **IrZn1** and **IrZn2**, where both the reduction and the oxidation waves of ZnTPP-py are shifted cathodically ($E^{ox}_{1/2}$ = 0.69 V, $E^{ox}_{1/2}$ = 0.36 V, $E^{red}_{1/2}$ = -1.61 V) relative to ZnTPP.

The electrochemistry of **Ir3**, **IrZn3** and **IrZn4** was also investigated (**Figure S221**, appendix) and the trends match those presented above. CVs of **Ir2** and **IrZn5** are shown in **Figure 87b**. In deaerated CH_2Cl_2, **Ir2** exhibits one irreversible reduction at E^{pc} = –1.15 V attributed to the reduction of the dtBubpy ligand and one reversible oxidation at $E^{ox}_{1/2}$ = 1.17 V, assigned to the Ir(III)/Ir(IV) redox couple with contribution from the C^N ligands (**Ir2** in **Figure 87b**).[378] In line with NMR and absorption data, the CV of **IrZn5** contains the superposition of the CVs of **Ir2** and ZnTPP. These control experiments show that, as expected, there is no ground-state electronic communication between **Ir2** and ZnTPP.

4.4.3 Emission studies

The emission properties of the complexes **Ir2**, **Ir3** and **Ir4** were previously discussed in chapter 2 and 3. Upon excitation of ZnTPP into either the Soret or Q bands (λ_{exc} = 420 or 550 nm, respectively), a vibronic emission, characteristic of ZnTPP,[371] is observed between 570 and 740 nm (light blue line in **Figure 88**).

In order to investigate the nature of the emission of **IrZn1**, **IrZn2**, **IrZn3** and **IrZn4** and the presence of energy and/or electron transfer between the iridium moiety and ZnTPP, these assemblies were excited into both the ^{1}CT band (centred on the iridium complex, λ_{exc} = 360 nm), and the Soret and Q bands at concentrations of 3 x 10^{-5} M and 5 x 10^{-4} M. Unfortunately, the emission of **Ir3** and ZnTPP coincidentally overlap and consequently the study of this system proved challenging (**Figure 88a**). In contrast, due to the introduction of the fluorine atoms on the C^N ligands, the emissions of **Ir4** and ZnTPP are better resolved (**Figure 88b**), which makes this system much more amenable towards the study of electronic communication between the chromophores.

As reported in **Table 6**, assemblies **IrZn3** and **IrZn4** show decreased Φ_{PL} of 10% and 6.2%, respectively, after excitation at 360 nm; Φ_{PL} for each is ca. 5% after excitation at 420 nm. Bi-exponential emission lifetimes (λ_{ex}= 378 nm) of 1.88 ns and 906 ns for **IrZn3** and 1.89 ns and 866 ns for **IrZn4** were also observed. These results indicate that the emission

of the iridium moiety in these assemblies is not particularly quenched compared to **Ir4** and the Φ_{PL} for **IrZn3** and **IrZn4** was only marginally reduced. Upon photoexcitation of **Ir2** and **IrZn5** at 360 nm, similar Φ_{PL} have been obtained (Φ_{PL} for **Ir2**: 40% vs Φ_{PL} for **IrZn5**: 38%). Photoexcitation into the Soret or Q bands of ZnTPP in **IrZn3** and **IrZn4** (λ_{exc} = 420 nm or 550 nm, respectively) results in only the characteristic emission of ZnTPP (Φ_{PL} = 5.0%, τ_{PL} = 1.88 ns, 172 ns for **IrZn3** and Φ_{PL} = 5.1%, τ_{PL} = 1.89 ns, 203 ns for **IrZn4** vs. Φ_{PL} = 3.8%, τ_{PL} = 1.70 ns for ZnTPP).

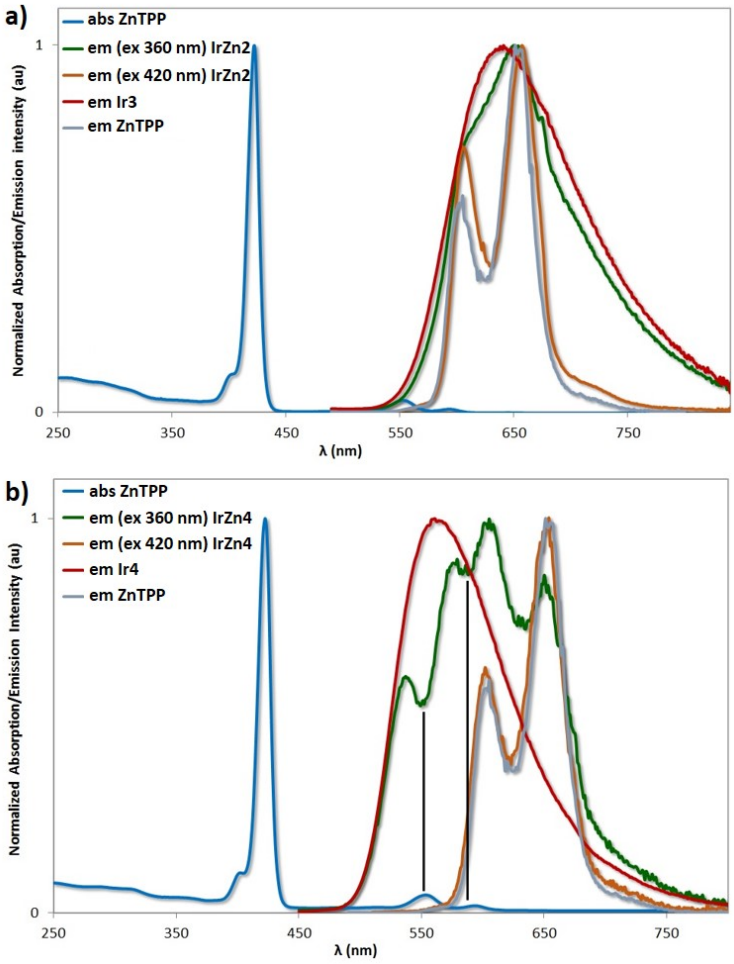

Figure 88. **a)** Normalised UV-Vis spectrum of **IrZn2** and normalised luminescence spectra of **IrZn2**, **Ir3** and ZnTPP recorded in degassed CH_2Cl_2 at 298 K with a concentration on the order of 10^{-6}. **b)** Normalised absorption spectrum of **IrZn4** and normalised luminescence spectra of **IrZn4**, **Ir4** and ZnTPP recorded in degassed CH_2Cl_2 at 298 K with a concentration of 3 x 10^{-5} M. Dark green and red lines indicate the emissions recorded with λ_{exc} = 360 nm and light blue and orange lines indicate the emissions recorded with λ_{exc} = 420 nm.

These results demonstrate that in these assemblies energy transfer processes through

electron exchange (Dexter energy transfer) or dipole-dipole interaction (Förster energy transfer) are negligible at a concentration of the order of 10^{-5} M in which less than 10% of ZnTPP is actually coordinated to complex **Ir4**. Photoluminescence excitation spectra measured by detecting the emissions of both ZnTPP and the iridium chromophoric units in **IrZn2** and **IrZn4** are further consistent with the absence of Dexter or Förster energy transfer, with the appearance of both the ZnTPP-based and iridium-based absorptions (see the spectra reported in **Figure S208-S210** in the appendix).

The lowest triplet excited states of **Ir3**, **IrZn1** and **IrZn3** were optimised with DFT (see the spin density distributions in **Figure 89**). The lowest triplet excited state for **IrZn1** and **IrZn3** is a ^{3}CT state involving the HOMO located on the ZnTPP moiety and the LUMO located on the qpy ligand. They are theoretically located in the NIR region (for example, at ca. 1250 nm for **IrZn1**, see **Figure 89**). Therefore, these ^{3}CT states are likely not involved in the emission of the assemblies and may play an important role in their non-radiative deactivation pathways. Thus, the emission observed for the assemblies is merely monomer-based and the hypothesis of emission arising from new transitions can be ruled out. The same findings also hold for **IrZn2** and **IrZn4**.

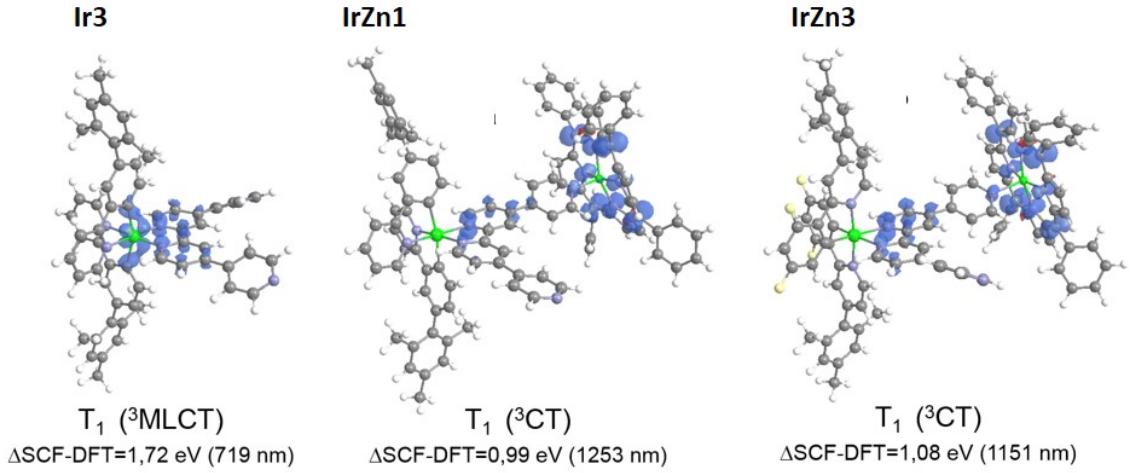

Figure 89. Spin-density distributions (B3LYP/6-31G(d) - ecp-60-mwb for Ir) at the optimised geometry of the lowest triplet excited state of **Ir3**, **IrZn1** and **IrZn3**. ΔSCF-DFT emission energies determined at the same level of theory are indicated below the structures.

Figure 88b reveals that the Q absorption bands of ZnTPP in **IrZn4** overlap with the emission profile of the iridium moiety. At the absorption maxima of these bands (λ_{abs} = 550 and 595 nm) the emission of the iridium complex in **IrZn4** correspondingly decreases, resulting in an apparently structured emission with maxima at 538, 577, 610 and 650 nm. Thus, in **IrZn3** and **IrZn4**, radiative energy transfer due to the absorption of the emission

of the iridium donor by the ZnTPP acceptor is promoted. This self-absorption contributes to the lower Φ_{PL} observed for the iridium complexes in **IrZn3** and **IrZn4** compared to **Ir4**.

4.4.3.1 Studies at a concentration of 5 x 10^{-4} M

In order to ensure that **IrZn3** and **IrZn4** constitute the predominant species in solution and to further probe the radiative energy transfer observed at low concentration (**Figure 88b)** we next investigated their photophysical behaviour at a concentration of the iridium complexes of 5 x 10^{-4} M. Based on the speciation plots illustrated in **Figure 82**, when **Ir3** and **Ir4** are mixed in a 1:1 ratio at this concentration a speciation of **IrZn3**:**IrZn4** = 0.8:0.2 exist, while when a second equivalent of ZnTPP is added a speciation of **IrZn3**:**IrZn4** = 0.5:0.5 exist. It is important to note that at a concentration of 5 x 10^{-4} M (which is close to K_d of 10^{-4} M^{-1}) little amount of free **Ir3** and ZnTPP are also present in solution. Emission titration of ZnTPP into a 5 x 10^{-4} M solution of **IrZn4** is illustrated in **Figure 90**. The emission intensity of the iridium complex corresponding to the maxima of the Q bands decreased dramatically (absorption of Q bands is shown in green profile in **Figure 90**). The intensity of emission bands of ZnTPP correspondingly increased as a function of increasing ZnTPP concentration (illustrated in red lines in **Figure 90**). For **IrZn4**, only porphyrin-based emission (titration 16 in **Figure 90**) could be observed by steady-state measurements.

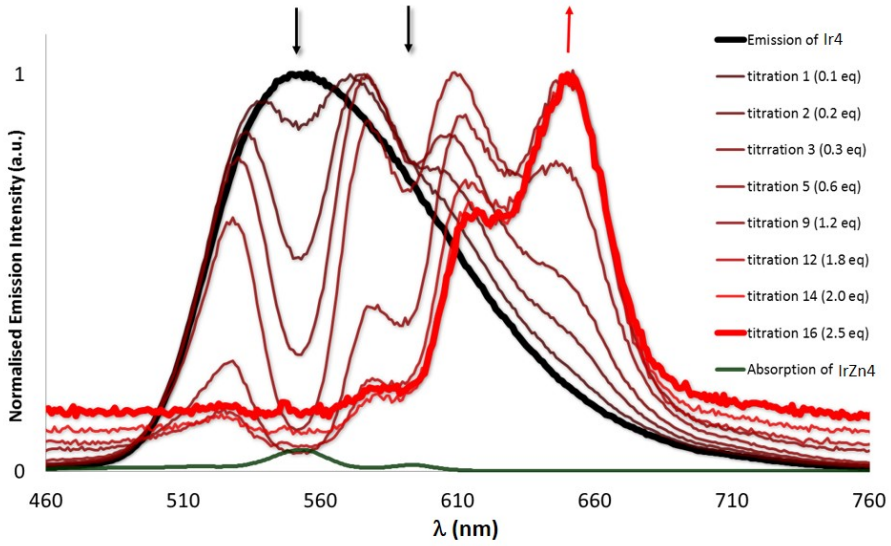

Figure 90. Room-temperature emission spectra of **Ir4** (black line) and **Ir4** upon addition of ZnTPP (from 0 to 2.5 equivalents, from dark red to red) collected in deaerated CH_2Cl_2 (λ_{exc} = 360 nm). The Q absorption band of ZnTPP is shown in green. The concentration of **Ir4** was maintained constant at 5 x 10^{-4} M while the concentration of ZnTPP varied from 5 x 10^{-5} M to 1.25 x 10^{-3} M. Only selected emissions are being shown.

These results clearly demonstrate that in **IrZn3** and **IrZn4**, due to the presence of ZnTPP, the emission of the iridium complex **IrZn4** is strongly quenched by self-absorption (radiative energy transfer). However, these experiments do not exclude rapid Dexter or Förster energy transfer processes between the iridium and ZnTPP.

High-time-resolution streak camera measurements of **IrZn4** and **IrZn5** have been carried out to investigate the presence of picosecond energy transfer processes between the iridium center and ZnTPP. As illustrated in **Figures 91a** and **Figure S224**, upon photoexcitation of **IrZn4** and **IrZn5** at 310 nm, the streak camera decays monitored at the iridium emission wavelength (λ_{em} = 560 nm) are almost the same for **IrZn4** and the control **IrZn5**, with the decay essentially completed after 100 ps. Thus, in **IrZn4**, despite N-Zn coordination, it appears unlikely that there is any Förster energy transfer between the chromophoric units. However, self-absorption was observed also on the picoseconds timescale (from 0 to 140 ps in **Figure 91b**) and therefore the presence of rapid ET processes between the units cannot be fully excluded.

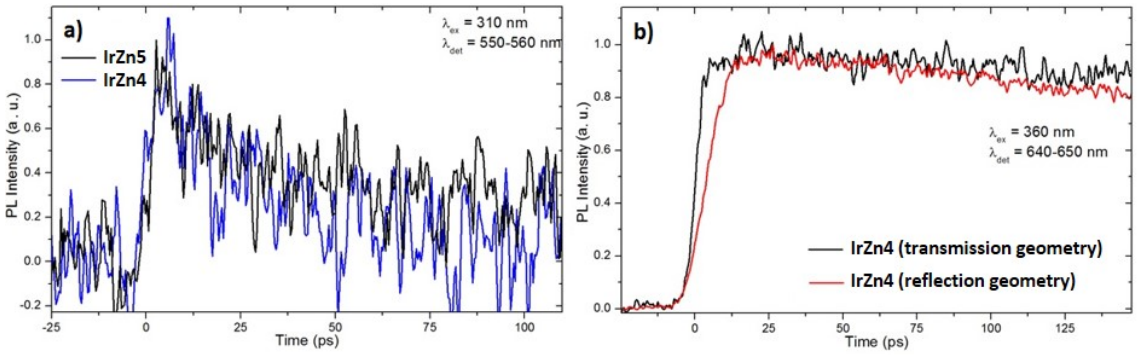

Figure 91. **a)** Streak camera decays at the iridium emission (λ_{PL}: 550–560 nm) upon excitation at 310 nm of **IrZn4** (blue line) and **IrZn5** (black line). **b)** Streak camera decays at the ZnTPP emission (λ_{PL}: 640–650 nm) upon excitation at 360 nm of **IrZn4** at a concentration of 3 x 10^{-5} M (black line) and at a concentration of 5 x 10^{-4} M (red line).

To discern whether the self-absorption observed for **IrZn3** and **IrZn4** is favored through the coordination of ZnTPP to the qpy, emission titration experiments were also conducted by adding ZnTPP to the control complex **Ir2** (at a concentration of 5 x 10^{-4} M) where coordination is not possible (see the spectra reported in **Figure S215** in the appendix). We noted that the emission of **Ir2** was, likewise, strongly quenched and presented similar behaviour to that observed in the titration experiments with **Ir4**. The same behaviour was also observed by time-resolved streak camera studies (**Figure 91**). Thus, we can confirm that the N-Zn coordination in **IrZn3** and **IrZn4** is not necessary for self-quenching. We further investigated the photophysical properties of the assemblies in the solid state as spin-coated films but, unfortunately, the emissions of all of the assemblies were totally

quenched in the solid state and no information could be extracted.

Table 6. Relevant photophysical data for ZnTPP, **Ir3**, **IrZn1**, **IrZn2**, **Ir4**, **IrZn3**, **IrZn4**, **Ir2**, **IrZn5**

	λ_{PL} (nm)[a,b]		Φ_{PL} (%)[d]		τ_{PL} (ns)[a]	
	λ_{exc}: 360 nm	λ_{exc}: 420 nm	λ_{exc}: 360 nm	λ_{exc}: 420 nm	3 x 10^{-5} M	5 x 10^{-4} M
ZnTPP	605 [0.6], 651 [1], 716 [0.04]	605 [0.6], 651 [1], 716 [0.04]	1	4	1.7	1.7
Ir3	638	-	14	29	300	306
IrZn1	607 [0.74], 651 [1], 713 [0.48]	606 [0.72], 658 [1], 723 [0.07]	6	4	2.3 (0.32), 294 (0.68)	1.9 (0.45), 193 (0.55)
IrZn2	611 [0.70]), 653 [1], 710 [0.56]	610 [0.72], 661 [1], 730 [0.06]	2	5	9.3 (0.52), 343 (0.48)	1.9 (0.55), 161 (0.45)
Ir4	565	-	34	-	993	1000
IrZn3	541 [0.64], 583 [1], 612 [1], 647 [0.68], 715 [0.17]	537 [0.02], 610 [0.66], 661 [1], 717 [0.07]	10	5	1.88 (0.38), 906 (0.62)	1.9 (0.60), 384 (0.40)
IrZn4	537 [0.60], 580 [0.87], 605 [1], 650 [0.86], 716 [0.13]	602 [0.62], 654 [1], 713 [0.06]	6	5	1.89 (0.40), 866 (0.60)	1.9 (0.80), 192 (0.20)
Ir2	576	-	40	-	757	800
IrZn5	576 [0.97], 604 [1], 651 [0.63]	601 [0.72], 651 [1], 720 [0.07]	38	4	1.90 (0.32), 759 (0.68)	1.9 (0.70), 194 (0.30)

[a]Measurements in deaerated CH_2Cl_2 at 298 K at ca. 10^{-5} M. [b]Relative intensity of principal emission peaks listed in [ ]. [c]Using quinine sulfate as the standard (Φ_{PL} = 54.6% in 0.5 M H_2SO_4 at 298 K). [d]Using $[Ru(bpy)_3]Cl_2$ as the standard (Φ_{PL} = 4% in aerated H_2O at 298 K).[379] [e]λ_{exc} = 378 nm. The values in parentheses are relative pre-exponential weighting factors.

4.4.4 Theoretical estimation of photoinduced electron transfer processes

As introduced in the first chapter, photoinduced Electron Transfer (PeT) in a typical Donor–Acceptor system (D-A, bimolecular process) is an electron exchange process between the two chromophoric units upon initial photoexcitation of the donor component, resulting in the formation of a non-emissive charge separated state ($D^{\cdot+}$-$A^{\cdot-}$).[22, 27]

The first step in determining the feasibility of a PeT process in a bimolecular system involves the determination of the free energy (ΔG_{CS}) associated with the charge-separated state, which can be calculated following the Rehm-Weller equation (**3**).[22]

$$\Delta G_{CS} = e\,[E_{1/2}\,(D^{\cdot+}/D^{*}) - E_{1/2}\,(A^{*}/A^{\cdot-})] - E_{0,0} + G_S \quad \textbf{(3)}$$

In equation **(3)** the term on the right side, e[$E_{1/2}$($D^{\cdot+}$/D*)-$E_{1/2}$(A*/$A^{\cdot-}$)] contains the redox potentials for the excited state couples (Donor, D and Acceptor, A), which can be inferred given:[27, 380]

$$E_{1/2}\,(D^{\cdot+}/D^{*}) = E_{1/2}\,(D^{+}/D) - E_{0,0} \quad \textbf{(4)}$$

$$E_{1/2}\,(A^{*}/A^{\cdot-}) = E_{1/2}\,(A/A^{-}) + E_{0,0} \quad \textbf{(5)}$$

The G_S in equation **(3)** is the ion-pair stabilization energy and involves both the solvent-dependent columbic interactions and structural parameters of the system and it can be calculated from:[22]

$$G_S = \frac{e^2}{4\pi\varepsilon^0}\left[\left(\frac{1}{2R_D + 2R_A - R_{DA}}\right)\frac{1}{\varepsilon_S} - \left(\frac{1}{2R_D + 2R_A}\right)\frac{1}{\varepsilon_R}\right] \quad \textbf{(6)}$$

where R_D and R_A are, respectively, the radius of the donor and acceptor, R_{DA} is the center-to-center distance between the donor and the acceptor and ε_S and ε_R are, respectively, the dielectric constants of the solvents used for the photophysical and electrochemical studies.

The structural parameters of the assemblies elucidated by X-ray diffraction (**Figure 84**) were used to calculate G_S, with R_D = 7.21 Å, R_A = 9.20 Å and R_{DA} = 11.33 Å for **IrZn1** and R_{DA} = 11.24 Å for **IrZn2**. R_D is defined as the distance from the Zn to the C_4 of the one of the phenyl groups on the TPP ligand; R_A is defined as the Ir-N_{qpy} distance, where N_{qpy} is the distal nitrogen on the quaterpyridine, and R_{DA} is defined as the Ir-Zn distance. All distances are determined from the crystal structure of **IrZn1** and **IrZn2**. For both optical and electrical studies, CH_2Cl_2 was used as the solvent and, therefore, $\varepsilon_S = \varepsilon_R$ = 8.93. Next, ΔG_{CS} was determined for the assemblies **IrZn1**, **IrZn2**, **IrZn3** and **IrZn4**.

In the following discussion only the assemblies **IrZn1** and **IrZn3** will be considered but due to the very similar optoelectronic data obtained for **IrZn2** and **IrZn4**, the same results can be readily extended to the 1:2 assemblies.

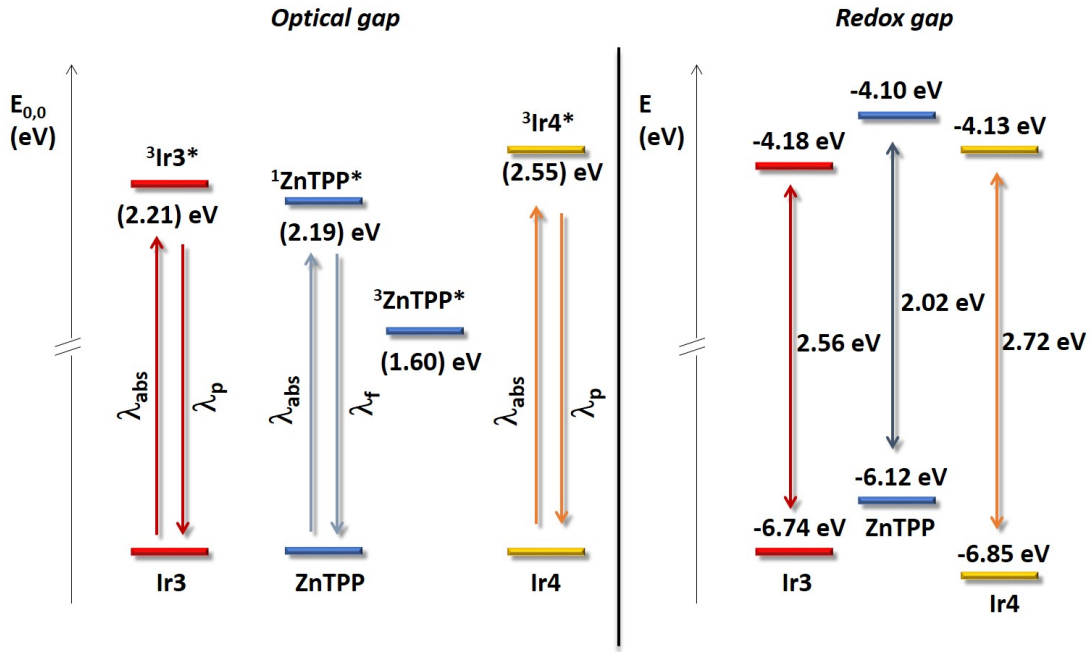

Figure 92. **a)** Representation of the energy of the zero-zero transition ($E_{0,0}$) to the lowest excited states of **Ir3**, ZnTPP and **Ir4** obtained by spectroscopic analysis. As the energy of the lowest triplet state of ZnTPP (^{3}ZnTPP*) we used the value previously reported.[374] **b)** Representation of the energies of the first oxidation and first reduction waves, the associated redox gap and inferred HOMO – LUMO levels of complex **Ir3**, ZnTPP and **Ir4** obtained by electrochemical analysis. E_{HOMO} = -($E^{ox}_{pa\ vs\ Fc/Fc^+}$ + 5.39) eV, E_{LUMO} = -($E^{red}_{pc\ vs\ Fc/Fc^+}$ + 5.39) eV.[381]

Figure 92a shows the lowest exited triplet-state energies of **Ir3** and **Ir4** and the lowest exited singlet-state energy of ZnTPP estimated from the intersection point between their respective absorption and luminescence spectra (**Tables 5** and **6**). The $E_{0,0}$ values reported in **Table 5** and **Figure 92a** have been estimated from the room-temperature rather than the low-temperature (77 K) emissions required for a rigorous estimation of the zero-zero excited states values.[22] However, we are confident that this approximation does not significantly influence our qualitative approach for evaluating possible PeT pathways in our systems. The lowest transition energy ($E_{0,0}$) is located at 2.55 eV for **Ir4**, and at 2.21 eV for **Ir3**, both of which are higher than $E_{0,0}$ calculated for ZnTPP (2.19 eV). As the energy of the lowest triplet state of ZnTPP (^{3}ZnTPP*) we used the previously reported value of 1.60 eV.[374]

Figure 92b represents the inferred energies of HOMO and LUMO levels of **Ir3** and **Ir4** and ZnTPP obtained by CV analysis (**Table 5**). The HOMO and LUMO levels of ZnTPP are located at –6.12 and –4.10 eV, respectively, whereas for both **Ir3** and **Ir4** the HOMO and LUMO are stabilised respectively at –6.74 and –4.18 eV for **Ir3** and –6.85 and –4.13 eV for **Ir4**. Thus, the ground state electrochemical data suggest that, from an electron transfer point of view, ZnTPP is a better donor than the iridium complexes due to its higher ionization potential, whereas both **Ir3** and **Ir4** are better electron acceptors due to their higher electron affinity. This is consistent with the DFT calculations (**Figure 89**). Following this assumption, we calculated ΔG_{CS} for a PeT process in **IrZn1** and **IrZn3**, where ZnTPP is the donor and the iridium complex acts as the acceptor. The excited state oxidation potential of ZnTPP (vs. SCE) is -0.84 V, while the excited state reduction potentials of **Ir3** and **Ir4** (vs. SCE) are 0.92 V and 1.26 V, respectively. Therefore, the excited-state redox gaps e[$E_{1/2}(D^{\cdot+}/D^*)$-$E_{1/2}(A^*/A^{\cdot-})$] for **IrZn1** and **IrZn3** are respectively 1.76 and 2.10 eV. The ion-pair stabilisation energy, G_{CS}, for both **IrZn1** and **IrZn3** is –0.14 eV and $E_{0,0}$ for the ZnTPP donor was determined to be 2.19 eV (**Figure 92**). Thus, for **IrZn1** and **IrZn3**, ΔG_{CS}, is found to be exergonic in CH_2Cl_2 (ΔG_{CS} = -0.57 eV for **IrZn1** and -0.23 eV for **IrZn3**), suggesting that upon photoexcitation of ZnTPP, electron transfer to the iridium centers is thermodynamically favorable. By contrast, due to the higher energy required to extract an electron from the iridium complexes, ΔG_{CS} for PeT processes, in which **Ir3** and **Ir4** act as donors and ZnTPP acts as the acceptor, are found to be +0.13 eV for **IrZn1** and +0.42 eV for **IrZn3**. Thus, in this direction the processes are slightly endergonic and not thermodynamically favourable. From the steady-state and time-resolved photophysical studies presented, we only observed emission quenching of the iridium complexes by self-absorption due to the presence of ZnTPP. Consequently, we have no evidence of emission quenching due to charge recombination following PeT, despite the favourable thermodynamics. The photophysical properties of **IrZn1**, **IrZn2**, **IrZn3** and **IrZn4** (**Table 6**) were used to estimate the rate constants k_{et} for the possible PeT from the ZnTPP donor to the iridium acceptors, which are closely related to the ration between Φ_{PL} of ZnTPP and τ_{PL} of the iridium complexes. This is only valid with the assumption that in an encounter between the excited states of the donor and acceptor molecules enough energy will be available to promote the formation of the charge separated state $[ZnTPP]^{\cdot+}$-$[Ir]^{\cdot-}$, which result in the deactivation of their excited state energies.[22] With this assumption we calculated k_{eT} of 4.857 x 10^6 s^{-1}, 6.076 x 10^6 s^{-1}, 2.340 x 10^6 s^{-1} and 4.888 x 10^6 s^{-1} respectively for **IrZn1**, **IrZn2**, **IrZn3** and **IrZn4** (Further information about k_{eT} are reported in the experimental section, Chapter 6). Efficient PeT in multichromophoric systems are generally observed when the rate constant for photoinduced electron transfer, k_{eT}, are greater than 10^7 s^{-1}.[382] Therefore, despite the favourable thermodynamic for the formation of the charge state $[ZnTPP]^{\cdot+}$-$[Ir]^{\cdot-}$, the PeT process is not fast enough to compete with the other deactivation processes, including the radiative energy transfer experimentally observed.

4.5 Ruthenium-phorphyrin assemblies

In the previous section of this chapter we have reported the dynamic [Ir]···[ZnTPP] and [Ir]···[ZnTPP]$_2$ dyad and triad systems, **IrZn1**, **IrZn2**, **IrZn3** and **IrZn4** (**Figure 80a**). We showed that in these systems only self-absorption (radiative energy transfer) occurs between the [Ir] complex and ZnTPP. PeT from [Ir] to ZnTPP is not thermodynamically favourable while PeT from ZnTPP to [Ir] was found to be exergonic (ΔG_{CS} = -0.57 eV in **IrZn3**); however there was no experimental evidence to support the formation of the charge separated [ZnTPP]$^{\cdot+}$-[Ir]$^{\cdot-}$ state. This is most likely due to the fact that the PeT processes in these systems are kinetically slow with calculated k_{eT} of the order of 10^6 s^{-1}.

By contrast, as illustrated in **Figure 79**, when zinc tetratolylporphyrin (ZnTPP) is either covalently or non-covalently connected to a ruthenium(II) trisbipyridyl complex, PeT from ZnTPP to the ruthenium centre is experimentally observed on an ultrafast time scale (<100 ps).[352, 360] With this in mind, we decided to investigate the assemblies based on the non-covalent axial coordination between ZnTPP as the donor unit and our ruthenium complex [Ru(dtBubpy)$_2$(qpy)]2PF$_6$, **Ru1** as the acceptor moiety (**Figure 80c**).

4.5.1 Self-assembly investigation by ^{1}H NMR spectroscopy

Similar to the formation of the IrZn assemblies, the assemblies **RuZn1** and **RuZn2** were rapidly obtained after mixing **Ru1** with one or two equivalents of ZnTPP, respectively, in CD_2Cl_2 at room temperature. The four tert-butyl moieties present in **Ru1** conferred the requisite solubility in CD_2Cl_2, a solvent chosen to not interfere with the axial coordination of the distal pyridines present in **Ru1** with ZnTPP. The formation of the assemblies was monitored by ^{1}H NMR, 2D COSY, HMBC and HMQC spectroscopy methods (^{1}H NMR, 2D COSY, HMBC and HMQC spectra are reported in the appendix).

^{1}H NMR titration experiments of ZnTPP (from 0.1 to 2.5 equivalents, ranging from 0 to 9.44 mM) carried out in a 3.06 mM solution of **Ru1** in CD_2Cl_2 resulted in a broadening and gradual up-field shift of the proton resonances associated with **Ru1** (**Figure 93**). As observed for the IrZn assemblies (see **Figure 81**), due to the axial coordination of the pyridine ring to ZnTPP, the proton resonances associated with the qpy moiety (H_a, H_b, H_c, H_d in **Figure 93**) were shifted up-field the most. The ^{1}H NMR titration data extracted from the chemical shift of the resonance of ^1H_a (**Figure S230**, appendix from δ 8.77 to δ 7.84 ppm) could be fitted to a sequential binding model using EQNMR software (**Figure 94a**). The best fit of the binding model affords equilibrium constants of 7200 ± 300 M^{-1} for the formation of **RuZn1** from **Ru1** and ZnTPP and 2500 ± 350 M^{-1} for the formation of **RuZn2** from **RuZn1** and ZnTPP. These association constants are very similar to those obtained for the analogous IrZn assemblies **IrZn1** and **IrZn2** (**Figure 82**). Speciation

plots for the formation of **RuZn1** and **RuZn2** as a function of the initial concentration and stoichiometry of the mixture have been determined using the parameter scan mode implemented in Gepasi[367, 368] (**Figure 94b,c**). For solutions containing a 1 : 1 mixture of **Ru1** and ZnTPP, **RuZn1** is the dominant complex at all concentrations between 100 µM and 100 mM. For solutions containing a 1 : 2 mixture of **Ru1** and ZnTPP, **RuZn1** is the dominant complex at concentrations below 600 µM and **RuZn2** is the dominant complex between this concentration and 100 mM.

As illustrated in **Figure 93b**, the ^{1}H NMR spectrum for **RuZn1** is relatively simple, indicating local C_2 symmetry around the ruthenium centre. This observation suggests that the exchange of bound and unbound ZnTPP is fast on the NMR timescale and that the ^{1}H NMR spectrum observed reflects a mixed speciation of ZnTPP – both free ZnTPP and ZnTPP bound to **Ru1**. When **Ru1** and ZnTPP are mixed in a 1 : 1 ratio at a concentration of 3.06 mM (NMR spectrum shown in **Figure 93b**), a speciation of **RuZn1** : **RuZn2** = 0.60 : 0.40 is present, whereas when a second equivalent of ZnTPP is added (NMR spectrum shown in **Figure 93c**), a speciation of **RuZn1** : **RuZn2** = 0.40 : 0.60 is obtained. As expected, when the control Ru complex **Ru2** was mixed with two equivalents of ZnTPP (**Figure 80c**) no change was observed in the ^{1}H NMR spectra (see **Figure S232** in the appendix).

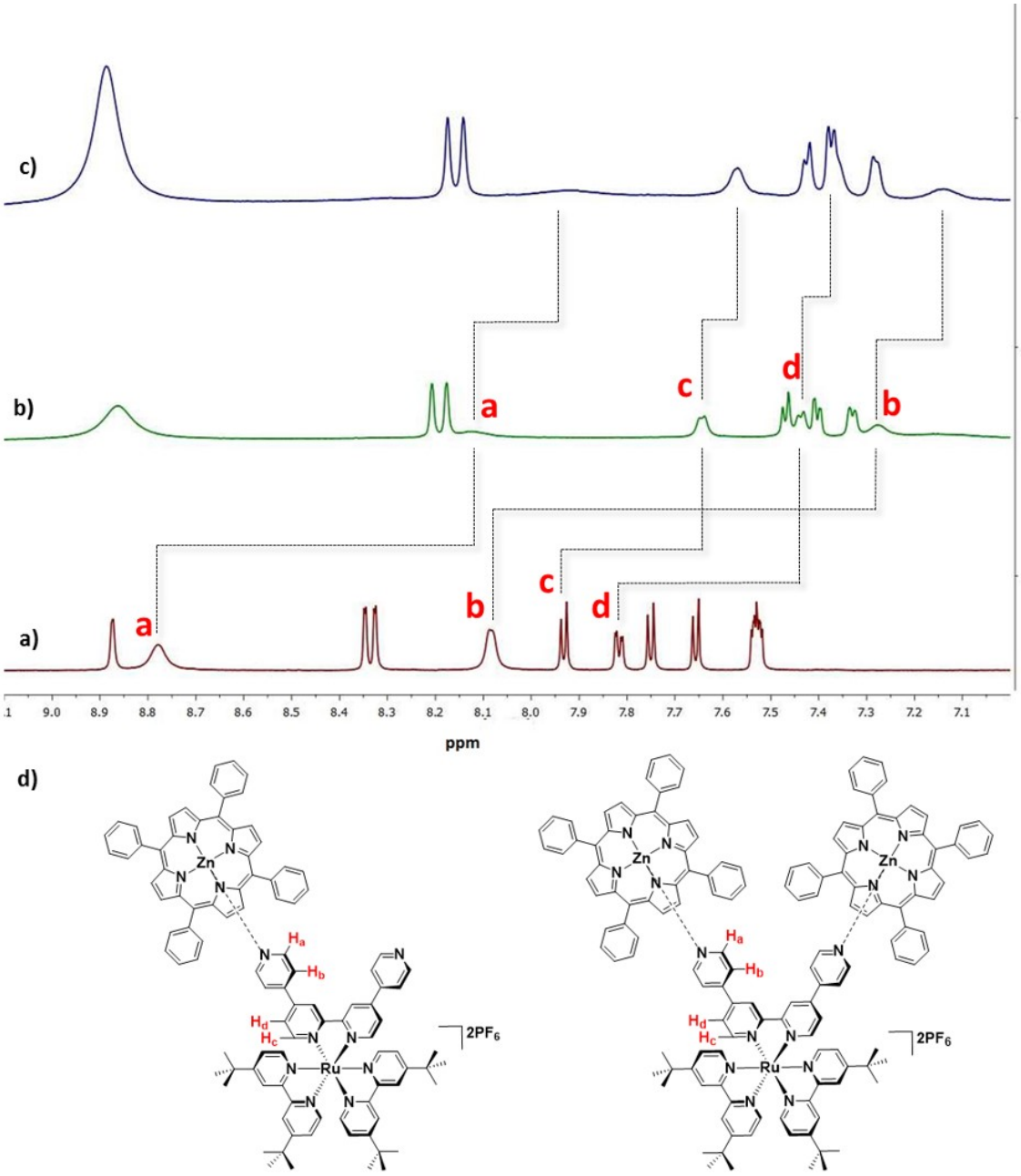

Figure 93. ^{1}H NMR spectra in CD_2Cl_2, 500 MHz at 298 K. The concentration of **Ru1** was kept constant at 3.06 mM. **(a)** ^{1}H NMR spectrum of **Ru1**; **(b)** ^{1}H NMR spectrum of the assembly **RuZn1**, [ZnTPP] = 3.06 mM; **(c)** ^{1}H NMR spectrum of the assembly **RuZn2**, [ZnTPP] = 6.12 mM; **(d)** chemical structures of **RuZn1** and **RuZn2**. The assignments correspond to the labelling shown in **(d)**.

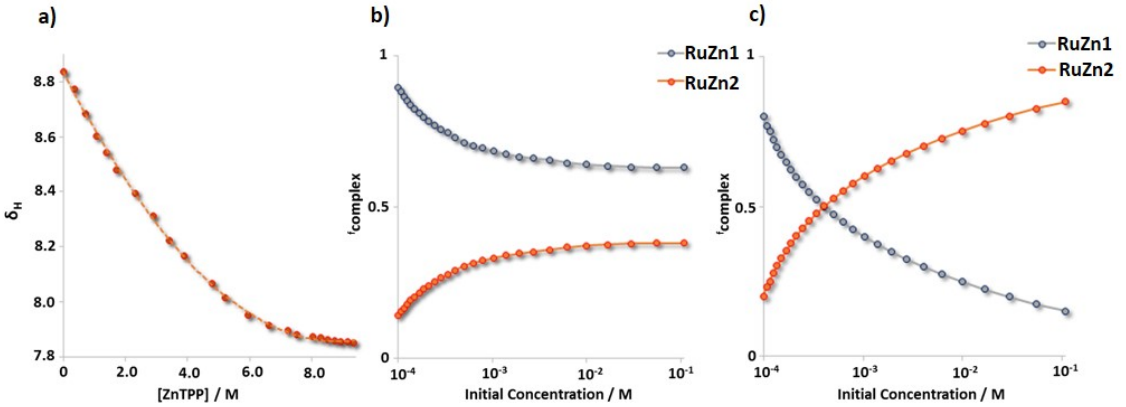

Figure 94. **a)** Chemical shift changes observed in the ^{1}H NMR spectrum of a 3.06 mM solution of **Ru1** in CD_2Cl_2 on addition of aliquots of ZnTPP (red points) that can be fitted (dotted orange line) to a sequential binding model for the formation of **RuZn1** and **RuZn2**. Fractions of 1:1 complex **RuZn1** (blue lines) and 1:2 complex **RuZn2** (red lines) present in solution as a function of concentration when **(b)** $[ZnTPP]_{initial} = [\mathbf{Ru1}]_{initial}$ and **(c)** $[ZnTPP]_{initial} = 2$ x $[\mathbf{Ru1}]_{initial}$.

4.5.2 Optoelectronic properties

4.5.2.1 Absorption

The optoelectronic properties of ZnTPP, **Ru1**, **RuZn1**, **RuZn2**, **Ru2** and **RuZn3** have been investigated in CH_2Cl_2 solutions at room temperature and the results are summarised in **Table 7** and **Table 8**. The UV-visible absorption spectra of **Ru1** and **Ru2** (**Figure 95**) are both characterized by an intense band at ca. 285 nm assigned to a spin-allowed ligand-centred $^1\pi \rightarrow \pi^*$ transition localised on the dtBubpy ligand and a broad band in the visible region, at ca. 440 nm and 494 nm for **Ru1** and at ca. 432 and 469 nm for **Ru2**. These transitions are assigned to the typical metal-to-ligand charge transfer transition (^{1}MLCT) to the dtBubpy ligand for **Ru2** whereas, as theoretically predicted, the ^{1}MLCT bands for **Ru1** involve both the dtBubpy and the quaterpyridine ligands.[383–385] Indeed, time-dependent density functional theory (TD-DFT) calculations on complex **Ru1** corroborate the nature of the main UV-Vis bands (see the computational details in the appendix). The CT absorption of **Ru1** is red-shifted (λ_{max} = 439 nm and 493 nm) compared to **Ru2** (λ_{max} = 434 nm and 465 nm) due to the enhanced conjugation present in the qpy ligand.[385, 386] The absorption spectra of the 1 : 1 and 1 : 2 ratios of **Ru1** and ZnTPP at 10^{-6} M where less than 1% of ZnTPP is bound to **Ru1**, show the expected superposition of the respective absorption spectra of the two complexes (**Figure 95**).

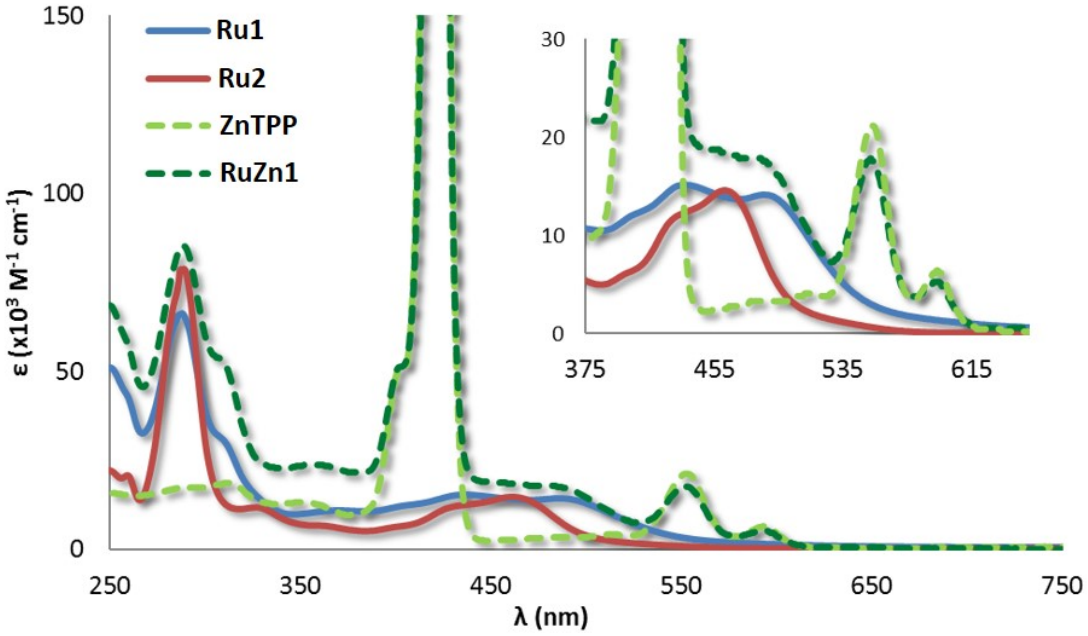

Figure 95. UV-vis spectra of **Ru1** (solid blue line), **Ru2** (solid red line), ZnTPP (dashed light-green line) and **Ru1** : ZnTPP = 1 : 1 (**RuZn1**, dashed green line) collected in CH_2Cl_2 at 298 K with a concentration in the order of 10^{-6} M.

4.5.2.2 Electrochemical properties

The ground-state electronic communication between [Ru] and ZnTPP in **RuZn1** and **RuZn2** has been investigated by cyclic voltammetry (CV) and differential pulse voltammetry (DPV) in a deaerated CH_2Cl_2 solution at a concentration of 1.24 x 10^{-3} M. At this concentration we can consider ZnTPP as completely bound to **Ru1**, where **RuZn1** and **RuZn2** are present in a ratio of **RuZn1** : **RuZn2** = 0.70 : 0.30 when **Ru1** and ZnTPP are mixed in a 1 : 1 ratio and **RuZn1** : **RuZn2** = 0.45 : 0.55 when a second equivalent of ZnTPP is added. Similarly to the CVs of other cationic ruthenium complexes,[384, 387, 388] **Ru1** and **Ru2** exhibit a one-electron reversible oxidation wave at, respectively, $E^{ox}_{1/2}$ = 1.43 V and $E^{ox}_{1/2}$ = 1.37 V attributed to the Ru(II)/Ru(III) redox couple (**Figure 96** and **Figure S236** in the appendix). The presence of the two additional tert-butyl groups in **Ru2** destabilises the oxidation compared to **Ru1** while the distal pyridines on the qpy ligand inductively withdraw electron density leading to an anodic shift of the oxidation wave relative to **Ru2**.[385] Two quasi-reversible one-electron reduction waves at $E^{red}_{1/2}$ = -1.04 V and $E^{red}_{1/2}$ = -1.51 V localised on the quaterpyridine ligands are observed for **Ru1**. Single one-electron reversible reduction at $E^{red}_{1/2}$ = -1.24 V localised on one of the dtBubpy ligands is observed for complex **Ru2**. These redox processes are also observed in the DPV spectra illustrated in the supporting information in **Figure S235** and **S237** for complex

Ru1 and **Ru2**, respectively.

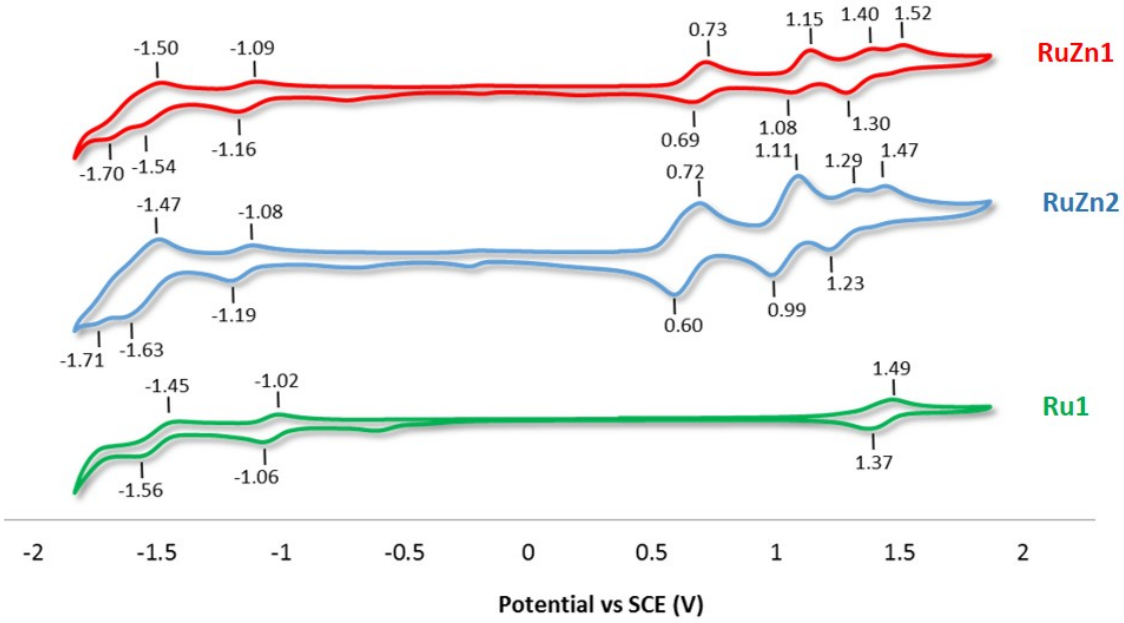

Figure 96. CVs reported versus SCE for ZnTPP, **RuZn1**, **RuZn2** and **Ru1** recorded at 298 K in deaerated CH_2Cl_2 solution containing n-NBu_4PF_6 as the supporting electrolyte and using Fc/Fc^+ as an internal standard (Fc/Fc^+ = 0.46 V in CH_2Cl_2 with respect to SCE).[375]

For assemblies **RuZn1** and **RuZn2** the oxidation potentials localised on the ruthenium complex are slightly cathodically shifted to lower potentials compared to **Ru1** (E^{pa} = 1.43 V for **Ru1** vs. $E^{ox}_{1/2}$ = 1.35 V for **RuZn1** and $E^{ox}_{1/2}$ = 1.26 V for **RuZn2**, **Figure 97**). However, similar to the iridium–ZnTPP assemblies **IrZn1**, **IrZn2**, **IrZn3** and **IrZn4**, upon ZnTPP coordination with the distal pyridine moieties of **Ru1**, the porphyrin-centered oxidation waves of both **RuZn1** and **RuZn2** are significantly cathodically shifted ($E^{ox}_{1/2}$ = 0.71 V for **RuZn1**, $E^{ox}_{1/2}$ = 0.66 V for **RuZn2**) while their first reduction processes are likewise cathodically shifted ($E^{red}_{1/2}$ = -1.52 V for **RuZn1**, $E^{red}_{1/2}$ = -1.55 V for **RuZn2**). In addition, an extra wave at around 1.52 V and 1.47 V can be observed, respectively, in the CVs of **RuZn1** and **RuZn2**, which are assigned to the oxidation of uncomplexed **Ru1**. The CVs of **Ru2** and of "non-assembly" **RuZn3** were also investigated in deaerated CH_2Cl_2 as a control system and, as expected, the CV **RuZn3** contains only the superposition of the redox processes of **Ru2** and ZnTPP, with no ground-state electronic communication between the two units (see the CV and DPV spectra reported in the appendix in **Figure S236**).

Table 7. Electrochemical data and $E_{0,0}$ values of **Ru1**, **RuZn1**, **RuZn2**, **Ru2**, **RuZn3**

	E_{ox} (V)	E_{ox} (V)	E_{ox} (V)	E_{red} (V)	E_{red} (V)	E_{gap} (V)[c]	$E_{0,0}$ (eV)[d]
Ru1	1.43[a]	-	-	-1.04[a]	-1.51[a]	2.47	2.08
RuZn1	0.71[a]	1.12[a]	1.35[a]	-1.13[a]	-1.52[b]	1.84	-
RuZn2	0.66[a]	1.05[a]	1.26[a]	-1.14[a]	-1.55[b]	1.80	-
Ru2	1.37[a]	-	-	-1.24[b]	-	2.61	2.29
RuZn3	0.84[b]	1.22[a]	1.37[a]	-1.36[a]	-	2.20	-

CV traces recorded in CH_2Cl_2 solution with 0.1 M n-NBu_4PF_6 at 298 K at 50 mV·s^{-1}. Values are in V vs. SCE (Fc/Fc^+ vs. SCE = 0.46 V).[375] [a]$E_{1/2} = (E_{pa} + E_{pc})/2$ and result from one-electron processes. [b]Irreversible oxidation and reduction peak potentials. [c]Calculated from E_{ox} - E_{red} where E_{ox} is the first oxidation potential and E_{red} is the first reduction potential. [d]$E_{0,0}$ estimated from the intersection point of the absorption and emission spectra at 298 K in CH_2Cl_2.

4.5.2.3 Prediction of photoinduced electron transfer processes

As for the IrZn assemblies, the redox potentials and optical data were used to estimate the energetics of the electron transfer processes exhibited by the compounds under investigation.

Figure 97a shows the lowest excited triplet-state energy of **Ru1** and the lowest excited singlet-state energy of ZnTPP ($E_{0,0}$) estimated from the intersection point between their respective absorption and luminescence spectra collected in CH_2Cl_2 at room temperature. **Figure 97b** represents the inferred energies of oxidation and reduction potentials of **Ru1** and ZnTPP obtained by CV analysis. The $E_{0,0}$ energies and the redox potentials of ZnTPP, **Ru1**, **Ru2** and the assemblies **RuZn1** and **RuZn2** are reported in **Table 7**.

The HOMO and LUMO of ZnTPP are located at -6.12 and -4.10 eV, respectively, whereas for **Ru1**, both these levels are stabilised at -6.82 and -4.35 eV. Therefore, for **RuZn1** and **RuZn2**, ZnTPP acts as the electron-donor unit while **Ru1** acts as the electron-accepting moiety.[22, 26]

The free energy (ΔG_{CS}) associated with the formation of the charge-separated state $[ZnTPP]^{\cdot+}$-$[Ru]^{\cdot-}$ is calculated following the Rehm–Weller equation **(3)**. The excited state oxidation potential of ZnTPP (vs. SCE) is -0.84 V, while the excited state reduction potential of **Ru1** (vs. SCE) is 0.79 V. Therefore, the excited state redox gap [$E_{1/2}(D^{\cdot+}/D^*)$-$E_{1/2}(A^*/A^{\cdot-})$] for **RuZn1** and **RuZn2** is 1.63 eV. The structural parameters of the analogous assemblies **IrZn1** and **IrZn2**, elucidated by X-ray diffraction, (**Figure 84**) were used to estimate G_S, with R_A = 9.20 Å, R_D = 7.21 Å and R_{DA} = 11.30 Å for both **RuZn1** and

RuZn2. R_A is defined as the Ru-N_{qpy} distance, where N_{qpy} is the distal nitrogen on the quaterpyridine; R_D is defined as the distance from the Zn to the carbon atom of the one of the phenyl groups on the TPP ligand; and R_{DA} is defined as the Zn-Ru distance. The ion-pair stabilization energy, G_S, for both **RuZn1** and **RuZn2** was inferred to be -0.14 eV and $E_{0,0}$ for the ZnTPP donor is 2.19 eV. Consequently, following photoexcitation of **RuZn1** and **RuZn2**, electron transfer from ZnTPP to complex **Ru1** is found to be exergonic in CH_2Cl_2 (ΔG_{CS} = -0.70 eV for **RuZn1** and **RuZn2**). In addition, a rate constant of 4.995 x 10^7 s^{-1} for the formation of the charge state $[ZnTPP]^{\cdot+}$-$[Ru]^{\cdot-}$ following PeT was calculated for both **RuZn1** and **RuZn2**. The rate of PeT in these assemblies is approximately one order of magnitude faster than the k_{eT} of around 10^6 calculated for the IrZn assemblies. Therefore, the kinetics of the process may also play an important role for the activation of PeT.[389, 390] By contrast, ΔG_{CS} = +0.17 eV was calculated for the formation of the charge-separated state $[Ru]^{\cdot+}$-$[ZnTPP]^{\cdot-}$ and so is not a thermodynamically favourable process.

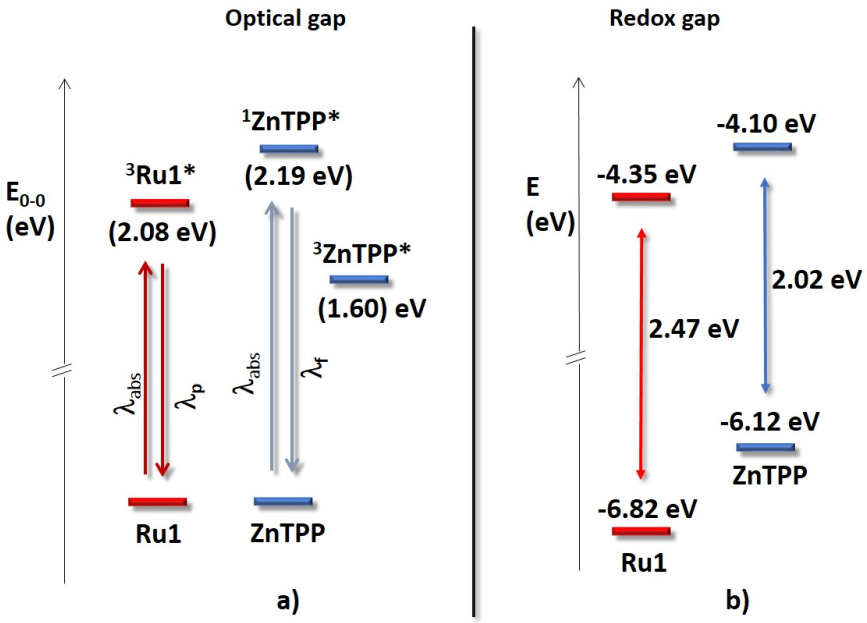

Figure 97. **a)** Representation of the energy of the zero-zero transition ($E_{0,0}$) to the lowest excited states of **Ru1** and ZnTPP obtained by spectroscopic analysis. As the energy of the lowest triplet state of ZnTPP (^{3}ZnTPP*) we used the value previously reported.[374] **b)** Representation of the energies of the first oxidation and first reduction waves, the associated redox gap and inferred HOMO – LUMO levels of complex **Ru1** and ZnTPP obtained by electrochemical analysis. E_{HOMO} = -($E^{ox}_{\text{pa vs Fc/Fc}^+}$ + 5.39) eV, E_{LUMO} = -($E^{red}_{\text{pc vs Fc/Fc}^+}$ + 5.39) eV.[381]

4.5.2.4 Emission studies

Emission studies were carried out in CH_2Cl_2 solution at a concentration of 3 x 10^{-4} M in order to verify experimentally the presence of PeT in **RuZn1** and **RuZn2**. At this concentration we can consider ZnTPP as completely bound to the ruthenium complex with a ratio of **RuZn1** : **RuZn2** = 0.75 : 0.25 when **Ru1** is mixed with 1 equivalent of ZnTPP and with a ratio of **RuZn1** : **RuZn2** = 0.60 : 0.40 when a second equivalent of ZnTPP is added. Upon photoexcitation of **Ru1** and **Ru2** into either their CT or LC absorption bands (at around 500 or 400 nm, respectively), broad and unstructured emissions from the ^{3}MLCT state at, respectively, 674 nm and 615 nm are observed (red lines in **Figure 98**).

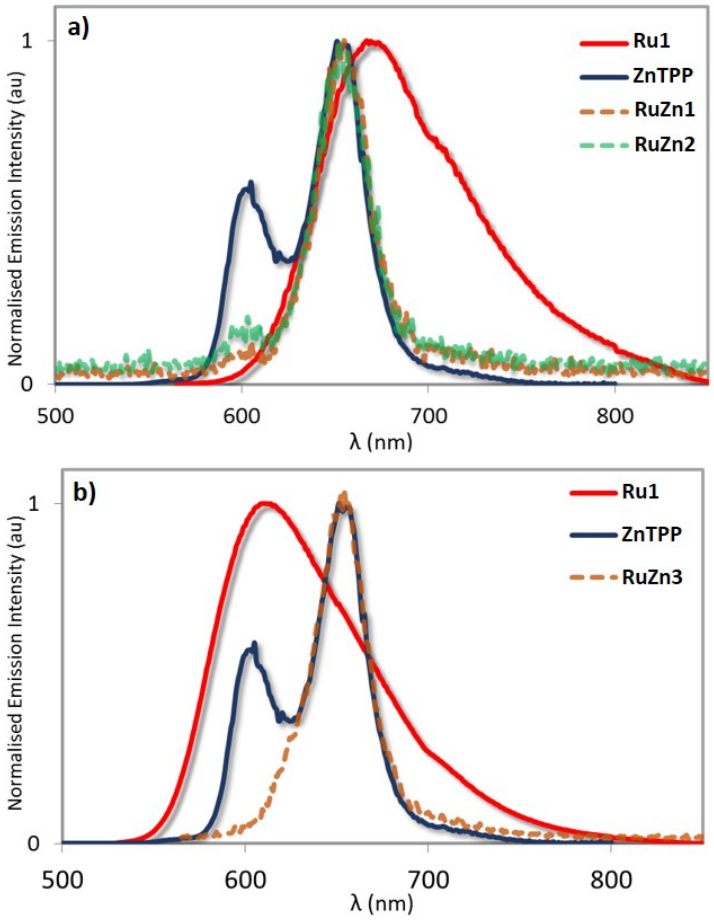

Figure 98. **(a)** Normalised luminescence spectra of **Ru1** (solid red line), ZnTPP (solid blue line), **RuZn1** (dotted orange line) and **RuZn2** (dotted green line) recorded in degassed CH_2Cl_2 at 298 K (λ_{exc} = 555 nm) with a concentration in the order of 3 x 10^{-4} M. **(b)** Normalised luminescence spectra of **Ru2** (solid red line), ZnTPP (solid blue line) and of the "non-assembly" **RuZn3** (dotted orange line) recorded in degassed CH_2Cl_2 at 298 K (λ_{exc} = 555 nm) with a concentration in the order of 10^{-4} M.

Due to the increased conjugation present in the qpy ligand, the emission of **Ru1** is

red-shifted compared to **Ru2**. As reported in **Table 8**, the Φ_{PL} for **Ru1** and **Ru2** are similar at 7 and 9%, respectively. The character of the emissive state was confirmed by a DFT optimisation of the lowest excited triplet-state (T_1). The spin density distribution for **Ru1** in **Figure 99**.

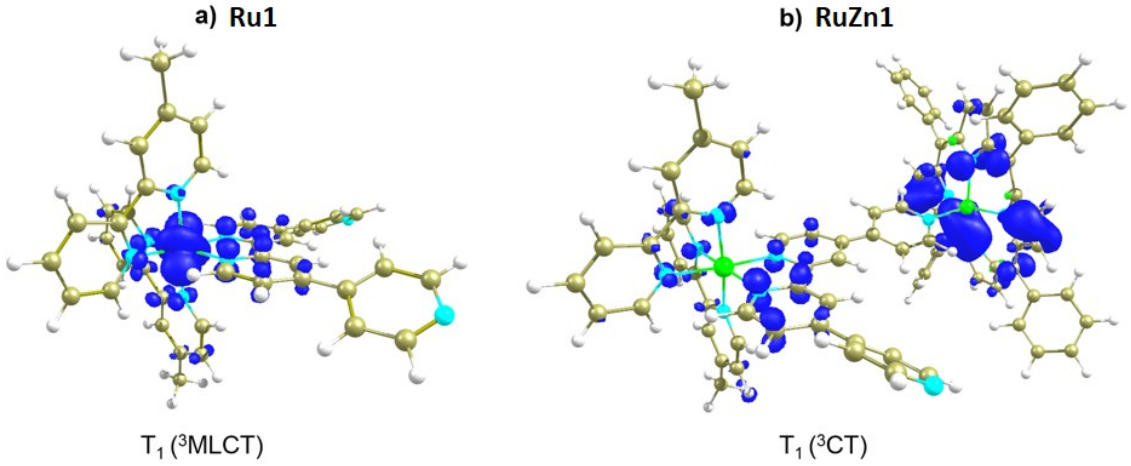

Figure 99. Spin-density distributions [B3LYP/6-31G(d) – ecp-28-mwb for Ru] at the optimised geometry of the lowest triplet excited state of **Ru1 (a)** and **RuZn1 (b)**.

Emission spectra acquired at different excitation wavelengths during the titration of one to three equivalents of ZnTPP into a 3 x 10^{-4} M solution of **Ru1** to form the assemblies **RuZn1** and **RuZn2** are reported in **Figure S238-S240**, appendix. Upon excitation of **RuZn1** and **RuZn2** into either the CT absorption band of Ru (λ_{exc} = 500 nm), the Q-band of ZnTPP (λ_{exc} = 550 nm) or the Soret band of ZnTPP (λ_{ex} = 420 nm), resulted in a significant reduction in the Φ_{PL} for ZnTPP (Φ_{PL}(ZnTPP) = 4%; Φ_{PL}(ZnTPP) < 1% in **RuZn1** and **RuZn2**, **Table 8**), while the emission of **Ru1** was completely quenched (**Figure 98a**). The efficient quenching of the phosphorescence of **Ru1** and the fluorescence of ZnTPP are attributed to the formation of the non-emissive charge-separated state $[ZnTPP]^{\cdot+}$-$[Ru]^{\cdot-}$ as was predicted following the Rehm–Weller equation and supported by a fast PeT kinetic (k_{eT} = 4.995 x 10^7 s^{-1}), which is in agreement with the PeT processes reported for the systems illustrated in **Figure 79**. Indeed, by contrast to **Ru1**, the optimisation of the lowest triplet excited state of **RuZn1** leads to a non-emissive CT state (**Figure 99b**). The enhanced non-radiative decay from this dark-state (that eventually leads to the formation of the charge-separated states) is most likely responsible for the emission quenching observed in the assemblies.[391] As a result of the strong emission quenching observed for **RuZn1** and **RuZn2**, no emission lifetimes could be measured.

To discern whether the formation of the non-emissive charge-separated state observed for **RuZn1** and **RuZn2** is favored through the coordination of ZnTPP to qpy, emission spectra were also collected after addition of ZnTPP to the control complex **Ru2** (at a

concentration of 3 x 10^{-4} M) where coordination is not possible (the emission spectra are reported in the appendix in **Figure S241-S243**). We noted that upon excitation at 420, 500 or 550 nm, the emission of **Ru2** was likewise strongly quenched and presented similar behaviour to that observed for **RuZn1** and **RuZn2** (**Figure 98b**). Thus, we attribute the strong emission quenching of both the ruthenium complex and ZnTPP as a result of long-distance collisional processes between the two chromophoric units.[392]

Table 8. Emission data for **Ru1**, **RuZn1**, **RuZn2**, **Ru2**, **RuZn3**

	λ_{PL} (nm)[a,b]		Φ_{PL} (%)[a,c]	
	λ_{exc}: 420 nm	λ_{exc}: 555 nm	λ_{exc}: 420 nm	λ_{exc}: 555 nm
Ru1	674	674	-	7.3
RuZn1	601 [0.09], 655 [1]	601 [0.09], 655 [1]	<1[d]	<1[d]
RuZn2	603 [0.19], 655 [1]	603 [0.19], 605 [1]	<1[d]	<1[d]
Ru2	615	615	-	9.1
RuZn3	599 [0.05], 655 [1]	599 [0.05], 655 [1]	1.4	<1[d]

[a]Measurements in degassed CH_2Cl_2 at 298 K at a concentration of 3 x 10^{-4} M. [b]Principal emission peaks listed with values in parentheses indicating relative intensity. [c]Φ_{PL} measurements were carried out in degassed CH_2Cl_2 under nitrogen (λ_{exc} = 360 nm) using $[Ru(bpy)_3]Cl_2$ as the external reference (Φ_{PL} = 4% in aereated H_2O at 298 K).[379] [d]Values estimated from the reduction of the emission counting compared to neat ZnTPP.

4.6 Conclusions

In this chapter we reported the synthesis and optoelectronic study of supramolecular assemblies composed of cationic iridium and ruthenium complexes of the form of $[M(L\hat{}X)_2(qpy)]PF_6$ (M is either Ir with L^X: mesppy and dFmesppy or Ru with L^X: dtBubpy) and ZnTPP, through dynamic and non-covalent interactions between the distal pyridine moieties of the qpy ligands of the Ir and Ru complexes and zinc of ZnTPP. ^{1}H NMR titration experiments reveal equilibrium constants in the range of 7000 - 8000 M^{-1} for the formation of the 1 : 1 assemblies from **Ir3** or **Ru1** and ZnTPP and 2200 - 2500 M^{-1} for the formation of 1 : 2 assemblies from **InZn1** or **RuZn1** and ZnTPP. The structures of the assemblies **InZn1** and **InZn2** have been elucidated by X-ray single-crystal structure analyses. For the Ir-Zn assemblies **InZn1**, **InZn2**, **InZn3** and **InZn4** radiative energy transfer (self-absorption) from the iridium donor to the ZnTPP acceptor was observed with no evidence of Förster or Dexter energy transfer between the units. Furthermore, despite favourable thermodynamics

for electron transfer from ZnTPP to iridium, no evidence of the formation of a charge separated state following electron transfer was observed by steady-state and time-resolved emission spectroscopy. This is attributed to the slow PeT kinetic (k_{eT} of about 10^6 s^{-1}) calculated for these processes. By contrast, for the Ru-Zn assemblies **RuZn1** and **RuZn2**, as a result of the faster PeT processes (k_{eT} of 4.995 x 10^7 s^{-1}), emission quenching through the formation of the non-emissive charge-separated $[ZnTPP]^{\cdot+}$-$[Ru]^{\cdot-}$ state was experimentally observed by steady-state emission spectroscopy and theoretically supported by TD-DFT calculations and exergonic ΔG_{CS} values by Rehm-Weller equation.

Chapter 5

Phosphorescent Iridium-Silver Coordination Polymer

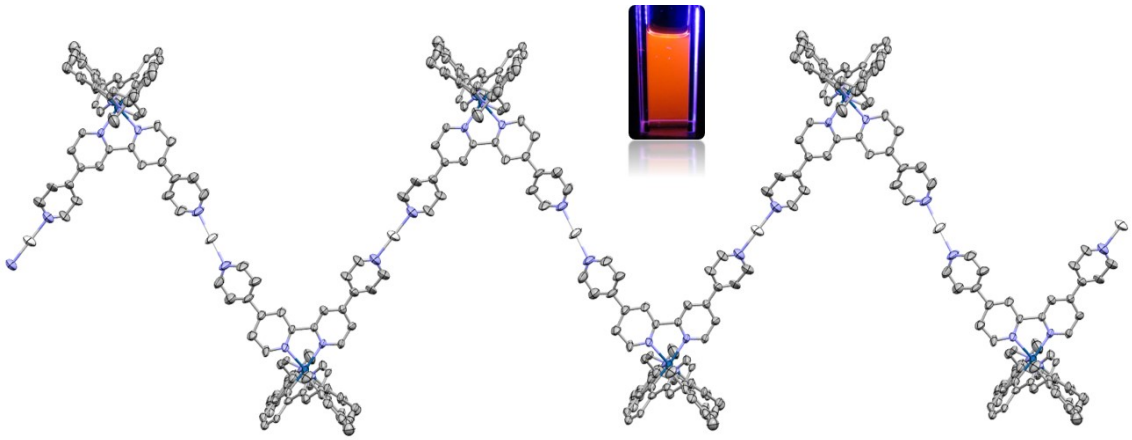

5.1 Introduction

As documented in the first chapter when discussing Ir-based coordination networks, polymers and MOFs, crystal engineering is a powerful approach to prepare infinite 1D-, 2D- and 3D- metal-organic supramolecular materials with predefined properties, functions and applications.[138, 294] The main factors controlling the self-assembly of simple building blocks are now reasonably well-understood; appropriate matching of the coordination geometry preferences of metal ion(s), the nature and denticity of the ligand scaffold, and the length, angle and flexibility of the linking units between binding sites on the ligands usually provide good control on the resulting assembly.[140, 297] The combination of suitable metal ions with rigid bent bridging ligands reliably generate discrete cage-like structures with various shapes such as tetrahedra, octahedra, cubes and other platonic shapes, or continuous metal-organic framework materials.[140, 298]

In recent years, the supramolecular chemistry of Ag(I) coordination polymers has been attracting a great deal of attention, primarily owing to their intrinsic structural diversity.[393, 394] Indeed, the coordination sphere of Ag^+ ions is flexible and can adopt a coordination number between one and six, corresponding to the coordination geometries of linear,[395] trigonal,[396] tetrahedral,[397] square planar,[398, 399] square pyramidal,[398] trigonal bipyramidal[400] and octahedral.[401] This geometric flexibility thus gives rise to intricate coordination structures, the self-assembly process of which is generally highly influenced by the modification of the ligand functionalities, anions, solvents, ligand-to-Ag ratio, as well as crystallisation conditions.[402] Particularly investigated are Ag(I)-N_{py} coordination architectures. The nature of this interaction is predominantly donation of the pyridine electron lone pair to the metal cation and its energy is comparable with that of a strong H-bond (for example, 47 $kJ{\cdot}mol^{-1}$ for pyridine-Ag(I)).[403] Ag(I)-N_{py} bonding have been exploited quite extensively to form linear and zig-zag supramolecular chains.[394] Linear structures can be easily formed by the assembly a ligand containing two pyridine units disposed in a linear arrangement with Ag^+ ions in a 1:1 stoichiometry.[394, 403, 404] On the other hand, if bent ditopic ligands are assembled with Ag(I), or if the linear Ag(I) coordination geometry is distorted by coordinating anions or solvents, zig-zag chains are likely to be formed.[405] The latter can further assemble into a network or a macrocycle in the presence of a connecting entity such as solvent molecules or coordinating anions.

In this chapter we present a phosphorescent zig-zag coordination polymer, **IrP1**, formed through the self-assembly in a 1:1 ratio between our iridium metalloligand **Ir3** (**Figure 58**, chapter 3) and Ag^+ ions. The x-ray structure and the solution emission properties of **IrP1** are herein discussed. To the best of our knowledge, this is the first example of a coordination polymer formed through the assembly between an iridium metalloligand and silver ions. Phosphorescent silver(I) coordination polymers themselves are rare and only limited to silver-triazolates.[406–408] Zhou and co-workers.[406, 407]

reported cyanide-containing polymers obtained from solvothermal reaction between CN^-, generated from decomposition of acetonitrile, and triazolate-type ligands. These are 3D networks of compositions $[Ag_3(dmtrz)_2(CN)]_n$ and $[Ag_3(dptrz)_2(CN)]_n$, 2D grid-type polymers of compositions $[Ag_3(detrz)_2(CN)]_n$ and $[Ag_4(dptrz)_2(CN)_2]_n$ or 1D polymeric chain of composition $[Ag_3(trz)_2(CN)]_n$ (Hdmtrz = 3,5-dimethyl-1H-1,2,4-triazole; Hdptrz = 3,5-dipropyl-1H-1,2,4-triazole; Hdetrz = 3,5-diethyl-1H-1,2,4-triazole; Htrz = 1H-1,2,4-triazole). At room temperature these silver polymers exhibited broad green emissions located at λ_{PL} between 500 and 520 nm. The emission from triplet states in these coordination polymers is induced by the heavy atom effect of silver(I) ions and is ascribed to a mixture of an ^{3}MLCT transition, where electron is transferred from Ag(I) centre to π^* orbitals of the triazolates, and an ^{3}LLCT, cyanide-to-triazole charge transfer transition. Hu and co-workers[408] reported a 3D silver coordination polymer $[Ag(dmtrz)]_n$, where Ag(I) centres are firstly linked through the dmtrz ligand to form an infinite helix. This structure is further interconnected to four neighbouring anti-parallel helices to give rise to an infinite 3D framework. This polymer exhibited light-blue phosphorescence with a maximum at 485 nm, which is red-shifted compared to the blue emission at 410 nm exhibited by the 2D net-type network of composition $[Ag(trz)]_n$.[409]

3D heterometallic coordination polymers containing Ag(I) nodes were also reported by the groups of Englert,[410, 411] Hosseini,[412, 413] Mahon,[414] Severin[415] and Cohen[416] by reacting tritopic octahedral Fe(III),[414] Al(III),[411] Cr(III),[417] In(III) and Ga(III)[415] metalloligands or ditopic tetrahedral Cu(II)[414] and Pd(II)[418] metalloligands, all containing 3-cyano acetylacetonato units, with Ag^+ metal ions. Carlucci and co-workers[419] assembled hexadentate metalloligands of the type of $M^{III}L_3$ (M: Fe^{3+} and Co^{3+}) and $M^{II}L_3$ (M: Mn^{2+}, Co^{2+}, Zn^{2+} and Cd^{2+}), where L is a β-diketonate ligand appended with two benzonitrile groups, with Ag^+ ions obtaining porous 3D-MOF structures. Schulz and co-workers[420] have reported crystalline Ag(I) coordination polymer networks by assembling the tetrahedral p-cyanophenoxy aluminate metalloligand $[Al(OC_6H_4CN)_4]^-$ with Ag^+ ions. All of these 3D heterometallic coordination polymers or MOFs were found to be either non-emissive or there is no comment on their emission properties. On the other hand, when fluorescent BODIPY derivatives bearing peripheral benzonitrile as ligand scaffolds were assembled with Ag(I) metal centres, luminescent [2+2] macrocycles of composition $[Ag_2(BODIPY)_2]^{2+}$ were obtained.[402, 421] The $[Ag_2(BODIPY)_2]^{2+}$ macrocycles exhibited in the crystalline state the characteristic BODIPY-centred emission with two bands at λ_{PL} = 750, 790 nm, which resulted red-shifted when compared to the CH_2Cl_2 emission of the free BODIPY (λ_{PL} = 645, 705 nm). The photoluminescence quantum yields of the $[Ag_2(BODIPY)_2]^{2+}$ macrocycles were not reported.

5.2 Self-assembly and x-ray structure

The self-assembly between **Ir3** and $AgPF_6$ was firstly investigated at room temperature by ^1H and ^1H-DOSY NMR spectroscopy in $MeNO_2$-d_3, a solvent chosen to not interfere with the linear coordination of the distal pyridines present in **Ir3** with Ag^+ ions. When a 3.0 mM $MeNO_2$-d_3 solution of **Ir3** was mixed for five minutes with 1 equivalent of $AgPF_6$, the proton resonances associated with **Ir3** slightly broadened and were shifted (**Figure 100**).

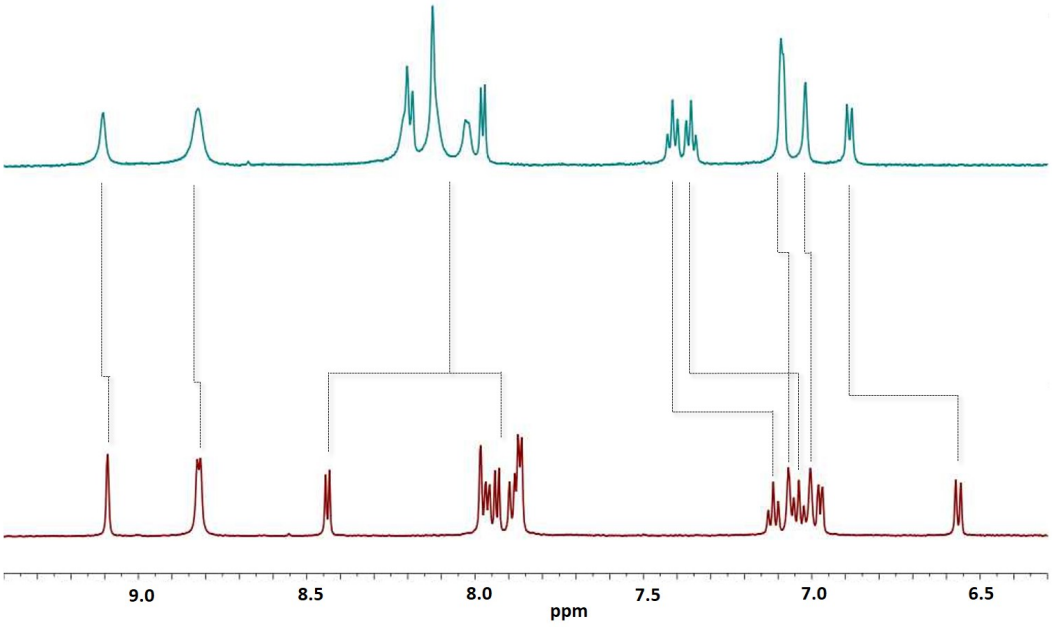

Figure 100. ^1H NMR spectra of **Ir3** (in red) and a 1:1 mixture of **Ir3**:$AgPF_6$ (**IrP1**, in light-blue) collected in $MeNO_2$-d_3 at room temperature.

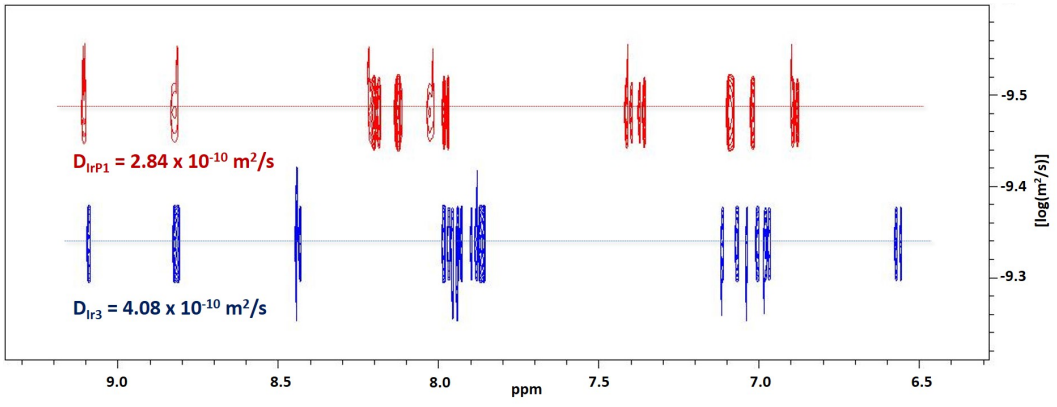

Figure 101. ^1H-DOSY NMR spectra of **Ir3** (in blue) and a 1:1 mixture of **Ir3**:$AgPF_6$ (**IrP1**, in red) collected in $MeNO_2$-d_3 at room temperature.

^{1}H DOSY NMR showed the formation of a single species in solution with a single diffusion coefficient in $MeNO_2$-d_3 of D = 2.84 x 10^{-10} m^2/s. This diffusion coefficient is smaller than that measured for **Ir3** in $MeNO_2$-d_3 (D = 4.08 x 10^{-10} m^2/s), indicating that the assembled structure, **IrP1**, is larger than **Ir3** (**Figure 101**). The corresponding hydrodynamic radius (r_s) for **IrP1** in $MeNO_2$-d_3 was calculated to be 12.4 Å, which is approximately 50% larger than that calculated for **Ir3** (r_s = 8.6 Å). This result indicates that in $MeNO_2$-d_3 the N_{py}-Ag coordination is dynamic and relatively weak. Therefore, **IrP1** in $MeNO_2$ solution comprises only a few **Ir3**-Ag repeating units. The addition of a larger amount of $AgPF_6$ (2 or 5 equivalents) to the $MeNO_2$-d_3 solution of **IrP1** did not cause any changes to the ^{1}H and ^{1}H-DOSY NMR spectra of **IrP1**, indicating the assembly is formed with a 1:1 stoichiometry between **Ir3** and Ag^+.

The structure of **IrP1** was confirmed by x-ray crystallography. We were able to obtain suitable single crystals of **IrP1** for x-ray diffraction through a slow diffusion of diethyl ether into a 3 mM CH_2Cl_2 solution **Ir3** (1 mL) layered with a 1:1 CH_2Cl_2/MeOH mixture (1 mL) and then with a MeOH solution of $AgPF_6$ (1 mL). The crystals were formed at room temperature over a period of 10 days. **IrP1** crystallised in the triclinic space group $P\bar{1}$, with two independent Ag(I) ions situated on inversion centers, and coordinating to the two N_{qpy} atoms of one molecule of **Ir3**. The inversion symmetry leads to a linear coordination geometry at Ag(I), and gives rise to a 1D zig-zag coordination polymer (**Figure 102**).

The N_{qpy}···Ag···N_{qpy} distances are 2.141(19) and 2.156(19) Å, in agreement with the N_{py}···Ag···N_{py} distances of 1.9 – 2.2 Å reported for the X-ray structures of related silver(I) coordination polymers. However, in many of these structures the linear Ag(I) coordination (N_{qpy}···Ag···N_{qpy}) is distorted by the presence of coordinating anions (PF_6^-, BF_4^- or AsF_6^- or ClO_4^-) or solvent molecules.[402] This is not the case for polymer **IrP1**. Indeed, for **IrP1** despite the presence in the crystal lattice of weakly coordinating PF_6^- anions, the Ag(I) centres coordinate to the N_{qpy} atoms with a perfect symmetry-induced linear geometry without any interaction with the fluorine atoms of PF_6^-.

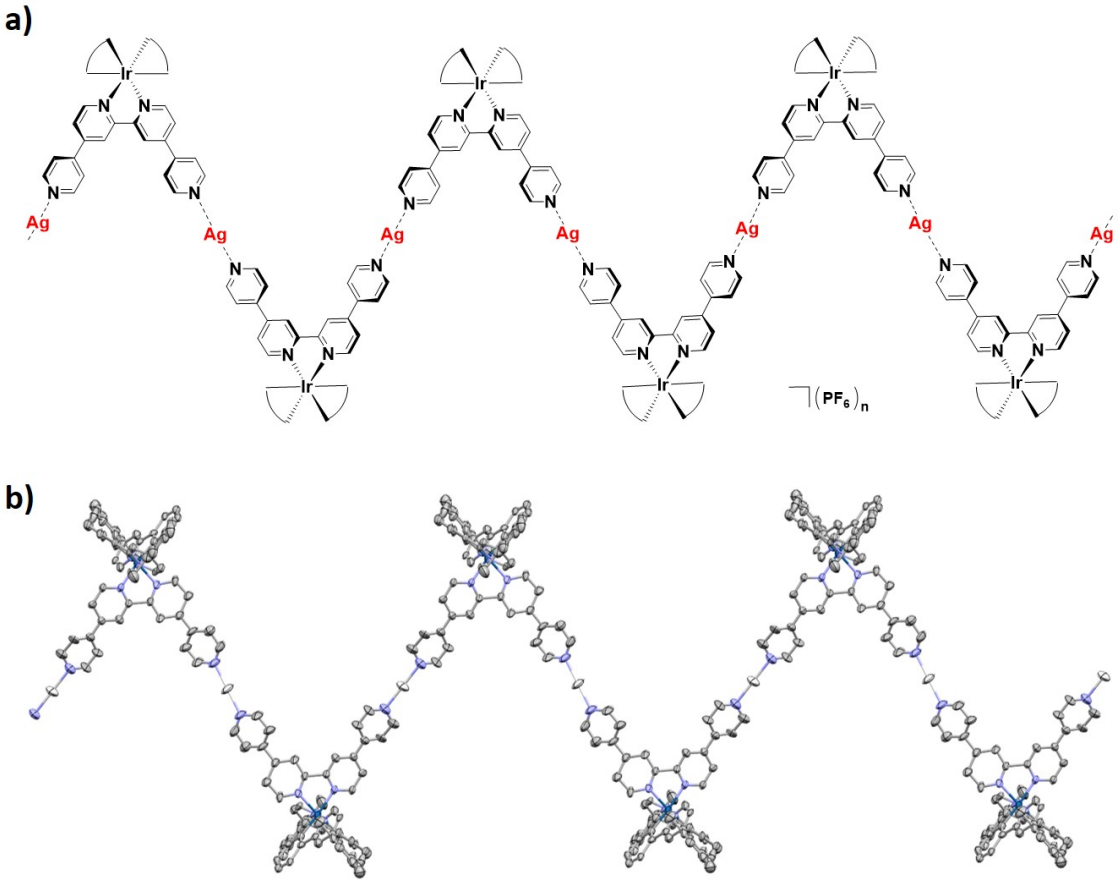

Figure 102. **a)** Representation of the structure of the zig-zag coordination polymer **IrP1**. The mesppy C^N ligand have been omitted for clarity; **b)** View of the x-ray structure of one 1D chain of **IrP1**. Hydrogen atoms, solvent molecules and counterions have been omitted for clarity.

The packing of the 1D chains of **IrP1** shows weak hydrogen bonds between the fluorine atoms of the PF_6^- counterions and C-H hydrogen atoms of various of the pyridine rings of the **Ir3** metalloligand [C-H···F-PF_5^- distances of 2.36 - 2.50 Å, with corresponding C···F separations of 3.13(2) - 3.35(5)] (**Figure 103**). This gives rise to weakly hydrogen-bonded layers in the *ab*-plane. However, **IrP1** does not show any direct chain-to-chain intermolecular interactions, such as π-π stacking, likely due to the presence of the bulky mesityl substituents. The Ir···Ir separations between two adjacent metalloligand connected by the Ag(I) bridge is 22.409(3) Å, while the Ir···Ir distance between two iridium complexes located in parallel 1D chains mediated by PF_6^- counterions is less than half this, at 10.8838(18) Å, although shorter Ir···Ir distance are found between Ir centres in adjacent sheets, at 8.806(16) Å. **IrP1** packs forming a complex three-dimensional network of narrow pores, giving a total free space of approximately 1285 $Å^3$ (about 33% of the volume of the unit cell).

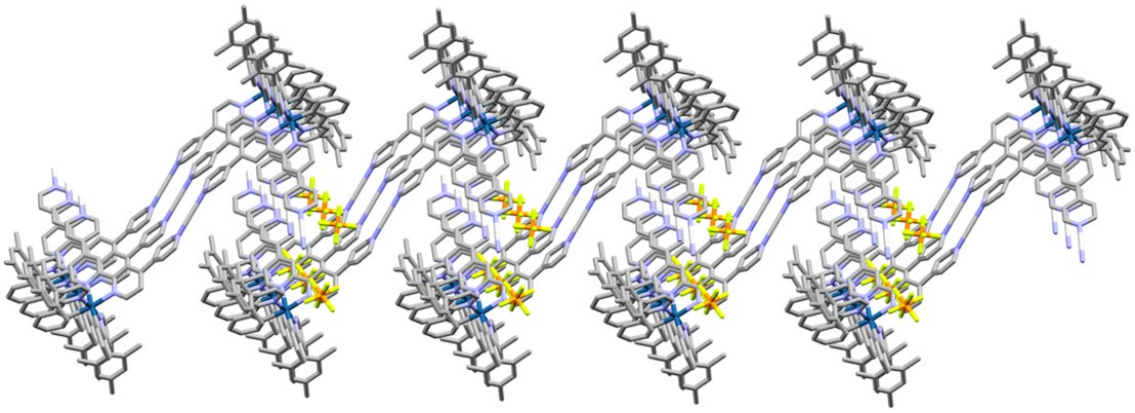

Figure 103. View of the 2D network in the x-ray structure of **IrP1**. Hydrogen atoms have been omitted for clarity.

5.3 Emission properties

The emission properties of **Ir3** and polymer **IrP1** were investigated in deaerated $MeNO_2$ and are reported in **Table 9**. Complex **Ir3** has a broad emission at λ_{PL} = 609 nm with a Φ_{PL} of 12% and a τ_{PL} of 284 ns. These emission properties match with those of **Ir3** collected in deaerated CH_2Cl_2 and reported in chapters 3 and 4. Interestingly, the emission profile of **IrP1** is slightly broader and red-shifted at 646 nm (**Figure 104**), with a slightly higher Φ_{PL} of 15% and a slightly longer τ_{PL} of 375 nm compared to **Ir3**.

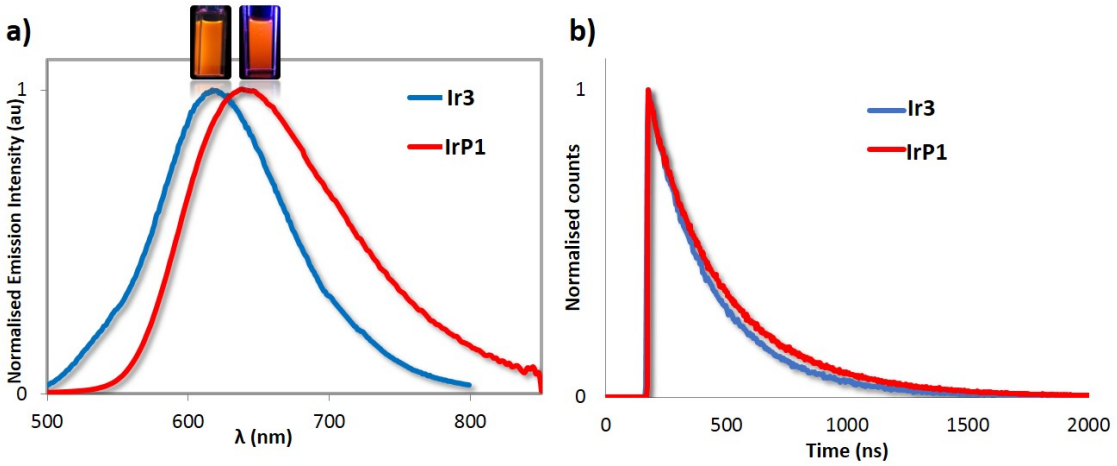

Figure 104. **a)** emission spectra of **Ir3** (blue line) and **IrP1** (red line), λ_{exc} = 360 nm and **b)** emission lifetimes of **Ir3** (blue line) and **IrP1** (red line), λ_{exc} = 378 nm. The spectra were collected in deaerated $MeNO_2$ at 298 K.

Table 9. [a]Relevant photophysical data for **Ir3** and **IrP1**

	$\lambda_{\mathbf{PL}}$ (nm)	$\Phi_{\mathbf{PL}}$(%)[b]	$\tau_{\mathbf{PL}}$ (ns)[c]	k_r x 10^5 (s^{-1})	k_{nr} x 10^5 (s^{-1})
Ir3	609	12	284	4.2	30.9
IrP1	646	15	375	4.0	22.7

[a]Measurements in degassed $MeNO_2$ at 298 K (λ_{exc} = 360 nm). [b]Φ_{PL} measurements were carried out in degassed $MeNO_2$ under nitrogen (λ_{exc} = 360 nm) using quinine sulfate as the external reference (Φ_{PL} = 54.6% in 0.5 M H_2SO_4 at 298 K).[287] [c](λ_{exc} = 378 nm)

Similar to the red-shifted emissions of **IrC1**, **IrC2** and **RuC1** compared to the corresponding metalloligands due to the N_{qpy}-Pd coordination, the red-shifted emission of **IrP1** compared to **Ir3** is the result of the coordination of the pyridine units of qpy to the Lewis-acidic Ag(I), which stabilises the LUMO of **Ir3** in **IrP1**, resulting in a smaller HOMO-LUMO gap. The radiative constant, k_r, calculated for **IrP1** of 4.0 x 10^5 s^{-1} is similar to that of **Ir3** while its non-radiative constant, k_{nr}, of 2.3 x 10^6 s^{-1} is slightly lower (for **Ir3** k_r = 4.2 x 10^5 s^{-1}, k_{nr} = 3.9 x 10^6 s^{-1}). Thus, the silver ions do not adversely affect the emission properties of **IrP1** in $MeNO_2$ where, as evidenced by ^{1}H-DOSY NMR measurements, short coordinated oligomers are present. This contrasts with the behavior reported by Hosseini and co-workers for the Ir-Cu coordination network (chapter 1, **Figure 34a**).[158] Indeed, the Ir-Cu network was found to be non-emissive both in solution and in the crystalline state, indicating that the Cu^+ metal ions completely quenched the luminescence of the Ir metalloligand Δ- and rac-**L15**, which itself exhibited a Φ_{PL} of 19% in deaerated THF and of 2% in the solid state. By contrast, the Ir-Cd network reported by the same group[159] (chapter 1, **Figure 34b**) exhibited in the crystalline state a weak emission (Φ_{PL} of 1%), which was, as observed for **IrP1**, slightly red-shifted ($\Delta\lambda$ = 6.67 x 10^5 cm^{-1}, 15 nm) and of similar intensity when compared with the solid-state emission of the corresponding Ir metalloligand Δ-, *rac*-**L16** (Φ_{PL} of 2%).

5.4 Conclusions

We have herein reported the first example of a phosphorescent zig-zag coordination polymer formed through the self-assembly between the iridium complex $[Ir(mesppy)_2(qpy)]PF_6$ and Ag^+ metal ions through N_{qpy}-Ag coordination. The zig-zag structure of the polymer, which has been elucidated by x-ray crystallography, is the result of the linear coordination of Ag(I) metal centres with the ditopic qpy ligand. Interestingly, the silver metal ions promoted a red-shift in the emission of the coordination polymer in $MeNO_2$ but do not adversely influence the photoluminescence quantum yield and emission lifetime of the polymer, which remained almost unchanged compared to the Ir metalloligand. We therefore believe that the assembly of suitably functionalised phosphorescent metal complexes with Ag^+ ions as

structural components opens up the possibility to prepare a wide range of supramolecular architectures such as coordination polymers, networks and macrocycles, that retain the optoelectronic properties of the photoactive complexes.

Chapter 6

Experimental

6.1 General synthetic methods

Commercial chemicals were used as supplied. All reactions were carried out using solvents of reagent grade or better. Flash column chromatography was performed using silica gel (60 Å, 40-63 µm). Analytical thin layer chromatography (TLC) was performed using silica plates with aluminum backings (250 µm with indicator F-254). Compounds were visualized under UV light. ^{1}H (including ^{1}H DOSY), ^{13}C and ^{19}F, ^{31}P and ^{11}B NMR spectra were recorded on Bruker Avance spectrometers at 300 – 500 MHz, 126 MHz and 376 MHz respectively. The following abbreviations have been used for multiplicity assignments: 's' for singlet, 'd' for doublet, 't' for triplet, 'q' for quartet, 'p' for pentet, 'm' for multiplet and 'b' for broad. Deuterated chloroform ($CDCl_3$), deuterated dichloromethane (CD_2Cl_2), deuterated acetonitrile (CD_3CN), deuterated water (D_2O), deutertated methanol (CD_3OD), deuterated nitromethane (CD_3NO_2) and deuterated dimethylsulfoxide (DMSO-d_6) were used as the NMR solvents of record. ^{1}H and ^{13}C NMR spectra were referenced to the solvent peak. High-resolution mass spectra of molecular compounds and complexes were recorded at the EPSRC UK National Mass Spectrometry Facility at Swansea University on a quadrupole time-of-flight (ESI-Q-TOF), model ABSciex 5600 Triple TOF in positive electrospray ionization mode and spectra were recorded using sodium formate solution as the calibrant. The high-resolution mass spectra of $NBu_4[Ir(dFppy)_2(CN)_2]$ was recorded at the University of Leeds on a Bruker MaXis Impact instrument in negative ion mode. High-resolution mass spectra of supramolecular cages were recorded at the University of Leeds on a Bruker MaXis Impact instrument in positive ion mode. The cage samples were injected by direct infusion from DMSO solutions of a concentration of ca. 1 x 10^{-4} M. Transmission Electron Microscopy measurements were carried out by Ross Blackley at the University of St Andrews on a Jeol JEM 2011 HRTEM instrument equipped with a LaB6 filament as the electron source and a GATAN CCD camera for collecting pictures. Melting

points (Mp) were recorded using open-ended capillaries on an Electrothermal melting point apparatus.

6.2 Syntheses of ligands and intermediates

6.2.1 Suzuki-Miyaura cross-coupling reactions

General procedure

The boronic acid and aryl halide were added to a round bottom flask along with base and a mixture of 1,4-dioxane and distilled water (4:1 v/v) to obtain a concentration of 0.15 to 0.20 M. The reaction mixture was degassed via three purging cycles of N_2 and vacuum. Under positive N_2 pressure, $Pd(PPh_3)_4$ (5.0 mol%) was added to the flask and the flask was sealed. The mixture was refluxed for the specified time, before adding distilled water, extracting with organic solvent and washing with water and saturated aqueous sodium hydrogen carbonate to remove residual boronic acid. Evaporation under reduced pressure gave the crude product, which was purified by flash column chromatography.

2-Chloro-4-(2,4,6-trimethylphenyl)pyridine

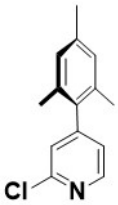

The synthesis of this compound is by a previously reported method.[277] 2,4,6-Trimethylphenylboronic acid (1.5 equiv.), 2-chloro-4-iodopyridine (1.0 equiv.) and potassium carbonate (3.0 equiv.) were added to a round bottomed flask containing 50 mL of a mixture of 1,4-dioxane and water (4:1 v/v). Note: an excess of boronic acid is required to ensure full consumption of 2-chloro-4-iodopyridine, since the boronic acid is prone to deborylation in situ and separation of 2-chloro-4-(2,4,6- trimethylphenyl)pyridine from 2-chloro-4-iodopyridine by chromatography is not possible. The mixture was refluxed for 72 h. The crude was extracted with toluene. The compound was purified by silica gel chromatography (hexanes/ethyl acetate, 95:5) to give the product as a colourless oil (2.561 g). **Yield:** 85%. **Rf:** 0.40 (silica, hexanes/ethyl acetate, 95:5). **^{1}H NMR (400 MHz, $CDCl_3$)** δ **(ppm):** 8.46 (d, J = 5.1 Hz, 1H), 7.18 (s, 1H), 7.06 (dd, J = 5.1, 1.4 Hz, 1H) 6.99 (s, 2H) 2.36 (s, 3H), 2.04 (s, 6H). **^{13}C [^{1}H] NMR (126 MHz, $CDCl_3$)** δ **(ppm):** 152.9, 151.8, 149.8, 138.0, 134.9, 128.5, 125.1, 123.6, 21.0, 20.5. **HR-MS ($APCI^+$):**

[M+H]$^+$ Calculated: ($C_{14}H_{14}ClNH$) 234.0858; **Found:** 234.0856. The characterisation matches that reported.[277]

2-Phenyl-4-(2,4,6-trimethylphenyl)pyridine (**mesppy**)

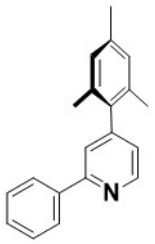

Phenylboronic acid (1.6 equiv.), 2-chloro-4-(2,4,6-trimethylphenyl)pyridine (1.0 equiv.) and potassium carbonate (2.8 equiv.) were added to a round bottomed flask containing 50 mL of a mixture of 1,2-dimethoxyethane and water (4:1 v/v). The reaction mixture was refluxed for 19 h. The crude was extracted with DCM. The compound was purified by silica gel chromatography (hexanes/ethyl acetate, gradient from 10:0 to 8:2) to give the product as a colourless oil (3.190 g). **Yield:** 87%. **Rf:** 0.38 (silica, hexanes/ethyl acetate, 9:1). **^{1}H NMR (500 MHz, $CDCl_3$)** δ **(ppm):** 8.77 (dd, J = 5.0, 0.8 Hz, 1H), 8.05 (m, 2H), 7.60 (q, J = 0.8 Hz, 1H), 7.54 – 7.42 (m, 2H), 7.54 – 7.42 (m, 1H) 7.09 (dd, J = 5.3, 1.3 Hz, 1H), 7.01 (s, 2H), 2.44 (s, 3H), 2.15 (s, 6H). **^{13}C [^{1}H] NMR (126 MHz, CD_2Cl_2)** δ **(ppm):** 157.7, 150.3, 149.9, 139.4, 137.6, 136.5, 135.2, 129.1, 128.8, 128.6, 128.4, 127.0, 123.2, 121.5, 21.1, 20.7. **HR-MS (FTMS$^+$): [M+H]$^+$ Calculated:** ($C_{20}H_{19}NH$) 274.1585; **Found:** 274.1585. The characterisation matches that reported.[278]

2-(2,4-Difluorophenyl)-4-(2,4,6-trimethylphenylpyridine (**dFmesppy**)

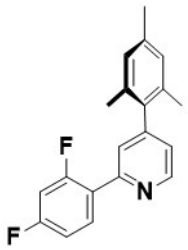

The synthesis of this compound is by a previously reported method.[277]
2,4-Difluorophenylboronic acid (1.4 equiv.), 2-chloro-4-(2,4,6-trimethylphenyl)pyridine (1.0 equiv.) and potassium carbonate (2.5 equiv.) were added to a 50 mL of a mixture of 1,4-dioxane and water (4:1 v/v). The reaction mixture was refluxed for 19 h. The crude was extracted with DCM. The compound was purified by silica gel chromatography (hexanes/ethyl acetate, gradient from 10:0 to 6:1) to give the product as a colourless oil (3.590 g). **Yield:** 94%. **Rf:** 0.43 (hexanes/ethyl acetate, 6:1 on silica). **^{1}H [^{19}F] NMR**

(500 MHz, $CDCl_3$) δ (ppm): 8.75 (dd, J = 7.5, 1.5 Hz, 1H), 8.08 (dt, J = 10.0, 8.5 Hz, 1H), 7.59 (m, 1H), 7.09 (dd, J = 5.0, 1.5 Hz, 1H), 7.02 (tdd, J = 10.0, 3.3, 1.0 Hz, 1H), 6.97 (d, J = 1.0 Hz, 2H), 6.90 (dt, J = 12.5, 3.0 Hz, 1H), 2.34 (s, 3H), 2.05 (s, 6H). **^{13}C [^{1}H] NMR (126 MHz, $CDCl_3$) δ (ppm):** 164.7, 162.0, 159.5, 152.9, 122.8, 150.2, 150.1, 137.8, 136.4, 135.4, 132.4, 132.4, 132.3, 132.3, 128.5, 125.5, 125.4, 123.7, 112.2, 112.1, 111.9, 111.9, 104.8, 104.5, 104.3, 21.2, 20.8. **^{19}F [^{1}H] NMR (471 MHz, $CDCl_3$) δ (ppm):** -109.3 (d, J = 9.4 Hz, 1F), -112.7 (d, J = 9.4 Hz, 1F). **HR-MS (APCI$^+$): [M+H]$^+$ Calculated:** ($C_{20}H_{17}F_2NH$) 310.1402; **Found:** 310.1402. The characterisation matches that reported.[277]

6.2.2 4,4′:2′,2″:4″,4‴-Quaterpyridine (qpy)

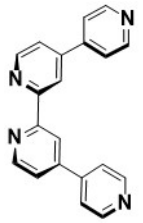

The synthesis of this compound is by a previously reported method.[329] 4,4′-Bipyridine (5.0 g, 0.032 mol), Pd/C (0.70 g, 10% weight Pd) and DMF (50 mL) were added to a dry round bottomed flask, and the reaction mixture was sonicated and oxygenated by bubbling air through the solution. The mixture was refluxed for 48 h, cooled to room temperature and the solvent was removed using a high-vacuum rotary evaporator. The crude product was dissolved in $CHCl_3$ (50 mL) and the catalyst was filtered. A bright yellow solution was obtained and $CHCl_3$ was removed under vacuum to obtain a brown solid. The crude product was purified by flash chromatography (5% methanol / DCM) to give 0.903 g of pure compound as a white solid. **Yield:** 15%. **Rf:** 0.40 (5% MeOH/DCM on silica). **^{1}H NMR (500 MHz, $CDCl_3$) δ (ppm):** 8.86 (d, J = 5.4 Hz, 2H),8.82 – 8.79 (m, 6H), 7.71 (d, J = 5.1 Hz, 4H), 7.64 (d, J = 5.5, 2H). **^{13}C NMR (126 MHz, $CDCl_3$) δ (ppm):** 156.6, 150.7, 150.1, 146.7, 145.6, 121.7, 121.5, 119.1. The characterization matches that reported.[329]

6.3 Synthesis of organometallic complexes

6.3.1 Racemic μ-chloro-bridged iridium dimers

General procedure for synthesis of racemic iridium dimers by Nonoyama's method

This procedure is a modified version of that originally reported by Nonoyama.[283] To a flask containing $IrCl_3.3H_2O$ (1.0 equiv.) and C^N ligand (2.2 equiv.) was added 2-ethoxyethanol and distilled water (3:1 v/v) to give a concentration of ca. 0.2 M. The reaction mixture was degassed via three purging cycles of N_2 and vacuum. The mixture was heated to reflux under nitrogen atmosphere, whereupon a yellow precipitate formed after 1 h. The mixture was refluxed for a further 18 h, before cooling. Water was added and the precipitate was collected by filtration. The solid was washed with multiple times with a mixture of water and ethanol (1:1 v/v) and then multiple times with a mixture of hexanes and diethyl ether (1:1 v/v), before drying to give the title compound.

General procedure for synthesis of racemic iridium dimers using [Ir(COD)(Cl)]$_2$

This synthetic protocol is a modification of that reported in the literature.[422] A suspension of *bis*[(1,5-cyclooctadiene)diiridium(I)] dichloride (1.0 equiv.) in 2-ethoxyethanol was degassed via vigorous N_2 bubbling. A solution of C^N ligand (4.0 equiv.) in 2-ethoxyethanol (ca. 1.8 M) was added to the reaction mixture to give a concentration of ca. 0.5 M, and the mixture was further degassed via nitrogen bubbling. The reaction mixture was heated to reflux. After 30 min, the reaction mixture turned dark red/black. At 1 h, a precipitate had formed. After 3 h, the reaction mixture was cooled and MeOH was added. The precipitate was filtered, washed with MeOH and acetone, and then multiple times with a mixture of hexanes and diethyl ether (1:1 v/v), before drying to give the title compound.

***Rac*-tetrakis[2-phenylpyridinato-N,C$^{2\prime}$]-bis(μ-chloro)diiridium(III), *rac*-[Ir(ppy)$_2$(μ-Cl)]$_2$**

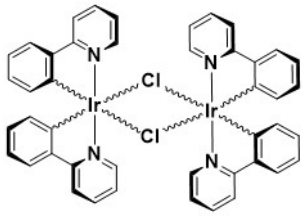

Preparation by Nonoyama's method: yellow powder. **Yield:** 85%. **^{1}H NMR (500 MHz, $CDCl_3$) δ (ppm):** 9.26 (dd, J = 5.5, 1.0 Hz, 4H), 7.88 (d, J = 7.5 Hz, 4H), 7.76 (td, J = 7.5, 1.5 Hz, 4H), 7.51 (dd, J = 7.5, 1.5 Hz, 4H), 6.81 - 6.74 (m, 8H), 6.58 (td, J = 7.5, 1.5 Hz, 4H), 5.95 (dd, J = 7.5, 1.0 Hz, 4H).[278]

***Rac*-tetrakis[2-(phenyl)-4-(2,4,6-trimethylphenyl)pyridinato-N,C$^{2\prime}$]-bis (μ-chloro)diiridium(III), *rac*-[Ir(mesppy)$_2$(μ-Cl)]$_2$**

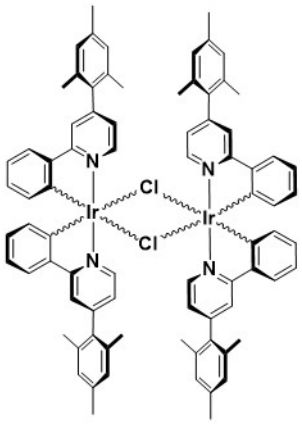

Preparation using [Ir(COD)(Cl)]$_2$ precursor: yellow powder. **Yield:** 70%. **^{1}H NMR (500 MHz, CD_2Cl_2) δ (ppm):** 9.69 (d, J = 6.4 Hz, 4H), 7.77 (d, J = 1.8 Hz, 4H), 7.55 (dd, J = 7.8, 1.3 Hz, 4H), 7.05 (d, J = 9.0 Hz, 8H), 6.86 (m, 8H), 6.72 (dt, J = 8.1, 7.1, 4H), 5.95 (dd, J = 8.1, 1.1 Hz, 4H), 2.42 (s, 12H), 2.16 (s, 12H), 2.15 (s, 12H). The characterisation matches that reported.[278]

***Rac*-tetrakis[2-(4′,6′-difluorophenyl)-4-(2,4,6-trimethylphenyl) pyridinato-N,C$^{2\prime}$]-bis(μ-chloro)diiridium(III), *rac*-[Ir(dFmesppy)$_2$(μ-Cl)]$_2$**

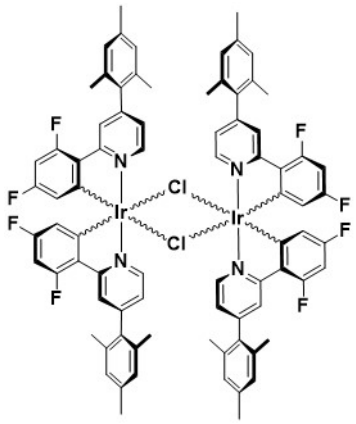

Preparation using [Ir(COD)(Cl)]$_2$ precursor: yellow powder. **Yield:** 81%. **^{1}H [^{19}F] NMR (400 MHz, CD_2Cl_2) δ (ppm):** 9.57 (d, J = 6.0 Hz, 4H), 8.13 (d J = 1.2 Hz, 4H), 7.02 (d, J = 10.4 Hz, 8H), 6.89 (dd, J = 6.0, 2.0 Hz, 4H), 6.38 (d, J = 2.4 Hz, 4H), 5.28 (d, J = 2.4 Hz, 4H), 2.38 (s, 12H), 2.12 (s, 12H), 2.10 (s, 12H). **^{19}F [^{1}H] NMR (471 MHz, CD_2Cl_2) δ (ppm):** -108.07 (d, J = 11.1 Hz, 4F), -110.22 (d, J = 10.8 Hz, 4F). The characterisation matches that reported.[278]

6.3.2 Racemic iridium(III) complexes

General procedure for synthesis of racemic iridium(III) complexes

To a round bottom flask containing the appropriate dichloro-bridged iridium dimer (1.0 equiv.) and N^N ligand (2.2 equiv.) were added DCM and MeOH (1:1 v/v) or 2-methoxyethanol to give a suspension with a concentration of ca. 0.02 M. The mixture was degassed via bubbling with N_2 for 10 min, before the reaction vessel was sealed. The reaction mixture was heated to reflux for 19 h under nitrogen atmosphere. The solution was cooled to room temperature, and the solvent evaporated. For preparing the PF_6^- salts: the solution was cooled to room temperature and solid NH_4PF_6 (10.0 equiv.) was added and the reaction mixture was left to stir for a further 1 h. For preparing the BF_4^- salts: a 2 M solution of KBF_4 in MeOH (10 mL) was added at room temperature to the reaction mixture and the resulting suspension was stirred at room temperature for 4 h. For preparing SbF_6^- salts: a 2 M solution of $KSbF_6$ in MeOH (10 mL) was added at room temperature to the reaction mixture and the resulting suspension was stirred at room temperature for 4 h. For all three anions, the resulting suspensions were evaporated to dryness, with the residue then copiously washed with Et_2O and distilled water. This crude product was purified by flash column chromatography. Fractions containing the desired complex were combined and solid NH_4PF_6 (10.0 equiv.) or KBF_4 (10.0 equiv.) or SbF_6 (10.0 equiv.) was added. The suspension was stirred at room temperature for 0.5 h. This mixture was then evaporated to dryness, washed vigorously with distilled water and diethyl ether and dried to afford the pure material.

***Rac*-iridium(III)bis[2-phenylpyridinato]-4,4′-di-tert-butyl-2,2′-bipyridine hexafluorophosphate, *rac*-[Ir(ppy)$_2$(dtBubpy)](PF$_6$)**

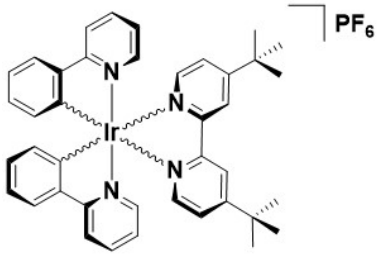

Preparation using DCM and MeOH (1:1 v/v) as solvent mixture: yellow powder. **Yield:** 92%. **Rf:** 0.45 (5% MeOH/DCM on silica). **Mp:** 284 - 288 °C. **^{1}H NMR (500 MHz, CD_2Cl_2) δ (ppm):** 8.31 (d, J = 1.3 Hz, 2H), 8.01 (d, J = 8.5 Hz, 2H), 7.96 (d, J = 6.0 Hz, 2H), 7.83 (dt, J = 7.2, 1.2 Hz, 2H), 7.78 (dd, J = 7.8, 1.0 Hz, 2H), 7.54 (dd, J = 5.8, 0.9 Hz, 2H), 7.48 (dd, J = 5.7, 1.8 Hz, 2H), 7.11 (td, J = 7.8, 1.4 Hz, 2H), 7.04 (td, J = 6.1, 1.5 Hz, 2H), 6.97 (td, J = 7.6, 1.2 Hz, 2H), 6.34 (dd, J = 8.0, 0.5 Hz, 2H), 1.46 (s, 18H). **HR-MS (FTMS$^+$): [M-PF$_6$]$^+$ Calculated:** ($C_{40}H_{40}IrN_4$) 769.2882; **Found:**

769.2853. The characterization matches that reported.[285]

***Rac*-iridium(III)bis[2-phenyl-4-(2,4,6-trimethylphenyl)pyridinato]-4,4′-di-tert-butyl-2,2'-bipyridine hexafluorophosphate, *rac*-[Ir(mesppy)$_2$(dtBubpy)](PF$_6$)**

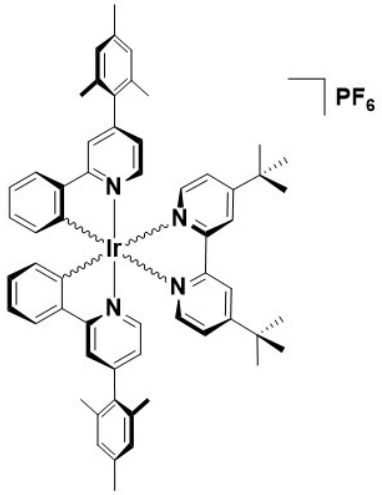

Preparation using DCM and MeOH (1:1 v/v) as solvent mixture: yellow powder. **Yield:** 89%. **Rf:** 0.55 (5% MeOH/DCM on silica). **Mp:** 264 - 268 °C. **^{1}H NMR (500 MHz, CD$_2$Cl$_2$) δ (ppm):** 8.36 (d, J = 1.7 Hz, 2H), 8.08 (d, J = 6.5 Hz, 2H), 7.82 (d, J = 2.3 Hz, 2H), 7.73 (dd, J = 8.2, 1.3 Hz, 2H), 7.58 (dd, J = 6.8, 1.0 Hz, 2H), 7.54 (dd, J = 6.0, 2.1 Hz, 2H), 7.11 (dt, J = 8.1, 1.5 Hz, 2H), 7.05 - 7.00 (m, 6H), 6.88 (dd, J = 6.0, 1.9 Hz, 2H), 6.43 (d, J = 10.0 Hz, 2H), 2.36 (s, 6H), 2.16 (s, 6H), 1.97 (s, 6H), 1.48 (s, 18H). **^{13}C NMR (126 MHz, CD$_2$Cl$_2$) δ (ppm):** 167.7, 164.2, 156.0, 151.8, 151.0, 149.7, 143.8, 138.2, 135.1, 134.9, 131.7, 130.7, 128.6, 128.5, 125.2, 124.8, 124.6, 122.4, 122.2, 120.5, 30.3, 21.1, 20.5. **HR-MS (FTMS$^+$): [M-PF$_6$]$^+$ Calculated:** ($C_{58}H_{60}IrN_4$) 1005.4447; **Found:** 1005.4427. The characterization matches that reported.[278]

***Rac*-iridium(III)bis[2-phenyl-4-(2,4,6-trimethylphenyl)pyridinato]-4,4′:2′,2″:4″,4‴-quaterpyridine hexafluorophosphate, *rac*-[Ir(mesppy)$_2$(qpy)](PF$_6$)**

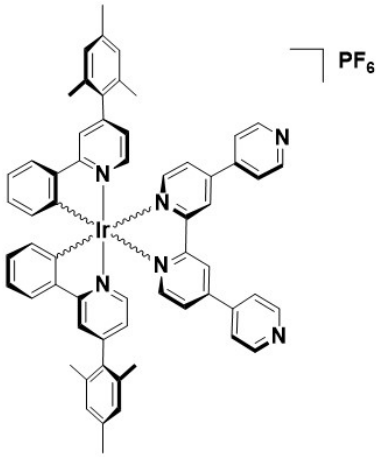

Preparation using 2-methoxyethanol as solvent: orange powder. **Yield:** 55%. **Rf:** 0.20 (DCM + 3% MeOH + 2% NEt_3 on silica). **Mp:** 348 - 352 °C (decomposed). **^{1}H NMR (500 MHz, CD_2Cl_2) δ (ppm):** 9.20 (s, 2H), 8.86 (d, J = 5.7 Hz, 4H), 8.30 (d, J = 5.3 Hz, 2H), 7.91 (m, 4H), 7.84 (s, 2H), 7.81 (dd, J = 6.1, 1.5 Hz, 2H), 7.76 (d, J = 7.8 Hz, 2H), 7.69 (d, J = 6.8 Hz, 2H), 7.14 (dt, J = 6.9, 1.0 Hz, 2H), 7.05 (m, 6H), 6.93 (dd, J = 6.4, 0.5 Hz, 2H), 6.46 (d, J = 6.4 Hz, 2H), 2.36 (s, 6H), 2.17 (s, 6H), 1.99 (s, 6H). **^{13}C NMR (126 MHz, CD_2Cl_2) δ (ppm):** 167.8, 165.5, 152.4, 151.5, 150.9, 149.8, 149.0, 148.6, 143.9, 143.0, 138.3, 134.9, 133.2, 131.5, 130.8, 128.5, 126.2, 125.1, 124.9, 122.9, 122.3, 121.3, 29.7, 20.8, 20.3. **^{1}H DOSY NMR (500 MHz, DMSO-d_6) D (m^2/s):** 1.3 x 10^{-10}. **^{1}H DOSY NMR (500 MHz, CD_2Cl_2) D (m^2/s):** 1.32 x 10^{-9}. **HR-MS (FTMS$^+$): [M-PF$_6$]$^+$ Calculated:** ($C_{60}H_{50}IrN_6$) 1047.3726; **Found:** 1047.3719.

***Rac*-iridium(III)bis[2-phenyl-4-(2,4,6-trimethylphenyl)pyridinato]-4,4′:2′,2″:4″,4‴-quaterpyridine tetrafluoroborate, *rac*-[Ir(mesppy)$_2$(qpy)](BF$_4$)**

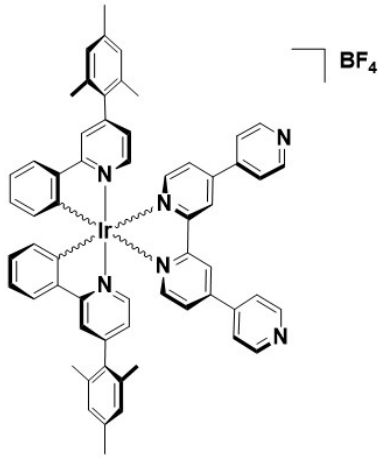

Preparation using 2-methoxyethanol as solvent: orange powder. **Yield:** 55%. **Rf:** 0.20 (DCM + 3% MeOH + 2% NEt_3 on silica). **Mp:** 346 - 353 °C (decomposed). **^{1}H NMR (500 MHz, CD_2Cl_2) δ (ppm):** 9.21 (s, 2H), 8.97 - 8.66 (m, 4H), 8.29 (d, J = 5.5 Hz, 2H), 8.07 - 7.54 (m, 12H), 7.32 - 6.74 (m, 10H), 6.46 (d, J = 7.7 Hz, 2H), 2.35 (s, 6H), 2.17 (s, 6H), 1.99 (s, 6H). **^{1}H DOSY NMR (500 MHz, DMSO-d_6) D (m^2/s):** 1.3 x 10^{-10}. **HR-MS (FTMS$^+$): [M-BF$_4$]$^+$ Calculated:** ($C_{60}H_{50}IrN_6$) 1047.3726; **Found:** 1047.3719.

***Rac*-iridium(III)bis[2-(2,4-difluoro)phenyl-4-(2,4,6-trimethylphenyl) pyridinato]-4,4′:2′,2″:4″,4‴-quaterpyridine hexafluorophosphate, *rac*-[Ir(dFmesppy)$_2$(qpy)](PF$_6$)**

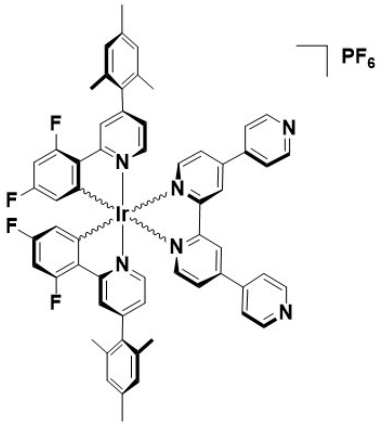

Preparation using 2-methoxyethanol as solvent: yellow powder. **Yield:** 39%. **Rf:** 0.18 (DCM + 3% MeOH + 2% NEt_3 on silica). **Mp:** 340 - 344 °C (decomposed). **^{1}H NMR (500 MHz, CD_2Cl_2) δ (ppm):** 8.83 (m, 5H), 8.31 (d, J = 5.4 Hz, 1H), 8.22 (bs, 2H), 7.85 (d, J = 5.9 Hz, 1H), 7.80 (d, J = 5.3 Hz, 2H), 7.69 (d, J = 5.8 Hz, 2H), 7.04 (m, 6H), 6.68 (m, 4H), 5.81 (m, 4H), 2.35 (s, 6H), 2.16 (s, 6H), 1.99 (s, 6H). **^{19}F [^{1}H] NMR (471 MHz, CD_2Cl_2) δ (ppm):** -72.50 (d, J = 707.5 Hz, 6F), -106.01 (d, J = 10.3 Hz, 2F), -108.31 (d, J = 10.3 Hz, 2F). **^{1}H DOSY NMR (500 MHz, DMSO-d_6) D (m^2/s):** 1.2 x 10^{-10}. **HR-MS (FTMS$^+$): [M-PF$_6$]$^+$ Calculated:** ($C_{60}H_{46}F_4IrN_6$) 1119.3349; **Found:** 1119.3326.

***Rac*-iridium(III)bis[2-(2,4-difluoro)phenyl-4-(2,4,6-trimethylphenyl) pyridinato]-4,4′:2′,2″:4″,4‴-quaterpyridine tetrafluoroborate, *rac*-[Ir(dFmesppy)$_2$(qpy)](BF$_4$)**

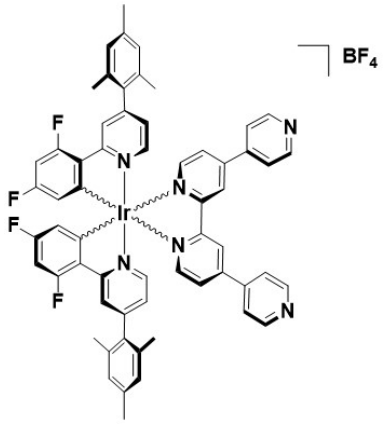

Preparation using 2-methoxyethanol as solvent: yellow powder. **Yield:** 40%. **Rf:** 0.19 (DCM + 3% MeOH + 2% NEt_3 on silica). **Mp:** 340 - 344 °C (decomposed). **^{1}H NMR (500 MHz, CD_2Cl_2) δ (ppm):** 9.40 (d, J = 1.8 Hz, 2H), 8.87 (d, J = 5.2 Hz, 4H), 8.44 - 8.13 (m, 4H), 7.99 (d, J = 5.3 Hz, 4H), 7.87 (dd, J = 5.9, 1.7 Hz, 2H), 7.72 (d, J = 6.0 Hz, 2H), 7.24 - 6.91 (m, 6H), 6.69 (ddd, J = 11.9, 9.0, 2.3 Hz, 2H), 5.85 (dd, J = 8.5, 2.4 Hz, 2H), 2.36 (s, 6H), 2.17 (s, 6H), 2.00 (s, 6H). **^{19}F [^{1}H] NMR (471 MHz, CD_2Cl_2) δ (ppm):** -106.20 (d, J = 10.3 Hz, 2F), -108.40 (d, J = 10.3 Hz, 2F), -150.9 (d, J = 10.0 Hz, 4F). **^{1}H DOSY NMR (500 MHz, DMSO-d_6) D (m^2/s):** 1.2 x 10^{-10}. **HR-MS (FTMS$^+$): [M-BF$_4$]$^+$ Calculated:** ($C_{60}H_{46}F_4IrN_6$) 1119.3349; **Found:** 1119.3326.

***Rac*-tetrabutyl ammonium bis(cyanide)-bis[2-(2,4-difluoro)-phenyl pyridinato]-iridium(III), *rac*-$NBu_4[Ir(dFppy)_2(CN)_2]$**

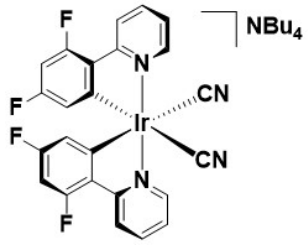

The synthesis of this complex follows a previously reported method.[72] Light brown powder. **Yield:** 70%. **^{1}H NMR (500 MHz, DMSO-d_6) δ (ppm):** 9.54 (d, J = 5.8 Hz, 2H), 8.36 - 7.86 (m, 5H), 7.45 (t, J = 6.8 Hz, 2H), 6.61 (t, J = 11.3 Hz, 3H), 5.53 (d, J = 8.1 Hz, 2H). **^{19}F [^{1}H] NMR (471 MHz, DMSO-d_6) δ (ppm):** -109.90 (d, J = 11.3 Hz, 2F), -111.00 (d, J = 11.3 Hz, 2F). **^{1}H DOSY NMR (500 MHz, DMSO-d_6) D (m^2/s):** 1.9 x 10^{-10}. **HR-MS (ESIMS$^-$): $[NBu_4M]^-$ Calculated:** ($C_{24}H_{12}F_4IrN_4$) 625.0627; **Found:** 625.0525. The characterisation matches that reported.[72]

***Rac*-iridium(III)bis[2-(2,4-difluoro)-phenylpyridinato]-4,4'-dimethyl -2,2′-bypiridine hexafluorophosphate, *rac*-$[Ir(dFppy)_2(dmbpy)_2](PF_6)$**

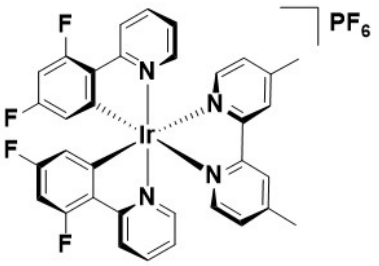

Preparation using DCM and MeOH (1:1 v/v) as solvent mixture: yellow powder. **Yield:** 80%. **Rf:** 0.30 (DCM + 3% MeOH on silica). **Mp:** 290 - 300 °C. **^{1}H NMR (500 MHz, CD_2Cl_2) δ (ppm):** 8.47 - 8.26 (m, 4H), 7.92 - 7.78 (m, 4H), 7.60 - 7.48 (m, 2H), 7.33 (d, J = 5.2 Hz, 2H), 7.09 (ddd, J = 7.4, 5.8, 1.5 Hz, 2H), 6.64 (ddd, J = 12.1, 9.2, 2.4 Hz, 2H), 5.78 (dd, J = 8.4, 2.4 Hz, 2H), 2.65 (s, 6H). **^{19}F [^{1}H] NMR (471 MHz, CD_2Cl_2) δ (ppm):** -109.01 (d, J = 13.4 Hz, 2F), -106.60 (d, J = 13.2 Hz, 2F), -73.10 (d, J = 704.1 Hz 6F). **^{1}H DOSY NMR (500 MHz, DMSO-d_6) D (m^2/s):** 1.7 x 10^{-10}. **HR-MS (FTMS$^+$): $[M\text{-}BF_4]^+$ Calculated:** ($C_{34}H_{24}F_4IrN_4$) 757.1549; **Found:** 757.1562. The characterisation matches that reported.[423]

6.3.3 Enantiopure Λ- and Δ-iridium(III) complexes

General procedure for synthesis of enantiopure Λ,Λ- and Δ,Δ-iridium dimers

The enantiopure iridium (III) dimers, Λ,Λ- and Δ,Δ-$[Ir(ppy)_2(\mu\text{-}Cl)]_2$, Λ,Λ- and Δ,Δ-$[Ir(mesppy)_2(\mu\text{-}Cl)]_2$ and Λ,Λ- and Δ,Δ-$[Ir(dFmesppy)_2(\mu\text{-}Cl)]_2$ were prepared according to the procedure described by Lusby and co-workers with some modifications.[162] To a Schlenk tube containing *rac*-$[Ir(ppy)_2(\mu\text{-}Cl)]_2$ or *rac*-$[Ir(mesppy)_2(\mu\text{-}Cl)]_2$ or *rac*-$[Ir(dFmesppy)_2(\mu\text{-}Cl)]_2$ (0.30 mmol, 1 equiv.), L or D-serine (0.63 mmol, 2.1 equiv.) and NaOEt (0.63 mmol, 2.1 equiv.) were added DCM and MeOH (1:1 v/v) to give a concentration of 0.03 M. The reaction mixture was degassed by multiple vacuum and N_2 purging cycles and the mixture was heated to 50 °C for 19 h under nitrogen atmosphere. The solvent was removed in vacuo and the crude product purified using silica-gel flash column chromatography ($CH_2Cl_2/CH_3OH/NEt_3$ (96:3:1) as eluent). The pure fractions of the faster running diastereoisomers, Δ-$[Ir(ppy)_2$(L-serine)] or Δ-$[Ir(mesppy)_2$(L-serine)] or Δ-$[Ir(dFmesppy)_2$(L-serine)], and Λ-$[Ir(ppy)_2$(D-serine)] or Λ-$[Ir(mesppy)_2$(D-serine)] or Λ-$[Ir(dFmesppy)_2$(D-serine)] could be obtained, whereas, the slower eluting compounds, Λ-$[Ir(ppy)_2$(L-serine)] or Λ-$[Ir(mesppy)_2$(L-serine)] or Λ-$[Ir(dFmesppy)_2$(L-serine)], and Δ-$[Ir(ppy)_2$(D-serine)] or Δ-$[Ir(mesppy)_2$(D-serine)] or Δ-$[Ir(dFmesppy)_2$(D-serine)] were always contaminated with the other isomer. The pure Δ-Lser and Λ-Dser complexes isolated from the column were dissolved in CH_3OH and CH_2Cl_2 (5:1 v/v) and to this was added 1M HCl solution (2 mL). A precipitate was formed after stirring the solutions for 10 min at room temperature. The solids were filtered, washed with hexane and diethyl ether (1:1 v/v) and air dried to give yellow powders.

Δ-iridium(III)bis[2-phenylpyridinato]-L-serine, Δ-$[Ir(ppy)_2$(L-serine)] and Δ,Δ-tetrakis[2-phenylpyridinato-N,$C^{2'}$]-bis(μ-chloro)diiridium(III), Δ,Δ-$[Ir(ppy)_2(\mu\text{-}Cl)]_2$

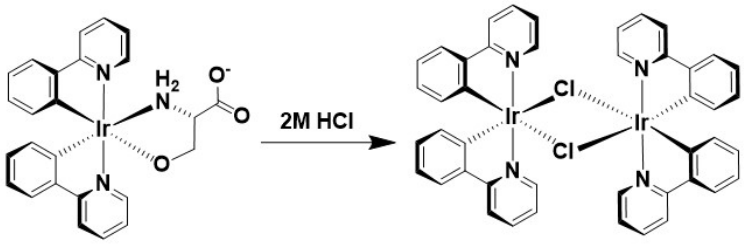

Δ-$[Ir(ppy)_2$(L-serine)] Δ, Δ-$[Ir(ppy)_2Cl]_2$

Δ-$[Ir(ppy)_2$(L-serine)]: Yield: 37%. **Rf:** 0.30 ($CH_2Cl_2/CH_3OH/NEt_3$: 96/3/1) on silica). **Mp:** 255 - 260 °C. **^{1}H NMR (500 MHz, CD_2Cl_2) δ (ppm):** 9.58 (dd, J = 5.8, 0.9 Hz, 2H), 8.73 (dd, J = 6.2, 0.9 Hz, 2H), 7.98 (m, 2H), 7.87 (m, 2H), 7.61 (dd, J = 7.9, 1.1 Hz, 2H), 7.37 (ddd, J = 10.4, 5.8, 1.4 Hz, 2H), 7.30 (ddd, J = 9.7, 5.8, 1.6 Hz, 2H),

6.87 (ddd, J = 10.4, 8.2, 0.9 Hz, 2H), 6.72 (ddd, J = 7.5, 3.6, 1.0 Hz, 2H), 6.35 (dd, J = 7.9, 1.0 Hz, 2H), 6.19 (dd, J = 7.7, 0.8 Hz, 2H), 4.00 (dd, J = 5.2, 0.9 Hz, 2H), 3.82 (dd, J = 3.9, 0.4 Hz, 1H).

Δ,Δ-[Ir(ppy)$_2$(μ-Cl)]$_2$: Yield: 35%. **^{1}H NMR (500 MHz,CD_2Cl_2) δ (ppm):** 9.26 (dd, J = 5.2, 1.3 Hz, 4H), 7.86 (d, J = 7.1 Hz, 4H), 7.77 (td, J = 7.8, 1.4 Hz, 4H), 7.52 (dd, J = 7.4, 1.3 Hz, 4H), 6.84 - 6.77 (m, 8H), 6.58 (td, J = 7.4, 1.9 Hz, 4H), 5.93 (dd, J = 7.2, 1.1 Hz, 4H). The characterisation matches that of *rac*-[Ir(ppy)$_2$(μ-Cl)]$_2$.

Λ-iridium(III)bis[2-phenylpyridinato]-D-serine, Λ-[Ir(ppy)$_2$(D-serine)] and Λ,Λ-tetrakis[2-phenylpyridinato-N,C$^{2'}$]-bis(μ-chloro)diiridium(III), Λ,Λ-[Ir(ppy)$_2$(μ-Cl)]$_2$

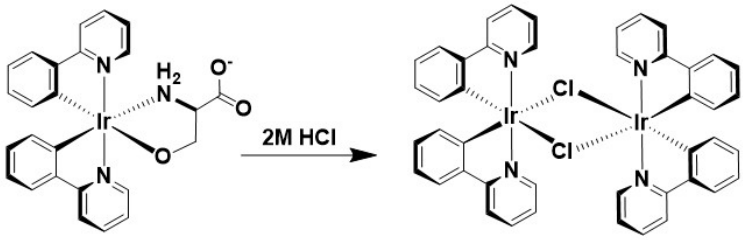

Λ-[Ir(ppy)$_2$(D-serine)] Λ, Λ-[Ir(ppy)$_2$Cl]$_2$

Λ-[Ir(ppy)$_2$(D-serine)]: Yield: 40%. **Rf:** 0.30 (CH_2Cl_2/CH_3OH/NEt_3 : 96/3/1 on silica). **Mp:** 255 - 260 °C. **^{1}H NMR (500 MHz, CD_2Cl_2) δ (ppm):** 9.67 (dd, J = 7.2, 1.0 Hz, 2H), 8.71 (dd, J = 6.1, 1.2 Hz, 2H), 7.98 (m, 2H), 7.93 (m, 2H), 7.87 (m, 4H), 7.63 (dd, J = 6.4, 1.0 Hz, 2H), 7.39 (ddd, J = 8.2, 5.4, 1.1 Hz, 2H), 7.31 (ddd, J = 7.4, 6.0, 1.3 Hz, 2H), 6.88 (td, J = 5.1, 0.8, 2H), 6.72 (dd, J = 7.4, 0.9, 2H), 6.36 (dd, J = 7.8, 1.0 Hz, 2H), 6.20 (td, J = 7.8, 0.9 Hz, 2H), 4.02 (dd, J = 6.1, 0.8 Hz, 2H), 3.87 (dd, J = 3.6, 0.3 Hz, 1H).

Λ,Λ-[Ir(ppy)$_2$(μ-Cl)]$_2$: Yield: 38%. **^{1}H NMR (500 MHz, CD_2Cl_2) δ (ppm):** 9.25 (dd, J = 5.0, 1.4 Hz, 4H), 7.85 (d, J = 7.3 Hz, 4H), 7.76 (td, J = 7.6, 1.0 Hz, 4H), 7.50 (dd, J = 7.2, 1.3 Hz, 4H), 6.80 - 6.74 (m, 8H), 6.58 (td, J = 7.3, 1.3 Hz, 4H), 5.92 (dd, J = 7.0, 1.1 Hz, 4H). The characterisation matches that of *rac*-[Ir(ppy)$_2$(μ-Cl)]$_2$.

Δ-iridium(III)bis[2-phenyl-4-(2,4,6-trimethylphenyl)pyridinato]-L-serine, Δ-[Ir(mesppy)$_2$(L-serine)] and Δ,Δ-tetrakis[2-phenyl-4-(2,4,6-trimethylphenyl)pyridinato-N,C$^{2\prime}$]-bis(μ-chloro)diiridium(III), Δ,Δ-[Ir(mesppy)$_2$(μ-Cl)]$_2$

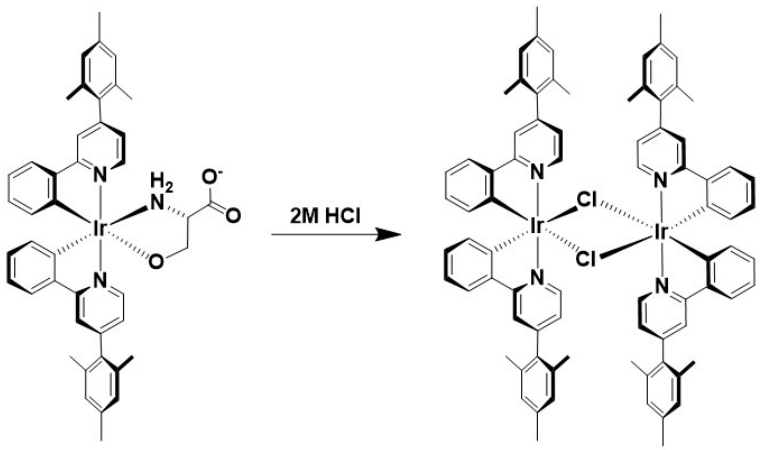

Δ-[Ir(mesppy)$_2$(L-serine)]: Yield: 52%. **Rf:** 0.35 (CH_2Cl_2/CH_3OH/NEt_3 : 96/3/1 on silica). **Mp:** 282 - 286 °C. **^{1}H NMR (500 MHz, CD_2Cl_2) δ (ppm):** 9.56 (d, J = 6.2 Hz, 2H), 8.77 (d, J = 5.3 Hz, 2H), 7.77 (dd, J = 23.5, 0.9 Hz, 4H), 7.57 (dt, J = 5.9, 0.4 Hz, 4H), 7.22 (dd, J = 5.7, 1.7 Hz, 2H), 7.15 (dd, J = 5.9, 1.7 Hz, 2H), 7.07 (m, 8H), 6.87 (m, 4H), 6.75 (m, 4H), 6.42 (dd, J = 8.1, 1.0 Hz, 2H), 6.31 (dd, J = 6.7, 0.7 Hz, 2H), 4.08 (dd, J = 5.6, 0.9 Hz, 2H), 3.89 (dd, J = 8.5, 3.2 Hz, 1H), 2.21 (s, 6H), 2.20 (s, 6H), 2.19 (s, 6H).

Δ,Δ-[Ir(mesppy)$_2$(μ-Cl)]$_2$: Yield: 44%. **^{1}H NMR (500 MHz, CD_2Cl_2) δ (ppm):** 9.69 (d, J = 6.1 Hz, 4H), 7.75 (d, J = 1.7 Hz, 4H), 7.56 (dd, J = 7.2, 1.5 Hz, 4H), 7.04 (d, J = 9.4 Hz, 8H), 6.84 (m, 8H), 6.70 (dt, J = 8.1, 7.9, 4H), 5.94 (dd, J = 8.5, 1.1 Hz, 4H), 2.42 (s, 12H), 2.16 (s, 12H), 2.15 (s, 12H). The characterisation matches that of *rac*-[Ir(mesppy)$_2$(μ-Cl)]$_2$.

Λ-iridium(III)bis[2-phenyl-4-(2,4,6-trimethylphenyl)pyridinato]-D-serine, Λ-[Ir(mesppy)$_2$(D-serine)] and Λ,Λ-tetrakis[2-phenyl-4-(2,4,6-trimethylphenyl)pyridinato-N,C$^{2\prime}$]-bis(μ-chloro)diiridium(III), Λ,Λ-[Ir(mesppy)$_2$(μ-Cl)]$_2$

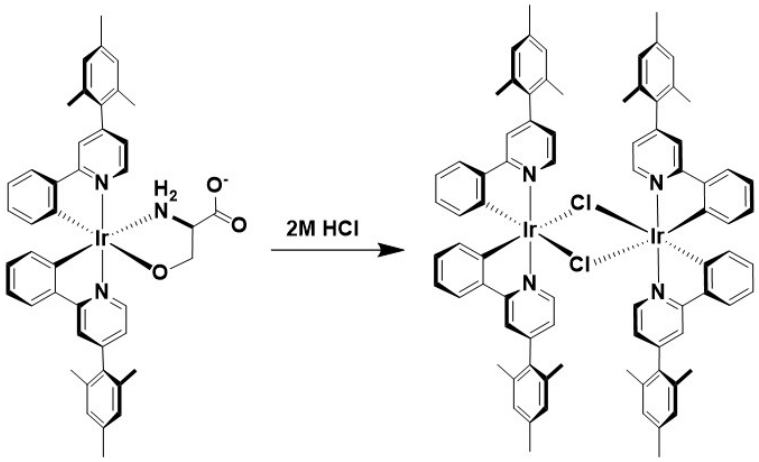

Λ-[Ir(mesppy)$_2$(D-serine)]: Yield: 52%. **Rf:** 0.35 (CH_2Cl_2/CH_3OH/NEt_3 : 96/3/1 on silica). **Mp:** 282 - 286 °C. **^{1}H NMR (500 MHz, CD_2Cl_2)** δ **(ppm):** 9.62 (d, J = 6.5 Hz, 2H), 8.77 (d, J = 5.3 Hz, 2H), 7.72 (dd, J = 17.8, 1.6 Hz, 4H), 7.55 (dt, J = 5.8, 1.1 Hz, 4H), 7.15 (ddd, J = 9.5, 5.9, 1.5 Hz, 2H), 7.04 (m, 8H), 6.84 (m, 4H), 6.73 (m, 4H), 6.47 (dd, J = 8.0, 1.6 Hz 2H), 6.28 (dd, J = 7.4, 0.6 Hz, 2H), 3.90 (dd, J = 11.0, 3.7 Hz, 2H), 3.82 (dd, J = 10.8, 5.3 Hz, 1H), 2.21 (s, 6H), 2.20 (s, 6H), 2.19 (s, 6H).

Λ,Λ-[Ir(mesppy)$_2$(μ-Cl)]$_2$: Yield: 47%. **^{1}H NMR (500 MHz, CD_2Cl_2)** δ **(ppm):** 9.68 (d, J = 6.0 Hz, 4H), 7.74 (d, J = 1.6 Hz, 4H), 7.56 (dd, J = 7.7, 1.5 Hz, 4H), 7.05 (d, J = 9.3 Hz, 8H), 6.83 (m, 8H), 6.71 (dt, J = 7.4, 6.6 Hz, 4H), 5.92 (dd, J = 8.9, 1.1 Hz, 4H), 2.41 (s, 12H), 2.16 (s, 12H), 2.15 (s, 12H). The characterisation matches that of *rac*-[Ir(mesppy)$_2$(μ-Cl)]$_2$.

Δ-iridium(III)bis[2-(4′,6′-difluorophenyl)-4-(2,4,6-trimethylphenyl) pyridinato]-L-serine, Δ-[Ir(dFmesppy)$_2$(L-serine)] and Δ,Δ-tetrakis[2-(4′, 6′-difluorophenyl)-4-(2,4,6-trimethylphenyl)pyridinato-N,C$^{2\prime}$]-bis(μ-chloro) diiridium(III), Δ,Δ-[Ir(dFmesppy)$_2$(μ-Cl)]$_2$

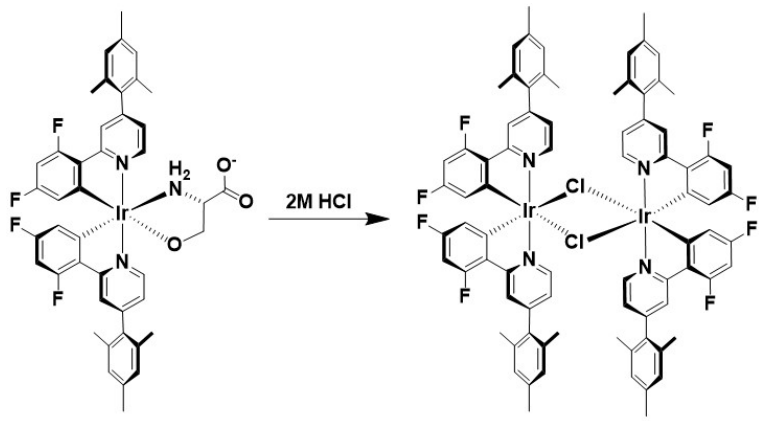

Δ-[Ir(dFmesppy)$_2$(L-serine)]: Yield: 55%. **Rf:** 0.30 (CH_2Cl_2/CH_3OH/NEt_3 : 96/3/1 on silica). **Mp:** 293 - 296 °C. **^{1}H NMR (500 MHz, CD_2Cl_2) δ (ppm):** 9.90 (d, J = 5.2 Hz, 2H), 8.78 (d, J = 5.9 Hz, 2H), 8.18 (dd, J = 9.6, 0.8 Hz, 4H), 7.26 (dd, J = 6.0, 1.5 Hz, 2H), 7.21 (dd, J = 5.8, 1.7 Hz, 2H), 7.08 (m, 2H), 6.43 (m, 2H), 5.80 (dd, J = 8.8, 2.6 Hz 2H), 5.64 (dd, J = 8.8, 2.2 Hz, 2H), 5.53 (t, J = 1.0 Hz, 2H), 5.18 (t, J = 1.1 Hz, 2H), 4.36 (dd, J = 10.0, 2.0 Hz, 2H), 3.89 (dd, J = 10.1, 1.3 Hz, 2H), 2.40 (s, 6H), 2.22 (s, 6H), 2.19 (s, 6H). **^{19}F [^{1}H] NMR (471 MHz, CD_2Cl_2) δ (ppm):** -108.30 (q, J = 10.0 Hz, 2F), -108.80 (q, J = 10.1 Hz, 2F).

Δ,Δ-[Ir(dFmesppy)$_2$(μ-Cl)]$_2$: Yield: 42%. **^{1}H [^{19}F] NMR (400 MHz, CD_2Cl_2) δ (ppm):** 9.55 (d, J = 5.7 Hz, 4H), 8.11 (d, J = 1.4 Hz, 4H), 7.03 (d, J = 10.7 Hz, 8H), 6.85 (dd, J = 6.1, 2.2 Hz, 4H), 6.35 (d, J = 2.3 Hz, 4H), 5.23 (d, J = 2.1 Hz, 4H), 2.38 (s, 12H), 2.12 (s, 12H), 2.11 (s, 12H). **^{19}F [^{1}H] NMR (471 MHz, CD_2Cl_2) δ (ppm):** -108.05 (d, J = 11.15 Hz, 4F), -110.29 (d, J = 10.9 Hz, 4F). The characterisation matches that of *rac*-[Ir(dFmesppy)$_2$(μ-Cl)]$_2$.

Λ-iridium(III)bis[2-(4′,6′-difluorophenyl)-4-(2,4,6-trimethylphenyl) pyridinato]-D-serine, Λ-[Ir(dFmesppy)$_2$(D-serine)] and Λ,Λ-tetrakis[2-(4',6'-difluorophenyl)-4-(2,4,6-trimethylphenyl)pyridinato-N,C$^{2\prime}$]-bis (μ-chloro)diiridium(III), Λ,Λ-[Ir(dFmesppy)$_2$(μ-Cl)]$_2$

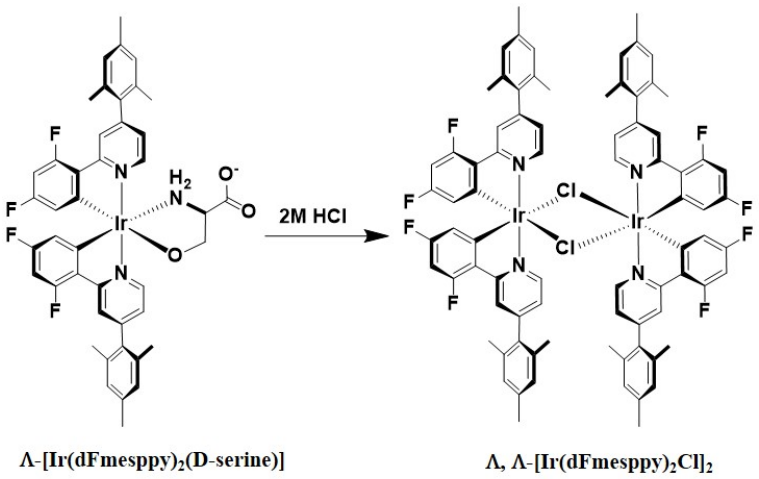

Λ-[Ir(dFmesppy)$_2$(D-serine)]: Yield: 47%. **Rf:** 0.35 (CH_2Cl_2/CH_3OH/NEt_3 : 96/3/1 on silica). **Mp:** 292 - 296 °C. **^{1}H NMR (500 MHz, CD_2Cl_2) δ (ppm):** 8.93 (d, J = 6.0 Hz, 2H), 8.69 (d, J = 6.8 Hz, 2H), 8.15 (dd, J = 15.6, 1.0 Hz, 4H), 7.19 (dd, J = 5.7, 1.7 Hz, 2H), 7.05 (m, 4H), 6.41 (dt, J = 8.8, 2.4 Hz, 2H), 6.29 (dt, J = 10.2, 2.7 Hz, 2H), 5.85 (dd, J = 8.5, 2.0 Hz, 2H), 5.65 (dd, J = 9.2, 2.6 Hz, 2H), 5.53 (t, J = 1.2 Hz, 2H), 5.18 (t, J = 1.1 Hz, 2H), 4.26 (dd, J = 10.4, 2.2 Hz, 2H), 3.84 (m, 2H), 2.40 (s, 6H), 2.39 (s, 6H), 2.20 (s, 6H). **^{19}F [^{1}H] NMR (471 MHz, CD_2Cl_2) δ (ppm):** -108.40 (q, J = 10.0 Hz, 2F), -108.00 (q, J = 10.1 Hz, 2F).

Λ,Λ-[Ir(dFmesppy)$_2$(μ-Cl)]$_2$: Yield: 35%. **^{1}H [^{19}F] NMR (400 MHz, CD_2Cl_2) δ (ppm):** 9.56 (d, J = 5.9 Hz, 4H), 8.09 (d, J = 1.3 Hz, 4H), 7.02 (d, J = 10.8 Hz, 8H), 6.88 (dd, J = 5.4, 2.2 Hz, 4H), 6.35 (d, J = 2.1 Hz, 4H), 5.22 (d, J = 2.7 Hz, 4H), 2.37 (s, 12H), 2.12 (s, 12H), 2.10 (s, 12H). **^{19}F [^{1}H] NMR (471 MHz, CD_2Cl_2) δ (ppm):** -108.00 (d, J = 11.2 Hz, 4F), -110.23 (d, J = 10.3 Hz, 4F). The characterisation matches that of *rac*-[Ir(dFmesppy)$_2$(μ-Cl)]$_2$.

General procedure for synthesis of enantiopure Λ- and Δ-iridium complexes

To a round bottom flask containing the appropriate enantiopure Λ,Λ- and Δ,Δ-dichloro-bridged iridium dimer (1.0 equiv.) and N^N ligand (2.2 equiv.) were added DCM and MeOH (1:1 v/v) or 2-methoxyethanol to give a suspension with a concentration of ca. 0.02 M. The mixture was degassed via bubbling with N_2 for 10 min, before the reaction vessel was sealed. The reaction mixture was heated to reflux for 19 h under nitrogen atmosphere. The solution was cooled to room temperature, and the solvent evaporated. For preparing the PF_6^- salts: the solution was cooled to room temperature and solid NH_4PF_6 (10.0 equiv.) was added and the reaction mixture was left to stir for a further 1 h. For preparing the BF_4^- salts: a 2 M solution of KBF_4 in MeOH (10 mL) was added at room temperature to the reaction mixture and the resulting suspension was stirred at room temperature for 4 h. For preparing SbF_6^- salts: a 2 M solution of $KSbF_6$ in MeOH (10 mL) was added at room temperature to the reaction mixture and the resulting suspension was stirred at room temperature for 4 h. For all three anions, the resulting suspensions were evaporated to dryness, with the residue then copiously washed with Et_2O and distilled water. This crude product was purified by flash column chromatography. Fractions containing the desired complex were combined and solid NH_4PF_6 (10.0 equiv.) or KBF_4 (10.0 equiv.) or SbF_6 (10.0 equiv.) was added. The suspension was stirred at room temperature for 0.5 h. This mixture was then evaporated to dryness, washed vigorously with distilled water and diethyl ether and dried to afford the pure material.

Λ- and Δ-iridium(III)bis[2-phenylpyridinato]-4,4′-di-tert-butyl-2,2′-bipyridine hexafluorophosphate, Λ- and Δ-[Ir(ppy)$_2$(dtBubpy)](PF$_6$)

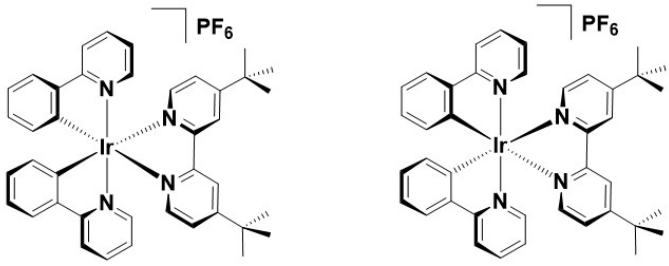

Λ-[Ir(ppy)$_2$(dtBubpy)](PF$_6$) Δ-[Ir(ppy)$_2$(dtBubpy)](PF$_6$)

Preparation using DCM and MeOH (1:1 v/v) as solvent mixture: yellow powders. **Yield: Λ-[Ir(ppy)$_2$(dtBubpy)](PF$_6$):** 85%; **Δ-[Ir(ppy)$_2$(dtBubpy)](PF$_6$):** 73%. **Rf:** 0.45 (5% MeOH/DCM on silica). **Mp: Λ-[Ir(ppy)$_2$(dtBubpy)](PF$_6$):** 280 - 285 °C; **Δ-[Ir(ppy)$_2$(dtBubpy)](PF$_6$):** 286 - 289 °C. **^{1}H NMR (500 MHz, CD$_2$Cl$_2$) δ (ppm):** 8.31 (d, J = 1.1 Hz, 2H), 8.01 (d, J = 8.7 Hz, 2H), 7.94 (d, J = 5.8 Hz, 2H), 7.83 (dt, J = 0.9, 7.3 Hz, 2H), 7.77 (dd, J = 1.3, 7.9 Hz, 2H), 7.53 (dd, J = 0.8, 5.2 Hz, 2H), 7.48 (dd, J = 1.3, 5.5 Hz, 2H), 7.11 (td, J = 1.3, 7.7 Hz, 2H), 7.05 (td, J = 1.7, 6.2 Hz, 2H), 6.97 (td, J = 1.2, 7.6 Hz, 2H), 6.33 (dd, J = 0.8, 8.4 Hz, 2H), 1.46 (s, 18H). **HR-MS (FTMS$^+$): [M-**

PF_6]$^+$ Calculated: ($C_{40}H_{40}IrN_4$) 769.2882; **Found:** **Λ-[Ir(ppy)$_2$(dtBubpy)](PF$_6$):** 769.2853; **Δ-[Ir(ppy)$_2$(dtBubpy)](PF$_6$):** 769.2854. The characterization matches that of *rac*-[Ir(ppy)$_2$(dtBubpy)](PF$_6$).

Λ- and Δ-iridium(III)bis[2-phenyl-4-(2,4,6-trimethylphenyl)pyridinato]-4,4′-di-tert-butyl-2,2′-bipyridine hexafluorophosphate,
Λ- and Δ-[Ir(mesppy)$_2$(dtBubpy)](PF$_6$)

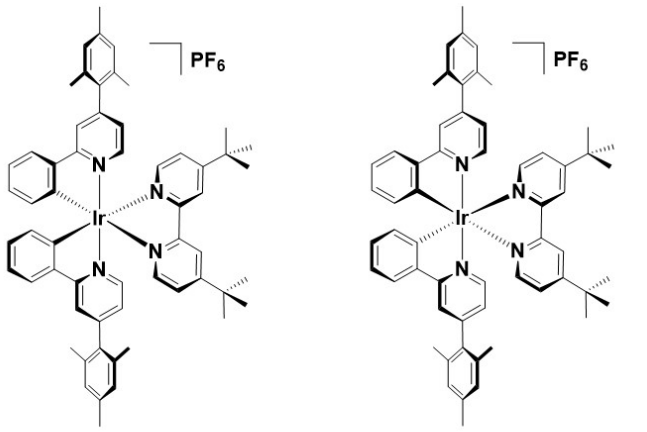

Λ-[Ir(mesppy)$_2$(dtBubpy)](PF$_6$) **Δ-[Ir(mesppy)$_2$(dtBubpy)](PF$_6$)**

Preparation using DCM and MeOH (1:1 v/v) as solvent mixture: yellow powders. **Yield:** **Λ-[Ir(mesppy)$_2$(dtBubpy)](PF$_6$):** 92%; **Δ-[Ir(mesppy)$_2$(dtBubpy)](PF$_6$):** 87% **Rf:** 0.55 (5% MeOH/DCM on silica). **Mp:** **Λ-[Ir(mesppy)$_2$(dtBubpy)](PF$_6$):** 267 - 270 °C; **Δ-[Ir(mesppy)$_2$(dtBubpy)](PF$_6$):** 263 - 267 °C **^{1}H NMR (500 MHz, CD_2Cl_2)** δ **(ppm):** 8.36 (d, J = 1.9 Hz, 2H), 8.09 (d, J = 6.1 Hz, 2H), 7.79 (d, J = 2.2 Hz, 2H), 7.74 (dd, J = 8.6, 1.4 Hz, 2H), 7.57 (dd, J = 6.7, 0.9 Hz, 2H), 7.54 (dd, J = 6.5, 2.3 Hz, 2H), 7.10 (dt, J = 8.3, 1.8 Hz, 2H), 7.04 - 6.99 (m, 6H), 6.89 (dd, J = 6.2, 1.8 Hz, 2H), 6.43 (d, J = 10.5 Hz, 2H), 2.36 (s, 6H), 2.15 (s, 6H), 1.97 (s, 6H), 1.47 (s, 18H). **^{13}C NMR (126 MHz, CD_2Cl_2)** δ **(ppm):** 167.7, 164.2, 156.2, 151.6, 151.1, 149.7, 143.9, 138.2, 135.3, 134.9, 131.5, 130.4, 128.6, 128.9, 125.3, 125.0, 124.6, 122.4, 122.1, 120.3, 30.3, 21.3, 20.1. **HR-MS (FTMS$^+$): [M-PF$_6$]$^+$ Calculated:** ($C_{58}H_{60}IrN_4$) 1005.4447; **Found:** **Λ-[Ir(mesppy)$_2$(dtBubpy)](PF$_6$):** 1005.4427; **Δ-[Ir(mesppy)$_2$(dtBubpy)](PF$_6$):** 1005.4427. The characterization matches that of *rac*-[Ir(mesppy)$_2$(dtBubpy)](PF$_6$).

Λ- and Δ-iridium(III)bis[2-phenyl-4-(2,4,6-trimethylphenyl)pyridinato-4,4′:2′,2″:4″,4‴-quaterpyridine hexafluorophosphate, Λ- and Δ-[Ir(mesppy)$_2$(qpy)](PF$_6$)

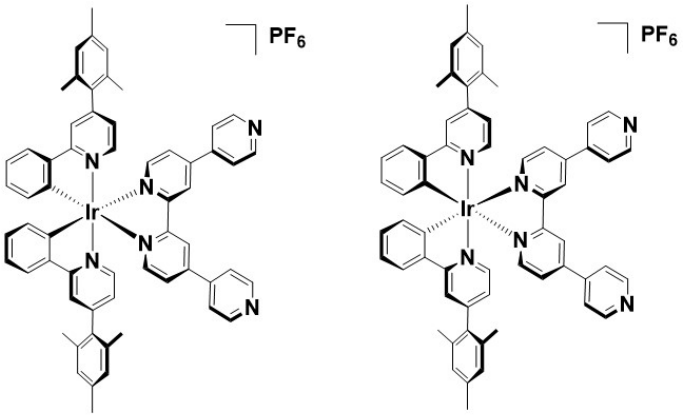

Λ-[Ir(mesppy)$_2$(qpy)](PF$_6$) Δ-[Ir(mesppy)$_2$(qpy)](PF$_6$)

Preparation using 2-methoxyethanol as solvent: orange powders. **Yield: Λ-[Ir(mesppy)$_2$(qpy)](PF$_6$):** 55%; **Δ-[Ir(mesppy)$_2$(qpy)](PF$_6$):** 45%. **Rf:** 0.20 (DCM + 3% MeOH + 2% NEt$_3$ on silica). **Mp: Λ-[Ir(mesppy)$_2$(qpy)](PF$_6$):** 348 - 352 °C; (decomposed); **Δ-[Ir(mesppy)$_2$(qpy)](PF$_6$):** 343 - 348 °C (decomposed). **^{1}H NMR (500 MHz, CD$_2$Cl$_2$) δ (ppm):** 9.19 (s, 2H), 8.86 (d, J = 5.5 Hz, 4H), 8.31 (d, J = 5.5 Hz, 2H), 7.92 (m, 4H), 7.84 (s, 2H), 7.80 (dd, J = 6.9, 1.4 Hz, 2H), 7.77 (d, J = 8.2 Hz, 2H), 7.70 (d, J = 6.1 Hz, 2H), 7.13 (dt, J = 6.2, 1.4 Hz, 2H), 7.03 (m, 6H), 6.93 (dd, J = 6.1, 0.9 Hz, 2H), 6.43 (d, J = 6.3 Hz, 2H), 2.36 (s, 6H), 2.17 (s, 6H), 1.99 (s, 6H). **^{13}C NMR (126 MHz, CD$_2$Cl$_2$) δ (ppm):** 167.5, 165.6, 152.4, 151.5, 160.0, 149.7, 149.0, 148.5, 143.9, 143.1, 138.3, 134.9, 133.1, 131.5, 130.8, 128.4, 126.2, 125.0, 124.9, 123.0, 122.3, 121.3, 29.6, 20.8, 20.3. **^{1}H DOSY NMR (500 MHz, DMSO-d_6) D (m^2/s):** 1.3 x 10^{-10}. **HR-MS (FTMS$^+$): [M-PF$_6$]$^+$ Calculated:** (C$_{60}$H$_{50}$IrN$_6$) 1047.3726; **Found: Λ-[Ir(mesppy)$_2$(qpy)](PF$_6$):** 1047.3719; **Δ-[Ir(mesppy)$_2$(qpy)](PF$_6$):** 1047.3720. The characterization matches that of *rac*-[Ir(mesppy)$_2$(qpy)](PF$_6$).

Λ- and Δ-iridium(III)bis[2-phenyl-4-(2,4,6-trimethylphenyl)pyridinato]-4,4′:2′,2″:4″,4‴-quaterpyridine tetrafluoroborate,
Λ- and Δ-[Ir(mesppy)$_2$(qpy)](BF$_4$)

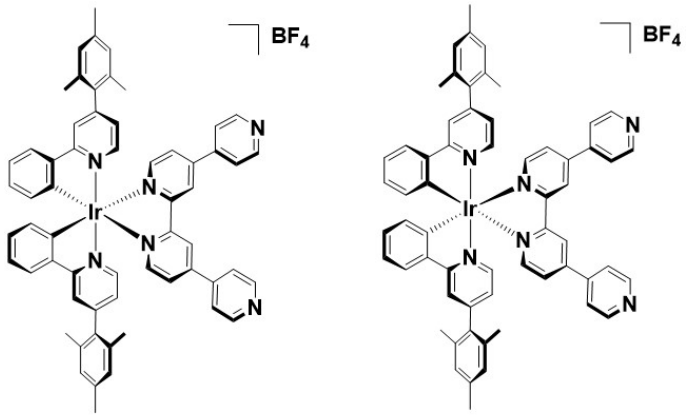

Λ-[Ir(mesppy)$_2$(qpy)](BF$_4$) **Δ-[Ir(mesppy)$_2$(qpy)](BF$_4$)**

Preparation using 2-methoxyethanol as solvent: orange powders. **Yield: Λ-[Ir(mesppy)$_2$(qpy)](BF$_4$):** 53%; **Δ-[Ir(mesppy)$_2$(qpy)](BF$_4$):** 58%. **Rf:** 0.21 (DCM + 3% MeOH + 2% NEt$_3$ on silica). **Mp: Λ-[Ir(mesppy)$_2$(qpy)](BF$_4$):** 346 - 353 °C (decomposed); **Δ-[Ir(mesppy)$_2$(qpy)](BF$_4$):** 348 - 352 °C (decomposed). **^{1}H NMR (500 MHz, CD$_2$Cl$_2$) δ (ppm):** 9.21 (s, 2H), 8.95 - 8.64 (m, 4H), 8.30 (d, J = 5.8 Hz, 2H), 8.04 - 7.53 (m, 12H), 7.31 - 6.72 (m, 10H), 6.47 (d, J = 7.9 Hz, 2H), 2.34 (s, 6H), 2.17 (s, 6H), 1.99 (s, 6H). **^{1}H DOSY NMR (500 MHz, DMSO-d_6) D (m^2/s):** 1.3 x 10^{-10}. **HR-MS (FTMS$^+$): [M-BF$_4$]$^+$ Calculated:** ($C_{60}H_{50}IrN_6$) 1047.3726; **Found: Λ-[Ir(mesppy)$_2$(qpy)](BF$_4$):** 1047.3721; **Δ-[Ir(mesppy)$_2$(qpy)](BF$_4$):** 1047.3719. The characterization matches that of *rac*-[Ir(mesppy)$_2$(qpy)](BF$_4$).

Δ-iridium(III)bis[2-phenyl-4-(2,4,6-trimethylphenyl)pyridinato]-4,4′ :2′,2″:4″,4‴-quaterpyridine hexafluoroantimonate, Δ-[Ir(mesppy)$_2$(qpy)](SbF$_6$)

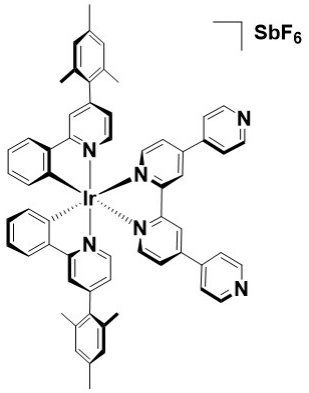

Preparation using 2-methoxyethanol as solvent: orange powder. **Yield:** 50%. **Rf:** 0.23 (DCM + 3% MeOH + 2% NEt_3 on silica). **Mp:** 358 - 364 °C (decomposed). **^{1}H NMR (500 MHz, CD_2Cl_2) δ (ppm):** 9.51 (d, J = 2.0 Hz, 2H), 8.99 - 8.81 (m, 4H), 8.25 (dd, J = 5.8, 1.8 Hz, 2H), 8.17 (d, J = 1.9 Hz, 2H), 8.11 (d, J = 5.8 Hz, 2H), 8.08 (d, J = 6.3 Hz, 4H), 8.03 (dd, J = 7.7, 1.5 Hz, 2H), 7.78 (d, J = 6.0 Hz, 2H), 7.09 - 6.90 (m, 10H), 6.33 - 6.25 (m, 2H), 2.28 (s, 6H), 2.09 (s, 6H), 1.90 (s, 6H). **^{1}H DOSY NMR (500 MHz, DMSO-d_6) D (m^2/s):** 1.3 x 10^{-10}. **HR-MS (FTMS$^+$): [M-SbF$_6$]$^+$ Calculated:** ($C_{60}H_{50}IrN_6$) 1047.3726; **Found:** 1047.3718.

Λ- and Δ-iridium(III)bis[2-(2,4-difluoro)-phenyl-4-(2,4,6-trimethyl phenyl)pyridinato]-4,4′:2′,2″:4″,4‴-quaterpyridine tetrafluoroborate, Λ- and Δ-[Ir(dFmesppy)$_2$(qpy)](BF$_4$)

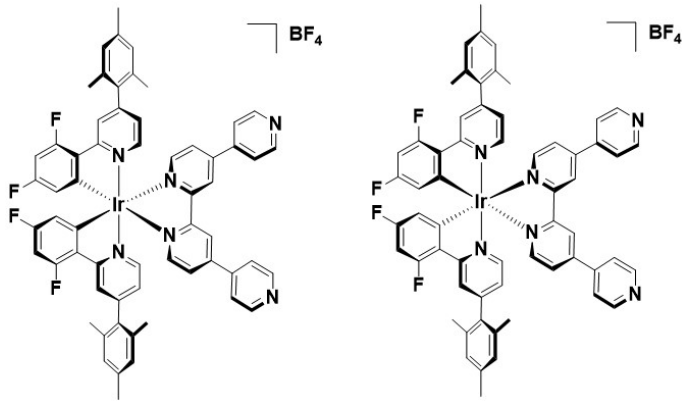

Λ-[Ir(dFmesppy)$_2$(qpy)](BF$_4$) Δ-[Ir(dFmesppy)$_2$(qpy)](BF$_4$)

Preparation using 2-methoxyethanol as solvent: yellow powders. **Yield: Λ-[Ir(dFmesppy)$_2$(qpy)](BF$_4$):** 38%; **Δ-[Ir(dFmesppy)$_2$(qpy)](BF$_4$):** 25%. **Rf:** 0.17 (DCM + 3% MeOH + 2% NEt_3 on silica). **Mp: Λ-[Ir(dFmesppy)$_2$(qpy)](BF$_4$):** 335 - 340 °C (decomposed); **Δ-[Ir(dFmesppy)$_2$(qpy)](BF$_4$):** 329 - 335 °C (decomposed). **^{1}H NMR (500 MHz, CD_2Cl_2) δ (ppm):** 9.40 (d, J = 1.5 Hz, 2H), 8.86 (d, J = 5.6 Hz, 4H), 8.43 - 8.11 (m, 4H), 7.96 (d, J = 5.1 Hz, 4H), 7.87 (dd, J = 5.8, 1.4 Hz, 2H), 7.72 (d, J = 6.0 Hz, 2H), 7.22 - 6.90 (m, 6H), 6.68 (ddd, J = 11.7, 9.1, 2.1 Hz, 2H), 5.85 (dd, J = 8.1, 2.3 Hz, 2H), 2.36 (s, 6H), 2.17 (s, 6H), 2.00 (s, 6H). **^{19}F [^{1}H] NMR (471 MHz, CD_2Cl_2) δ (ppm):** -106.22 (d, J = 10.9 Hz, 2F), -108.35 (d, J = 10.9 Hz, 2F), -150.94 (d, J = 11.5 Hz, 4F). **^{1}H DOSY NMR (500 MHz, DMSO-d_6) D (m^2/s):** 1.2 x 10^{-10}. **HR-MS (FTMS$^+$): [M-BF$_4$]$^+$ Calculated:** ($C_{60}H_{46}F_4IrN_6$) 1119.3349; **Found: Λ-[Ir(dFmesppy)$_2$(qpy)](BF$_4$):** 1119.3324; **Δ-[Ir(dFmesppy)$_2$(qpy)](BF$_4$):** 1119.3325. The characterization matches that of *rac*-[Ir(dFmesppy)$_2$(qpy)](BF$_4$).

6.3.4 Racemic ruthenium(II) complexes

Synthesis of bis[4,4′-di-tert-butyl-2,2′-bypiridine)-dichloro ruthenium(II), Ru(dtBubpy)$_2$Cl$_2$

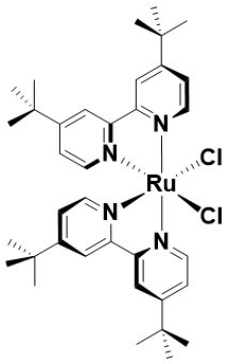

This synthetic protocol is a modification of that reported in the literature.[424] $RuCl_3$*xH_2O (207 mg, 0.792 mmol, 1 equiv.), 4,4'-Di-tert-butyl-2,2'-dipyridyl (400 mg, 1.490 mmol, 2 equiv.) and LiCl (126.3 mg, 2.98 mmol, 4 equiv.) were added to a round bottom flask containing 15 mL of anhydrous DMF. The reaction mixture was degassed by multiple vacuum and N_2 purging cycles and heated to reflux for 6 h under nitrogen atmosphere in absence of light. The crude mixture was cooled to room temperature and most of the solvent removed by evaporation under reduced pressure. Diethyl ether was added and the resultant solution was cooled at -25 °C overnight. Filtering the resulting mixture yielded a red to red-violet filtrate and a nearly black microcrystalline product. The black solid was washed with several portions of cold water, followed by several portions of diethyl ether. **Yield:** 19%. **^{1}H NMR (400 MHz, DMSO-*d*$_6$) δ (ppm):** 9.83 (d, J = 2.0 Hz, 2H), 8.83 (d, J = 2.0 Hz, 2H), 8.47 (d, J = 2.1 Hz, 2H), 7.77 (dd, J = 6.1, 2.1 Hz, 2H), 7.38 (d, J = 6.2 Hz, 2H), 7.14 (dd, J = 6.2, 2.1 Hz, 2H), 1.51 (s, 18H), 1.28 (s, 18H). The characterisation matches that reported.[425]

Synthesis of bis[4,4′-di-tert-butyl-2,2′-bypiridine)ruthenium(II) 4,4′:2′, 2″:4″,4‴-quaterpyridine hexafluorophosphate, [Ru(dtBubpy)$_2$(qpy)](PF$_6$)$_2$

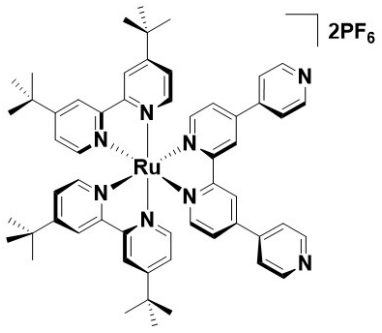

This synthetic protocol is a modification of that reported in the literature.[385] Ru(dtBubpy)$_2$Cl$_2$ (91 mg, 0.129 mmol, 1 equiv.) and 4,4′:2′,2″:4″,4‴-quaterpyridine (40 mg, 0.129 mmol, 1 equiv.) were added to a round bottom flask containing 13 mL of ethylene glycol. The reaction mixture was degassed by multiple vacuum and N_2 purging cycles and was heated to reflux for 1 h under nitrogen atmosphere. The crude mixture was cooled to room temperature and filtered. A saturated, aqueous NH_4PF_6 solution was added to the filtrate and a red precipitate was filtered and washed with water and diethyl ether. The crude product was purified by silica flash chromatography (acetone/MeCN : 1/1 with aqueous NH_4PF_6 0.3 M on silica); an initial orange fraction was firstly eluted and removed. The subsequently eluted major red fraction was evaporated to dryness, washed with water and dried to yield the pure complex as an orange powder. **Yield:** 47.5%. **Rf:** 0.30 acetone/MeCN, 1:1 with aqueous NH_4PF_6 0.3 M on silica). **Mp:** 362 - 368 °C (decomposed). **^{1}H NMR (500 MHz, CD$_2$Cl$_2$) δ (ppm):** 8.86 (d, J = 1.9 Hz, 2H), 8.71 (m, 4H), 8.31 (d, J = 2.0 Hz, 2H), 8.29 (d, J = 2.0 Hz, 2H), 8.05 (m, 4H), 7.89 (d, J = 6.0 Hz, 2H), 7.77 (dd, J = 6.0, 1.9 Hz, 2H), 7.71 (d, J = 6.1 Hz, 1H), 7.62 (d, J = 6.0 Hz, 2H), 7.48 (m, 4H), 1.43 (s, 18H), 1.39 (s, 18H). **^{13}C NMR (126 MHz, CD$_2$Cl$_2$) δ (ppm):** 163.3, 158.1, 156.8, 156.6, 152.5, 151.4, 150.9, 147.8, 147.7, 147.4, 145.7, 126.2, 125.9, 123.7, 123.7, 122.6, 121.2, 121.2, 121.2, 121.2, 35.9, 35.9, 30.4, 30.4, 30.4, 30.3, 30.3, 30.3. **^{1}H DOSY NMR (500 MHz, DMSO-d_6) D (m^2/s):** 1.3 x 10^{-10}. **HR-MS (FTMS$^+$): [M-PF$_6$]$^{2+}$ Calculated:** ($C_{56}H_{62}N_8Ru$) 474.2070; **Found:** 474.2060.

Synthesis of tris[4,4′-di-tert-butyl-2,2′-bypiridine)ruthenium(II) hexafluorophosphate, [Ru(dtBubpy)$_3$](PF$_6$)$_2$

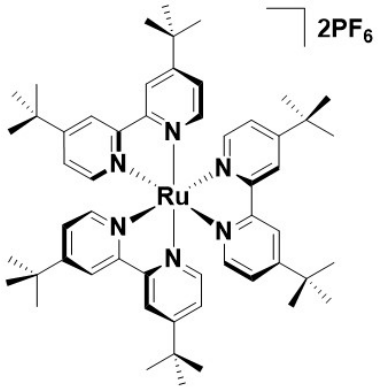

This synthetic protocol is a modification of that reported in the literature.[426] $RuCl_3$*xH_2O (55 mg, 0.210 mmol, 1 equiv.) and 4,4′-Di-tert-butyl-2,2′-dipyridyl (198 mg, 0.736 mmol, 3.5 equiv.) were added to a round bottom flask containing 25 mL of ethylene glycol. The reaction mixture was degassed by multiple vacuum and N_2 purging cycles and was heated to reflux for 1 h under nitrogen atmosphere. The crude mixture was cooled to room temperature and a saturated, aqueous NH_4PF_6 solution was added to the solution. An orange precipitate was formed upon stirring the mixture at room temperature for 1h. The precipitate was filtered, washed vigorously with water, diethyl ether and hexane and dried under vacuum to afford the clean product as an orange powder. **Yield:** 68.7%. **Rf:** 0.40 DCM + 5% MeOH on silica). **Mp:** 322 - 326 °C. **^{1}H NMR (400 MHz, CD_2Cl_2) δ (ppm):** 8.25 (d, J = 2.0 Hz, 6H), 7.57 (d, J = 6.0 Hz, 6H), 7.45 (dd, J = 6.0, 2.0 Hz, 6H), 1.42 (s, 54H). **HR-MS (FTMS$^+$): [M-PF$_6$]$^{2+}$ Calculated:** ($C_{54}H_{72}N_6Ru$) 453.2429; **Found:** 453.2415. The characterisation matches that reported.[388]

6.4 Iridium(III) and ruthenium(II) metallocages

6.4.1 Racemic and homochiral *rac*-, Λ_8- and Δ_8-$[Ir_8Pd_4]^{16+}$ metallocages

General procedure for synthesis of racemic and homochiral rac-, Λ_8- *and* Δ_8-$[Ir_8Pd_4]^{16+}$ *metallocages*

In a dry 10 mL Schlenk vial, one of the racemic or enantiopure quanterpyridine iridium complex (*rac*-, Λ- or Δ-$[Ir(C^{\wedge}N)_2(qpy)]^+$, 2 equiv.) and $[Pd(NCMe)_4](BF_4)_2$ (1 equiv.) were dissolved in DMSO-d_6 (1 mL) to give a concentration of the iridium metallo-ligands of approximately 0.05 M. The solution was degassed for five minutes by bubbling nitrogen and heated at 85 °C for 12 h under a nitrogen atmosphere. The solution was cooled to room temperature and the black solid was filtered through celite. A 2 M aqueous solution of NH_4PF_6 (5 mL) or a 2M MeOH/H_2O solution (1:1 v/v) of KBF_4 (5 mL) or a 2M MeOH/H_2O solution (1:1 v/v) of SbF_6 (5 mL) was added to the resulting DMSO solution and the mixture was stirred at room temperature for 4h. The solution was cooled in an ice bath for 30 minutes and the obtained precipitate was filtered, washed with water and diethyl ether to yield the pure cages. The assembly of the Λ-$[Ir(C^{\wedge}N)_2(qpy)]^+$ complexes with $[Pd(NCMe)_4](BF_4)_2$ afforded homochiral cage of the composition of Λ_8-$[Ir_8Pd_4]^{16+}$. The assembly of the Δ-$[Ir(C^{\wedge}N)_2(qpy)]^+$ complexes with $[Pd(NCMe)_4](BF_4)_2$ afforded homochiral cages of the composition of Δ_8-$[Ir_8Pd_4]^{16+}$, while the assembly of complexes *rac*-$[Ir(C^{\wedge}N)_2(qpy)]^+$ with $[Pd(NCMe)_4](BF_4)_2$ afforded racemic cages of the composition of *rac*-$[Ir_8Pd_4]^{16+}$.

***Rac*-, Λ_8- and Δ_8-$[Ir_8Pd_4](BF_4)_{16}$ metallocages**

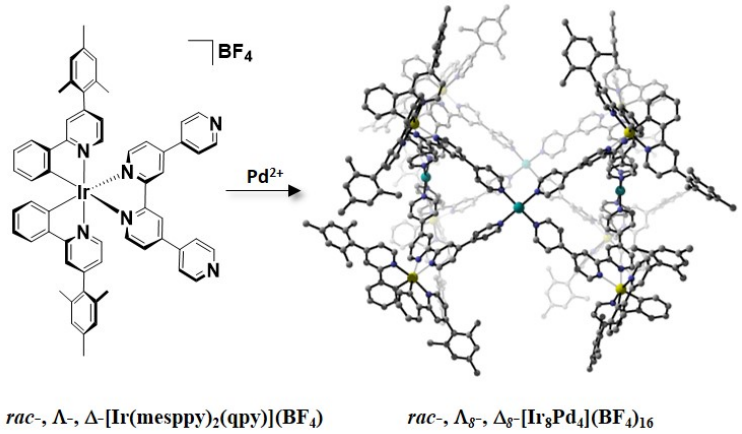

***Rac*-$[Ir_8Pd_4](BF_4)_{16}$:** red powder. **Yield:** 80%. **^{1}H NMR (500 MHz, DMSO-d_6) δ (ppm):** 9.67 (bd, J = 14.0 Hz, 16H), 9.08 (bd, J = 43.7 Hz, 11H), 8.37 (bs, 20H), 8.25 - 7.84 (m, 38H), 7.76 (bs, 6H), 7.41 (bs, 5H), 7.09 - 6.71 (m, 44H), 6.53 (bs, 6H), 6.20 (bd, J = 11.4 Hz, 11H), 2.34 (s, 48H), 2.15 (s, 48H), 1.95 (s, 48H). **^{19}F [BF_4^-] NMR (471 MHz, DMSO-d_6) δ (ppm):** -148.09 (d, J = 10.0 Hz, 4F). **^{1}H DOSY NMR (500 MHz, DMSO-d_6) D (m^2/s):** 5.2 x 10^{-11}. **HR-MS (ESIMS$^+$): [M-BF_4]$^+$ Calculated:** $[(C_{60}H_{50}IrN_6)_8Pd_4(BF_4)_{11}]^{5+}$ 1951.3302; **Found:** 1951.7285; **Calculated:** $[(C_{60}H_{50}IrN_6)_8Pd_4(BF_4)_{10}]^{6+}$ 1612.9401; **Found:** 1612.1056; **Calculated:** $[(C_{60}H_{50}IrN_6)_8Pd_4(BF_4)_9]^{7+}$ 1369.2538; **Found:** 1369.2345; **Calculated:** $[(C_{60}H_{50}IrN_6)_8Pd_4(BF_4)_8]^{8+}$ 1187.3291; **Found:** 1187.3294.

Λ_8-$[Ir_8Pd_4](BF_4)_{16}$: red powder. **Yield:** 82%. **^{1}H NMR (500 MHz, DMSO-d_6) δ (ppm):** 9.71 (bs, 16H), 9.12 (bd, J = 40.3 Hz, 8H), 8.94 (bs, 8H), 8.35 (bs, 8H), 8.22 - 7.93 (m, 49H), 7.77 (bs, 9H), 7.13 - 6.67 (m, 62H), 6.55 (bs, 5H), 6.37 - 6.10 (m, 15H), 2.35 (s, 48H), 2.13 (s, 48H), 1.91 (s, 48H). **^{19}F [BF_4^-] NMR (471 MHz, DMSO-d_6) δ (ppm):** -148.05 (d, J = 10.3 Hz, 4F). **^{1}H DOSY NMR (500 MHz, DMSO-d_6) D (m^2/s):** 5.2 x 10^{-11}. **HR-MS (ESIMS$^+$): [M-BF_4]$^+$ Calculated:** $[(C_{60}H_{50}IrN_6)_8Pd_4(BF_4)_{11}]^{5+}$ 1951.3302; **Found:** 1951.7289; **Calculated:** $[(C_{60}H_{50}IrN_6)_8Pd_4(BF_4)_{10}]^{6+}$ 1612.9401; **Found:** 1612.1035; **Calculated:** $[(C_{60}H_{50}IrN_6)_8Pd_4(BF_4)_9]^{7+}$ 1369.2538; **Found:** 1369.2337; **Calculated:** $[(C_{60}H_{50}IrN_6)_8Pd_4(BF_4)_8]^{8+}$ 1187.3291; **Found:** 1187.3267.

Δ_8-$[Ir_8Pd_4](BF_4)_{16}$: red powder. **Yield:** 79%. **^{1}H NMR (500 MHz, DMSO-d_6) δ (ppm):** 9.68 (bd, J = 14.2 Hz, 16H), 9.10 (bd, J = 42.7 Hz, 11H), 8.34 (bs, 20H), 8.24 - 7.88 (m, 38H), 7.76 (bs, 6H), 7.43 (bs, 5H), 7.10 - 6.73 (m, 45H), 6.54 (bs, 6H), 6.22 (bd, J = 12.6 Hz, 11H), 2.35 (s, 48H), 2.13 (s, 48H), 1.91 (s, 48H). **^{19}F [BF_4^-] NMR (471 MHz, DMSO-d_6) δ (ppm):** -148.05 (d, J = 10.3 Hz, 4F). **^{1}H DOSY NMR (500 MHz, DMSO-d_6) D (m^2/s):** 5.2 x 10^{-11}. **HR-MS (ESIMS$^+$): [M-BF_4]$^+$ Calculated:** $[(C_{60}H_{50}IrN_6)_8Pd_4(BF_4)_{11}]^{5+}$ 1951.3302; **Found:** 1951.7289;

Calculated: $[(C_{60}H_{50}IrN_6)_8Pd_4(BF_4)_{10}]^{6+}$ 1612.9401; **Found:** 1612.1035; **Calculated:** $[(C_{60}H_{50}IrN_6)_8Pd_4(BF_4)_9]^{7+}$ 1369.2538; **Found:** 1369.2337;
Calculated: $[(C_{60}H_{50}IrN_6)_8Pd_4(BF_4)_8]^{8+}$ 1187.3291; **Found:** 1187.3267.

Λ_8- and Δ_8-[Ir_8Pd_4]$(PF_6)_{16}$ metallocages

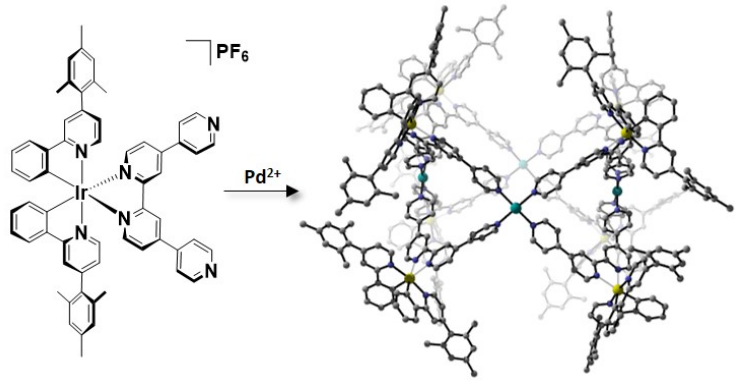

rac-, Λ-, Δ-[Ir(mesppy)$_2$(qpy)](PF$_6$) *rac*-, Λ_8-, Δ_8-[Ir_8Pd_4](PF$_6$)$_{16}$

Λ_8-**[Ir_8Pd_4]$(PF_6)_{16}$:** red powder. **Yield:** 82%. **^{1}H NMR (500 MHz, DMSO-d_6) δ (ppm):** 9.67 (bd, J = 11.8 Hz, 16H), 9.58 - 9.40 (m, 11H), 9.33 (bs, 7H), 9.21 - 8.77 (m, 28H), 8.61 - 7.85 (m, 10H), 7.74 (bd, J = 16.8 Hz, 14H), 7.44 (bs, 8H), 7.14 - 6.68 (m, 82H), 6.57 (bs, 7H), 6.35 - 6.12 (m, 20H), 2.31 (s, 48H), 2.12 (s, 48H), 1.95 (s, 48H). **^{19}F [PF_6^-] NMR (471 MHz, DMSO-d_6) δ (ppm):** -69.35 (bs, 3F), -70.86 (bs, 3F). **^{1}H DOSY NMR (500 MHz, DMSO-d_6) D (m^2/s):** 5.2 x 10^{-11}. **HR-MS (ESIMS$^+$): [M-PF_6]$^+$ Calculated:** $[(C_{60}H_{50}IrN_6)_8Pd_4(PF_6)_{12}]^{4+}$ 2635.5650; **Found:** 2635.7938; **Calculated:** $[(C_{60}H_{50}IrN_6)_8Pd_4(PF_6)_{11}]^{5+}$ 2079.6497; **Found:** 2079.6421;
Calculated:$[(C_{60}H_{50}IrN_6)_8Pd_4(PF_6)_{10}]^{6+}$ 1709.0431; **Found:** 1708.7056; **Calculated:** $[(C_{60}H_{50}IrN_6)_8Pd_4(PF_6)_9]^{7+}$ 1404.1881; **Found:** 1404.0402;
Calculated: $[(C_{60}H_{50}IrN_6)_8Pd_4(PF_6)_8]^{8+}$ 1245.2926; **Found:** 1245.4146.

Δ_8-**[Ir_8Pd_4]$(PF_6)_{16}$:** red powder. **Yield:** 82%. **^{1}H NMR (500 MHz, DMSO-d_6) δ (ppm):** 9.67 (bd, J = 12.2 Hz, 16H), 9.05 (bd, J = 36.6 Hz, 11H), 8.84 (bs, 15H), 8.44 - 8.22 (m, 19H), 8.06 (bd, J = 45.9 Hz, 38H), 7.72 (bs, 6H), 7.44 (bs, 6H), 7.13 - 6.68 (m, 46H), 6.57 (bs, 4H), 6.22 (bd, J = 10.4 Hz,12H), 2.32 (bs, 48H), 2.12 (bs, 48H), 1.95 (bs, 48H). **^{19}F [PF_6^-] NMR (471 MHz, DMSO-d_6) δ (ppm):** -69.35 (bs, 3F), -70.86 (bs, 3F). **^{1}H DOSY NMR (500 MHz, DMSO-d_6) D (m^2/s):** 5.2 x 10^{-11}. **HR-MS (ESIMS$^+$): [M-PF_6]$^+$ Calculated:** $[(C_{60}H_{50}IrN_6)_8Pd_4(PF_6)_{12}]^{4+}$ 2635.5650; **Found:** 2635.7938; **Calculated:** $[(C_{60}H_{50}IrN_6)_8Pd_4(PF_6)_{11}]^{5+}$ 2079.6497; **Found:** 2079.6421;
Calculated:$[(C_{60}H_{50}IrN_6)_8Pd_4(PF_6)_{10}]^{6+}$ 1709.0431; **Found:** 1708.7056; **Calculated:** $[(C_{60}H_{50}IrN_6)_8Pd_4(PF_6)_9]^{7+}$ 1404.1881; **Found:** 1404.0402;
Calculated: $[(C_{60}H_{50}IrN_6)_8Pd_4(PF_6)_8]^{8+}$ 1245.2926; **Found:** 1245.4146.

Δ_8-[Ir_8Pd_4](SbF_6)$_{16}$ metallocages

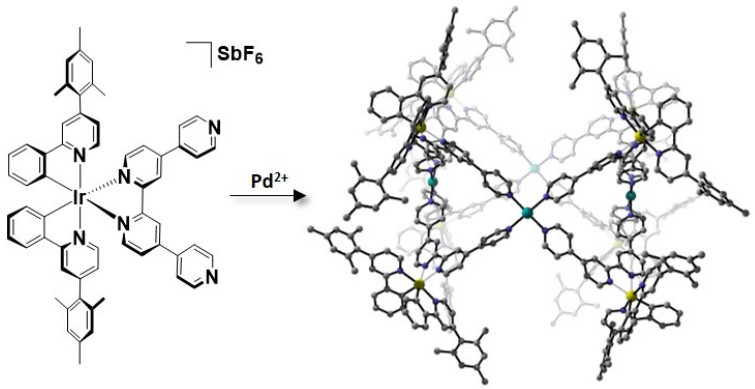

Δ_8-[Ir_8Pd_4](SbF_6)$_{16}$: red powder. **Yield:** 74%. **^{1}H NMR (500 MHz, DMSO-d_6)** δ **(ppm):** 9.68 (bs, 16H), 9.07 (bd, J = 30.1 Hz, 11H), 8.30 (bs, 15H), 8.20 - 7.87 (m, 20H), 7.71 (bd, J = 17.5 Hz, 38H), 7.46 (bs, 10H), 7.13 - 6.50 (m, 48H), 6.20 (bd, J = 34.6 Hz, 46H), 2.34 (bs, 48H), 2.11 (bs, 48H), 1.95 (bs, 48H). **^{19}F [SbF_6^-] NMR (471 MHz, DMSO-d_6)** δ **(ppm):** -148.10 (bd, J = 10.3 Hz, 6F). **^{1}H DOSY NMR (500 MHz, DMSO-d_6) D (m^2/s):** 5.2 x 10^{-11}.

***Rac*-, Λ_8- and Δ_8-[FIr_8Pd_4](BF_4)$_{16}$ metallocages**

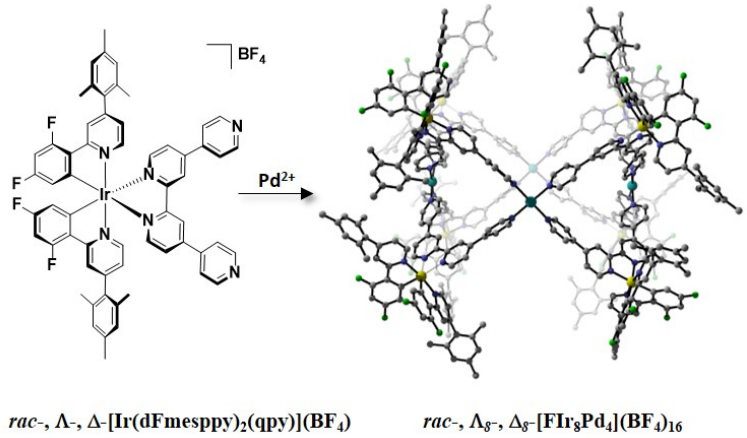

rac-, Λ-, Δ-[Ir(dFmesppy)$_2$(qpy)](BF$_4$) *rac*-, Λ_8-, Δ_8-[FIr_8Pd_4](BF$_4$)$_{16}$

***Rac*-[FIr_8Pd_4](BF_4)$_{16}$:** yellow powder. **Yield:** 73%. **^{1}H NMR (500 MHz, DMSO-d_6) δ (ppm):** 9.71 (bs, 16H), 8.29 (bd, J = 73.6 Hz, 34H), 7.93 (bs, 14H), 7.21 - 6.45 (m, 28H), 5.60 (bs, 10H), 2.37 (s, 48H), 2.13 (s, 48H), 1.95 (s, 48H). **^{19}F NMR (471 MHz, DMSO-d_6) δ (ppm):** -106.06 (bs, 32F), -108.33 (bs, 32F), -146.17 (bd, J = 17.9 Hz, 4F). **^{1}H DOSY NMR (500 MHz, DMSO-d_6) D (m^2/s):** 4.9 x 10^{-11}. **HR-MS (ESIMS$^+$): [M-BF_4]$^+$ Calculated:** $[(C_{60}H_{46}F_4IrN_6)_8Pd_4(BF_4)_{11}]^{5+}$ 2067.0798; **Found:** 2067.0695; **Calculated:** $[(C_{60}H_{46}F_4IrN_6)_8Pd_4(BF_4)_{10}]^{6+}$ 1707.9986; **Found:** 1708.0556; **Calculated:** $[(C_{60}H_{46}F_4IrN_6)_8Pd_4(BF_4)_9]^{7+}$ 1451.4815; **Found:** 1451.6469; **Calculated:** $[(C_{60}H_{46}F_4IrN_6)_8Pd_4(BF_4)_8]^{8+}$ 1259.2943; **Found:** 1259.2897.

Λ_8-[FIr_8Pd_4](BF_4)$_{16}$: yellow powder. **Yield:** 73%. **^{1}H NMR (500 MHz, DMSO-d_6) δ (ppm):** 9.73 (bs, 16H), 9.54 (bs, 10H), 9.17 (bd, J = 29.2 Hz, 16H), 8.98 (bs, 14H), 8.37 (bs, 21H), 8.22 (bd, J = 33.3 Hz, 50H), 7.94 (bd, J = 60.4 Hz, 35H), 7.17 (bs, 11H), 7.13 - 6.67 (m, 16H), 2.35 (s, 48H), 2.09 (s, 48H), 1.94 (s, 48H). **^{19}F NMR (471 MHz, DMSO-d_6) δ (ppm):** -106.27 (bs, 32F), -108.48 (bs, 32F), -146.21 (bd, J = 17.9 Hz, 4F). **^{1}H DOSY NMR (500 MHz, DMSO-d_6) D (m^2/s):** 4.9 x 10^{-11}. **HR-MS (ESIMS$^+$): [M-BF_4]$^+$ Calculated:** $[(C_{60}H_{46}F_4IrN_6)_8Pd_4(BF_4)_{11}]^{5+}$ 2067.0798; **Found:** 2067.0646; **Calculated:** $[(C_{60}H_{46}F_4IrN_6)_8Pd_4(BF_4)_{10}]^{6+}$ 1707.9986; **Found:** 1708.0532; **Calculated:** $[(C_{60}H_{46}F_4IrN_6)_8Pd_4(BF_4)_9]^{7+}$ 1451.4815; **Found:** 1451.6165; **Calculated:** $[(C_{60}H_{46}F_4IrN_6)_8Pd_4(BF_4)_8]^{8+}$ 1259.2943; **Found:** 1259.2890.

Δ_8-[FIr_8Pd_4](BF_4)$_{16}$: yellow powder. **Yield:** 78%. **^{1}H NMR (500 MHz, DMSO-d_6) δ (ppm):** 9.72 (bs, 16H), 8.27 (bd, J = 75.6 Hz, 34H), 7.96 (bs, 15H), 7.22 - 6.72 (m, 28H), 5.63 (bs, 14H), 2.37 (s, 48H), 2.10 (s, 48H), 1.96 (s, 48H). **^{19}F NMR (471 MHz, DMSO-d_6) δ (ppm):** -106.07 (bs, 32F), -108.33 (bs, 32F), -148.11 (bd, J = 15.3 Hz, 4F). **^{1}H DOSY NMR (500 MHz, DMSO-d_6) D (m^2/s):** 4.9 x 10^{-11}. **HR-MS (ESIMS$^+$): [M-BF_4]$^+$ Calculated:** $[(C_{60}H_{46}F_4IrN_6)_8Pd_4(BF_4)_{11}]^{5+}$ 2067.0798; **Found:** 2067.0646; **Calculated:** $[(C_{60}H_{46}F_4IrN_6)_8Pd_4(BF_4)_{10}]^{6+}$ 1707.9986; **Found:** 1708.0532;

Calculated: $[(C_{60}H_{46}F_4IrN_6)_8Pd_4(BF_4)_9]^{7+}$ 1451.4815; **Found:** 1451.6165;
Calculated: $[(C_{60}H_{46}F_4IrN_6)_8Pd_4(BF_4)_8]^{8+}$ 1259.2943; **Found:** 1259.2890.

6.4.2 Racemic $[Ru_8Pd_4]^{24+}$ metallocage

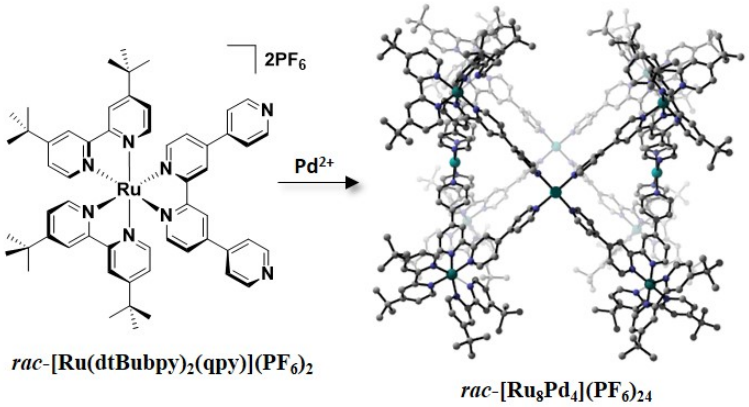

In a dry 10 mL Schlenk vial, the Ru(II) complex $[Ru(dtBubpy)_2(qpy)](PF_6)_2$ (2 equiv.) and $[Pd(NCMe)_4](BF_4)_2$ (1 equiv.) were dissolved in DMSO-d_6 (1 mL) to give a concentration of the ruthenium metallo-ligands of approximately 0.05 M. The solution was degassed for five minutes by bubbling nitrogen and heated at 85 °C for 12 h under a nitrogen atmosphere. The solution was cooled to room temperature and the black solid was filtered through celite. A 2 M aqueous solution of NH_4PF_6 (5 mL) or a 2M MeOH/H_2O solution (1:1 v/v) of KBF_4 (5 mL) was added to the resulting DMSO solution and the mixture was stirred at room temperature for 4h. The solution was cooled in an ice bath for 30 minutes and the obtained precipitate was filtered, washed with water and diethyl ether to yield the pure cage. **Yield:** 88%. **^{1}H NMR (500 MHz, DMSO-d_6) δ (ppm):** 9.63 (bd, 16H), 8.96 (bd, J = 45.6 Hz, 12H), 8.88 - 8.81 (m, 18H), 8.25 (bs, 18H), 7.91 - 7.82 (m, 18H), 7.56 - 7.45 (m, 18H), 1.40 - 1.42 (m, 288H). **^{19}F [PF_6^-] NMR (471 MHz, DMSO-d_6) δ (ppm):** -69.38 (bs, 3F), -70.86 (bs, 3F). **^{1}H DOSY NMR (500 MHz, DMSO-d_6) D (m^2/s):** 5.3 x 10^{-11}. **HR-MS (ESIMS$^+$): [M-BF_4]^2+ Calculated:** $[(C_{56}H_{62}N_8Ru)_8Pd_4(BF_4)_{18}(H_2O)_2]^{6+}$ 1601.6724; **Found:** 1601.6721; **Calculated:** $[(C_{56}H_{62}N_8Ru)_8Pd_4(BF_4)_{18}(H_2O)_2]^{6+}$ 1707.9986; **Found:** 1708.0532; **Calculated:** $[(C_{56}H_{62}N_8Ru)_8Pd_4(BF_4)_{17}(H_2O)_2]^{7+}$ 1360.4329; **Found:** 1360.4390;
Calculated: $[(C_{56}H_{62}N_8Ru)_8Pd_4(BF_4)_{16}(H_2O)_2]^{8+}$ 1179.5033; **Found:** 1179.5078.

6.5 Iridium(III)- and ruthenium(II)-porphyrin assemblies

6.5.1 Synthesis of zinc tetraphenylporphyrin (ZnTPP)

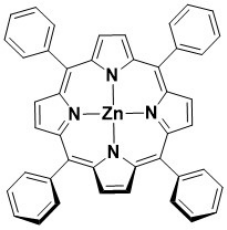

This synthetic protocol is a modification of that reported in the literature.[371] Tetraphenylporphyrin TPP (100 mg, 0.162 mmol, 1 equiv.) was dissolved in 25 mL of chloroform. The solution was purged with nitrogen for 10 min. Zinc acetate (73 mg, 0.334 mmol, 2 equiv.) was dissolved in 5 mL methanol and then added to the porphyrin solution. The mixture was stirred under nitrogen atmosphere at room temperature for 24 h. The solvents were removed under reduced pressure leaving a purple solid. The solid was dissolved in DCM and washed with 5% w/v aqueous sodium bicarbonate solution, followed by water. The organic layer was dried over $MgSO_4$ and the solvent was removed under reduced pressure. Zinc porphyrin was purified by flash column chromatography on a silica gel using 100% chloroform as the eluent. **Yield:** 90%. **Rf:** 0.65 $CHCl_3$ on silica). **^{1}H NMR (500 MHz, CD_2Cl_2) δ (ppm):** 8.88 (s, 8H), 8.15 (dd, J = 7.4, 1.6 Hz, 8H), 7.69 (m, 12H). **^{13}C NMR (126 MHz, CD_2Cl_2) δ (ppm):** 150.2, 142.8, 134.4, 131.9, 127.5, 126.6, 121.1. **HR-MS (FTMS$^+$): [M+H]$^+$ Calculated:** ($C_{44}H_{28}N_4Zn$) 677.1671; **Found:** 677.1678. The characterisation matches that reported.[371]

6.5.2 Supramolecular Ir-ZnTPP and Ru-ZnTPP assemblies

.

In a dry 2 mL vial, one of the complex *rac*-[Ir(mesppy)$_2$(qpy)](PF$_6$), *rac*-[Ir(dFmesppy)$_2$(qpy)](PF$_6$) or *rac*-[Ru(dtBubpy)$_2$(qpy)](PF$_6$)$_2$, and ZnTPP (1 or 2 equiv.) were dissolved in CD_2Cl_2 (1 mL) to give a concentration of the iridium or ruthenium complex of approximately 0.05 M. The solution was sonicated for few seconds and subsequently transferred to an NMR tube for characterization.

***Rac*-[Ir(mesppy)$_2$(qpy)](PF$_6$)-ZnTPP assembly**

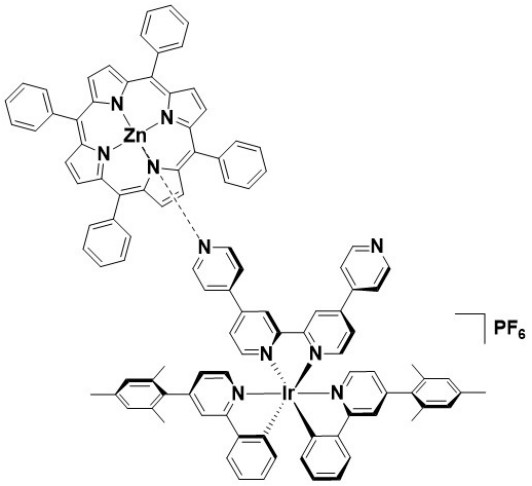

^{1}H NMR (500 MHz, CD_2Cl_2) δ (ppm): 8.94 (s, 8H), 8.25 (d, J = 7.8 Hz, 8H), 7.90 (m, 4H), 7.80 (m, 12H), 7.64 (s, 2H), 7.93 (d, J = 8.6 Hz, 2H), 7.26 (d, J = 6.0 Hz, 2H), 7.05 (d, J = 6.5 Hz, 2H), 6.99 (m, 4H), 6.89 (m, 4H), 6.66 (dd, J = 6.5, 1.5 Hz, 2H), 6.52 (bs, 3H), 6.20 (d, J = 7.4 Hz, 2H), 5.36 (s, 4H), 2.31 (s, 6H), 2.02 (s, 6H), 1.71 (s, 6H). **^{13}C NMR (126 MHz, CD_2Cl_2) δ (ppm):** 167.28, 152.21, 151.08, 149.31, 148.31, 147.42, 143.62, 143.24, 142.82, 138.30, 134.69, 131.70, 131.92, 131.24, 130.67, 128.41, 127.30, 126.42, 125.63, 124.78, 122.75, 122.09, 120.73, 20.72, 20.01. **^{1}H DOSY NMR (500 MHz, CD_2Cl_2) D (m^2/s):** 1.37 x 10^{-9}.

***Rac*-[Ir(mesppy)$_2$(qpy)](PF$_6$)-(ZnTPP)$_2$ assembly**

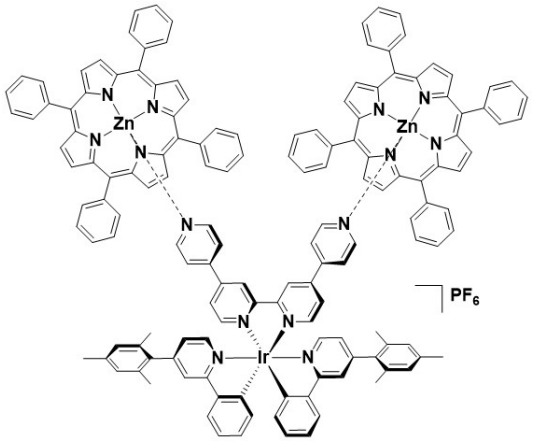

^{1}H NMR (500 MHz, CD_2Cl_2) δ (ppm): 8.94 (s, 16H), 8.38 (d, J = 7.8 Hz, 16H), 7.95 (bs, 2H), 7.80 (m, 24H), 7.72 (d, J = 4.9 Hz, 2H), 7.49 (d, J = 8.1 Hz, 2H), 7.44 (bs, 2H), 7.42 (s, 1H), 7.09 (d, J = 5.7 Hz, 2H), 6.92 (t, J = 7.1 Hz, 4H), 6.86 (bs, 2H), 6.81 (t, J = 7.4 Hz, 3H), 6.71 (bd, J = 7.2 Hz, 2H), 6.53 (dd, J = 7.2, 2.1 Hz, 4H), 6.09 (s, J = 9.4 Hz, 2H), 5.95 (d, J = 5.8 Hz, 2H), 2.29 (s, 6H), 1.95 (s, 6H), 1.67 (s, 6H). **^{13}C NMR (126 MHz, CD_2Cl_2) δ (ppm):** 167.23, 162.08, 157.40, 155.55, 155.20, 152.12, 150.62, 150.14, 149.10, 143.20, 146.65, 144.48, 143.01, 141.59, 138.24, 135.66, 134.48, 131.80, 131.13, 130.59, 128.37, 127.40, 126.50, 125.32, 124.68, 122.68, 121.40, 120.95, 120.35, 20.63, 19.90. **^{1}H DOSY NMR (500 MHz, CD_2Cl_2) D (m^2/s):** 1.39 x 10^{-9}.

***Rac*-[Ir(dFmesppy)$_2$(qpy)](PF$_6$)-ZnTPP assembly**

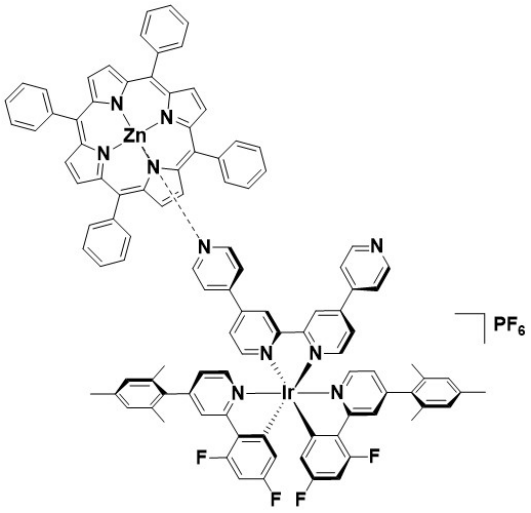

^{1}H NMR (500 MHz, CD_2Cl_2) δ (ppm): 8.98 (s, 8H), 8.26 (bs, 8H), 7.98 (s, 2H), 7.82 (m, 12H), 7.23 (d, J = 5.3 Hz, 2H), 7.94 (m, 12H), 6.69 (d, J = 5.9 Hz, 4H), 6.53 (m, 4H), 6.35 (bs, 4H), 6.10 (d, J = 6.2 Hz, 3H), 5.95 (m, 4H), 5.13 (s, 1H), 2.30 (s, 6H), 2.06 (s, 6H), 1.99 (s, 6H). **^{19}F NMR (471 MHz, CD_2Cl_2) δ (ppm):** -72.82 (d, J = 707.5 Hz, 6F), -106.34 (d, J = 14.6 Hz, 2F), -108.61 (d, J = 14.6 Hz, 2F). **MALDI-MS$^+$: [M-PF$_6$]$^+$ Calculated:** ($C_{105}H_{77}F_{10}IrN_{10}PZn$) 1942.33; **Found:** 1943.56.

***Rac*-[Ir(dFmesppy)$_2$(qpy)](PF$_6$)-(ZnTPP)$_2$ assembly**

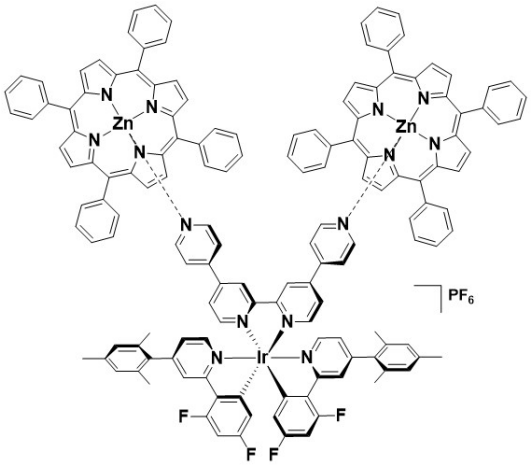

^{1}H NMR (500 MHz, CD_2Cl_2) δ (ppm): 8.97 (s, 16H), 8.27 (bs, 16H), 7.95 (s, 4H), 7.80 (m, 24H), 7.60 (m, 6H), 7.15 (d, J = 7.8 Hz, 3H), 6.91 (m, 8H), 6.64 (d, J = 4.2 Hz, 4H), 6.48 (bt, J = 9.1 Hz, 4H), 6.12 (bs, 4H), 5.95 (m, 3H), 5.54 (m, 4H), 5.18 (s, 3H), 2.29 (s, 6H), 1.97 (s, 6H), 1.71 (s, 6H). **^{19}F NMR (471 MHz, CD_2Cl_2) δ (ppm):** -72.30 (d, J = 707.6 Hz, 6F), -106.3 (d, J = 14.8 Hz, 2F), -108.6 (d, J = 14.8 Hz, 2F).

***Rac*-[Ru(dtBubpy)$_2$(qpy)](PF$_6$)$_2$-(ZnTPP) assembly**

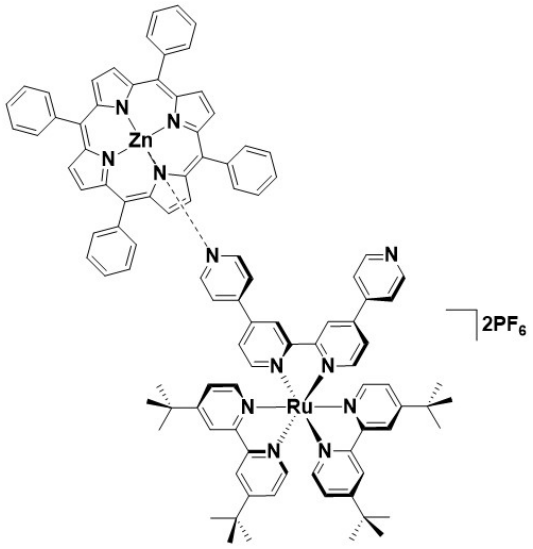

^{1}H NMR (500 MHz, CD_2Cl_2) δ (ppm): 8.82 (bs, 8H), 8.17 (dd, J = 14.6, 2.0 Hz, 8H), 8.10 (bs, 12H), 7.64 (d, J = 6.0 Hz, 4H), 7.44 (t, J = 7.6 Hz, 4H), 7.38 (dd, J = 6.2, 2.0 Hz, 2H), 7.34 - 7.26 (m, 4H), 1.36 (s, 18H), 1.30 (s, 18H).

***Rac*-[Ru(dtBubpy)$_2$(qpy)](PF$_6$)$_2$-(ZnTPP)$_2$ assembly**

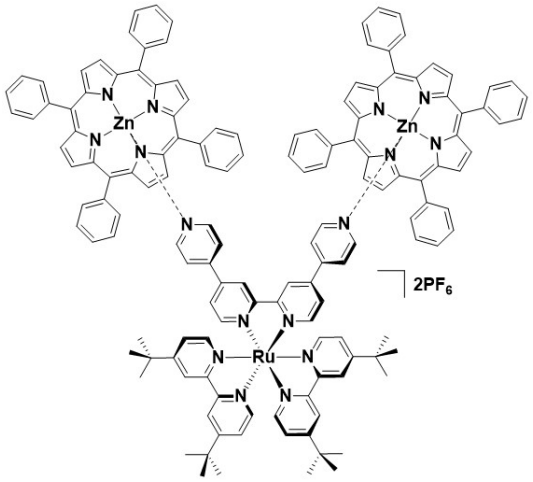

^{1}H NMR (500 MHz, CD_2Cl_2) δ (ppm): 8.85 (bs, 16H), 8.12 (d, J = 16.4 Hz, 16H), 7.90 (bs, 24H), 7.53 (bs, 8H), 7.44 - 7.16 (m, 16H), 7.10 (s, 4H), 1.33 (s, 18H), 1.27 (s, 18H).

6.5.3 Supramolecular Ir,Ag-coordination polymer

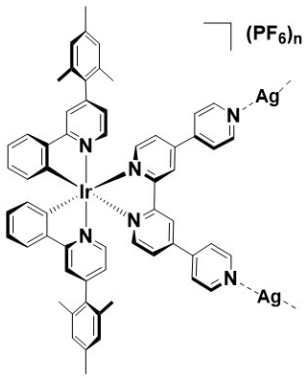

The Ir,Ag coordination polymer **IrP1** was obtained by crystallisation techniques. Crystals of **IrP1** were grown through slow diffusion of diethyl ether into a 3 mM CH_2Cl_2 solution of **Ir3** (1 mL) layered with a 1:1 CH_2Cl_2/MeOH mixture (1 mL) and then with a MeOH solution of $AgPF_6$ (1 mL). The crystals were formed at room temperature over a period of 10 days. The structure of **IrP1** was characterised by x-ray diffraction and NMR spectroscopy. **^{1}H NMR (500 MHz, MeNO2d_3) δ (ppm):** 9.11 (bs, 4H), 8.82 (bs, 8H), 8.19 (d, J = 5.9 Hz, 4H), 7.39 (dt, J = 27.2, 7.4 Hz 8H), 7.09 (q, J = 2.2 Hz, 8H), 7.02 (s, 2H), 6.89 (d, J = 7.2 Hz, 2H), 2.34 (s, 6H), 2.23 (s, 6H), 1.91 (s, 6H). **^{1}H DOSY NMR (500 MHz, MeNO2d_3) D (m^2/s):** 2.84 x 10^{-10}

6.6 General spectroscopic methods

Photophysical measurements

All samples were prepared in HPLC grade solvents with varying concentrations on the order of μM. Absorption spectra were recorded at RT using a Shimadzu UV-1800 double beam spectrophotometer. Molar absorptivity determination was verified by linear least-squares fit of values obtained from at least three independent solutions at varying concentrations with absorbances of less than 1.0 for each absorption band. The sample solutions for the emission spectra were degassed by vigorous bubbling for ca. 20 min or *via* freeze-pump-thaw cycles using a quartz cuvette designed in-house. Steady-state emission was recorded at 77 K or 298 K using an Edinburgh Instruments F980 or a Gilden Photonics fluoroSENS spectrophotometer. All samples for steady-state measurements were excited at 360 nm or 440 nm using a xenon lamp, while samples for time-resolved measurements were excited at 378 nm using a PDL 800-D pulsed diode laser, and recorded using a time-correlated single photon counting (TCSPC) method. Emission quantum yields were determined using the optically dilute method.[427, 428]. A stock solution with absorbance of ca. 0.5 on the excitation band was prepared and then four dilutions were prepared with dilution factors of 5, 6.6, 10 and 20 to obtain solutions with absorbances of ca. 0.1 0.075, 0.05 and 0.025, respectively. The Beer-Lambert law was found to be linear at the concentrations of the solutions. The emission spectra were then measured after the solutions were degassed *via* freeze-pump-thaw cycles or by nitrogen purging for ca. 20 min per sample prior to spectrum acquisition. For each sample, linearity between absorption and emission intensity was verified through linear regression analysis and additional measurements were acquired until the Pearson regression factor (R^2) for the linear fit of the data set surpassed 0.9. Individual relative quantum yield values were calculated for each solution and the values reported represent the slope value. The equation:

$$\Phi_s = \Phi_r \left(\frac{A_r}{A_s}\right)\left(\frac{I_s}{I_r}\right)\left(\frac{n_s}{n_r}\right)^2$$

was used to calculate the relative quantum yield of each of the sample, where Φ_r is the absolute quantum yield of the reference, n is the refractive index of the solvent, A is the absorbance at the excitation wavelength, and I is the integrated area under the corrected emission curve. The subscripts s and r refer to the sample and reference, respectively. For the reference sample, either a solution of quinine sulfate in 0.5 M H_2SO_4 (Φ_r = 54.6%)[287] or $[Ru(bpy)_3]Cl_2$ in air-satured water (Φ_r = 2.8%)[429, 430] was used.

Samples for solid-state measurements were prepared by spin-coating solutions of each complex (5 mg / 1 mL) onto quartz substrates. Neat thin films were prepared by spin coating the samples from a solution of 2-methoxyethanol (HPLC grade) 10^{-2} M on a

pristine quartz substrate. PMMA (poly-methyl methacrylate)-doped films were prepared by spin coating the samples from a solution of 2-methoxyethanol (HPLC grade) containing 5% w/w of the desired sample and 95% w/w of PMMA. Steady-state emission and excitation spectra and time-resolved emission spectra of both powders and doped films were recorded at 298 K using an Edinburgh Instruments F980. All samples for steady-state measurements were excited at 360 nm xenon lamp while samples for time-resolved measurements were excited at 378 nm using a PDL 800-D pulsed diode laser. Solid-state photoluminescence quantum yield measurements of thin films and powders were performed in an integrating sphere under a nitrogen purge in a Hamamatsu C9920-02 luminescence measurement system.[431] Solution quantum yield measurements are affected by an error of ± 5%, solid-state quantum yields measured with an integrating sphere are affected by an error of ± 1%. Time-resolved emission lifetime measurements are affected by an error of approximately ± 2%. Finally, steady-state emission spectra are affected by an error of approximately ± 1 nm.

Streak camera measurements

Picosecond temporal dynamics were measured with a Hamamatsu synchroscan universal streak camera. The solution cuvette was mounted in either transmission or reflection geometry with respect to the camera spectrograph. Excitation (310 nm, 360 nm) was provided by the tuneable output of an Orpheus optical parametric amplifier, pumped by a Pharos regenerative amplifier, both from Light Conversion. Laser excitation was at 100 kHz, with 300 fs full-width half-maximum pulses.

Electrochemical measurements

Cyclic voltammery (CV) and differential pulse voltammetry (DPV) measurements were performed on an Electrochemical Analyzer potentiostat model 600D from CH Instruments. Solutions for were prepared in MeCN or DCM and degassed with solvent-saturated nitrogen by bubbling for ca. 10 min prior to scanning. Tetra(n-butyl)ammoniumhexafluorophosphate ($TBAPF_6$; ca. 0.1 M in MeCN or DCM) was used as the supporting electrolyte. A Pt wire was used as the pseudo-reference electrode; a Pt wire coil was used as the counter electrode and a Pt disk electrode was used for the working electrode. The redox potentials are reported relative to a saturated calomel electrode (SCE) electrode with a ferrocenium/ferrocene (Fc^+/Fc) redox couple as an internal reference (0.38 V vs SCE).[432]

The rate constants for photoinduced electron electron transfer k_{eT} for the IrZn and RuZn assemblies were estimated as previously reported.[433]

$$k_{\mathrm{eT}} = \left(\frac{k_{\mathrm{em}}}{\Phi_{\mathrm{PL}}}\right) - k_{\mathrm{em}} \qquad k_{\mathrm{em}} = \left(\frac{\Phi_{\mathrm{PL}}}{\tau_{\mathrm{PL}}}\right)$$

Bibliography

(1) H. Yersin, *Highly efficient OLEDs with phosphorescent materials*, John Wiley & Sons, 2008.

(2) E. Zysman-Colman, *Iridium (III) in Optoelectronic and Photonics Applications*, John Wiley & Sons, 2017.

(3) L. Flamigni, A. Barbieri, C. Sabatini, B. Ventura and F. Barigelletti, in *Photochemistry and Photophysics of Coordination Compounds II*, Springer, 2007, pp. 143–203.

(4) S. Fanni, T. E. Keyes, C. M. O'Connor, H. Hughes, R. Wang and J. G. Vos, *Coord. Chem. Rev.*, 2000, **208**, 77–86.

(5) K. Kalyanasundaram and M. Grätzel, *Coord. Chem. Rev.*, 1998, **177**, 347–414.

(6) S. Campagna, F. Puntoriero, F. Nastasi, G. Bergamini and V. Balzani, in *Photochemistry and Photophysics of Coordination Compounds I*, Springer, 2007, pp. 117–214.

(7) H. Suzuki, *Electronic absorption spectra and geometry of organic molecules: An application of molecular orbital theory*, Elsevier, 2012.

(8) Y. Jean, *Molecular orbitals of transition metal complexes*, OUP Oxford, 2005.

(9) M. K. Nazeeruddin and M. Grätzel, in *Photofunctional Transition Metal Complexes*, Springer, 2007, pp. 113–175.

(10) D. M. Roundhill, *Photochemistry and photophysics of metal complexes*, Springer Science & Business Media, 2013.

(11) A. F. Henwood and E. Zysman-Colman, *Chem. Commun.*, 2017, **53**, 807–826.

(12) M. S. Lowry and S. Bernhard, *Chem. Eur. J.*, 2006, **12**, 7970–7977.

(13) S. Ladouceur and E. Zysman-Colman, *Eur. J. Inorg. Chem.*, 2013, **2013**, 2985–3007.

(14) H. Yersin and A. Vogler, *Photochemistry and photophysics of coordination compounds*, Springer, 1987.

(15) A. J. Lees, *Photophysics of organometallics*, Springer Science & Business Media, 2010, vol. 29.

(16) E. Hirschlaff, *Fluorescence and phosphorescence*, Chemical Catalog Company, Inc; New York, 1939.

(17) B. Valeur and M. N. Berberan-Santos, *Molecular fluorescence: principles and applications*, John Wiley & Sons, 2012.

(18) H. Yersin, A. F. Rausch, R. Czerwieniec, T. Hofbeck and T. Fischer, *Coord. Chem. Rev.*, 2011, **255**, 2622–2652.

(19) A. F. Rausch, H. H. Homeier and H. Yersin, in *Photophysics of Organometallics*, Springer, 2010, pp. 193–235.

(20) N. J. Turro, *Modern molecular photochemistry*, University science books, 1991.

(21) V. Balzani and V. Carassiti, *Photochemistry of Coordination Compounds*, 1969, 1970.

(22) G. J. Kavarnos and N. J. Turro, *Chem. Rev.*, 1986, **86**, 401–449.

(23) E. H. White, J. D. Miano, C. J. Watkins and E. J. Breaux, *Angew. Chem. Int. Ed.*, 1974, **13**, 229–243.

(24) M. A. Fox, *Photochem. Photobiol.*, 1990, **52**, 617–627.

(25) A. Weller, *J. Phys. Chem.*, 1982, **133**, 93–98.

(26) V. Balzani, F. Bolletta, F. Scandola and R. Ballardini, *Pure Appl. Chem.*, 1979, **51**, 299–311.

(27) F. Scandola, C. Chiorboli, A. Prodi, E. Iengo and E. Alessio, *Coord. Chem. Rev.*, 2006, **250**, 1471–1496.

(28) S.-H. Lin, W. Xiao and W. Dietz, *Phys. Rev. E*, 1993, **47**, 3698–3706.

(29) D. L. Dexter, *J. Chem. Phys.*, 1953, **21**, 836–850.

(30) T. Főrster, *Faraday Discuss.*, 1959, **27**, 7–17.

(31) M. Kasha, *Radiat Res.*, 1963, **20**, 55–70.

(32) M. Inokuti and F. Hirayama, *Journal Chem. Phys.*, 1965, **43**, 1978–1989.

(33) J. B. Larnbert, *Physical organic chemistry*, Wiley Online Library, 1970.

(34) R. A. Alberty and G. G. Hammes, *J. Phys. Chem.*, 1958, **62**, 154–159.

(35) G. D. Scholes, *Annu. Rev. Phys. Chem.*, 2003, **54**, 57–87.

(36) S. Jang, Y.-C. Cheng, D. R. Reichman and J. D. Eaves, *Theory of coherent resonance energy transfer*, AIP, 2008.

(37) J. Birks, *Phys. Rev.*, 1954, **94**, 1567–1573.

(38) D. Philp and J. F. Stoddart, *Angew. Chem. Int. Ed.*, 1996, **35**, 1154–1196.

(39) J. M. Grimes, J. N. Burroughs, P. Gouet, J. M. Diprose, R. Malby, S. Ziéntara, P. P. Mertens and D. I. Stuart, *Nature*, 1998, **395**, 470–478.

(40) A. W. Roszak, T. D. Howard, J. Southall, A. T. Gardiner, C. J. Law, N. W. Isaacs and R. J. Cogdell, *Science*, 2003, **302**, 1969–1972.

(41) G. M. Whitesides and B. Grzybowski, *Science*, 2002, **295**, 2418–2421.

(42) W. R. Wikoff, L. Liljas, R. L. Duda, H. Tsuruta, R. W. Hendrix and J. E. Johnson, *Science*, 2000, **289**, 2129–2133.

(43) G. McDermott, S. Prince, A. Freer, A. Hawthornthwaite-Lawless, M. Papiz, R. Cogdell and N. Isaacs, *Nature*, 1995, **374**, 517–521.

(44) S. Bahatyrova, R. N. Frese, C. A. Siebert, J. D. Olsen, K. O. van der Werf, R. van Grondelle, R. A. Niederman, P. A. Bullough, C. Otto and C. N. Hunter, *Nature*, 2004, **430**, 1058–1062.

(45) K. Goossens, K. Lava, C. W. Bielawski and K. Binnemans, *Chem. Rev.*, 2016, **116**, 4643–4807.

(46) D. Kim, S. Cheong, Y. G. Ahn, S. W. Ryu, J.-K. Kim and J. Cho, *Nanoscale*, 2016, **8**, 7000–7016.

(47) S. S. Babu, V. K. Praveen and A. Ajayaghosh, *Chem. Rev.*, 2014, **114**, 1973–2129.

(48) Z. Qi and C. A. Schalley, *Acc. Chem. Res.*, 2014, **47**, 2222–2233.

(49) A. Winter and U. S. Schubert, *Chem. Soc. Rev.*, 2016, **45**, 5311–5357.

(50) L. Yang, X. Tan, Z. Wang and X. Zhang, *Chem. Rev.*, 2015, **115**, 7196–7239.

(51) M. C. Das, S. Xiang, Z. Zhang and B. Chen, *Angew. Chem. Int. Ed.*, 2011, **50**, 10510–10520.

(52) D. Fujita, Y. Ueda, S. Sato, N. Mizuno, T. Kumasaka and M. Fujita, *Nature*, 2016, **540**, 563–566.

(53) D. Fujita, H. Yokoyama, Y. Ueda, S. Sato and M. Fujita, *Angew. Chem. Int. Ed.*, 2015, **54**, 155–158.

(54) H. K. Bisoyi and Q. Li, *Acc. Chem. Res.*, 2014, **47**, 3184–3195.

(55) M. Antonietti and C. Göltner, *Angew. Chem. Int. Ed.*, 1997, **36**, 910–928.

(56) C. F. Faul, *Acc. Chem. Res.*, 2014, **47**, 3428–3438.

(57) E. Caló and V. V. Khutoryanskiy, *Eur. Polym. J.*, 2015, **65**, 252–267.

(58) A. S. Hoffman, *Adv. Drug Deliv. Rev.*, 2012, **64**, 18–23.

(59) V. K. Thakur and M. R. Kessler, *Polymer*, 2015, **69**, 369–383.

(60) L. Sun, M. G. Campbell and M. Dincă, *Angew. Chem. Int. Ed.*, 2016, **55**, 3566–3579.

(61) J.-L. Wang, C. Wang and W. Lin, *ACS Catalysis*, 2012, **2**, 2630–2640.

(62) T. H. Noh and O.-S. Jung, *Acc. Chem. Res.*, 2016, **49**, 1835–1843.

(63) Z. Hu, B. J. Deibert and J. Li, *Chem. Soc. Rev.*, 2014, **43**, 5815–5840.

(64) L. Xu, Y.-X. Wang and H.-B. Yang, *Dalton Trans.*, 2015, **44**, 867–890.

(65) M. W. Cooke, D. Chartrand and G. S. Hanan, *Coord. Chem. Rev.*, 2008, **252**, 903–921.

(66) S. Durot, J. Taesch and V. Heitz, *Chem. Rev.*, 2014, **114**, 8542–8578.

(67) D. B. Amabilino, D. K. Smith and J. W. Steed, *Chem. Soc. Rev.*, 2017, **46**, 2404–2420.

(68) H. Xu, R. Chen, Q. Sun, W. Lai, Q. Su, W. Huang and X. Liu, *Chem. Soc. Rev.*, 2014, **43**, 3259–3302.

(69) T. Zhang and W. Lin, *Chem. Soc. Rev.*, 2014, **43**, 5982–5993.

(70) A. Tsuboyama, H. Iwawaki, M. Furugori, T. Mukaide, J. Kamatani, S. Igawa, T. Moriyama, S. Miura, T. Takiguchi, S. Okada et al., *J. Am. Chem. Soc.*, 2003, **125**, 12971–12979.

(71) C. Wu, H.-F. Chen, K.-T. Wong and M. E. Thompson, *J. Am. Chem. Soc.*, 2010, **132**, 3133–3139.

(72) M. Mauro, K. C. Schuermann, R. Prétôt, A. Hafner, P. Mercandelli, A. Sironi and L. De Cola, *Angew. Chem. Int. Ed.*, 2010, **49**, 1222–1226.

(73) M. Sandroni and E. Zysman-Colman, *Dalton Trans.*, 2014, **43**, 3676–3680.

(74) K. N. Swanick, M. Sandroni, Z. Ding and E. Zysman-Colman, *Chem. Eur. J.*, 2015, **21**, 7435–7440.

(75) E. H. Doeven, E. M. Zammit, G. J. Barbante, C. F. Hogan, N. W. Barnett and P. S. Francis, *Angew. Chem. Int. Ed.*, 2012, **124**, 4430–4433.

(76) G. J. Barbante, N. Kebede, C. M. Hindson, E. H. Doeven, E. M. Zammit, G. R. Hanson, C. F. Hogan and P. S. Francis, *Chem. Eur. J.*, 2014, **20**, 14026–14031.

(77) E. H. Doeven, E. M. Zammit, G. J. Barbante, P. S. Francis, N. W. Barnett and C. F. Hogan, *Chem. Sci.*, 2013, **4**, 977–982.

(78) A. Ionescu, E. I. Szerb, Y. J. Yadav, A. M. Talarico, M. Ghedini and N. Godbert, *Dalton Trans.*, 2014, **43**, 784–789.

(79) V. Fiorini, A. D'Ignazio, K. D. Magee, M. I. Ogden, M. Massi and S. Stagni, *Dalton Trans.*, 2016, **45**, 3256–3259.

(80) S. Lamansky, P. Djurovich, D. Murphy, F. Abdel-Razzaq, R. Kwong, I. Tsyba, M. Bortz, B. Mui, R. Bau and M. E. Thompson, *Inorg. Chem.*, 2001, **40**, 1704–1711.

(81) S. Lamansky, P. Djurovich, D. Murphy, F. Abdel-Razzaq, H.-E. Lee, C. Adachi, P. E. Burrows, S. R. Forrest and M. E. Thompson, *J. Am. Chem. Soc.*, 2001, **123**, 4304–4312.

(82) Y. Chi and P.-T. Chou, *Chem. Soc. Rev.*, 2010, **39**, 638–655.

(83) A. F. Henwood and E. Zysman-Colman, *Top. Curr. Chem.*, 2016, **374**, 36–41.

(84) C. E. Housecroft and E. C. Constable, *Coord. Chem. Rev.*, 2017, **350**, 155–177.

(85) R. D. Costa, G. Fernández, L. Sánchez, N. Martın, E. Ortı and H. J. Bolink, *Chem. Eur. J.*, 2010, **16**, 9855–9863.

(86) E. A. Plummer, A. van Dijken, J. Hofstraat, L. De Cola and K. Brunner, *Adv. Funct. Mater.*, 2005, **15**, 281–289.

(87) X. Yang, X. Xu, J.-s. Dang, G. Zhou, C.-L. Ho and W.-Y. Wong, *Inorg. Chem.*, 2016, **55**, 1720–1727.

(88) X. Yang, Z. Feng, J. Zhao, J.-S. Dang, B. Liu, K. Zhang and G. Zhou, *ACS Appl. Mater. Interfaces*, 2016, **8**, 33874–33887.

(89) A. M'hamedi, A. S. Batsanov, M. A. Fox, M. R. Bryce, K. Abdullah, H. A. Al-Attar and A. P. Monkman, *J. Mater. Chem.*, 2012, **22**, 13529–13540.

(90) Y. Zheng, A. S. Batsanov, M. A. Fox, H. A. Al-Attar, K. Abdullah, V. Jankus, M. R. Bryce and A. P. Monkman, *Angew. Chem. Int. Ed.*, 2014, **53**, 11616–11619.

(91) K. He, N. Su, Y. Junting, Y. Liu, W. Xiong, Z. Hao, D. Ma and W. Zhu, *Tetrahedron*, 2016, **72**, 7164–7169.

(92) M. Y. Wong, G. Xie, C. Tourbillon, M. Sandroni, D. B. Cordes, A. M. Slawin, I. D. Samuel and E. Zysman-Colman, *Dalton Trans.*, 2015, **44**, 8419–8432.

(93) M. Baldo, S. Lamansky, P. Burrows, M. Thompson and S. Forrest, *Appl. Phys. Lett.*, 1999, **75**, 4–6.

(94) F. Dumur, G. Nasr, G. Wantz, C. R. Mayer, E. Dumas, A. Guerlin, F. Miomandre, G. Clavier, D. Bertin and D. Gigmes, *Org. Electron.*, 2011, **12**, 1683–1694.

(95) G. Nasr, A. Guerlin, F. Dumur, L. Beouch, E. Dumas, G. Clavier, F. Miomandre, F. Goubard, D. Gigmes, D. Bertin et al., *Chem. Commun.*, 2011, **47**, 10698–10700.

(96) C. He, K. Lu and W. Lin, *J. Am. Chem. Soc.*, 2014, **136**, 12253–12256.

(97) H. Izumi, T. Torigoe, H. Ishiguchi, H. Uramoto, Y. Yoshida, M. Tanabe, T. Ise, T. Murakami, T. Yoshida, M. Nomoto et al., *Cancer Treat. Rev.*, 2003, **29**, 541–549.

(98) S. Chen, Y. Hong, Y. Liu, J. Liu, C. W. Leung, M. Li, R. T. Kwok, E. Zhao, J. W. Lam, Y. Yu et al., *J. Am. Chem. Soc.*, 2013, **135**, 4926–4929.

(99) Y. Ma, H. Liang, Y. Zeng, H. Yang, C.-L. Ho, W. Xu, Q. Zhao, W. Huang and W.-Y. Wong, *Chem. Sci.*, 2016, **7**, 3338–3346.

(100) S. Liu, A. Xu, Z. Chen, Y. Ma, H. Yang, Z. Shi and Q. Zhao, *Opt. Express*, 2016, **24**, 28247–28255.

(101) J. H. Vella, A. Parthasarathy and K. S. Schanze, *J. Phys. Chem. A*, 2013, **117**, 7818–7822.

(102) K. Binnemans, *Chem. Rev.*, 2005, **105**, 4148–4204.

(103) S. A. Hudson and P. M. Maitlis, *Chem. Rev.*, 1993, **93**, 861–885.

(104) P. Berdagué, J. Courtieu and P. M. Maitlis, *J. Chem. Soc., Chem. Commun.*, 1994, 1313–1314.

(105) M. Esteruelas, L. Oro, E. Sola, M. Ros and J. Serrano, *J. Chem. Soc., Chem. Commun.*, 1989, 55–56.

(106) R. LeáLagadec et al., *J. Mater. Chem.*, 1991, **1**, 251–254.

(107) S. T. Trzaska and T. M. Swager, *Chem. Mater.*, 1998, **10**, 438–443.

(108) E. I. Szerb, A. M. Talarico, I. Aiello, A. Crispini, N. Godbert, D. Pucci, T. Pugliese and M. Ghedini, *Eur. J. Inorg. Chem.*, 2010, **2010**, 3270–3277.

(109) A. Santoro, A. M. Prokhorov, V. N. Kozhevnikov, A. C. Whitwood, B. Donnio, J. G. Williams and D. W. Bruce, *J. Am. Chem. Soc.*, 2011, **133**, 5248–5251.

(110) A. M. Prokhorov, A. Santoro, J. Williams and D. W. Bruce, *Angew. Chem. Int. Ed.*, 2012, **51**, 95–98.

(111) Y. Wang, C. P. Cabry, M. Xiao, L. Male, S. J. Cowling, D. W. Bruce, J. Shi, W. Zhu and E. Baranoff, *Chem. Eur. J.*, 2016, **22**, 1618–1621.

(112) J. W. Steed, *Chem. Soc. Rev.*, 2010, **39**, 3686–3699.

(113) N. M. Sangeetha and U. Maitra, *Chem. Soc. Rev.*, 2005, **34**, 821–836.

(114) X. Du, J. Zhou, J. Shi and B. Xu, *Chem. Rev.*, 2015, **115**, 13165–13307.

(115) C. D. Jones and J. W. Steed, *Chem. Soc. Rev.*, 2016, **45**, 6546–6596.

(116) M.-O. M. Piepenbrock, G. O. Lloyd, N. Clarke and J. W. Steed, *Chem. Rev.*, 2009, **110**, 1960–2004.

(117) X. Cao, Y. Wu, K. Liu, X. Yu, B. Wu, H. Wu, Z. Gong and T. Yi, *J. Mater. Chem.*, 2012, **22**, 2650–2657.

(118) L. Xiong, Q. Zhao, H. Chen, Y. Wu, Z. Dong, Z. Zhou and F. Li, *Inorg. Chem.*, 2010, **49**, 6402–6408.

(119) Y. J. Yadav, B. Heinrich, G. De Luca, A. M. Talarico, T. F. Mastropietro, M. Ghedini, B. Donnio and E. I. Szerb, *Adv. Opt. Mater.*, 2013, **1**, 844–854.

(120) M. Mauro, A. Aliprandi, D. Septiadi, N. S. Kehr and L. De Cola, *Chem. Soc. Rev.*, 2014, **43**, 4144–4166.

(121) N. Vogel, M. Retsch, C.-A. Fustin, A. del Campo and U. Jonas, *Chem. Rev.*, 2015, **115**, 6265–6311.

(122) A. Guerrero-Martínez, Y. Vida, D. Domínguez-Gutiérrez, R. Q. Albuquerque and L. De Cola, *Inorg. Chem.*, 2008, **47**, 9131–9133.

(123) A. M. Talarico, M. Ghedini, C. O. Rossi and E. I. Szerb, *Soft Matter*, 2012, **8**, 11661–11669.

(124) M. Mauro, G. De Paoli, M. Otter, D. Donghi, G. D'Alfonso and L. De Cola, *Dalton Trans.*, 2011, **40**, 12106–12116.

(125) D. Aiello, A. M. Talarico, F. Teocoli, E. I. Szerb, I. Aiello, F. Testa and M. Ghedini, *New J. Chem.*, 2011, **35**, 141–148.

(126) J. M. Fernandez-Hernandez, T. B. de Queiroz, H. Eckert, L. De Cola, A. S. S. de Camargo et al., *J. Mater. Chem.*, 2011, **21**, 8829–8834.

(127) U. M. Tefashe, K. L. Metera, H. F. Sleiman and J. Mauzeroll, *Langmuir*, 2013, **29**, 12866–12873.

(128) K. L. Metera, K. D. Hänni, G. Zhou, M. K. Nayak, H. S. Bazzi, D. Juncker and H. F. Sleiman, *ACS Macro Lett.*, 2012, **1**, 954–959.

(129) A.-H. Liang, K. Zhang, J. Zhang, F. Huang, X.-H. Zhu and Y. Cao, *Chem. Mater.*, 2013, **25**, 1013–1019.

(130) A.-h. Liang, S. Dong, K. Zhang, X. Xiao, F. Huang, X.-H. Zhu and Y. Cao, *Macromol. Rapid Commun.*, 2013, **34**, 1301–1305.

(131) A. M. Talarico, E. I. Szerb, T. F. Mastropietro, I. Aiello, A. Crispini and M. Ghedini, *Dalton Trans.*, 2012, **41**, 4919–4926.

(132) L. Donato, P. Abel and E. Zysman-Colman, *Dalton Trans.*, 2013, **42**, 8402–8412.

(133) J. M. Rawson, L. Donato and E. Zysman-Colman, *Cryst. Eng. Comm.*, 2014, **16**, 8531–8536.

(134) C. E. Welby, L. Gilmartin, R. R. Marriott, A. Zahid, C. R. Rice, E. A. Gibson and P. I. Elliott, *Dalton Trans.*, 2013, **42**, 13527–13536.

(135) S. Kammer, H. Müller, N. Grunwald, A. Bellin, A. Kelling, U. Schilde, W. Mickler, C. Dosche and H.-J. Holdt, *Eur. J. Inorg. Chem.*, 2006, **2006**, 1547–1551.

(136) S. Kammer, A. Kelling, H. Baier, W. Mickler, C. Dosche, K. Rurack, A. Kapp, F. Lisdat and H.-J. Holdt, *Eur. J. Inorg. Chem.*, 2009, **2009**, 4648–4659.

(137) S. Kammer, I. Starke, A. Pietrucha, A. Kelling, W. Mickler, U. Schilde, C. Dosche, E. Kleinpeter and H.-J. Holdt, *Dalton Trans.*, 2012, **41**, 10219–10227.

(138) L. Chen, Q. Chen, M. Wu, F. Jiang and M. Hong, *Acc. Chem. Res.*, 2014, **48**, 201–210.

(139) W. Wang, Y.-X. Wang and H.-B. Yang, *Chem. Soc. Rev.*, 2016, **45**, 2656–2693.

(140) P. J. Stang and B. Olenyuk, *Acc. Chem. Res.*, 1997, **30**, 502–518.

(141) S. Kitagawa, R. Kitaura and S.-i. Noro, *Angew. Chem. Int. Ed.*, 2004, **43**, 2334–2375.

(142) C. Wang, D. Liu, Z. Xie and W. Lin, *Inorg. Chem.*, 2014, **53**, 1331–1338.

(143) Z. Xie, L. Ma, K. E. deKrafft, A. Jin and W. Lin, *J. Am. Chem. Soc.*, 2009, **132**, 922–923.

(144) M.-L. Ho, Y.-A. Chen, T.-C. Chen, P.-J. Chang, Y.-P. Yu, K.-Y. Cheng, C.-H. Shih, G.-H. Lee and H.-S. Sheu, *Dalton Trans.*, 2012, **41**, 2592–2600.

(145) K.-Y. Cheng, J.-C. Wang, C.-Y. Lin, W.-R. Lin, Y.-A. Chen, F.-J. Tsai, Y.-C. Chuang, G.-Y. Lin, C.-W. Ni, Y.-T. Zeng et al., *Dalton Trans.*, 2014, **43**, 6536–6547.

(146) Y. Xu, L. Li, S. Zhang, S. Zhao and J. Luo, *Cryst. Growth Des.*, 2015, **16**, 406–411.

(147) L. Li, S. Zhang, L. Xu, J. Wang, L.-X. Shi, Z.-N. Chen, M. Hong and J. Luo, *Chem. Sci.*, 2014, **5**, 3808–3813.

(148) D. Zeng, M. Ren, S.-S. Bao, L. Li and L.-M. Zheng, *Chem. Commun.*, 2014, **50**, 8356–8359.

(149) N. M. Ali, V. L. MacLeod, P. Jennison, I. V. Sazanovich, C. A. Hunter, J. A. Weinstein and M. D. Ward, *Dalton Trans.*, 2012, **41**, 2408–2419.

(150) L. Li, S. Zhang, L. Xu, L. Han, Z.-N. Chen and J. Luo, *Inorg. Chem.*, 2013, **52**, 12323–12325.

(151) C. Wang, Z. Xie, K. E. deKrafft and W. Lin, *J. Am. Chem. Soc.*, 2011, **133**, 13445–13454.

(152) C. Wang, J.-L. Wang and W. Lin, *J. Am. Chem. Soc.*, 2012, **134**, 19895–19908.

(153) C. Wang, K. E. DeKrafft and W. Lin, *J. Am. Chem. Soc.*, 2012, **134**, 7211–7214.

(154) P. Contreras Carballada, N. Mourtzis, M. Felici, S. Bonnet, R. J. Nolte, R. M. Williams, L. De Cola and M. C. Feiters, *Eur. J. Org. Chem.*, 2012, **2012**, 6729–6736.

(155) N. Mourtzis, P. C. Carballada, M. Felici, R. J. Nolte, R. M. Williams, L. de Cola and M. C. Feiters, *Phys. Chem. Chem. Phys.*, 2011, **13**, 7903–7909.

(156) S.-L. Huang, N. Liu, Y. Ling and H.-K. Luo, *Chem. Asian J.*, 2017, **12**, 3110–3113.

(157) C. Bronner, S. A. Baudron and M. W. Hosseini, *Inorg. Chem.*, 2010, **49**, 8659–8661.

(158) C. Xu, A. Guenet, N. Kyritsakas, J.-M. Planeix and M. W. Hosseini, *Chem. Commun.*, 2015, **51**, 14785–14788.

(159) C. Xu, A. Guenet, N. Kyritsakas, J.-M. Planeix and M. W. Hosseini, *Inorg. Chem.*, 2015, **54**, 10429–10439.

(160) E. Baranoff, E. Orselli, L. Allouche, D. Di Censo, R. Scopelliti, M. Grätzel and M. K. Nazeeruddin, *Chem. Commun.*, 2011, **47**, 2799–2801.

(161) C.-T. Wang, L.-C. Shiu and K.-B. Shiu, *Chem. Eur. J.*, 2015, **21**, 7026–7029.

(162) O. Chepelin, J. Ujma, X. Wu, A. M. Slawin, M. B. Pitak, S. J. Coles, J. Michel, A. C. Jones, P. E. Barran and P. J. Lusby, *J. Am. Chem. Soc.*, 2012, **134**, 19334–19337.

(163) X. Li, J. Wu, C. He, R. Zhang and C. Duan, *Chem. Commun.*, 2016, **52**, 5104–5107.

(164) X. Li, J. Wu, L. Chen, X. Zhong, C. He, R. Zhang and C. Duan, *Chem. Commun.*, 2016, **52**, 9628–9631.

(165) C. D. Boone, S. Gill, A. Habibzadegan and R. McKenna, *Int. J. Chem. Eng.*, 2013, **2013**.

(166) V. E. Pritchard, D. Rota Martir, S. Oldknow, S. Kai, S. Hiraoka, N. J. Cookson, E. Zysman-Colman and M. J. Hardie, *Chem. Eur. J.*, 2017, **23**, 6290–6294.

(167) V. E. Pritchard, D. Rota Martir, E. Zysman-Colman and M. J. Hardie, *Chem. Eur. J.*, 2017, **23**, 8839–8849.

(168) S. Horiuchi, H. Tanaka, E. Sakuda, Y. Arikawa and K. Umakoshi, *Chem. Eur. J.*, 2016, **22**, 17533–17537.

(169) L. R. Alrawashdeh, A. I. Day and L. Wallace, *Dalton Trans.*, 2013, **42**, 16478–16481.

(170) C. Xu, D. Mochizuki, Y. Hashimoto, T. Honda, Y. Tsukahara, T. Yamauchi and Y. Wada, *Eur. J. Inorg. Chem.*, 2012, **2012**, 3113–3120.

(171) C. Xu, D. Mochizuki, M. M. Maitani and Y. Wada, *Eur. J. Inorg. Chem.*, 2014, **2014**, 1470–1476.

(172) M. Waki, N. Mizoshita, T. Tani and S. Inagaki, *Angew. Chem. Int. Ed.*, 2011, **50**, 11667–11671.

(173) M. Waki, Y. Maegawa, K. Hara, Y. Goto, S. Shirai, Y. Yamada, N. Mizoshita, T. Tani, W.-J. Chun, S. Muratsugu et al., *J. Am. Chem. Soc.*, 2014, **136**, 4003–4011.

(174) W. J. Finkenzeller and H. Yersin, *Chem. Phys. Lett.*, 2003, **377**, 299–305.

(175) D. Mochizuki, M. Sugiyama, M. M. Maitani and Y. Wada, *Eur. J. Inorg. Chem.*, 2013, **2013**, 2324–2329.

(176) C.-Y. Sun, X.-L. Wang, X. Zhang, C. Qin, P. Li, Z.-M. Su, D.-X. Zhu, G.-G. Shan, K.-Z. Shao, H. Wu et al., *Nat. Commun.*, 2013, **4**, 2717–2724.

(177) Y. Sun, Z. Chen, E. Puodziukynaite, D. M. Jenkins, J. R. Reynolds and K. S. Schanze, *Macromolecules*, 2012, **45**, 2632–2642.

(178) J. E. Beves, E. C. Constable, S. Decurtins, E. L. Dunphy, C. E. Housecroft, T. D. Keene, M. Neuburger and S. Schaffner, *Cryst. Eng. Comm.*, 2008, **10**, 986–990.

(179) J. E. Beves, E. C. Constable, C. E. Housecroft, C. J. Kepert and D. J. Price, *Cryst. Eng. Comm.*, 2007, **9**, 456–459.

(180) W. Sun, S. Li, B. Häupler, J. Liu, S. Jin, W. Steffen, U. S. Schubert, H.-J. Butt, X.-J. Liang and S. Wu, *Adv. Mater.*, 2017, **29**, 1603702–1603708.

(181) C. Friebe, H. Görls, M. Jäger and U. S. Schubert, *Eur. J. Inorg. Chem.*, 2013, **2013**, 4191–4202.

(182) C. A. Kent, D. Liu, L. Ma, J. M. Papanikolas, T. J. Meyer and W. Lin, *J. Am. Chem. Soc.*, 2011, **133**, 12940–12943.

(183) W. A. Maza, R. Padilla and A. J. Morris, *J. Am. Chem. Soc.*, 2015, **137**, 8161–8168.

(184) W. Zhang, B. Li, H. Ma, L. Zhang, Y. Guan, Y. Zhang, X. Zhang, P. Jing and S. Yue, *ACS Appl. Mater. Interfaces*, 2016, **8**, 21465–21471.

(185) R. Chen, J. Zhang, J. Chelora, Y. Xiong, S. V. Kershaw, K. F. Li, P.-K. Lo, K. W. Cheah, A. L. Rogach, J. A. Zapien et al., *ACS Appl. Mater. Interfaces*, 2017, **9**, 5699–5708.

(186) S. Zhang, L. Li, S. Zhao, Z. Sun and J. Luo, *Inorg. Chem.*, 2015, **54**, 8375–8379.

(187) W. Zhang, M. Kauer, O. Halbherr, K. Epp, P. Guo, M. I. Gonzalez, D. J. Xiao, C. Wiktor, L. i Xamena, X. Francesc et al., *Chem. Eur. J.*, 2016, **22**, 14297–14307.

(188) G. R. Newkome, T. J. Cho, C. N. Moorefield, P. P. Mohapatra and L. A. GodÌnez, *Chem. Eur. J.*, 2004, **10**, 1493–1500.

(189) A. Schultz, X. Li, B. Barkakaty, C. N. Moorefield, C. Wesdemiotis and G. R. Newkome, *J. Am. Chem. Soc.*, 2012, **134**, 7672–7675.

(190) J. R. Piper, L. Cletheroe, C. G. Taylor, A. J. Metherell, J. A. Weinstein, I. V. Sazanovich and M. D. Ward, *Chem. Commun.*, 2017, **53**, 408–411.

(191) T. R. Cook, V. Vajpayee, M. H. Lee, P. J. Stang and K.-W. Chi, *Acc. Chem. Res.*, 2013, **46**, 2464–2474.

(192) Y.-F. Han, W.-G. Jia, W.-B. Yu and G.-X. Jin, *Chem. Soc. Rev.*, 2009, **38**, 3419–3434.

(193) M. Wang, V. Vajpayee, S. Shanmugaraju, Y.-R. Zheng, Z. Zhao, H. Kim, P. S. Mukherjee, K.-W. Chi and P. J. Stang, *Inorg. Chem.*, 2011, **50**, 1506–1512.

(194) N. P. Barry, O. Zava, W. Wu, J. Zhao and B. Therrien, *Inorg. Chem. Commun.*, 2012, **18**, 25–28.

(195) J. Y. Ryu, J. M. Lee, Y. J. Park, N. V. Nghia, M. H. Lee and J. Lee, *Organometallics*, 2013, **32**, 7272–7274.

(196) J. Y. Ryu, Y. J. Park, H.-R. Park, M. L. Saha, P. J. Stang and J. Lee, *J. Am. Chem. Soc.*, 2015, **137**, 13018–13023.

(197) J. Y. Ryu, E. H. Wi, M. Pait, S. Lee, P. J. Stang and J. Lee, *Inorg. Chem.*, 2017, **56**, 5471–5477.

(198) T.-Z. Xie, S.-Y. Liao, K. Guo, X. Lu, X. Dong, M. Huang, C. N. Moorefield, S. Z. Cheng, X. Liu, C. Wesdemiotis et al., *J. Am. Chem. Soc.*, 2014, **136**, 8165–8168.

(199) C. Shen, A. D. Kennedy, W. A. Donald, A. M. Torres, W. S. Price and J. E. Beves, *Inorganica Chim. Acta*, 2017, **458**, 122–128.

(200) C. E. Hauke, A. N. Oldacre, C. R. P. Fulong, A. E. Friedman and T. R. Cook, *Inorg. Chem.*, 2017, **57**, 3587–3595.

(201) K. Li, L.-Y. Zhang, C. Yan, S.-C. Wei, M. Pan, L. Zhang and C.-Y. Su, *J. Am. Chem. Soc.*, 2014, **136**, 4456–4459.

(202) K. Wu, K. Li, Y.-J. Hou, M. Pan, L.-Y. Zhang, L. Chen and C.-Y. Su, *Nat. Commun.*, 2016, **7**, 10487–10497.

(203) M. Yoshizawa, J. K. Klosterman and M. Fujita, *Angew. Chem. Int. Ed.*, 2009, **48**, 3418–3438.

(204) M. Yoshizawa, Y. Takeyama, T. Okano and M. Fujita, *J. Am. Chem. Soc.*, 2003, **125**, 3243–3247.

(205) Y. Nishioka, T. Yamaguchi, M. Yoshizawa and M. Fujita, *J. Am. Chem. Soc.*, 2007, **129**, 7000–7001.

(206) S. Karthikeyan and V. Ramamurthy, *J. Org. Chem.*, 2006, **71**, 6409–6413.

(207) M. Yoshizawa and M. Fujita, *Pure Appl. Chem.*, 2005, **77**, 1107–1112.

(208) M. Yoshizawa, S. Miyagi, M. Kawano, K. Ishiguro and M. Fujita, *J. Am. Chem. Soc.*, 2004, **126**, 9172–9173.

(209) J. D. Blakemore, R. H. Crabtree and G. W. Brudvig, *Chem. Rev.*, 2015, **115**, 12974–13005.

(210) S. Rau, B. Schäfer, D. Gleich, E. Anders, M. Rudolph, M. Friedrich, H. Görls, W. Henry and J. G. Vos, *Angew. Chem. Int. Ed.*, 2006, **45**, 6215–6218.

(211) H. Ozawa and K. Sakai, *Chem. Commun.*, 2011, **47**, 2227–2242.

(212) M. Hirahara, S. Masaoka and K. Sakai, *Dalton Trans.*, 2011, **40**, 3967–3978.

(213) T. A. White, S. L. Higgins, S. M. Arachchige and K. J. Brewer, *Angew. Chem. Int. Ed.*, 2011, **50**, 12209–12213.

(214) M. Elvington, J. Brown, S. M. Arachchige and K. J. Brewer, *J. Am. Chem. Soc.*, 2007, **129**, 10644–10645.

(215) H. Ozawa, M. Kobayashi, B. Balan, S. Masaoka and K. Sakai, *Chem. Asian J.*, 2010, **5**, 1860–1869.

(216) G. Ajayakumar, M. Kobayashi, S. Masaoka and K. Sakai, *Dalton Trans.*, 2011, **40**, 3955–3966.

(217) S. Chen, K. Li, F. Zhao, L. Zhang, M. Pan, Y.-Z. Fan, J. Guo, J. Shi and C.-Y. Su, *Nat. Commun.*, 2016, **7**, 13169–13177.

(218) J. Yang, M. Bhadbhade, W. A. Donald, H. Iranmanesh, E. G. Moore, H. Yan and J. E. Beves, *Chem. Commun.*, 2015, **51**, 4465–4468.

(219) E. G. Moore, M. Benaglia, G. Bergamini and P. Ceroni, *Eur. J. Inorg. Chem.*, 2015, **2015**, 414–420.

(220) A. B. Elliott, J. E. Lewis, H. van der Salm, C. J. McAdam, J. D. Crowley and K. C. Gordon, *Inorg. Chem.*, 2016, **55**, 3440–3447.

(221) J. E. Lewis, A. B. Elliott, C. J. McAdam, K. C. Gordon and J. D. Crowley, *Chem. Sci.*, 2014, **5**, 1833–1843.

(222) A. Schmidt, M. Hollering, J. Han, A. Casini and F. E. Kühn, *Dalton Trans.*, 2016, **45**, 12297–12300.

(223) J. G. Williams, S. Develay, D. L. Rochester and L. Murphy, *Coord. Chem. Rev.*, 2008, **252**, 2596–2611.

(224) H. Yersin and D. Braun, *Coord. Chem. Rev.*, 1991, **111**, 39–46.

(225) I. M. Dixon, J.-P. Collin, J.-P. Sauvage, L. Flamigni, S. Encinas and F. Barigelletti, *Chem. Soc. Rev.*, 2000, **29**, 385–391.

(226) C. K. Prier, D. A. Rankic and D. W. MacMillan, *Chem. Rev.*, 2013, **113**, 5322–5363.

(227) V. Sathish, A. Ramdass, M. Velayudham, K.-L. Lu, P. Thanasekaran and S. Rajagopal, *Dalton Trans.*, 2017, **46**, 16738–16769.

(228) X. He and V. W.-W. Yam, *Coord. Chem. Rev.*, 2011, **255**, 2111–2123.

(229) K. L. Haas and K. J. Franz, *Chem. Rev.*, 2009, **109**, 4921–4960.

(230) L. Neij, E. Heiskanen and L. Strupeit, *Energy Policy*, 2017, **101**, 274–283.

(231) N. DeForest, A. Shehabi, S. Selkowitz and D. J. Milliron, *Appl. Energy*, 2017, **192**, 95–109.

(232) K. Knoop and S. Lechtenböhmer, *Renew. Sustain. Energy Rev.*, 2017, **68**, 1097–1105.

(233) J. Y. Tsao, J. J. Wierer Jr, L. E. Rohwer, M. E. Coltrin, M. H. Crawford, J. A. Simmons, P.-C. Hung, H. Saunders, D. S. Sizov, R. Bhat et al., in *III-Nitride Based Light Emitting Diodes and Applications*, Springer, 2017, pp. 11–28.

(234) I. Chew, D. Karunatilaka, C. P. Tan and V. Kalavally, *Energy and Buildings*, 2017, **149**, 180–191.

(235) A. De Almeida, B. Santos, B. Paolo and M. Quicheron, *Renew. Sustain. Energy Rev.*, 2014, **34**, 30–48.

(236) Z. C. Feng, *Handbook of Solid-State Lighting and LEDs*, CRC Press, 2017.

(237) J. Y. Tsao, M. H. Crawford, M. E. Coltrin, A. J. Fischer, D. D. Koleske, G. S. Subramania, G. T. Wang, J. J. Wierer and R. F. Karlicek, *Adv. Opt. Mater.*, 2014, **2**, 809–836.

(238) M. Crawford, J. Wierer, A. Fischer, G. Wang, D. Koleske, G. Subramania, M. Coltrin, J. Tsao and R. Karlicek, *Solid-State Lighting: Toward Smart and Ultra-Efficient Materials, Devices, Lamps and Systems*, Wiley: New York, 2014, vol. 3, pp. 12–34.

(239) M. H. Crawford, J. Y. Tsao, D. Koleske, J. Wierer, A. J. Fischer, W. W. Chow, G. T. Wang, A. Armstrong, S. R. Lee and M. E. Coltrin, *Pathways to Ultra-Efficient Solid-State Lighting*, tech. rep., Sandia National Laboratories (SNL-NM), Albuquerque, NM (United States), 2015.

(240) R. Ferrini, O. Fernandez, S. Junger, K. Keränen, L. Barruetabeña, A. von Mühlenen and T. Dreyfus, *Large Area Intelligent Efficient High Quality Solid-state Lighting*, 2016, pp. 1–3.

(241) M. S. Shur and R. Zukauskas, *Proceedings of the IEEE*, 2005, **93**, 1691–1703.

(242) S. Reineke, *Nat. Mater.*, 2015, **14**, 459–462.

(243) J. Meyer and F. Tappe, *Adv. Opt. Mater.*, 2015, **3**, 424–430.

(244) M. H. Crawford, *IEEE J. Sel. Top. Quantum Electron.*, 2009, **15**, 1028–1040.

(245) C. J. Humphreys, *MRS Bulletin*, 2008, **33**, 459–470.

(246) C. W. Tang and S. A. VanSlyke, *Appl. Phys. Lett.*, 1987, **51**, 913–915.

(247) J. Burroughes, D. Bradley, A. Brown, R. Marks, K. Mackay, R. Friend, P. Burns and A. Holmes, *Nature*, 1990, **347**, 539–541.

(248) D. Fyfe, *Nat. Photonics*, 2009, **3**, 453–455.

(249) Z. R. Li, *Organic light-emitting materials and devices*, CRC press, 2015.

(250) M. Zhu and C. Yang, *Chem. Soc. Rev.*, 2013, **42**, 4963–4976.

(251) C. Bizzarri, E. Spuling, D. M. Knoll, D. Volz and S. Bräse, *Coord. Chem. Rev.*, 2017, **In Press**.

(252) D. Y. Kondakov, *J. Soc. Inf. Display*, 2009, **17**, 137–144.

(253) C. Adachi, M. A. Baldo, M. E. Thompson and S. R. Forrest, *J. Appl. Phys.*, 2001, **90**, 5048–5051.

(254) R. D. Costa, E. Ortı, H. J. Bolink, F. Monti, G. Accorsi and N. Armaroli, *Angew. Chem. Int. Ed.*, 2012, **51**, 8178–8211.

(255) H. Yersin, *Transition metal and rare earth compounds III: excited states, transitions, interactions*, Springer Science & Business Media, 2004, vol. 3.

(256) S. B. Meier, D. Tordera, A. Pertegas, C. Roldan-Carmona, E. Ortı and H. J. Bolink, *Mater. Today*, 2014, **17**, 217–223.

(257) J. D. Slinker, A. A. Gorodetsky, M. S. Lowry, J. Wang, S. Parker, R. Rohl, S. Bernhard and G. G. Malliaras, *J. Am. Chem. Soc.*, 2004, **126**, 2763–2767.

(258) T. Hu, L. He, L. Duan and Y. Qiu, *J. Mater. Chem.*, 2012, **22**, 4206–4215.

(259) S. Ladouceur, K. N. Swanick, S. Gallagher-Duval, Z. Ding and E. Zysman-Colman, *Eur. J. Inorg. Chem.*, 2013, **2013**, 5329–5343.

(260) Y. You and S. Y. Park, *Dalton Trans.*, 2009, 1267–1282.

(261) A. B. Tamayo, S. Garon, T. Sajoto, P. I. Djurovich, I. M. Tsyba, R. Bau and M. E. Thompson, *Inorg. Chem.*, 2005, **44**, 8723–8732.

(262) M. Helms, Z. Lin, L. Gong, K. Harms and E. Meggers, *Eur. J. Inorg. Chem.*, 2013, **2013**, 4164–4172.

(263) P. Göbel, F. Ritterbusch, M. Helms, M. Bischof, K. Harms, M. Jung and E. Meggers, *Eur. J. Inorg. Chem.*, 2015, **2015**, 1654–1659.

(264) G. Mazzeo, M. Fusè, G. Longhi, I. Rimoldi, E. Cesarotti, A. Crispini and S. Abbate, *Dalton Trans.*, 2016, **45**, 992–999.

(265) X. Chen, Y. Okamoto, T. Yano and J. Otsuki, *J. Sep. Sci.*, 2007, **30**, 713–716.

(266) E. Meggers, *Chem. Eur. J.*, 2010, **16**, 752–758.

(267) L. Yang, A. von Zelewsky, H. P. Nguyen, G. Muller, G. Labat and H. Stoeckli-Evans, *Inorganica Chim. Acta*, 2009, **362**, 3853–3856.

(268) C. Schaffner-Hamann, A. von Zelewsky, A. Barbieri, F. Barigelletti, G. Muller, J. P. Riehl and A. Neels, *J. Am. Chem. Soc.*, 2004, **126**, 9339–9348.

(269) A. Auffrant, A. Barbieri, F. Barigelletti, J. Lacour, P. Mobian, J.-P. Collin, J.-P. Sauvage and B. Ventura, *Inorg. Chem.*, 2007, **46**, 6911–6919.

(270) S. E. Howson, L. E. Allan, N. P. Chmel, G. J. Clarkson, R. J. Deeth, A. D. Faulkner, D. H. Simpson and P. Scott, *Dalton Trans.*, 2011, **40**, 10416–10433.

(271) C. Citti, U. M. Battisti, G. Ciccarella, V. Maiorano, G. Gigli, S. Abbate, G. Mazzeo, E. Castiglioni, G. Longhi and G. Cannazza, *J. Chromatogr. A*, 2016, **1467**, 335–346.

(272) F. J. Coughlin, M. S. Westrol, K. D. Oyler, N. Byrne, C. Kraml, E. Zysman-Colman, M. S. Lowry and S. Bernhard, *Inorg. Chem.*, 2008, **47**, 2039–2048.

(273) N. C. Fletcher, P. C. Junk, D. A. Reitsma and F. R. Keene, *J. Chem. Soc., Dalton Trans.*, 1998, 133–138.

(274) N. C. Fletcher, C. Martin and H. J. Abraham, *New J. Chem.*, 2007, **31**, 1407–1411.

(275) E. Marchi, R. Sinisi, G. Bergamini, M. Tragni, M. Monari, M. Bandini and P. Ceroni, *Chem. Eur. J.*, 2012, **18**, 8765–8773.

(276) M. Helms, C. Wang, B. Orth, K. Harms and E. Meggers, *Eur. J. Inorg. Chem.*, 2016, **2016**, 2896–2901.

(277) V. N. Kozhevnikov, Y. Zheng, M. Clough, H. A. Al-Attar, G. C. Griffiths, K. Abdullah, S. Raisys, V. Jankus, M. R. Bryce and A. P. Monkman, *Chem. Mater.*, 2013, **25**, 2352–2358.

(278) D. R. Martir, A. K. Bansal, V. Di Mascio, D. B. Cordes, A. F. Henwood, A. M. Slawin, P. C. Kamer, L. Martınez-Sarti, A. Pertegás, H. J. Bolink et al., *Inorg. Chem. Front.*, 2016, **3**, 218–235.

(279) C. Zhong, C. Duan, F. Huang, H. Wu and Y. Cao, *Chem. Mater.*, 2011, **23**, 326–340.

(280) A. F. Henwood, A. K. Bansal, D. B. Cordes, A. M. Slawin, I. D. Samuel and E. Zysman-Colman, *J. Mater. Chem. C*, 2016, **4**, 3726–3737.

(281) N. Miyaura, T. Yanagi and A. Suzuki, *Synth. Commun.*, 1981, **11**, 513–519.

(282) N. Miyaura and A. Suzuki, *Chem. Rev.*, 1995, **95**, 2457–2483.

(283) M. Nonoyama, *Bull. Chem. Soc. Jpn.*, 1974, **47**, 767–768.

(284) S. Ladouceur, D. Fortin and E. Zysman-Colman, *Inorg. Chem.*, 2010, **49**, 5625–5641.

(285) D. Tordera, M. Delgado, E. Ortı, H. J. Bolink, J. Frey, M. K. Nazeeruddin and E. Baranoff, *Chem. Mater.*, 2012, **24**, 1896–1903.

(286) C. Ulbricht, B. Beyer, C. Friebe, A. Winter and U. S. Schubert, *Adv. Mater.*, 2009, **21**, 4418–4441.

(287) W. Melhuish, *J. Phys. Chem.*, 1961, **65**, 229–235.

(288) S. T. Parker, J. D. Slinker, M. S. Lowry, M. P. Cox, S. Bernhard and G. G. Malliaras, *Chem. Mater.*, 2005, **17**, 3187–3190.

(289) E. Zysman-Colman, J. D. Slinker, J. B. Parker, G. G. Malliaras and S. Bernhard, *Chem. Mater.*, 2007, **20**, 388–396.

(290) F. AlTal and J. Gao, *Org. Electron.*, 2015, **18**, 1–7.

(291) G. E. Schneider, A. Pertegás, E. C. Constable, C. E. Housecroft, N. Hostettler, C. D. Morris, J. A. Zampese, H. J. Bolink, J. M. Junquera-Hernández, E. Ortı et al., *J. Mater. Chem. C*, 2014, **2**, 7047–7055.

(292) D. Tordera, A. Pertegás, N. M. Shavaleev, R. Scopelliti, E. Ortı, H. J. Bolink, E. Baranoff, M. Grätzel and M. K. Nazeeruddin, *J. Mater. Chem.*, 2012, **22**, 19264–19268.

(293) A. M. Bünzli, E. C. Constable, C. E. Housecroft, A. Prescimone, J. A. Zampese, G. Longo, L. Gil-Escrig, A. Pertegás, E. Ortı and H. J. Bolink, *Chem. Sci.*, 2015, **6**, 2843–2852.

(294) R. Chakrabarty, P. S. Mukherjee and P. J. Stang, *Chem. Rev.*, 2011, **111**, 6810–6918.

(295) T. R. Cook, Y.-R. Zheng and P. J. Stang, *Chem. Rev.*, 2012, **113**, 734–777.

(296) J.-M. Lehn, A. Rigault, J. Siegel, J. Harrowfield, B. Chevrier and D. Moras, *Proc. Natl. Acad. Sci. U.S.A*, 1987, **84**, 2565–2569.

(297) S. R. Seidel and P. J. Stang, *Acc. Chem. Res.*, 2002, **35**, 972–983.

(298) Q.-F. Sun, J. Iwasa, D. Ogawa, Y. Ishido, S. Sato, T. Ozeki, Y. Sei, K. Yamaguchi and M. Fujita, *Science*, 2010, **328**, 1144–1147.

(299) M. Yoneya, T. Yamaguchi, S. Sato and M. Fujita, *J. Am. Chem. Soc.*, 2012, **134**, 14401–14407.

(300) D. L. Caulder and K. N. Raymond, *Acc. Chem. Res.*, 1999, **32**, 975–982.

(301) S. M. Biros, R. M. Yeh and K. N. Raymond, *Angew. Chem. Int. Ed.*, 2008, **47**, 6062–6064.

(302) J.-L. Wang, X. Li, X. Lu, I.-F. Hsieh, Y. Cao, C. N. Moorefield, C. Wesdemiotis, S. Z. Cheng and G. R. Newkome, *J. Am. Chem. Soc.*, 2011, **133**, 11450–11453.

(303) Y.-T. Chan, X. Li, M. Soler, J.-L. Wang, C. Wesdemiotis and G. R. Newkome, *J. Am. Chem. Soc.*, 2009, **131**, 16395–16397.

(304) J. Heo, Y.-M. Jeon and C. A. Mirkin, *J. Am. Chem. Soc.*, 2007, **129**, 7712–7713.

(305) R. A. Bilbeisi, J. K. Clegg, N. Elgrishi, X. d. Hatten, M. Devillard, B. Breiner, P. Mal and J. R. Nitschke, *J. Am. Chem. Soc.*, 2011, **134**, 5110–5119.

(306) S. Mukherjee and P. S. Mukherjee, *Chem. Commun.*, 2014, **50**, 2239–2248.

(307) C.-C. You and F. Würthner, *J. Am. Chem. Soc.*, 2003, **125**, 9716–9725.

(308) M. Fujita, D. Oguro, M. Miyazawa, H. Oka, K. Yamaguchi and K. Ogura, *Nature*, 1995, **378**, 469–471.

(309) D. Preston, S. M. McNeill, J. E. Lewis, G. I. Giles and J. D. Crowley, *Dalton Trans.*, 2016, **45**, 8050–8060.

(310) D. K. Chand, K. Biradha, M. Fujita, S. Sakamoto and K. Yamaguchi, *Chem. Commun.*, 2002, 2486–2487.

(311) M. D. Ward and P. R. Raithby, *Chem. Soc. Rev.*, 2013, **42**, 1619–1636.

(312) M. Han, D. M. Engelhard and G. H. Clever, *Chem. Soc. Rev.*, 2014, **43**, 1848–1860.

(313) H. Amouri, C. Desmarets and J. Moussa, *Chem. Rev.*, 2012, **112**, 2015–2041.

(314) S. Zarra, D. M. Wood, D. A. Roberts and J. R. Nitschke, *Chem. Soc. Rev.*, 2015, **44**, 419–432.

(315) I. A. Riddell, M. M. Smulders, J. K. Clegg and J. R. Nitschke, *Chem. Commun.*, 2011, **47**, 457–459.

(316) A. Ahmedova, R. Mihaylova, D. Momekova, P. Shestakova, S. Stoykova, J. Zaharieva, M. Yamashina, G. Momekov, M. Akita and M. Yoshizawa, *Dalton Trans.*, 2016, **45**, 13214–13221.

(317) A. Mishra, S. Chang Lee, N. Kaushik, T. R. Cook, E. H. Choi, N. Kumar Kaushik, P. J. Stang and K.-W. Chi, *Chem. Eur. J.*, 2014, **20**, 14410–14420.

(318) P. P. Neelakandan, A. Jiménez and J. R. Nitschke, *Chem. Sci.*, 2014, **5**, 908–915.

(319) D. P. August, G. S. Nichol and P. J. Lusby, *Angew. Chem. Int. Ed.*, 2016, **55**, 15022–15026.

(320) A. Schmidt, A. Casini and F. E. Kühn, *Coord. Chem. Rev.*, 2014, **275**, 19–36.

(321) H.-B. Yang, K. Ghosh, Y. Zhao, B. H. Northrop, M. M. Lyndon, D. C. Muddiman, H. S. White and P. J. Stang, *J. Am. Chem. Soc.*, 2008, **130**, 839–841.

(322) H.-B. Yang, K. Ghosh, B. H. Northrop, Y.-R. Zheng, M. M. Lyndon, D. C. Muddiman and P. J. Stang, *J. Am. Chem. Soc.*, 2007, **129**, 14187–14189.

(323) X. Yan, B. Jiang, T. R. Cook, Y. Zhang, J. Li, Y. Yu, F. Huang, H.-B. Yang and P. J. Stang, *J. Am. Chem. Soc.*, 2013, **135**, 16813–16816.

(324) C. Gütz, R. Hovorka, C. Klein, Q.-Q. Jiang, C. Bannwarth, M. Engeser, C. Schmuck, W. Assenmacher, W. Mader, F. Topić et al., *Angew. Chem. Int. Ed.*, 2014, **53**, 1693–1698.

(325) K. Yazaki, S. Noda, Y. Tanaka, Y. Sei, M. Akita and M. Yoshizawa, *Angew. Chem. Int. Ed.*, 2016, **55**, 15031–15034.

(326) M. Krick, J. Holstein, C. Würtele and G. H. Clever, *Chem. Commun.*, 2016, **52**, 10411–10414.

(327) P. D. Frischmann, V. Kunz and F. Würthner, *Angew. Chem. Int. Ed.*, 2015, **127**, 7393–7397.

(328) Z. Li, N. Kishi, K. Hasegawa, M. Akita and M. Yoshizawa, *Chem. Commun.*, 2011, **47**, 8605–8607.

(329) A. Shi, M. R. Pokhrel and S. H. Bossmann, *Synthesis*, 2007, **2007**, 505–514.

(330) B. H. Northrop, Y.-R. Zheng, K.-W. Chi and P. J. Stang, *Acc. Chem. Res.*, 2009, **42**, 1554–1563.

(331) J.-R. Li and H.-C. Zhou, *Angew. Chem. Int. Ed.*, 2009, **121**, 8617–8620.

(332) Q.-F. Sun, S. Sato and M. Fujita, *Angew. Chem. Int. Ed.*, 2014, **53**, 13510–13513.

(333) C. Klein, C. Gütz, M. Bogner, F. Topić, K. Rissanen and A. Lützen, *Angew. Chem. Int. Ed.*, 2014, **53**, 3739–3742.

(334) K. Miki, G. Yoshida, Y. Kai, N. Yasuoka and N. Kasai, *J. Organomet. Chem.*, 1978, **149**, 195–208.

(335) K. Suzuki, M. Kawano and M. Fujita, *Angew. Chem. Int. Ed.*, 2007, **119**, 2877–2880.

(336) D. K. Chand, M. Fujita, K. Biradha, S. Sakamoto and K. Yamaguchi, *Dalton Trans.*, 2003, 2750–2756.

(337) W. M. Bloch, Y. Abe, J. J. Holstein, C. M. Wandtke, B. Dittrich and G. H. Clever, *J. Am. Chem. Soc.*, 2016, **138**, 13750–13755.

(338) P. Coppo, M. Duati, V. N. Kozhevnikov, J. W. Hofstraat and L. De Cola, *Angew. Chem. Int. Ed.*, 2005, **117**, 1840–1844.

(339) D. C. Di, S. Fantacci, F. A. De, C. Klein, N. Evans, K. Kalyanasundaram, H. Bolink, M. Grätzel and M. Nazeeruddin, *Inorg. Chem.*, 2008, **47**, 980–989.

(340) G. Szalóki, V. Croué, M. Allain, S. Goeb and M. Sallé, *Chem. Commun.*, 2016, **52**, 10012–10015.

(341) A. D. Kirk and C. Namasivayam, *J. Phys. Chem.*, 1989, **93**, 5488–5492.

(342) M. Biner, H. Buergi, A. Ludi and C. Röhr, *J. Am. Chem. Soc.*, 1992, **114**, 5197–5203.

(343) A. Prodi, M. T. Indelli, C. J. Kleverlaan, E. Alessio and F. Scandola, *Coord. Chem. Rev.*, 2002, **229**, 51–58.

(344) F. D'Souza, E. Maligaspe, K. Ohkubo, M. E. Zandler, N. K. Subbaiyan and S. Fukuzumi, *J. Am. Chem. Soc.*, 2009, **131**, 8787–8797.

(345) L. Yu, K. Muthukumaran, I. V. Sazanovich, C. Kirmaier, E. Hindin, J. R. Diers, P. D. Boyle, D. F. Bocian, D. Holten and J. S. Lindsey, *Inorg. Chem.*, 2003, **42**, 6629–6647.

(346) L. Flamigni, G. Marconi, I. M. Dixon, J.-P. Collin and J.-P. Sauvage, *J. Phys. Chem. B*, 2002, **106**, 6663–6671.

(347) F. Ito, Y. Ishibashi, S. R. Khan, H. Miyasaka, K. Kameyama, M. Morisue, A. Satake, K. Ogawa and Y. Kobuke, *J. Phys. Chem. A*, 2006, **110**, 12734–12742.

(348) B. Ventura, A. Barbieri, A. Degli Esposti, J. B. Seneclauze and R. Ziessel, *Inorg. Chem.*, 2012, **51**, 2832–2840.

(349) J. Osıo Barcina, N. Herrero-Garcıa, F. Cucinotta, L. De Cola, P. Contreras-Carballada, R. M. Williams and A. Guerrero-Martınez, *Chem. Eur. J.*, 2010, **16**, 6033–6040.

(350) R. A. Haycock, A. Yartsev, U. Michelsen, V. Sundström and C. A. Hunter, *Angew. Chem. Int. Ed.*, 2000, **112**, 3762–3765.

(351) M. D. Ward, *Chem. Soc. Rev.*, 1997, **26**, 365–375.

(352) D. Kim and E.-J. Shin, *Bull. Korean Chem. Soc.*, 2003, **24**, 1490–1494.

(353) J. L. Sessler, C. T. Brown, D. O'Connor, S. L. Springs, R. Wang, M. Sathiosatham and T. Hirose, *J. Org. Chem.*, 1998, **63**, 7370–7374.

(354) J. Otsuki, T. Akasaka and K. Araki, *Coord. Chem. Rev.*, 2008, **252**, 32–56.

(355) A. F. Nogueira, L. F. O. Furtado, A. L. Formiga, M. Nakamura, K. Araki and H. E. Toma, *Inorg. Chem.*, 2004, **43**, 396–398.

(356) D. E. Williams, J. A. Rietman, J. M. Maier, R. Tan, A. B. Greytak, M. D. Smith, J. A. Krause and N. B. Shustova, *J. Am. Chem. Soc.*, 2014, **136**, 11886–11889.

(357) A. Gabrielsson, F. Hartl, H. Zhang, J. R. Lindsay Smith, M. Towrie, A. Vlček and R. N. Perutz, *J. Am. Chem. Soc.*, 2006, **128**, 4253–4266.

(358) A. Harriman, M. Hissler, O. Trompette and R. Ziessel, *J. Am. Chem. Soc.*, 1999, **121**, 2516–2525.

(359) A. M. Soliman, M. Abdelhameed, E. Zysman-Colman and P. D. Harvey, *Chem. Commun.*, 2013, **49**, 5544–5546.

(360) D. LeGourriérec, M. Andersson, J. Davidsson, E. Mukhtar, L. Sun and L. Hammarström, *J. Phys. Chem. A*, 1999, **103**, 557–559.

(361) J.-P. Collin, A. Harriman, V. Heitz, F. Odobel and J.-P. Sauvage, *J. Am. Chem. Soc.*, 1994, **116**, 5679–5690.

(362) L. Flamigni, N. Armaroli, F. Barigelletti, V. Balzani, J.-P. Collin, J.-O. Dalbavie, V. Heitz and J.-P. Sauvage, *J. Phys. Chem. B*, 1997, **101**, 5936–5943.

(363) T. J. Meyer, *Acc. Chem. Res.*, 1989, **22**, 163–170.

(364) Y. Qin and Q. Peng, *Int. J. Photoenergy*, 2012, **2012**, 1–21.

(365) A. Satake and Y. Kobuke, *Tetrahedron*, 2005, **61**, 13–41.

(366) F. D'Souza, S. Gadde, M. E. Zandler, M. Itou, Y. Araki and O. Ito, *Chem. Commun.*, 2004, 2276–2277.

(367) P. Mendes, *Bioinformatics*, 1993, **9**, 563–571.

(368) P. Mendes and D. Kell, *Bioinformatics*, 1998, **14**, 869–883.

(369) P. Sobolev, V. Andreev and T. Ekimova, *Russ. J. Gen. Chem.*, 2014, **84**, 1399–1403.

(370) A. L. Litvinov, D. V. Konarev, A. Y. Kovalevsky, I. S. Neretin, P. Coppens and R. N. Lyubovskaya, *Cryst. Growth Des.*, 2005, **5**, 1807–1819.

(371) J. C. Manton, C. Long, J. G. Vos and M. T. Pryce, *Dalton Trans.*, 2014, **43**, 3576–3583.

(372) P. C. Ray and Z. Sainudeen, *J. Phys. Chem. A*, 2006, **110**, 12342–12347.

(373) E. Collini, C. Ferrante and R. Bozio, *J. Phys. Chem. C*, 2007, **111**, 18636–18645.

(374) V. A. Walters, J. C. de Paula, B. Jackson, C. Nutaitis, K. Hall, J. Lind, K. Cardozo, K. Chandran, D. Raible and C. M. Phillips, *J. Phys. Chem.*, 1995, **99**, 1166–1171.

(375) N. G. Connelly and W. E. Geiger, *Chem. Rev.*, 1996, **96**, 877–910.

(376) C.-W. Huang, K. Y. Chiu and S.-H. Cheng, *Dalton Trans.*, 2005, 2417–2422.

(377) F. D'Souza, Y.-Y. Hsieh and G. R. Deviprasad, *Inorg. Chem.*, 1996, **35**, 5747–5749.

(378) N. M. Shavaleev, G. Xie, S. Varghese, D. B. Cordes, A. M. Slawin, C. Momblona, E. Ortı, H. J. Bolink, I. D. Samuel and E. Zysman-Colman, *Inorg. Chem.*, 2015, **54**, 5907–5914.

(379) K. Suzuki, A. Kobayashi, S. Kaneko, K. Takehira, T. Yoshihara, H. Ishida, Y. Shiina, S. Oishi and S. Tobita, *Phys. Chem. Chem. Phys.*, 2009, **11**, 9850–9860.

(380) J.-L. Bredas, *Mater. Horiz.*, 2014, **1**, 17–19.

(381) C. M. Cardona, W. Li, A. E. Kaifer, D. Stockdale and G. C. Bazan, *Adv. Mater.*, 2011, **23**, 2367–2371.

(382) J. P. Claude, K. M. Omberg, D. S. Williams and T. J. Meyer, *J. Phys. Chem. A*, 2002, **106**, 7795–7806.

(383) M. J. Lundqvist, E. Galoppini, G. J. Meyer and P. Persson, *J. Phys. Chem. A*, 2007, **111**, 1487–1497.

(384) R. E. Piau, T. Guillon, E. Lebon, N. Perrot, F. Alary, M. Boggio-Pasqua, J.-L. Heully, A. Juris, P. Sutra and A. Igau, *New J. Chem.*, 2012, **36**, 2484–2492.

(385) B. J. Coe, E. C. Harper, M. Helliwell and Y. T. Ta, *Polyhedron*, 2011, **30**, 1830–1841.

(386) E. Rousset, D. Chartrand, I. Ciofini, V. Marvaud and G. Hanan, *Chem. Commun.*, 2015, **51**, 9261–9264.

(387) V. Leigh, W. Ghattas, R. Lalrempuia, H. Müller-Bunz, M. T. Pryce and M. Albrecht, *Inorg. Chem.*, 2013, **52**, 5395–5402.

(388) M. Schwalbe, B. Schäfer, H. Görls, S. Rau, S. Tschierlei, M. Schmitt, J. Popp, G. Vaughan, W. Henry and J. G. Vos, *Eur. J. Inorg. Chem.*, 2008, **2008**, 3310–3319.

(389) T. X. Nguyen, S. Landgraf and G. Grampp, *J. Photochem. Photobiol. B: Biology*, 2017, **166**, 28–34.

(390) B. Durham, L. P. Pan, J. E. Long and F. Millett, *Biochemistry*, 1989, **28**, 8659–8665.

(391) D. Escudero, *Acc. Chem. Res.*, 2016, **49**, 1816–1824.

(392) G. McLendon, *Acc. Chem. Res.*, 1988, **21**, 160–167.

(393) M. Munakata, L. P. Wu and T. Kuroda-Sowa, in *Adv. Inorg. Chem.* Elsevier, 1998, vol. 46, pp. 173–303.

(394) C.-L. Chen, B.-S. Kang and C.-Y. Su, *Aust. J Chem.*, 2006, **59**, 3–18.

(395) H. R. Dias and S. Singh, *Inorg. Chem.*, 2004, **43**, 7396–7402.

(396) S. Sailaja and M. Rajasekharan, *Inorg. Chem.*, 2003, **42**, 5675–5684.

(397) M. Pascu, F. Tuna, E. Kolodziejczyk, G. I. Pascu, G. Clarkson and M. J. Hannon, *Dalton Trans.*, 2004, 1546–1555.

(398) C.-L. Chen, C.-Y. Su, Y.-P. Cai, H.-X. Zhang, A.-W. Xu, B.-S. Kang and H.-C. zur Loye, *Inorg. Chem.*, 2003, **42**, 3738–3750.

(399) A. G. Young and L. R. Hanton, *Coord. Chem. Rev.*, 2008, **252**, 1346–1386.

(400) A. Kyono, M. Kimata and T. Hatta, *Inorganica Chim. Acta*, 2004, **357**, 2519–2524.

(401) L. Carlucci, G. Ciani, F. Porta, D. M. Proserpio and L. Santagostini, *Angew. Chem. Int. Ed.*, 2002, **41**, 1907–1911.

(402) F. Zhang, S. A. Baudron and M. W. Hosseini, *Cryst. Eng. Comm.*, 2017, **19**, 4393–4400.

(403) A. N. Khlobystov, A. J. Blake, N. R. Champness, D. A. Lemenovskii, A. G. Majouga, N. V. Zyk and M. Schröder, *Coord. Chem. Rev.*, 2001, **222**, 155–192.

(404) G. K. Patra and I. Goldberg, *Cryst. Growth Des.*, 2003, **3**, 321–329.

(405) M. Maekawa, H. Konaka, Y. Suenaga, T. Kuroda-Sowa and M. Munakata, *J. Chem. Soc., Dalton Trans.*, 2000, 4160–4166.

(406) Y. Ling, F.-P. Zhai, M.-L. Deng, D. Wu, Z.-X. Chen, X.-F. Liu, Y.-M. Zhou and L.-H. Weng, *Cryst. Eng. Comm.*, 2012, **14**, 1425–1431.

(407) Y. Ling, Z.-X. Chen, Y.-M. Zhou, L.-H. Weng and D.-Y. Zhao, *Cryst. Eng. Comm.*, 2011, **13**, 1504–1508.

(408) Q.-G. Zhai, M.-C. Hu, S.-N. Li and Y.-C. Jiang, *Inorganica Chim. Acta*, 2009, **362**, 1355–1357.

(409) J.-P. Zhang, Y.-Y. Lin, X.-C. Huang and X.-M. Chen, *J. Am. Chem. Soc.*, 2005, **127**, 5495–5506.

(410) A. Wang, C. Merkens and U. Englert, *Cryst. Eng. Comm.*, 2015, **17**, 4293–4300.

(411) C. Merkens, N. Becker, K. Lamberts and U. Englert, *Dalton Trans.*, 2012, **41**, 8594–8599.

(412) B. Kilduff, D. Pogozhev, S. A. Baudron and M. W. Hosseini, *Inorg. Chem.*, 2010, **49**, 11231–11239.

(413) D. Pogozhev, S. A. Baudron and M. W. Hosseini, *Inorg. Chem.*, 2009, **49**, 331–338.

(414) A. D. Burrows, K. Cassar, M. F. Mahon and J. E. Warren, *Dalton Trans.*, 2007, 2499–2509.

(415) M. Marmier, G. Cecot, A. V. Vologzhanina, J. L. Bila, I. Zivkovic, H. M. Ronnow, B. Nafradi, E. Solari, P. Pattison, R. Scopelliti et al., *Dalton Trans.*, 2016, **45**, 15507–15516.

(416) J. R. Stork, V. S. Thoi and S. M. Cohen, *Inorg. Chem.*, 2007, **46**, 11213–11223.

(417) M. Kondracka and U. Englert, *Inorg. Chem.*, 2008, **47**, 10246–10257.

(418) Q. Guo, C. Merkens, R. Si and U. Englert, *Cryst. Eng. Comm.*, 2015, **17**, 4383–4393.

(419) L. Carlucci, G. Ciani, S. Maggini, D. M. Proserpio and M. Visconti, *Chem. Eur. J.*, 2010, **16**, 12328–12341.

(420) M. Karsch, H. Lund, A. Schulz, A. Villinger and K. Voss, *Eur. J. Inorg. Chem.*, 2012, **2012**, 5542–5553.

(421) A. Mazel, S. A. Baudron and M. W. Hosseini, *Cryst. Eng. Comm.*, 2017, **19**, 897–900.

(422) E. Baranoff, B. F. Curchod, J. Frey, R. Scopelliti, F. Kessler, I. Tavernelli, U. Rothlisberger, M. Grätzel and M. K. Nazeeruddin, *Inorg. Chem.*, 2011, **51**, 215–224.

(423) K. P. Zanoni, B. K. Kariyazaki, A. Ito, M. K. Brennaman, T. J. Meyer and N. Y. Murakami Iha, *Inorg. Chem.*, 2014, **53**, 4089–4099.

(424) N. A. Al-Rawashdeh, S. Chatterjee, J. A. Krause and W. B. Connick, *Inorg. Chem.*, 2013, **53**, 294–307.

(425) N. Zabarska, J. G. Vos and S. Rau, *Polyhedron*, 2015, **102**, 173–175.

(426) H. Huang, B. Yu, P. Zhang, J. Huang, Y. Chen, G. Gasser, L. Ji and H. Chao, *Angew. Chem. Int. Ed.*, 2015, **127**, 14255–14258.

(427) J. Demas, *J. Phys. Chem.*, 1971, **75**, 991–1024.

(428) S. Fery-Forgues and D. Lavabre, *J. Chem. Educ.*, 1999, **76**, 1260–1264.

(429) K. Nakamaru, *Bull. Chem. Soc. Jpn.*, 1982, **55**, 2697–2705.

(430) H. Ishida, S. Tobita, Y. Hasegawa, R. Katoh and K. Nozaki, *Coord. Chem. Rev.*, 2010, **254**, 2449–2458.

(431) N. Greenham, I. Samuel, G. Hayes, R. Phillips, Y. Kessener, S. Moratti, A. Holmes and R. Friend, *Chem. Phys. Lett.*, 1995, **241**, 89–96.

(432) V. V. Pavlishchuk and A. W. Addison, *Inorganica Chim. Acta*, 2000, **298**, 97–102.

(433) J. C. Curtis, B. P. Sullivan and T. J. Meyer, *Inorg. Chem.*, 1980, **19**, 3833–3839.

Chapter 7

Appendix

7.1 Characterisation data

Relevant characterisation data is contained in electronic form in a CD at the end of this thesis.

7.2 Publications arising from work in this PhD

7.2.1 Publications as primary author

1. Enhancing the Photoluminescence Quantum Yields of Blue-Emitting Cationic Iridium(III) Complexes Bearing Bisphosphine Ligands. Diego Rota Martir, Ashu K. Bansal, Vincent Di Mascio, David B. Cordes, Adam F. Henwood, Alexandra M. Z. Slawing, Paul C. J. Kamer, Laura Martinez-Sarti, Antonio Pertegàs, Henk J. Bolink, Ifor D. W. Samuel and Eli Zysman-Colman, *Inorg. Chem. Front.* **2016**, 3, 218-235. Selected as the front cover: *Inorg. Chem. Front.* **2016**, 3, 167

2. Exploring the Self-Assembly and Energy Transfer of Dynamic Supramolecular Iridium-Porphyrin Systems. Diego Rota Martir, Gordon J. Hedley, David B. Cordes, Alexandra M.Z. Slawin, Daniel Escudero, Denis Jacquemin, Tamara Kosikova, Douglas Philp, Daniel M. Dowson, Sharon E. Ashbrook, Ifor D. W. Samuel and Eli Zysman-Colman, *Dalton Trans.* **2016**, 45, 17195-17205

3. Chiral Iridium(III) Complexes in Light-Emitting Electrochemical Cells: Exploring the Impact of Stereochemistry on the Photophysical Properties and Device Performances. Diego Rota Martir, Cristina Momblona, Antonio Pertegàs, David B. Cordes, Alexandra M.

Z. Slawin, Henk J. Bolink and Eli Zysman-Colman, *ACS Appl. Mater. Interfaces*, **2016**, 8, 33907-33915

4. Photoinduced Electron Transfer in Supramolecular Ruthenium–Porphyrin Assemblies. Diego Rota Martir, Mattia Averardi, Daniel Escudero, Denis Jacquemin and Eli Zysman-Colman, *Dalton Trans.* **2017**, 46, 2255-2262

5. Homochiral Emissive Λ_8- and Δ_8-$[Ir_8Pd_4]^{16+}$ Supramolecular Cages. Diego Rota Martir, Daniel Escudero, Denis Jacquemin, David B. Cordes, Alexandra M. Z. Slawin, Herbert A. Fruchtl, Stuart L. Warriner and Eli Zysman-Colman, *Chem. Eur. J.* **2017**, 23, 14358-14366. Article highlighted in Science Trends; https://sciencetrends.com/supramolecular-self-assembly-photoactive-cages/

6. Multimetallic and Mixed Environment Iridium(III) Complexes: A Modular Approach to Luminescence Tuning Using a Host Platform. Victoria E. Pritchard, Diego Rota Martir, Eli Zysman-Colman and Michaele J. Hardie, *Chem. Eur. J.* **2017**, 23, 8839-8849 (hot paper). Selected as the frontespiece: **2017**, 23, 8839

7. Supramolecular Iridium(III) Assemblies. Diego Rota Martir and Eli Zysman-Colman, *Coord. Chem. Rev.* **2018**, 364, 86-117

8. A Luminescent $[P4_4Ru_8]^{24+}$ Supramolecular Cage. Diego Rota Martir, David B. Cordes, Alexandra M. Z. Slawin, Daniel Escudero, Denis Jacquemin, Stuart L. Warriner and Eli Zysman-Colman, *Chem. Commun.* **2018**, accepted manuscript

9. Photoinduced Energy- and Electron- Transfer Between a Photoactive Cage Based on a Thermally Activate Delayed Fluorescence Ligand and Encapsulated Fluorescent Dyes. Diego Rota Martir, Antonella Pizzolante, Daniel Escudero, Denis Jacquemin, Stuart L. Warriner and Eli Zysman-Colman, *ACS Appl. Energy Mater.* **2018**, accepted manuscript

7.2.2 Publications as co-author

10. Homochiral Self-Sorted and Emissive Ir^{III} Metallo-Cryptophanes. Victoria E. Pritchard, Diego Rota Martir, Samuel Oldknow, Shumpei Kai, Shuichi Hiraoka, Nikki J. Cookson, Eli Zysman-Colman, and Michaele J. Hardie, *Chem. Eur. J.* **2017**, 23, 6290-6294

11. Tuning the Optical Properties of Silicon Quantum Dots via Surface Functionalization with Conjugated Aromatic Fluorophores. Mohammed Abdelhameed, Diego Rota Martir, Shaliman Chen, William Z. Xu, Olabode O. Oyeneye, Subrata Chakrabarti, Eli Zysman-Colman, and Paul A. Charpentier, *Sci. reports* **2018**, 8, 3050

12. Molecular Design Strategy for a Two-Component Gel Based on a Thermally Activated Delayed Fluorescence Emitter. Pachai Rajamalli, Diego Rota Martir, and Eli Zysman-Colman, *ACS Appl. Energy Mater.* **2018**, 1(2), 649

13. Pyridine-Functionalized Carbazole Donor and Benzophenone Acceptor Design for Thermally Activated Delayed Fluorescence Emitters in Blue Organic Light-Emitting Diodes. Pachai Rajamalli, Diego Rota Martir, and Eli Zysman-Colman, *J. Photon. Energy* **2018**, 8(3), 032106

7.2.3 Journals cover images

Front cover: *Inorg. Chem. Front.* **2016**, 3, 167

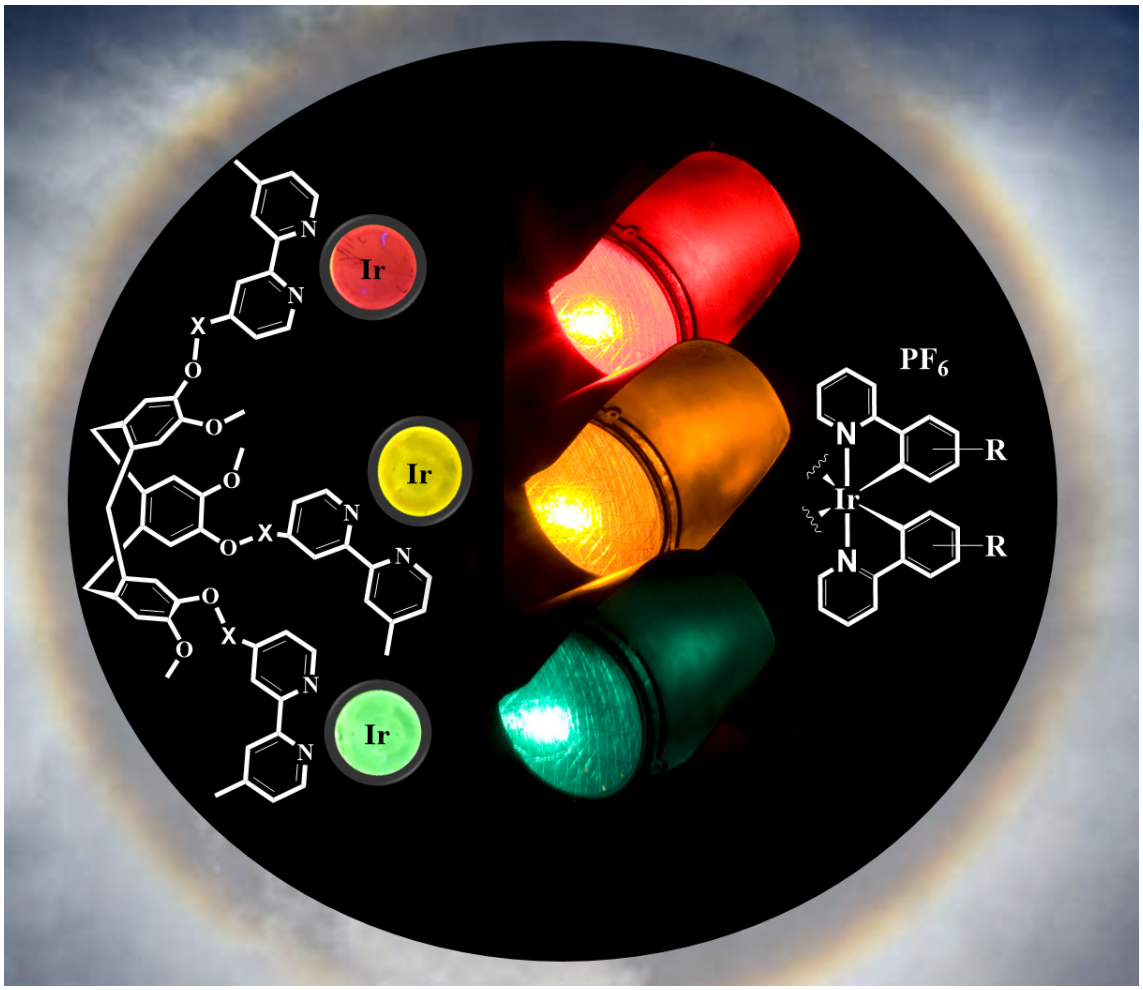

Frontespiece: *Chem. Eur. J.* **2017**, 23, 8839

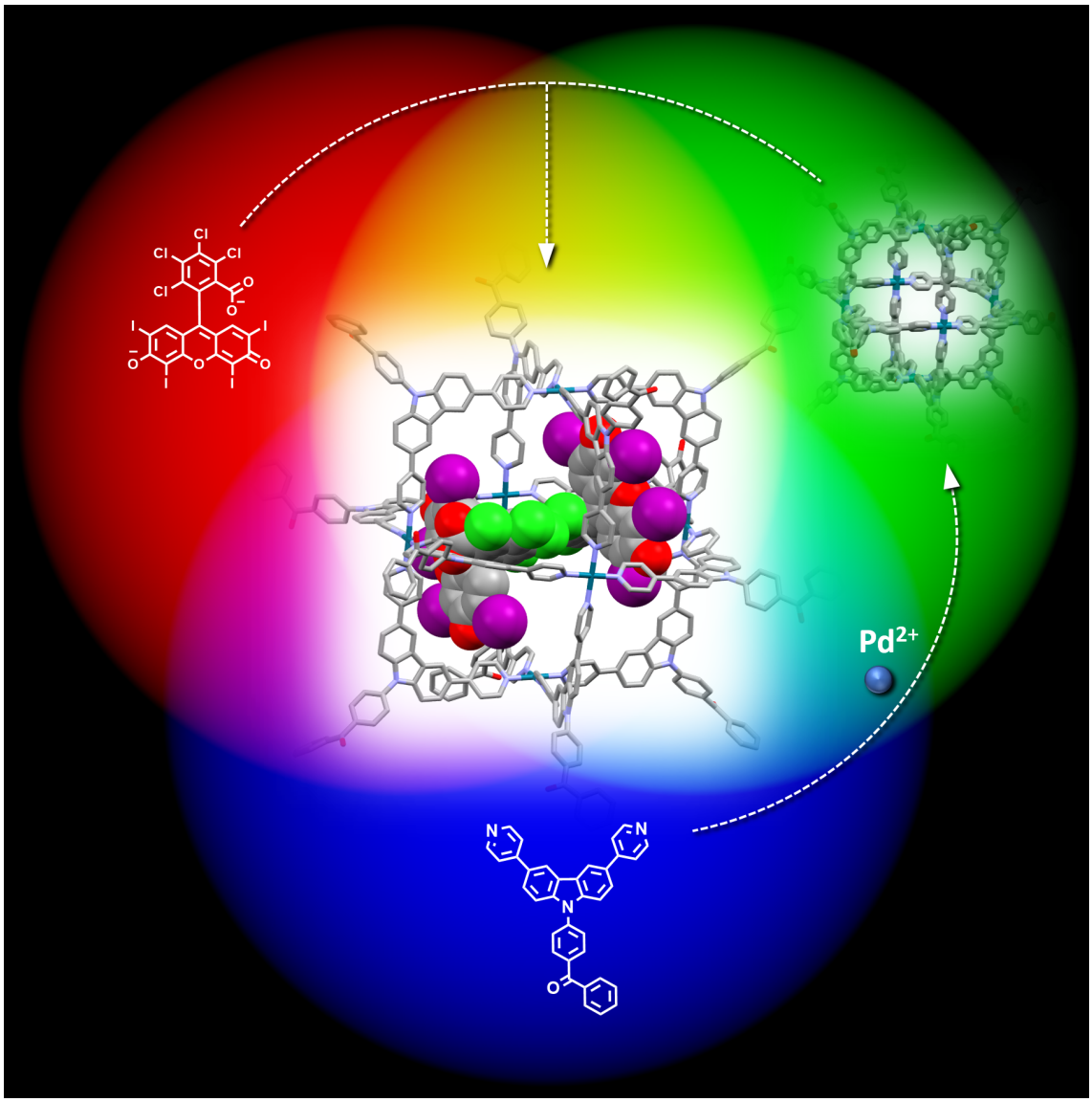

Cover image: *ACS. Appl. Energy Mater.* **2018**, accepted manuscript

7.3 Contributions to conferences

7.3.1 Oral contributions

1. RSC photochemistry meeting, 19 June 2015, Newcastle (UK). Enhancing The Photoluminescent Quantum Yields of Blue-Emitting Cationic Iridium(III) Complexes Bearing Bisphosphine Ligands.

2. Symposium on current challenges in supramolecular artificial photosynthesis, 2-4 September 2015, Gdansk (Poland). Controlled Energy Transfer in Dynamic Supramolecular Iridium-Porphyrin Systems.

3. Core-to-Core Leverhulme conference, fourth joint workshop on organic electronics of highly-correlated molecular systems, 10-12 April 2016, St Andrews (UK). Is Stereochemistry an Important Consideration in Solid-State Lighting Applications?

4. 6^{th} EuCheMs congress, 11-15 September 2016, Seville (Spain). Is Stereochemistry an Important Consideration in Solid-State Lighting Applications?

5. 43^{rd} International Conference on Coordination Chemistry (ICCC 2018), 01-04 August 2018, Sendai (Japan). Phosphorescent Supramolecular Cages

7.3.2 Poster contributions

1. 2^{nd} Asian-European Symposium on Organic Electronics, 27-29 October 2015, Edinburgh (UK). Enhancing The Photoluminescent Quantum Yields of Blue-Emitting Cationic Iridium(III) Complexes Bearing Bisphosphine Ligands.

2. 21^{st} International Symposium on Photochemistry and Photophysics of Coordination Compounds (ISPPCC), 5-9 July 2015, Krakow (Poland). Enhancing The Photoluminescent Quantum Yields of Blue-Emitting Cationic Iridium(III) Complexes Bearing Bisphosphine Ligands.

3. RSC Molecular photophysics in the North-East symposium, 18-19 April 2016, Newcastle (UK). Exploring the Self-Assembly and The Energy Transfer in Dynamic Supramolecular Iridium-Porphyrin Systems. Winner of the *Proctor and Gamble* award for the **best poster presentation**.

4. RSC Macrocyclic and Supramolecular Meeting (MASC), 15-16 December 2016, Edinburgh (UK). Homochiral Emissive Supramolecular $[Ir_8Pd_4]^{16+}$ Cages. Winner of the *Chem.*

Commun award for the **best poster**.

5. International Symposium on Macrocyclic and Supramolecular Chemistry (ISMSC) in conjunction with ISACS: challenges in organic materials and supramolecular chemistry, 2-6 July 2017, Cambridge (UK). Homochiral Emissive Supramolecular $[Ir_8Pd_4]^{16+}$ Cages.

6. Application of Photoactive Coordination Compounds (APCC) conference, 7-8 July 2017, St Andres, (UK). Homochiral Emissive Supramolecular $[Ir_8Pd_4]^{16+}$ Cages. Winner of the *J. Mater. Chem. C* award for the **best poster**.

7. 3rd Japan-UK Symposium on Coordination Chemistry, 1-2 May 2018, St Andrews, (UK). Homochiral Emissive Supramolecular $[Ir_8Pd_4]^{16+}$ Cages. Winner of the *Chem. Commun.* award for the **best poster**.

7.4 Exchange experiences

7.4.1 Exchange at National Chemical Laboratory, Pune

During the second year of my PhD I spent three months (June - August 2016) in Pune (India), working at CSIR-National Chemical Laboratory (NCL) in the research group of Dr. Nitin T Patil. This exchange was financially supported through a EPSRC-funded UKIERI mobility grant. During my stay in Dr. Patil's laboratory I investigated N,C-chelate, four-coordinate organoborons as ligand scaffolds for self-assembly. As part of this collaborative work I also studied the optoelectronic properties of a family of organoboron compounds prepared by Aslam C. Shaikh. The preparation of OLED devices by using these emitting materials is now under investigation in our laboratory in St Andrews.

7.4.2 Exchange at The University of Tokyo

Awarded with a RSC-funded research mobility grant, I worked from September to December 2017 at The University of Tokyo in the laboratory of Prof. Makoto Fujita. The following is a short summary of the work I carried out during this exchange.

Fujita and co-workers previously investigated the photo-oxidation of adamantane and of other alkane substrates such as cyclooctane, cycloheptane and cyclohexane, into the cavity of a tetrahedral cage of composition $[Pd_4L_6]^{12+}$ (where L is 2,4,6-tri(pyridine-4-yl)-1,3,5-triazine, tpt). It was discovered that the photo-oxidation of the guest compounds was promoted through photoinduced electron transfer from the encapsulated guests to the $[Pd_4L_6]^{12+}$ cage yielding, in the presence of oxygen, the corresponding guest alcohols.

However, due to the inefficient electronic interactions between the bound molecules and the cage, a low total yield of photoproduct per cage of around 25% was achieved.[208]

During my stay in Tokyo I investigated different methodologies to enhance the yield of photo-oxidation of guest compounds encapsulated into the $[Pd_4L_6]^{12+}$ cage, and to promote novel reactivities. As a result of this work, we have found that the photo-irradiation of the $[Pd_4L_6]^{12+}$ cage co-encapsulating nitrobenzene as a catalytic electron-acceptor and the alkane guests promotes a quantitative oxidation of the alkane compounds, yielding the corresponding alcohols and ketones. Interestingly, this approach could be easily extended to promote the photo-oxidation of other guest compounds such as benzene and toluene. We have found the photo-oxidation of toluene guest particularly interesting. Indeed, when toluene was encapsulated into the cage and photoirradiated in the presence of nitrobenzene, the selective oxidation of the methyl sp^3 carbon was promoted to yield, quantitatively, benzaldehyde as the main product and a small amount of benzoic acid. However, when toluene was encapsulated into the cage and photoirradiated without the addition of nitrobenzene, the oxidation of both the methyl sp^3 and aryl sp^2 carbons was promoted, yielding a mixture of benzaldehyde, benzoic acid, o-, m- and p-cresol and benzylic alcohol. As a result, nitrobenzene not only enhances the yields of the photo-oxidation of compounds bound to the $[Pd_4L_6]^{12+}$ cage, but it is also able to drive cavity-directed photo-reactions following selective paths.

Kiyohiro Adachi (a PhD student in Fujita's group) is presently investigating this research area. We have a high expectation to extend this methodology to promote novel photoreactivity involving a wide range of guest compounds bound to photoactive supramolecular cages.